Universitat Autònoma de Barcelona

Stellar activity and exoplanets ofM dwarfs from CARMENES visible to near-infrared spectroscopy

Marina Lafarga Magro

Universitat Autònoma de Barcelona

Institute of Space Sciences
CSIC IEEC

Stellar activity and exoplanets of M dwarfs from CARMENES visible to near-infrared spectroscopy

Tesi doctoral presentada per optar al títol de

Doctora en Física

Autora
Marina Lafarga Magro

Director
Ignasi Ribas Canudas

Tutor acadèmic
Lluís Font Guiteras

Programa de Doctorat en Física

Departament de Física

Universitat Autònoma de Barcelona

2020

Resum

Després del descobriment dels primers exoplanetes fa unes tres dècades, la detecció i caracterització de companys planetaris s'ha convertit en un tema de recerca prominent, especialment la cerca de planetes semblants a la Terra, cossos rocosos que orbiten a la zona habitable (HZ) de les seves estrelles hostes. Un dels principals mètodes utilitzats per trobar i caracteritzar exoplanetes és la tècnica de l'espectroscòpia Doppler o velocitat radial (RV), basada en l'ús d'espectres estel·lars per mesurar canvis periòdics en la RV d'una estrella causats per l'atracció gravitatòria d'un exoplaneta en òrbita.

Actualment, la variabilitat intrínseca de les estrelles hostes és el principal repte en l'estudi d'exoplanetes. Les estrelles no són cossos invariables i homogenis, sinó que presenten variabilitat en diferents escales de temps. La més rellevant és l'activitat magnètica estel·lar, que inclou fenòmens com ara taques o fàcules que apareixen a la superfície de l'estrella i estan modulades per la seva rotació. Aquests fenòmens distorsionen els espectres estel·lars, introduint biaixos en les RVs prou grans com per amagar o fins i tot imitar el senyal causat per un planeta. Per tant, per continuar detectant i estudiant exoplanetes de baixa massa, és clau aconseguir una millor comprensió d'aquests fenòmens estel·lars i els seus efectes en les nostres observacions.

Aquesta tesi se centra en l'estudi dels efectes de l'activitat estel·lar en observacions espectroscòpiques d'estrelles fredes obtingudes amb l'instrument CARMENES. CARMENES és un espectrògraf d'alta resolució capaç d'observar el rang de longitud d'ona visible i infraroig proper. Està realitzant un estudi de més de 300 nanes M, les estrelles amb menor massa de la seqüència principal, amb l'objectiu primordial de detectar exoplanetes petits.

En primer lloc, hem desenvolupat un codi que implementa el mètode de la funció de correlació creuada (CCF) per mesurar RVs i indicadors d'activitat estel·lar en observacions d'alta resolució, i l'hem aplicat a les dades de CARMENES. Aquest mètode utilitza màscares binàries ponderades, un template estel·lar simplificat construït mitjançant la selecció de línies espectrals. Hem creat diverses màscares en funció del subtipus espectral i de la velocitat de rotació de l'estrella a analitzar.

A continuació, hem utilitzat els indicadors d'activitat derivats de la CCF, juntament amb altres indicadors d'activitat espectroscòpics, per analitzar les seves variacions temporals en una mostra de quasi 100 nanes M de diverses masses i nivells d'activitat. Aproximadament la meitat de les estrelles analitzades mostren RVs amb senyals d'activitat clars. Diferents indicadors són sensibles a l'activitat de manera diferent segons les característiques de l'estrella: indicadors cromosfèrics són més útils per a estrelles de baixa activitat, indicadors relacionats amb el canvi de RV amb longitud d'ona funcionen millor per a les estrelles més actives, i altres indicadors relacionats amb el canvi d'amplada de les línies fotosfèriques proporcionen resultats similars en tot tipus d'estrelles, però són especialment útils per a les més actives i de menor massa.

Finalment, hem analitzat els efectes de l'activitat sobre línies d'absorció individuals presents en l'espectre d'estrelles actives. Estudiant les correlacions entre les RVs de línies individuals i els indicadors d'activitat, podem classificar les línies observades segons la seva sensibilitat a l'activitat. Això ens permet seleccionar línies afectades de forma diferent per l'activitat i utilitzar-les per tornar a calcular RVs. Així obtenim RVs per a les quals mitiguem o incrementem el senyal d'activitat en diversos graus. També observem que les mateixes línies en diferents estrelles mostren diferent sensibilitat a l'activitat.

Abstract

After the discovery of the first exoplanets about three decades ago, the detection and characterization of planetary companions has become a prominent research topic, especially the search for Earth-like planets, rocky bodies orbiting in the habitable zone (HZ) of their host stars. One of the main methods used to find and characterise exoplanets is the Doppler spectroscopy or radial velocity (RV) technique, based on using stellar spectra to measure periodic changes in the RV of a star caused by the gravitational pull of an orbiting exoplanet.

Currently, the intrinsic variability of the host stars is the major challenge faced in the study of exoplanets. Stars are not quiet, homogeneous bodies, but display variability on different timescales, the most concerning being stellar magnetic activity, phenomena such as spots or faculae appearing on the stellar surface and modulated by the stellar rotation. These features distort the stellar spectra, introducing biases in our RVs that can be large enough to hide or even mimic the signal caused by a planet. Therefore, to continue detecting and studying low-mass exoplanets, a better understanding of these stellar phenomena and their effects on our observations is key.

This thesis is focused on the study of stellar activity effects on spectroscopic observations of cool stars obtained with the CARMENES instrument. CARMENES is a high-resolution spectrograph capable of observing on the visible and near-infrared wavelength ranges. It is performing a survey of over 300 M dwarfs, stars at the low-mass end of the main sequence, with the main goal of detecting small exoplanets.

Firstly, we developed a pipeline that implements the cross-correlation function (CCF) method to measure RVs and indicators of stellar activity on high-resolution observations, and applied it to the CARMENES survey data. This method uses weighted binary masks, a simplified stellar template built by selecting sharp spectral lines, of which we created different kinds depending on the spectral subtype and the rotational velocity of the target star.

We then used the activity indicators derived from the CCF, together with other spectroscopic activity proxies, to analyse their temporal variations in a sample of almost 100 M dwarfs with a range of masses and activity levels. We found that about half of the stars analysed show RVs with clear signals of activity. Different indicators trace activity differently depending on the characteristics of the star: chromospheric indicators are the most useful for low-activity stars, indicators related to the change in RV with wavelength work better for the most active stars, and other indicators related to the change in width of the photospheric lines provide similar results in all types of stars, but are especially useful for the most active and lowest-mass ones.

Finally, we analysed the effects of activity on individual absorption features present on the spectra of active stars. By studying the correlations between the individual line RVs and activity indicators, we are able to classify the observed lines according to their sensitivity to activity. This allow us to select differently affected lines and use them to recompute RVs for which we mitigate or enhance the activity signal to varying degrees. We also observe that the same lines on different stars show different sensitivities to activity.

Acknowledgements

La realització d'aquest treball no hagués estat possible sense el suport i guiatge del meu director de tesi. Gràcies, Ignasi, per donar-me l'oportunitat de dedicar-me a la recerca, pel teu temps i experiència, i sobretot per confiar en mi. Espero emportar-me part del teu optimisme allà on vagi. Gràcies al grup d'exoplanetes per tot el que he après aquí, i a totes les persones que he conegut durant aquest temps a l'ICE.

This thesis would not exist without the efforts of the countless people behind CARMENES, I express my deepest gratitude to everyone involved. Being part of this project has given me an exceptional experience and great expectations. I would like to thank Ansgar for welcoming me in Göttingen and giving me the opportunity of being part of his group during some months, and to Mathias for useful discussions and always being willing to help. Thank you Martin for always being so encouraging and your invitation to visit Heidelberg.

Vull agrair a tots els companys de doctorat el bon ambient i tots els moments compartits dins i fora de la feina. Nacho, has sido un gran compi de despacho. Andrea, Anna, Mariona, David, no m'ho hagués passat tan bé sense vosaltres, gràcies per la vostra amistat. Berta, Oriol, gràcies pels vostres ànims sempre i des d'on sigui. Special thanks to Tako and the wonderful Hala and Moritz for their time and for making me feel at home.

Per últim, gràcies a la meva família i amics pel seu suport. No estaria aquí si els meus pares no haguessin cregut que aprendre coses era bona idea per espavilar-se en aquest món. Als meus pares, l'Alba i el Michele, gràcies per tot.

Aquest treball ha comptat amb suport econòmic del Ministerio de Ciencia e Innovación i del Fons Social Europeu a través d'un contracte FPI amb referència BES-2015-073708.

Contents

List of Figures

List of Tables

Chapter 1

Introduction

Less than 30 years ago, the discovery of the first planets outside of the solar system opened up the field of exoplanet research. Since then, we have found a wide variety of exoplanets orbiting different types of stars. The improvement in the precision of the instruments used to find and characterise exoplanets, together with the development of better analysis techniques, is paving the way towards the detection of Earth-like exoplanets capable of harbouring life.

So far, the main methods used to find and study exoplanets rely on observing the light coming from the photosphere of the stars, rather than directly imaging the planets themselves. Stars outshine the light coming from planets by a factor of more than a million. This high star-to-planet brightness contrast makes direct imaging of exoplanets very challenging. Currently, it is only possible to directly detect young, massive planets on wide orbits around their host stars, because they are still warm, and hence bright, and show a large sky projected separation from the star, which facilitates their observation. Direct detections of exoplanets are interesting because they allow the determination of their physical parameters, such as their temperature and pressure, and their chemical composition and atmospheric structure. However, due to the current limitations of the technique, most exoplanets have been detected with alternative indirect methods. The presence of an orbiting exoplanet induces periodic changes on the observed light, which allow us to indirectly infer its existence. The most successful methods are the Doppler spectroscopy and the photometric transit technique, with about 900 and 3000 discoveries, respectively, of the more than 4000 exoplanets confirmed to date[1].

The Doppler spectroscopy or radial velocity (RV) method consists on using stellar spectra to detect, as its name indicates, tiny periodic Doppler shifts caused by the wobble of the star as a result of the gravitational pull of an orbiting exoplanet. It pioneered the discovery of the first exoplanet orbiting a main sequence star, 51 Peg b (Mayor and Queloz, 1995), and since then, it has become one of the main methods

[1] http://exoplanet.eu/ as of August 2020

to detect, confirm, and characterise planetary companions. The photometric transit technique detects periodic dips in the observed stellar flux that occur as an exoplanet transits between its host star and our line of sight. Photometric ground-based, but especially, space-based missions such as *CoRoT, Kepler, K2*, or currently *TESS*, have contributed with thousands of detections using this method.

Aside from orbital parameters, from RV measurements one can obtain the minimum mass of an exoplanet, while photometric transits are used to determine the exoplanet's radius. The combination of mass estimates from spectroscopic measurements together with radii from photometry permits the determination of bulk densities of planets, which places constraints on their physical structure and composition. In turn, this characterisation is needed to study planet formation and evolution. Transiting exoplanets are also interesting targets because their atmospheres can be measured. As a planet transits its host star, part of the light reaching us has gone through the atmosphere of the planet, and therefore, contains information of the different constituents present, as well as about its structure, what is known as transmission spectrum. As the planet hides behind the star, information can also be obtained from its emission spectrum. Reliable detections of planetary atmospheres and modelling of the different physical and chemical processes are key if we want to understand and characterise transiting exoplanets, and the first steps to detect biosignatures in the coming future.

Currently, one of the main problems faced when trying to find and study exoplanets is the intrinsic variability of the host stars. Stars are far from being homogeneous, static bodies, but rather show varying features on their surfaces that change the light they emit. These sources of variability include oscillations, granulation, and features related to the stellar magnetic fields, such as cool spots or hot faculae. Phenomena related to magnetic effects are collectively called stellar magnetic activity or stellar 'jitter'. Observations of stellar light contain the signals induced by exoplanets as well as this stellar variability, which can be large enough to overshadow the planet signatures. Moreover, since stars rotate, stellar activity often appears as periodic signals modulated with the stellar rotation period, which can be mistakenly attributed to the periodic signal caused by a planet. Therefore, it is critical to understand how astrophysical variability affects our measurements.

The remainder of this introduction gives an overview of the basic topics needed to understand the work presented in this thesis, which focuses on the effects of stellar activity on spectroscopic observations of low-mass stars. In Sect. 1.1, we explain the basics of the Doppler spectroscopy technique, which we apply in the analysis of our observations. Sect. 1.2 describes the main manifestations of stellar variability that imprint spectroscopic observations with stellar signals. Throughout this thesis, we will use spectroscopic observations of M dwarf stars, stars with the smallest mass and

coolest temperature in the main sequence, obtained with the CARMENES instrument. We introduce the CARMENES project in Sect. 1.3. Finally, Sect. 1.4 summarises the structure and contents of the rest of the thesis.

1.1 Doppler spectroscopy

The Doppler spectroscopy or RV technique consists on measuring the movement of a star induced by the gravitational pull of an orbiting companion. As the star wobbles in its orbit around the centre of mass of the star-planet system, the light emitted along our line of sight is affected by the Doppler effect, i.e., the light's wavelength is periodically blueshifted and redshifted as the star moves towards and away from us. To measure those shifts we rely on the absorption lines of the stellar spectrum. For a specific observed line with wavelength λ, the relative velocity shift RV is given by the Doppler equation[2]

$$\frac{\lambda - \lambda_0}{\lambda_0} = \frac{\mathrm{RV}}{c}, \tag{1.1}$$

where λ_0 is the wavelength at rest, i.e., the wavelength in the star's reference frame, and c is the speed of light.

By measuring these Doppler shifts in time-series observations of the stellar spectra, we can build an RV curve that describes the movement of the star with time. We know that a planet and a star in a bound system orbit their common centre of mass in Keplerian orbits. By modelling the RV curve, we can determine several orbital parameters, like the orbital period P, the semi-amplitude of the reflex motion of the star K, the planet's orbit eccentricity e, its semi-major axis a_p, and, if the orbit is not perfectly circular, the argument of the periastron of the orbit. From orbital mechanics, the semi-amplitude of the stellar motion K can be expressed as

$$K = \frac{2\pi}{P} \frac{a_\mathrm{s} \sin i}{\left(1 - e^2\right)^{1/2}}, \tag{1.2}$$

where a_s is the semi-major axis of the stellar orbit, and i is the inclination of the orbital plane with respect to the observer. We can relate K with the mass of the star M_s and the planet M_p using Kepler's third law

$$P^2 = \frac{4\pi^2 a^3}{G\left(M_\mathrm{s} + M_\mathrm{p}\right)}, \tag{1.3}$$

together with the identities $a = a_\mathrm{s} + a_\mathrm{p}$ and $M_\mathrm{s} a_\mathrm{s} = M_\mathrm{p} a_\mathrm{p}$, where G is the gravitational

[2] We use the non-relativistic version because typically RV $\ll c$.

constant, and a is the semi-major axis of the orbital ellipse. This yields

$$K = \left(\frac{2\pi G}{P}\right)^{1/3} \frac{M_\mathrm{p} \sin i}{\left(M_\mathrm{s} + M_\mathrm{p}\right)^{2/3}} \left(1 - e^2\right)^{-1/2}. \tag{1.4}$$

If the stellar mass M_s is known, then it is possible to estimate the planet mass. If we assume that $M_\mathrm{p} \ll M_\mathrm{s}$, then the previous equation can be easily transformed into

$$M_\mathrm{p} \sin i = \left(\frac{P}{2\pi G}\right)^{1/3} K M_\mathrm{s}^{2/3} \left(1 - e^2\right)^{1/2}. \tag{1.5}$$

Actually, since we are only able to measure the RV of the star, i.e., the velocity of the star in its orbit along our line of sight, we can only estimate the minimum mass of the planet $M_\mathrm{p} \sin i$. Depending on the inclination of the orbit with respect to our line of sight, the mass of the planet could be significantly larger than $M_\mathrm{p} \sin i$. However, since orbital orientations are randomly distributed in space, edge-on systems (i close to $90°$) are more common than pole-on configurations (i close to $0°$), so we statistically expect the measured minimum masses not to differ significantly from the true planetary mass. Moreover, inclinations can be measured for the case of eclipsing (transiting) planets.

The gravitational effect exerted by a planet on a star increases with decreasing stellar-to-planet mass ratio and with decreasing distance. As we can see from the previous equations, this translates into the amplitude of the RV, K, increasing for decreasing stellar-to-planet mass ratio, and for decreasing star-to-planet distance (or decreasing rotational period). This makes this method more sensitive to massive, close-in planets, which induce larger RV variations. Indeed, the first exoplanets detected with this technique were the so-called hot Jupiters, planets with a mass close to that of Jupiter but that are orbiting very close to their host star (with periods shorter than 10 d, usually at $\lesssim 0.1$ AU), such as 51 Peg b. They can induce RVs of the order of a few tens of $\mathrm{m\,s^{-1}}$. In comparison, Jupiter in the solar system orbits at ~ 5 AU from the Sun and induces RV shifts of the order of $10\,\mathrm{m\,s^{-1}}$. To detect planets with smaller masses and orbiting at larger distances from the star, precisions of the order of the $\mathrm{m\,s^{-1}}$ are required. Even better precisions are needed if we want to detect an Earth analogue, a planet with the mass of the Earth orbiting a Sun-like star at 1 AU, which would induce RV variations of the order of $10\,\mathrm{cm\,s^{-1}}$. The period of the orbits also places constrains on the detectability of planets. Ideally, time coverage of more than one orbit is needed to detect a planet, so short-period planets are more easily found. Long-term monitoring surveys are necessary to detect planets in large orbits located far from the star.

The continuous detection of exoplanets of smaller masses has been possible with the improvement of the spectrographs used to measure RVs (Fischer et al., 2016). State-of-the-art instruments are stabilised, high-resolution, cross-dispersed echelle

spectrographs that allow precisions of the order of the $\mathrm{m\,s^{-1}}$ or better. They are located in ground-based facilities and hence observe in the visible and near-infrared spectral ranges. In cross-dispersed echelle spectrographs, the spectrum is obtained by dispersing the light entering the telescope with two dispersive elements with perpendicular dispersion directions. The main one is an echelle grating, a diffraction grating that is optimised for high diffraction orders. The higher the order, the larger is the dispersion, which means increased resolutions. High orders however overlap with each other, so that different wavelengths of different orders share the same spacial position. To avoid that, a second dispersive element known as the cross-disperser (such as a refraction prism or another diffraction grating with dispersion direction perpendicular to the echelle) is used, so that the different orders are spread across the direction perpendicular to the echelle dispersion direction.

The precision of the RV measured from a spectrum depends on the number of absorption lines present and the signal-to-noise (S/N) of the observation. Therefore, to maximise the number of lines available, spectrographs observe on broad wavelength ranges and have high-resolutions (resolving power $R = \lambda/\Delta\lambda \sim 100\,000$, where $\Delta\lambda$ is the minimum difference that can be distinguished at the wavelength λ), which can be achieved by cross-dispersed echelle instruments. They are employed with relatively large telescopes to obtain observations with high S/N. In order to minimise instrumental drifts, they have to be in controlled environments, and are usually housed in thermally-stabilised vacuum vessels.

Another important step towards high-precision RVs is the wavelength calibration of the observed spectrum. Several techniques exist. Cells containing a gas such as iodine (I_2) have been used for this purpose. The gas cell is placed on the path of the light entering the instrument, so that the absorption spectrum of the gas, which has been previously calibrated, is superimposed on the stellar spectrum (Marcy and Butler, 1992; Butler et al., 1996). Another approach is the simultaneous reference technique, in which the stellar spectrum and the spectrum of a calibrated emission lamp are recorded at the same time in a thermally- and pressure-stabilised spectrograph (Baranne et al., 1996). Each source of light goes through a different fibre, so that they are recorded on different positions on the spectrograph detector. These emission lamps typically have lines that cover wider wavelength ranges than gas cells, and their spectrum is not superimposed on the stellar one, allowing observations at lower S/Ns. Hollow-cathode lamps with well-calibrated emission lines (such as Th-Ar, Th-Ne, or U-Ne lamps) and Fabry-Pérot etalons are routinely used to obtain the wavelength solution of the observations and to track short-term instrumental RV drifts (Bauer, Zechmeister, and Reiners, 2015; Cersullo et al., 2019). Recently, laser-frequency combs, stable sources of light that provide a large number of lines evenly spaced in frequency with wavelengths known

to extreme precisions, are also starting to be used as calibration sources (e.g. Lo Curto et al., 2012; Coffinet et al., 2019; Petersburg et al., 2020).

Examples of high-precision instruments successfully used in the search for exoplanets in the last two decades are HARPS (High Accuracy Radial velocity Planet Searcher, Mayor et al., 2003) on the ESO 3.6 m telescope at La Silla Observatory, Chile, and its northen hemisphere twin HARPS-N (Cosentino et al., 2012) on the 3.6 m Telescopio Nazionale Galileo in La Palma, Spain. They observe on the visible range (from 380 nm to 690 nm) and have a resolution of $R = 115\,000$, which results in RV measurements with precisions at the m s^{-1} level. The next-generation of stabilised, high-resolution spectrographs with improved instrumentation such as EXPRES (EXtreme PREcision Spectrograph, Jurgenson et al., 2016), on the 4.3 m Lowell Discovery Telescope at the Lowell Observatory in the USA, or ESPRESSO (Echelle SPectrograph for Rocky Exoplanets and Stable Spectroscopic Observations, Pepe et al., 2010), on the Very Large Telescope array of four 8.2 m unit telescopes in Paranal Observatory in Chile, already on operation, are expected to achieve precisions of the order of a few tens of cm s^{-1}.

A number of high-precision ($R \sim 50\,000 - 100\,000$) spectrographs capable of observing on the near-infrared have also been recently developed. These instruments are suited to observe cool stars like M dwarfs, which emit most of their energy on wavelengths redder than solar-like stars and that have recently become the focus of several exoplanet searches (see Sect. 1.3.1). In this thesis we will use M dwarf observations obtained with one of these instruments, CARMENES (Calar Alto high-Resolution search for M dwarfs with Exo-earths with Near-infrared and optical Echelle Spectrographs, Quirrenbach et al., 2016; 2018), a high-resolution ($R \sim 100\,000$) spectrograph that covers the visible (520–960 nm) and the near-infrared (960–1710 nm) wavelength ranges (see details in Sect. 1.3.2).

Other examples of red-optical and near-infrared instruments include MAROON-X (M dwarf Advanced Radial velocity Observer Of Neighboring eXoplanets, $R \sim 80\,000$, $500 - 900$ nm, Seifahrt et al., 2018) at the 8 m Gemini North telescope in Hawaii, HPF (Habitable-Zone Planet Finder, $R \sim 55\,000$, $800 - 1280$ nm, Mahadevan et al., 2014) at the 10 m Hobby-Eberly Telescope in the USA, IRD (InfraRed Doppler, $R \sim 70\,000$, $970 - 1750$ nm, Kotani et al., 2014), at the 8.2 m Subaru Telescope in Hawaii, SPIRou (SpectroPolarimètre Infra-Rouge, $R \sim 75\,000$, $950 - 2500$ nm, Artigau et al., 2014; Donati et al., 2020) at the 3.6 m Canada-France-Hawaii-Telescope in Hawaii, a spectropolarimeter that can detect magnetic fields, GIANO-B ($R \sim 50\,000$, $950 - 2450$ nm, Oliva et al., 2006) on the 3.6 m Telescopio Nazionale Galileo, that can operate together with HARPS-N (known as GIARPS mode, Claudi et al., 2017), or spectrographs covering up to the 5300 nm like iSHELL ($R \sim 75\,000$, $1100 - 5300$ nm, Rayner et al., 2016) on the 3.2 m NASA InfraRed Telescope Facility in Hawaii.

1.2 Stellar variability

With the important advances experienced in the development of precise instrumentation, stellar variability has become the main challenge in detecting and characterising exoplanets. Stars show variability in the form of diverse phenomena. The most important sources of variability in low-mass stars (FGKM spectral type stars) are solar-like oscillations, surface granulation, magnetic features like spots and faculae, and long-term magnetic cycles. We refer to variability related to the stellar magnetic fields as stellar activity. These different manifestations of variability have a range of timescales and amplitudes, affecting our measurements to different extents.

Stellar activity is a result of the combination of stellar magnetic activity and photospheric dynamics. Magnetic fields on stars are thought to be maintained by a stellar dynamo (also called magnetohydrodynamical dynamo), which generates magnetic fields from the motion of an electrically conducting fluid (Parker, 1955). Depending on the characteristics of the star, different dynamo models exist. Magnetic fields on low-mass stars (from mid-F to early-M spectral types) are usually described by the so-called $\alpha\Omega$ dynamo, which seems to be able to describe the different phenomena related with the stellar magnetic field observed in the Sun (such as the appearance of highly magnetic regions like spots or the well known 11-year solar magnetic cycle). A key element of this mechanism is the existence of the tachocline, the boundary region between the inner radiative zone and the outer convective zone of the star (Spiegel and Zahn, 1992). Shear forces arise from the transition between the uniformly rotating radiative zone and the convective one, which experiences differential rotation, even in its lower layers. These forces are thought to store and amplify magnetic fields, and result in the source of the $\alpha\Omega$ dynamo. Stars with masses lower than $0.4 - 0.3\,M_{\odot}$ (which correspond to spectral types later than M3 V $-$ M4 V) are fully convective (Chabrier and Baraffe, 1997), so the dynamo mechanism is thought to be driven by turbulent motions within the convection zone, known as the α^2 dynamo (Durney, De Young, and Roxburgh, 1993), as opposed to a combination of convection and differential rotation as in hotter stars. However, the exact mechanism behind stellar magnetic fields in both partially and fully convective stars is not known (Charbonneau, 2020). Some observational studies even suggest that the tachocline could not be a critical element in the generation of magnetic fields in solar stars, because solar-like dynamos are observed in fully convective stars, which lack a tachocline (Wright and Drake, 2016; Wright et al., 2018). Since the stellar magnetic dynamo depends on the stellar rotation, the activity level of a star is observed to be related to its rotational velocity or period, with faster rotating stars showing larger activity levels (Noyes et al., 1984; Reiners, Schüssler, and Passegger, 2014; Newton et al., 2017). As low-mass stars evolve on the main sequence, they lose their initial angular momentum and spin down due to

magnetic braking (Schatzman, 1962; Mestel, 1968), which implies a decrease in their activity level with stellar age (Wilson, 1963; Kraft, 1967; Skumanich, 1972; Kiraga and Stepien, 2007).

With current instrumentation and data analysis techinques, we are reaching a point where stellar activity dominates over any other source of noise in RV measurements. Several efforts are being done within the exoplanet community to better understand these sources of variability and develop ways to mitigate these stellar signals, but there is no comprehensive solution, especially when it comes to magnetic features such as spots and faculae. In the next sections, we provide a summary of the main manifestations of stellar variability and some common strategies used to identify and mitigate their effects on RV measurements.

1.2.1 Solar-like oscillations

On short timescales, of the order of minutes to few hours, low-mass stars show solar-like oscillations (e.g. Leighton, Noyes, and Simon, 1962; Bedding et al., 2001). The internal pressure of stars is constantly changing due to the convection motions below the photosphere. These stochastic pressure fluctuations create pressure waves, known as pressure- or p-modes, which propagate through the stellar interior and result in the surface of the star expanding and contracting in a ripple-like pattern. As a result of this in and out movement of the stellar surface, the light emitted by the stars is Doppler shifted. The interference of several p-modes with similar frequencies has a net effect of a few $\mathrm{m\,s^{-1}}$ in solar-like stars. This value decreases for cooler stars and increases for more massive and more evolved stars. Pulsations in M dwarfs have been theoretically predicted (Gabriel and Grossman, 1977; Rodríguez-López et al., 2014) but so far have not been detected neither in photometric nor spectroscopic observations (e.g. Baran et al., 2013; Rodríguez et al., 2016; Berdiñas et al., 2017; Rodríguez-López, 2019).

1.2.2 Granulation and supergranulation

Convective motions in the external layers of the stars are also responsible for the phenomena of granulation (e.g. Rast, 2003; Cegla et al., 2013; Meunier et al., 2015; Cegla et al., 2018; 2019). Cool stars like the Sun show a granulation pattern on their surfaces in the form of hot, bright patches or granules, surrounded by colder, darker regions known as intergranular lanes. In the convective layer, hot plasma cells rise towards the stellar surface, creating the granules. The hot plasma then cools down and sinks back towards the stellar interior in the intergranular lanes, the regions surrounding the granules. Light emitted in the granules is therefore blueshifted, while light coming from the intergranular lanes is redshifted. In the Sun, plasma moves with velocities of a few $\mathrm{km\,s^{-1}}$. Granules are brighter and occupy a larger region of

the stellar surface than the darker intergranular lanes, where the plasma is colder and more compact. The result of these upward and downward shifts is then a net blueshift. This granulation pattern is reflected in the shape of the stellar line profiles, which are deformed due to the different granulation components (Dravins, 1982), resulting in asymmetries that can be interpreted as velocity shifts. The granules contribute with a blueshifted line profile. Intergranular lanes, which are darker and hence contribute with less flux, add a redshifted component that affects the upper region of the line. The result of this, is an asymmetric line with a blueshifted core and redshifted wings. This convective blueshift can have values of a few hundreds of $\mathrm{m\,s^{-1}}$, depending on the stellar properties, and decreases with temperature (Allende Prieto et al., 2002; Meunier et al., 2017; Meunier, Mignon, and Lagrange, 2017). For instance in the Sun, the convective blueshift has an average value of about $400\,\mathrm{m\,s^{-1}}$ (the exact value depends on wavelength and disk position, Löhner-Böttcher et al., 2019), and it is expected to be much smaller in M dwarfs (Baroch et al., 2020). Typically, solar granules have lifetimes of a few minutes. Fluctuations of the granulation pattern over this timescale results in a variability of tens of $\mathrm{cm\,s^{-1}}$ (Schrijver and Zwaan, 2000).

On larger scales, the Sun shows groups of individual granules that create larger convective patterns (with sizes of tens of Mm, while individual granules have sizes of the order of the Mm) with timescales of several hours, a phenomena known as supergranulation (Del Moro et al., 2004; Rieutord and Rincon, 2010). These supergranules have large horizontal flows of a few hundreds of $\mathrm{m\,s^{-1}}$ and small vertical flows, of tens of $\mathrm{m\,s^{-1}}$, so they have larger effects on the solar disk limb. Their average net effect is of the order of the $\mathrm{m\,s^{-1}}$.

1.2.3 Spots and faculae

The stellar photosphere also shows inhomogeneities like spots and faculae (sometimes called plages) that form in active regions, areas where there is an increased magnetic field compared to the surrounding regions that only show the granulation pattern. The presence of a strong magnetic field can locally attenuate the convective motions in the photosphere, which are the main source of heat transport. This lack of convection gives rise to spots, regions colder than the rest of the photosphere (a few hundreds of degrees less). As a result of this difference in temperature, they also appear darker than their surroundings. Individual spots have lifetimes ranging from a few days to several weeks, which is of the order of typical stellar rotation periods, and tend to appear at specific longitudes (the so-called active longitudes), so their signals can last longer. Faculae, on the other hand, are regions hotter and brighter than the rest of the photosphere (in the Sun, about 100 K more). Solar observations show that they are spread across all the surface, particularly surrounding spots, but are more abundant and have longer lifetimes. Their magnetic field is less strong than that in spots, an so is

the inhibition of convection. The magnetic field is however strong enough to reduce the opacity, so we see light coming from deeper layers of the photosphere. These layers are hotter and therefore, brighter, hence the appearance of faculae.

Since spots and faculae are on the surface of the star, they move in and out of view as the star rotates, so their effects on the RV are modulated with the stellar rotation period. They induce variations in the RV by two different processes, related to their temperature contrast and different convective velocity with respect to the rest of the stellar photosphere (e.g. Saar and Donahue, 1997; Hatzes, 2002; Desort et al., 2007; Lagrange, Desort, and Meunier, 2010; Meunier, Desort, and Lagrange, 2010).

Spots can be a few hundreds of degrees cooler than the surrounding stellar surface and therefore, emit less flux. As a star rotates, the half moving towards us emits blueshifted light, while the half moving away from us emits redshifted light. If the star has a spot, it will block different areas of the stellar surface as the star rotates, first blocking the blueshited light from the approaching half and then, the redshifted light from the receding half. This changes the amount of flux coming from different parts of the star, producing asymmetries on the stellar line profiles. These asymmetries change the lines centroid, which results in RV shifts. The temperature contrast between a spot and the rest of the photosphere decreases for cooler stars, which means that a spot on a late-type star will induce smaller RV changes than the same spot on a hotter star. RV variations due to spots can be of the order of the $\mathrm{m\,s^{-1}}$ for quiet stars like the Sun, up to more than $100\,\mathrm{m\,s^{-1}}$ for more active, younger stars (Tal-Or et al., 2018), where the number and size of spots is expected to be larger due to stronger magnetic fields. Faculae also induce a flux effect, but since their temperature contrast with the rest of the surface is smaller than that of spots, and they are more evenly spread on the surface, their effect has a smaller magnitude.

Aside from this flux effect, spots and faculae also induce RV shifts because of the partial suppression of convection caused by their high concentration of magnetic fields (e.g. Dravins, 1982; Livingston, 1982; Brandt and Solanki, 1990; Saar and Donahue, 1997; Kürster et al., 2003; Saar, 2003; Gray, 2009). These areas with weaker convective motions replace part of the granulation pattern on the stellar surface. The average effect of the granulation pattern was a net blueshift, therefore, spots and faculae appear redshifted compared to the other regions where convection is not inhibited. These redshifted regions induce RV variations as the star rotates.

In stars with low levels of activity like the Sun, the suppression of convection by faculae seems to be the larger effect on RV variations due to activity (Meunier, Desort, and Lagrange, 2010; Meunier, Lagrange, and Desort, 2010; Haywood et al., 2016), because of their larger brightness and larger coverage of the stellar surface compared to spots (spots are fainter and only cover small fractions of the surface of the Sun,

from 0.0001 % at its minimum activity level to 0.1% at its maximum, Strassmeier, 2009). More active stars seem to be spot-dominated, with higher magnetic fields allowing the appearance of more and/or larger spots (with filling factors more than 100 times larger than for the Sun at its maximum, Strassmeier, 2009). For these stars, the main source of RV variability is the flux effect induced by spots.

Moreover, magnetic fields extend towards the upper layers of the stars. Active regions on the photosphere have a counterpart in the stellar chromosphere, bright regions known as plages. They can be detected by measuring the emission in the core of specific lines that are formed on different levels on the chromosphere (see e.g. Hall, 2008).

1.2.4 Magnetic cycle

On the longest timescales, of the order of a few years to decades, stars can show long term magnetic cycles (e.g. Wilson, 1978; Saar and Fischer, 2000; Hall, Lockwood, and Skiff, 2007; Santos et al., 2010; Lovis et al., 2011; Suárez Mascareño, Rebolo, and González Hernández, 2016; Suárez Mascareño et al., 2018). For instance, the Sun experiences an activity cycle of 11 years, during which the average activity level increases and decreases (Hathaway, 2010). This is seen in an increase (and subsequent decrease) of the number of magnetic features on the surface (spots and faculae) and an increased frequency of events such as flares, prominences, and coronal mass ejections. There is also an increase and decrease in the total brightness of the star. The changes in these magnetic features result in long-term drifts in the RVs, which can be a problem for the detection of long-period planets. The amplitude of the magnetic cycle variations increases with the average activity level of the stars, and RVs are more sensitive to cycle variations in hotter stars (Santos et al., 2010; Lovis et al., 2011)

1.2.5 Identification and mitigation of stellar variability

Given the different extent in time and amplitude of the different stellar signals, there exist several ways to identify and try to mitigate their effect on RV measurements. In this section we mention some examples.

Solar-like oscillations are stable over time with timescales of a few minutes (e.g. in the Sun, they repeat with a 5 minute period). Therefore, their effect can be averaged out by taking observations longer than that (Dumusque et al., 2011b). In a similar manner, the $\mathrm{m\,s^{-1}}$ effects of granulation and supergranulation can be mitigated by an adequate observational strategy. One can average several observations taken on the same night to average out the granulation fluctuations (Dumusque et al., 2011b; Meunier et al., 2015). However, despite having short timescales, granules seem to repeatedly appear in similar positions, and this persistence still leaves residuals of the

order of the $cm\,s^{-1}$ (e.g. Hoekzema, Brandt, and Rutten, 1998; Getling and Brandt, 2002; Giannattasio et al., 2018).

RV shifts caused by spots and faculae pose the main problem in the detection of small exoplanets. These stellar signals are modulated with the stellar rotation period, whose timescales can often be close to the orbital periods of planetary companions. This makes it difficult to disentangle true planetary signals from activity effects. Moreover, activity signals can have amplitudes well above the $m\,s^{-1}$ level, hiding the smaller signals induced by small exoplanets. Actually, poorly understood stellar activity has led to a number of controversial exoplanet detection claims, and several of them have turned out to be spurious signals caused by the star itself (e.g. Queloz et al., 2001; Desidera et al., 2004; Bonfils et al., 2007; Huélamo et al., 2008; Boisse et al., 2009; Figueira et al., 2010; Hatzes, 2013; Haywood et al., 2014; Santos et al., 2014; Robertson et al., 2015; Rajpaul, Aigrain, and Roberts, 2016).

As happened with oscillations and granulations, tailored observational strategies can also be used to average the effect of spots, or to maximise the signal of a planet if its orbital period is notably different than that of the stellar rotation (Hatzes et al., 2010; Dumusque et al., 2011a; Pepe et al., 2013). This however requires certain previous knowledge of the system, and often stellar rotation and orbital periods are too similar. A standard test to identify magnetic activity is to compare the signals found in the RVs with different indicators of stellar activity. Commonly used indicators include parametrisations of the stellar line profiles, the emission flux in the core of chromospheric lines such as the Ca II H&K or the Hα line, or photometric observations (see Chapter 3 for more details). In the Sun, it is possible to measure the disc-averaged magnetic flux from magnetograms, which shows even better correlations with activity-induced RV variations (Haywood et al., 2016). The main idea is that, if the RVs and the indicators are correlated, or if they show modulations at similar periods, the RV variations have a stellar origin. The activity signal in the RVs then has to be decorrelated or appropriately modelled (e.g. Boisse et al., 2009; Queloz et al., 2009; Lanza et al., 2010; Haywood et al., 2014; Rajpaul et al., 2015; Herrero et al., 2016; Mallonn et al., 2018; Rosich et al., 2020).

Recently, several efforts have been focused on accounting for the stellar activity during the RV extraction from the observed spectrum, by studying the effects that activity has on the individual spectral lines, rather than trying to decorrelate it once the RVs have been measured. Different lines in the stellar spectrum react differently to activity-driven variations on the stellar surface, such as temperature, magnetic field, or convection velocity variations. Variations in the line profiles morphology correlated with activity proxies can be exploited to identify the most affected regions and correct for these effects (e.g. Meunier, Lagrange, and Borgniet, 2017; Thompson et al., 2017;

Dumusque, 2018; Wise et al., 2018; Cretignier et al., 2020; Zhao and Tinney, 2020, see Chapter 4 for a more in-depth discussion of some of these approaches).

1.3 CARMENES

1.3.1 M dwarfs

Early RV searches for exoplanets mainly focused on solar-type stars and, due to their intrinsic faintness, only included a handful of M-dwarf stars. Out of approximately the first hundred exoplanet detections, only a few were found orbiting M dwarfs (Delfosse et al., 1998a; Marcy et al., 1998; 2001; Butler et al., 2004). Nevertheless, in the last two decades, interest has rapidly grown regarding M dwarfs as exoplanets hosts, which now account for over 200 exoplanets orbiting about 100 hosts (Martínez-Rodríguez et al., 2019).

M dwarfs are the smallest and coolest type of stars, with masses ranging from 0.6 to $\sim 0.075\,M_\odot$, at the limit to start hydrogen fusion in the core, and effective temperatures from 3800 to 2300 K (see e.g. Table 4.1 on Reid and Hawley, 2005). Compared to more massive and hotter FGK-type stars, the star-to-planet mass ratio is lower for M dwarfs and their habitable zones (HZs) are located closer in. Therefore, the gravitational pull of an HZ-orbiting planet is stronger for M dwarfs, implying RV signals with larger amplitudes. Also, orbital periods are shorter, thus reducing the monitoring timescales. These circumstances make the detection of small, rocky exoplanets around M dwarfs feasible with current instrumentation. Moreover, M dwarfs are the most abundant stars in the solar neighbourhood, which makes them the most common potential exoplanet hosts.

One of the main issues with M dwarfs is that they can exhibit high levels of stellar activity. As seen above, this activity manifests itself mainly in the form of features in the stellar surface that create distortions on the spectral line profiles used to measure RVs, which hampers the detection of exoplanets. They are also relatively fainter than more massive stars and emit most of their bulk energy in the near-infrared, where instruments are not yet as precise as in the visual range (their spectral energy distribution peaks at ~ 1000 nm). Due to their cold temperatures, their spectra display a large number of lines due to molecules, which appear blended, which further complicates the computation of RVs.

1.3.2 The CARMENES instrument

The work of this thesis is based on spectroscopic observations obtained with the CARMENES instrument (Calar Alto high-Resolution search for M dwarfs with Exo-earths with Near-infrared and optical Echelle Spectrographs), which was designed to

obtain high-precision spectra of M dwarf stars (Quirrenbach et al., 2016; 2018). It is located at the 3.5 m telescope at Calar Alto Observatory in Almería, Spain, and was built by a consortium of German and Spanish institutions[3]. It consists of a pair of cross-dispersed, fibre-fed echelle spectrographs with different wavelength coverage, which allow simultaneous observations in the visual and the near-infrared wavelength range. The visual (VIS) channel covers the spectral range $\lambda = 520$–960 nm at a resolution of $R = 94\,600$, and the near-infrared (NIR) channel covers the range $\lambda = 960$–1710 nm at a resolution of $R = 80\,400$. It capable of high-precision RV measurements, of the order of the $\mathrm{m\,s^{-1}}$.

1.3.3 CARMENCITA and the GTO sample

More specifically, we used M dwarf observations obtained within the CARMENES survey (also guaranteed-time observations – GTO program), which has been ongoing since 2016. The program monitors over 300 M dwarfs across all spectral subtypes with the main goal of detecting orbiting exoplanets (Reiners et al., 2018b). The sample includes the brightest stars of each M spectral subtype visible from Calar Alto ($\delta > -23°$, to avoid strong atmospheric effects and ensure observations with good S/Ns), and with no evidence of stellar companions (at separations within $5''$ to avoid contamination). The sample does not exclude active stars, which are usually not present in RV planet searches, or stars with known planetary companions, which can overlap with other surveys.

The $\sim$ 300 M dwarfs of the GTO sample were selected from the CARMENCITA database (CARMENes Cool dwarf Information and daTa Archive), which currently contains relevant parameters of more than 2000 low-mass stars. Among the most important ones, the catalogue provides information about spectral types, the main stellar parameters (mass, radius, temperature, surface gravity, metallicity, luminosity), quantities related to stellar activity (rotational velocity, rotational period, emission of the Hα line, X-ray emission), astrometry and kinematics, photometry in several bands, and information about the presence of stellar or planetary companions, among others. The values are compiled from the literature or measured by the consortium itself.

Prior to the start of the survey, extensive science preparation was performed to select and characterise the sample stars. Aside from a literature search, Alonso-Floriano et al. (2015) derived spectral types and activity indices of more than 700 stars from new low-resolution spectroscopic observations, Cortés-Contreras et al. (2017) identified and characterised binary systems with high-resolution imaging of almost 500 M dwarfs,

[3]Max-Planck Institut für Astronomie (MPIA), Instituto de Astrofísica de Andalucía (IAA), Landessternwarte Königstuhl (LSW), Institut de Ciències de l'Espai (ICE), Institut für Astrophysik Göttingen (IAG), Universidad Complutense de Madrid (UCM), Thüringer Landessternwarte Tautenburg (TLS), Instituto de Astrofísica de Canarias (IAC), Hamburger Sternwarte (HS), Centro de Astrobiología (CAB), and the former Centro Astronómico Hispano-Alemán (CAHA)

and Jeffers et al. (2018) studied activity and rotation with high-resolution spectroscopy of almost 500 M dwarfs. More recently, Díez Alonso et al. (2019) measured photometric rotation periods in more than 100 stars.

Currently, the catalogue is being updated with values derived from the CARMENES observations themselves. Passegger et al. (2019) derived photospheric parameters (effective temperature, surface gravity and metallicity) from VIS and NIR observations, and Schweitzer et al. (2019) computed radii and masses of almost 300 stars in the sample. Schöfer et al. (2019) computed several activity indices derived from chromospheric and photospheric lines at both the visual and near-infrared ranges that are used to estimate the average activity level of the stars, including flux measurements of the Hα line. CARMENCITA contains the most up-to-date parameters computed as explained in the above references, which we used throughout this thesis.

1.3.4 Science with CARMENES

The main science case of the CARMENES survey is the detection of small planets orbiting M dwarfs. Accordingly, most of the CARMENES GTO observing time has been devoted to the discovery and characterisation of exoplanets, which so far has led to the discovery of over 20 new planets[4], with several more in preparation, and the confirmation and further study of almost 20 planets. The CARMENES discoveries contribute to the increasing sample of planets orbiting M dwarfs, which had been poorly studied until recently, especially those of lower mass. Among the different findings, some of the most outstanding ones are the discovery of a cool super-Earth ($\sim 3\,M_\oplus$ minimum mass) orbiting Barnard's star, a low-mass M dwarf ($\sim 0.17\,M_\odot$, M3.5 V), and the second star closest to the Sun after the Alpha Centauri triple system, only about 6 light-years away (Ribas et al., 2018); the discovery of 2 planets both with minimum masses close to that of the Earth in the HZ of the ultra-cool dwarf (M7.0 V) Teegarden's star (Zechmeister et al., 2019), the type of systems that CARMENES was designed for; and the discovery of a giant planet ($\sim 0.5\,M_J$) orbiting the very low-mass star GJ 3512 ($\sim 0.12\,M_\odot$, M5.5 V), one of the only very massive planets found around such a low-mass star, whose existence challenges current planetary formation models based on core accretion and instead favours a formation by gravitational instability of the star's protoplanetary disk (Morales et al., 2019).

Aside from planetary discovery and characterisation, CARMENES observations can be used to study a number of diverse topics[5]. Within the main survey time, there have been several studies of stellar activity in the M dwarf sample. Tal-Or et al. (2018) provided an overview of the relations between RVs, stellar activity indicators,

[4] https://carmenes.caha.es/ext/science/#anchor:planets

[5] See https://carmenes.caha.es/ext/science/ for an extensive list of works that used CARMENES data.

and the stellar parameters of the most active stars in the sample. The wide range of CARMENES covers an important number of lines that correlate with activity, including strong chromospheric lines such as the Hα, Ca IRT, Na I D, or He I IRT. Schöfer et al. (2019) measured pseudo-equivalent widths of several of these lines as well as the flux strength of photospheric molecular bands in both the visible and near-infrared ranges, for most of the sample stars. They studied the sensitivity of these different indicators with activity and their variability. A more in-depth study of the He I IRT in all M dwarf spectral-subtypes was performed in Fuhrmeister et al. (2019a). Chromospheric lines usually display complex line profiles with extended wings and asymmetries than can be used to study the structure and physical conditions of the chromosphere. Such profile variations was the subject of study of Fuhrmeister et al. (2018), where the authors analysed asymmetries in the wings of the Hα and other chromospheric lines. They proposed several explanations for the lines shape, such as the existence of rising and falling material in the chromosphere. Further insight on the structure of the chromosphere can be obtained by comparing the observed lines with theoretical models. Hintz et al. (2019) build parametrised chromospheric models and compared them to several lines in inactive and active early M dwarfs, as well as determined the coverage of inactive and active regions (filling factors). Hintz et al. (2020) extends the previous work to study the He I IRT in early M dwarfs more in depth. Due to their sensitivity to activity, chromospheric lines can also be used to determine rotation periods (Fuhrmeister et al., 2019b). Shulyak et al. (2019) measured magnetic fields from the Zeeman broadening of spectral lines in the NIR for several active stars.

The effects caused by activity features like spots have a wavelength dependence because of their temperature contrast, which is smaller towards longer wavelengths. This means that RVs suffer from smaller activity-induced variations on redder wavelengths. This chromatic dependency of the RV was used by Zechmeister et al. (2018) to define an activity indicator sensitive to such variations, the chromatic index. In a novel approach, Baroch et al. (2020) analysed the effect that stellar activity has on RV as a function of wavelength by comparing observations of an active star with simulations that account for spots, convective motions, and rotation. Since activity has a varying effect with wavelength, they were able to detect several properties of active regions, such as the spot-coverage, temperature contrast, and location, as well the amplitude of photospheric convective motions.

As mentioned above, CARMENES spectra, which have a high resolution and S/N, are suitable to determine stellar parameters of M dwarf stars (Passegger et al., 2018; 2019; Schweitzer et al., 2019; Passegger et al., 2020) as well as earlier FGK-type stars (Marfil et al., 2020) by model fitting. Several previously unknown double-lined M

dwarf spectroscopic binaries were discovered within the CARMENES sample. Baroch et al. (2018) used those observations to measure RVs and determine their orbital and physical properties.

CARMENES has also taken part on the follow-up of space missions such as *K2* and *TESS* to confirm and characterise the planetary nature of transiting planets around low-mass stars (e.g. Luque et al., 2019a; b; Bluhm et al., 2020; Nowak et al., 2020). Observations of transiting planets have also enabled the detection and study of planetary atmospheres. Elements such as He and water have been detected in the atmospheres of several hot exoplanets (e.g. Nortmann et al., 2018; Salz et al., 2018; Alonso-Floriano et al., 2019; Sánchez-López et al., 2019).

1.4 This thesis

In this thesis, we study the effects of stellar activity on spectroscopic observations of stars. Specifically, we focus on observations of M dwarf stars, the coolest stars in the main sequence, obtained with the CARMENES instrument, a visual and near-infrared high-resolution spectrograph. Our work is divided into three core chapters that we detail next. In Chapter 2, we present our implementation of one of the standard methods to measure RVs, the so-called cross-correlation function technique, and apply it to CARMENES observations of M dwarfs. Aside from determining RVs, this technique also yields key parameters that are used as proxies of stellar activity. In Chapter 3, we use these parameters, together with other spectroscopic activity indicators, to perform an analysis of their temporal behaviour for a range of M dwarfs with different masses and activity levels. In Chapter 4, we study the different effects that stellar activity has in the absorption lines present in CARMENES observations, and exploit these differences to recompute RVs in which we mitigate or enhance the effects of stellar variability. The final Chapter 5 is a summary of the three core projects and presents an outlook of future work that stems from the research presented in this thesis.

Chapter 2

Radial velocities and activity from cross-correlation with masks

The contents of this chapter have been published in the journal *Astronomy & Astrophysics*, volume 636, as the article with title "The CARMENES search for exoplanets around M dwarfs. Radial velocities and activity indicators from cross-correlation functions with weighted binary masks" (Lafarga et al., 2020).

2.1 Introduction

The traditional method of measuring Doppler shifts in spectra is to directly cross-correlate them with a template. This is known as the cross-correlation function (CCF) method (Queloz, 1995; Baranne et al., 1996). Binary masks are commonly used templates that represent a very simple model of the stellar spectrum. They consist of a set of boxcar functions (a rectangle-shaped function that has a constant value over a specific range and is zero elsewhere) centred at the minimum wavelength of a large number of absorption lines that are present in the stellar spectrum. In fact, early echelle spectrographs used physical masks, that is, spatial filters with real holes at the positions of absorption lines (Baranne, Mayor, and Poncet, 1979), thus explaining the name. Depending on how much radial velocity (RV) information (Bouchy, Pepe, and Queloz, 2001) each line contains, the boxcar functions can have different weights, which improve the RV measurements (Pepe et al., 2002). Deep and narrow lines, that is, lines with the steepest profiles, have more information than shallow and broad lines, hence their weight in the mask is larger.

The CCF method has been the standard approach to obtain precise RV measurements of FGK-type stars. Their spectra display a number of resolved and unblended absorption lines across the visible wavelength range, which are ideal features to be represented by a weighted binary mask. M dwarfs also show a large number of absorption lines. However, due to their lower temperatures, the number of lines is so high

that most of the features are blended, making their identification and, hence, the construction of a mask, more challenging. Different methods consisting in a least-squares matching of a full spectrum template to the observations (Anglada-Escudé and Butler, 2012; Astudillo-Defru et al., 2015; Zechmeister et al., 2018), rather than only using a selected set of absorption lines, have proven to work better for M-dwarf stars since they use more Doppler information contained in the spectrum. Recently, different methods have been proposed with the goal of improving RV extraction, such as using individual absorption lines (Dumusque, 2018) or approaches based on Gaussian processes (Rajpaul, Aigrain, and Buchhave, 2020).

The CCF continues to be useful for studying the stellar activity of stars, including M dwarfs. The CCF profile gathers information from each individual spectral line selected in the mask, which acts as a kernel, and converts this into an average high signal-to-noise ratio (S/N) line profile. Therefore, average changes in the individual line profiles due to stellar activity are reflected in changes in the CCF shape. Several parametrisations of the CCF profile describing its width, depth, or asymmetry are commonly used proxies of stellar activity. Another benefit is that one can estimate the absolute RV value of the observed stars using RV measurements obtained from the CCF. CCF masks are usually calibrated to an absolute RV scale, while template matching techniques provide RVs that are relative to the template used, which is not necessarily on an absolute scale. Of course, one could calibrate the template against an absolute reference, but the most straightforward way to do that would be by cross-correlation.

In this chapter, we study the CCF and its activity indicators in CARMENES visual (VIS) and near-infrared (NIR) observations of the GTO sample of M dwarfs. The CCF method is commonly used when analysing data from high resolution spectrographs, however, in-depth details of the technique are not usually available in the literature. For instance, in general it is not clear how CCF masks are built, how the method is implemented for specific instrumentation, or how to account for uncertainties. Here, we provide a detailed explanation of the method, from the creation of the masks, to the specific details of the CCF computation and modelling to extract the relevant parameters. We also explain how we apply it to observations obtained with the CARMENES instrument. We refer the reader to the previous Sects. 1.3.2 and 1.3.3 for an overview of the instrument and the M dwarf sample. In Sect. 2.2 we present an overview of the CCF method and its parameters. Then we explain the methodology we follow to build binary masks in Sect. 2.3 and to compute CCFs and their main parameters in detail in Sect. 2.4. Next, in Sect. 2.5 we apply these methods to the M dwarf observations of the CARMENES GTO sample. There, we also comment on the masks and CCFs obtained for different targets, compare the RVs obtained with the default CARMENES template matching pipeline, show the behaviour of the CCF activity indicators for an active

star in the sample, YZ CMi, and estimate the absolute RV of the CARMENES sample stars using the values derived from their CCFs. Finally in Sect. 2.6 we summarise our work.

2.2 Cross-correlation with a weighted binary mask

Measuring the radial velocity of an observed spectrum via cross-correlation relative to a binary mask implies Doppler-shifting the mask to cover a range of velocities when in search for the best match[1]. At each velocity step, the spectrum is multiplied by the mask. Since the mask has a zero value everywhere except at the positions of the selected absorption lines, only the spectrum pixels that totally or partially overlap with a mask line (non-zero values) contribute to the CCF value. For a given velocity shift v, the cross-correlation of a spectrum consisting of n pixels with a mask with m lines is computed according to the following equation

$$\mathrm{CCF}\,(v) = \sum_{l=1}^{m} \sum_{x=1}^{n} w_l \, f_x \, \Delta_{x\,l}\,(v)\,, \tag{2.1}$$

where f_x is the flux of the spectrum at pixel x, w_l is the weight of the mask line l, and $\Delta_{x\,l}$ is the fraction of pixel x covered by the mask line l when the mask is shifted by v. This equation corresponds to the cross-correlation function, CCF, of two discrete functions. Their product is computed pixel by pixel, and the term $\Delta_{x\,l}$ is employed to take partial overlaps between the pixels of the spectrum and the mask into account. The mask lines are defined as having a width of 1 pixel, which corresponds to the minimum interval containing relevant information. The minimum of the CCF corresponds to the Doppler shift of the stellar spectrum with respect to the mask. An analytic function, most frequently a Gaussian, is fitted to the CCF profile for a robust estimate of the position of the minimum and to characterise its profile.

Compared to template matching algorithms, the CCF method can be considered to be a simplistic least-squares minimisation in which we minimise the product of the observed spectrum and model (i.e. the CCF mask); afterwards, we fit the CCF with a function, such as a Gaussian, to estimate the Doppler shift. This is equivalent to computing the CCF between the spectrum and the mask previously convolved with a Gaussian (Baluev and Shaidulin, 2015). The only parameter in the model is the RV shift applied to the mask. Other corrections, such as normalisations or slope changes in the spectrum continuum, which are usually forward-modelled in template matching

[1]For convenience and to ensure the conservation of flux in the spectra, we did not rebin the spectra, but we worked with spectral bin sizes corresponding to the detector pixels. Since the wavelength scale is non-uniform due to the variation of the dispersion along each echelle order and instrumental distortions, this means that each line in the mask had to be shifted individually to the pixel position corresponding to its wavelength. For details, see Sect. 2.4.4.

procedures, are not simultaneously modelled when computing the CCF. But rather, they are adjusted a priori. Despite the number of simplifications, the CCF method is capable of yielding precise results. Another difference is that in template matching schemes that use co-added templates, the noise of each of the individual spectrum used is present in the template. This creates self-biases towards zero velocity due to the noise correlating with itself, especially if the S/N of the template is low (van Kerkwijk et al., 1995), which should not affect the CCF method.

As mentioned above, the CCF represents an average of the profiles of all the stellar absorption lines that are present in the mask used in velocity space. The different processes in the stellar atmosphere that affect the average position and shape of the individual spectral lines are reflected in the CCF. Therefore, the shape of the CCF contains information on the line profile distortions caused, for example, by stellar activity features present in the photosphere, such as dark spots or faculae.

Parameters, such as the full-width-at-half-maximum (FWHM) and the contrast of the CCF, which are obtained from the Gaussian fit, are used to measure temporal changes. Correlations of these parameters with the RV, or the presence of the same periodic signal in the RV and these parameters, may indicate the presence of activity-induced variations in the RVs. They can also trace instrumental variations, such as focus changes, or observational effects, such as barycentric broadening. The bisector of the CCF is used to analyse its asymmetry, which is also an indicator of changes caused by stellar activity for lines of a different strength, correlated with the atmospheric depth of their formation (e.g. Gray, 2009). Different ways to quantify the bisector have been proposed. A commonly used metric is the bisector inverse slope (BIS), which was introduced by Queloz et al. (2001). It is defined as the difference between the average velocity of the top region of the CCF (e.g. from 60 to 90%) and the average velocity of the bottom region (e.g. from 10 to 40%). Different fractions of the CCF can be used to compute the BIS, such as the BIS^{+}, which uses the 80–90% and 10–20% regions, and the BIS^{-}, which uses the 60–70% and 30–40% regions, as defined in Figueira et al. (2013). These alternative definitions have been shown to provide more significant results than the usual regions for some specific cases.

Other ways to quantify the asymmetry have also been proposed. In Boisse et al. (2011), the asymmetry was measured as the difference between the RVs obtained by fitting a Gaussian to the upper and lower part of the CCF. This indicator, known as velocity span, V_{span}, seems to be more robust than the BIS at a low S/N. Figueira et al. (2013) also defined two different indicators. Instead of fitting a Gaussian function to the CCF, they fitted a bi-Gaussian function (two half-Gaussians with different FWHM, each modelling one side of the CCF). This fit of a bi-Gaussian gives an estimate of the RV (the minimum of the CCF) that is different than the usual Gaussian fit, so the

difference between these two RVs, ΔV (first used in Nardetto et al., 2006), can be used as an asymmetry measure. In some cases, the amplitude of this indicator is larger than that of the BIS, allowing for the detection of correlations with the RV with a smaller amplitude. The second indicator, $V_{\rm asy}$, which was later modified by Lanza et al. (2018), compares the RV information content (the total flux and slope) between each side of the CCF to measure its asymmetry, and it is also found to provide stronger correlations with the RV than other indicators. Also, Simola, Dumusque, and Cisewski-Kehe (2019) fitted a non-symmetric function to the CCF, in this case a skew normal distribution (a Gaussian with a skewness parameter), to account for asymmetry in the CCF profile. The parameters derived from this fit seem to be more sensitive to stellar activity. Even though different asymmetry parametrisations are proposed in the literature, here, we focus on the original BIS definition because it is the most commonly used asymmetry metric (e.g. it is provided by the HARPS/HARPS-N data reduction software) and we do not find significant differences with the other definitions presented. A more in-depth study of the different asymmetry parametrisations is out of the scope of this work.

2.3 Weighted binary mask creation method

To compute a CCF, we need to obtain the appropriate weighted binary mask. The main issue is to select a set of absorption lines in the spectra that are appropriate for unbiased radial velocity determination. The lines that we find in the stellar spectrum mainly depend on both the instrument used (i.e. its wavelength coverage and resolution) and the target properties (i.e. its effective temperature and projected rotational velocity). In the case of M dwarfs, the spectrum contains a large number of lines and is rich in molecular bands. The lines are often not clearly separated and, in many cases, they can be severely blended.

Since we want to compute CCFs of M dwarfs observed with the CARMENES instrument, we chose to directly use the large number of available observations from the GTO survey to identify and select lines (Reiners et al., 2018b). We could have also used a high S/N, high-resolution synthetic stellar template, or information from line lists, but initial tests showed that using our observations yielded clearly better results and the procedure is more straightforward. The number of observations available for all the CARMENES survey targets is sufficient to build high S/N templates by co-adding them.

In the sections below, we describe the procedure we followed to build a mask that is suitable to compute the CCFs. The methods to build masks and compute CCFs with their moments described in the current and next sections have been implemented in the code `RACCOON` (Radial velocities and Activity indicators from Cross-COrrelatiON with

masks). Currently, the code works for CARMENES and HARPS/HARPS-N (Mayor et al., 2003; Cosentino et al., 2012) data, and it is publicly available[2].

2.3.1 High S/N stellar spectrum template

We employed the CARMENES survey observations as the starting point to select the lines. To minimise the effect of the photon noise of individual spectra, we created a high S/N spectral template by co-adding all of the different observations available of a specific star. The templates were obtained using the `SERVAL` software (Zechmeister et al., 2018), which is the main pipeline used to analyse RVs in the CARMENES survey. `SERVAL` creates a high S/N stellar template by co-adding observations. Then, it uses this template to compute a least-squares fit to each of the observations from which the RV time series is obtained iteratively. Before co-adding, the observations are corrected for the corresponding barycentric motion of the Earth and any other known drift so that the stellar lines are optimally aligned. The templates have a similar format as the observations, and echelle orders are considered individually. The CARMENES NIR orders have a middle gap because of the NIR detector configuration (it is a mosaic of two detectors with a middle gap). Due to this, throughout all this work, we treated the NIR half-orders as single ones.

We then normalised the template orders by dividing each of them by a fit to their 'continuum'. To measure the continuum of each order, we selected the pixels with the maximum flux over windows of a few tens to a few hundreds of pixels in width to avoid overfitting, as there are numerous absorption lines present in the spectrum. When selecting these pixels, we avoided spectral regions containing very strong lines or lines that can show strong chromospheric emission (such as He I D_3, the Na I D doublet, Hα, or the Ca II infrared triplet) as well as regions with strong telluric features to prevent biases in the polynomial fit. The selected pixels were used to fit a second-order polynomial, and finally the template spectrum was divided by it.

2.3.2 Excluded regions

Since we use observations obtained from the ground to create the template, some regions of the spectra are affected by telluric contamination. Absorption and emission features coming from the Earth's atmosphere on top of the stellar spectrum need to be excluded. The position of the telluric lines on the detector (pixel frame) is very stable. However, the position of the stellar spectral features on the detector depends on the relative velocity between the observer and the target, which is determined by the orbital and rotation motion of the Earth and by the absolute radial velocity of the target. The relative stellar velocity changes throughout the year, so the stellar spectrum

[2] https://github.com/mlafarga/raccoon

shifts across the detector depending on the observation date. Except for targets with large radial velocity amplitudes (e.g. binaries), the main contribution to this velocity shift comes from the Earth orbital motion (barycentric Earth radial velocity, BERV), which can be up to approximately $\pm 30\,\mathrm{km\,s^{-1}}$, depending on the sky position of the target. To be sure any contribution from the Earth's atmosphere at any moment of the year is removed, we disregarded wavelengths encompassing an enlarged region around each telluric feature and not only the telluric line itself. To define this region, we used the maximum BERV of the observations of the target used to build the template, which can be significantly smaller than $30\,\mathrm{km\,s^{-1}}$, and we broadened each telluric line by subtracting and adding this maximum BERV to the blue and red line limits, respectively. In the VIS range, we masked the regions around telluric lines that are deeper than 5%. In the NIR range, the threshold was 4% in the Y and H bands and 2% in the J band, where the stellar lines are less abundant and shallower (see Nagel et al., submitted, for details). Instead of completely masking telluric contaminated regions, we could attempt to correct shallow telluric features with techniques such as the one presented in Nagel et al. (submitted), which would increase the available spectral range. However, this is beyond the scope of this thesis and we leave it for future work. We also masked out regions close to chromospheric lines that can show a strong emission component in active stars, as was done before when normalizing the template orders.

2.3.3 Mask lines

2.3.3.1 Line identification

We used the normalised spectrum template to identify absorption features. Firstly, we searched for all local minima present in the template (except in the excluded regions mentioned above), which indicate the centre of the absorption lines. We considered the region around these minima (the pixels in the region going from the adjacent maxima at each side of a minimum, see the grey shaded region in Fig. 2.1) to represent the absorption lines of the stellar spectrum. Most of these spectral features do not come from a single elemental transition, but they are the result of line blending.

2.3.3.2 Line characterisation

For each identified minimum or line, we measured a set of parameters in the template to quantitatively characterise its shape. To have a more reliable estimation of these parameters, we fitted a Gaussian function to each spectral minimum

$$G(\lambda) = d + a \exp\left(-\frac{(\lambda - b)^2}{2c^2}\right). \tag{2.2}$$

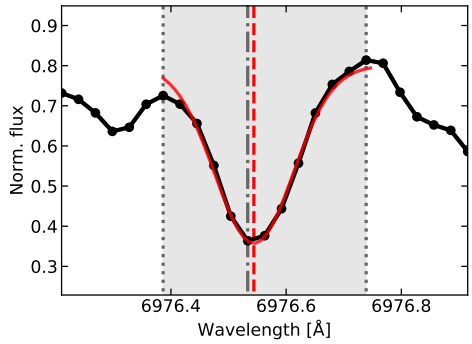

Figure 2.1: Minima characterisation. The black dots and solid line are the template data showing an absorption feature. The shaded light grey region defines the pixels corresponding to the feature shown, which go from the local maxima (dotted grey vertical lines) at each side of the minimum (dotted dashed grey vertical line). The solid red line is the best Gaussian fit, and the dashed red vertical line indicates its minimum.

Figure 2.1 shows an example of a line in a spectrum template with the best-fit Gaussian function. The pixels used in the fit are the ones between the two maxima at each side of the absorption feature.

To measure the central wavelength of each line, we used the position of the minimum of the Gaussian fit b. This gives a more robust and precise estimate than the wavelength corresponding to the local minimum of the spectrum template, which depends on the spectral sampling. The depth of each line is given by the flux at the Gaussian minimum, $a + d$, so small values correspond to deep lines. To measure the width of each line, we used the FWHM of the Gaussian fit, $2c\sqrt{2\ln(2)}$. We computed the contrast or prominence of the line as the difference between the flux at the edges of the line (the adjacent local maxima) and the flux at the minimum of the line (what we defined as the line depth). This gives two values for the contrast; one corresponds to each side of the minimum, whose difference can be used to study the asymmetry of the line.

2.3.3.3 Line selection

Figure 2.2 shows the distribution of the parameters we defined above for the lines[3] identified in the VIS template of the slowly-rotating ($v \sin i \leq 2\,\mathrm{km\,s^{-1}}$), M3.5 V, Luyten's star (GJ 273, Karmn J07274+052). We obtained similar values for low $v \sin i$ targets across all spectral subtypes. As mentioned above, we excluded minima close to very strong lines and those that fall in regions with strong telluric contamination. We also excluded minima that do not contain enough pixels to be properly characterised (due to noise or too weak lines) and minima with profiles that highly deviate from a

[3]Here and throughout this thesis, we use vacuum wavelengths rather than air, unless stated otherwise, as this is the format of the CARMENES reduced spectra.

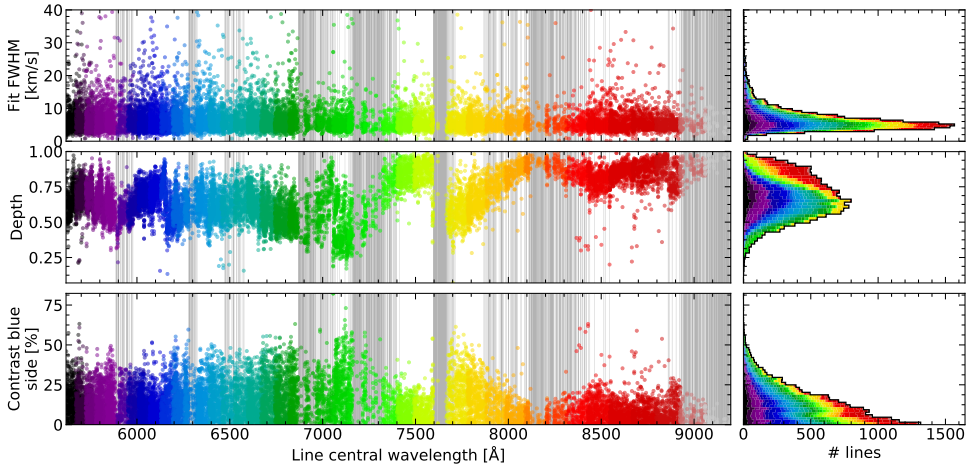

Figure 2.2: Line parameters (*top*: FWHM, *middle*: depth, and *bottom*: contrast) as a function of the line central wavelength (*left*) and the number of lines as a function of the parameters, where the values of each order have been stacked (*right*) for Luyten's star (Karmn J07274+035, M3.5 V, low $v \sin i$). In all panels, colours correspond to different spectral orders. Lines in order-overlap regions, which are wider in the blue, are duplicated. The shaded grey areas in the left panels correspond to regions contaminated by telluric features, broadened by $\pm 30\,\mathrm{km\,s^{-1}}$. The black lines in the right panels correspond to the distribution of the lines in all orders.

Table 2.1: Line parameter limits used to select the final lines of the low $v \sin i$ GTO masks.

FWHM range [$\mathrm{km\,s^{-1}}$]	Minimum contrast [%]	Depth quantile [%]
$2 - 30$	6	60

Gaussian (mainly blends for which the Gaussian fit gives unphysical values).

Based on these parameters, we defined some threshold values to select the lines that will become part of the final mask. We tried to select as many lines as possible so that the CCF has a high S/N, allowing us to derive its parameters with the best precision. At the same time, we want to avoid weak lines that contribute more noise than signal.

We tested several masks created using different parameter combinations (depth, width, contrast, asymmetry) and different selection values for each parameter. To analyse the performance of the masks, we used them to compute the CCFs of the observed spectra of some targets with low activity levels and low $v \sin i$, and we checked which mask yielded the smallest RV scatter. This analysis shows that using different combinations of parameters or slightly different selection values did not significantly change the masks or the CCF parameters obtained. The final parameters and values we adopted are shown in Table 2.1.

We selected lines with FWHM within a certain range. The FWHM values had to

be increased for targets with larger $v \sin i$, up to few hundreds of km s^{-1} for the most extreme cases, the ones with $v \sin i \sim 30$–40 km s^{-1}. In doing this, we made sure that most of the lines that were included in the CCF have a similar width while avoiding the narrowest lines, which tend to correspond to weak noisy lines that were not removed in previous steps, and the broadest lines, due to strong, unsuitable lines or blends. The removed lines do not provide significant RV information and they tended to increase the RV scatter. To avoid lines that are too asymmetric and to further remove weak lines, we found that the simplest method was to select lines for which the contrast at both sides is larger than a minimum value.

We also selected lines depending on their depth. However, for this parameter we did not use a single threshold value. The spectra of M dwarfs do not show a clear continuum due to the large number of features present; so across the spectral range we observe large differences in the line depths, with much deeper lines in regions containing strong molecular bands. This makes it difficult to just use a single cut value for the whole spectral range. Since we are using a normalised high S/N template, the depth values of the lines range from 1, for the shallowest lines, to 0 for the deepest ones. In some orders, all of the lines can be very shallow, with the deepest ones reaching values of only 0.8, for example, while other orders contain very deep lines, reaching values of 0.2, for instance. To minimise this bias, we rescaled the depth values so that, for each order, we considered that the depth goes from 1 to the average of the 10% deepest lines of the order. On this new scale, we selected lines with depths smaller than the 60% quantile of the new depth range.

We found that values around the ones shown in Table 2.1 allow us to select enough lines over the whole spectral range to obtain a CCF with a good S/N and precise parameters. Also, masks with these parameters worked well for most of the M dwarfs of the CARMENES survey sample. However, since the lines in the mask are weighted according to their RV information, changing these values to include more or less weak or wide lines did not change the CCF profiles significantly because these lines have lower weights (see next section).

Moreover, it is possible to fine-tune these values to a specific target and select optimum lines to study the velocity or the activity signals present in the spectrum. It has been shown that it is possible to classify spectral lines according to their sensitivity to stellar activity and, hence, according to their contribution to the activity signal in the final RVs (Dumusque, 2018; Wise et al., 2018; Lisogorskyi, Jones, and Feng, 2019; Cretignier et al., 2020). Using masks with lines selected to be more or less affected by activity should result in CCF profile parameters that are more or less sensitive to stellar activity variations.

2.3.4 Final mask

2.3.4.1 Position and weight

The final mask was comprised of the lines we selected following the approach explained above. Each line has a 'position', given by the minimum of the Gaussian fit in wavelength space, and a 'weight', which we calculated as the contrast divided by the FWHM of the line. In this way, the lines with the steepest profiles (i.e. the ones with more RV content) are the ones that contribute to the CCF the most.

When building the mask, all features are defined to have zero width (Dirac δ functions), independently of their measured values. At the time of computing the CCF of a specific observation, we forced each of the mask features to have the width of one pixel, which depends on the instrument and the position of the mask on the spectrum (see Sect. 2.4 for details).

In Fig. 2.3 we show a section of the normalised templates of stars of spectral types M0.0 V, M3.5 V, and M7.0 V. We also plot the local minima found and the final mask lines selected following the criteria explained here, along with their corresponding weight.

2.3.4.2 Order merging

Since CARMENES is an echelle spectrograph, the observed spectra and also the high S/N template created from these observations are split in different spectral orders across the detector. The bluest orders have some overlap at the order ends, so there are some duplicated lines in our list. To have a single final mask covering the entire spectral range, we merged the lines in overlapping order regions, which occur in the VIS channel and in the bluest NIR orders. We identified lines that are the same in two consecutive overlapping orders by comparing their central wavelengths. If the lines have central wavelengths that are close enough to be the same line (we chose a maximum separation of 0.05 Å), we took the mean of their positions and their weights, and these are the values that are included in the mask. If a line in an overlapping region is not found in both orders that overlap, we did not include it in the final mask.

2.3.4.3 Absolute velocity

We used the `SERVAL` template made by adding observations to build the mask so the mask wavelengths obtained are shifted to the RV of the star. To remove this contribution, we could just Doppler-shift the line wavelengths by the opposite of the star's velocity. But since these velocities are known to different accuracies, instead, we used a synthetic stellar spectrum as a reference. We cross-correlated the mask with a PHOENIX synthetic spectrum (Husser et al., 2013), which we assumed to define the zero-velocity frame, and we corrected the shift of the mask lines by the velocity

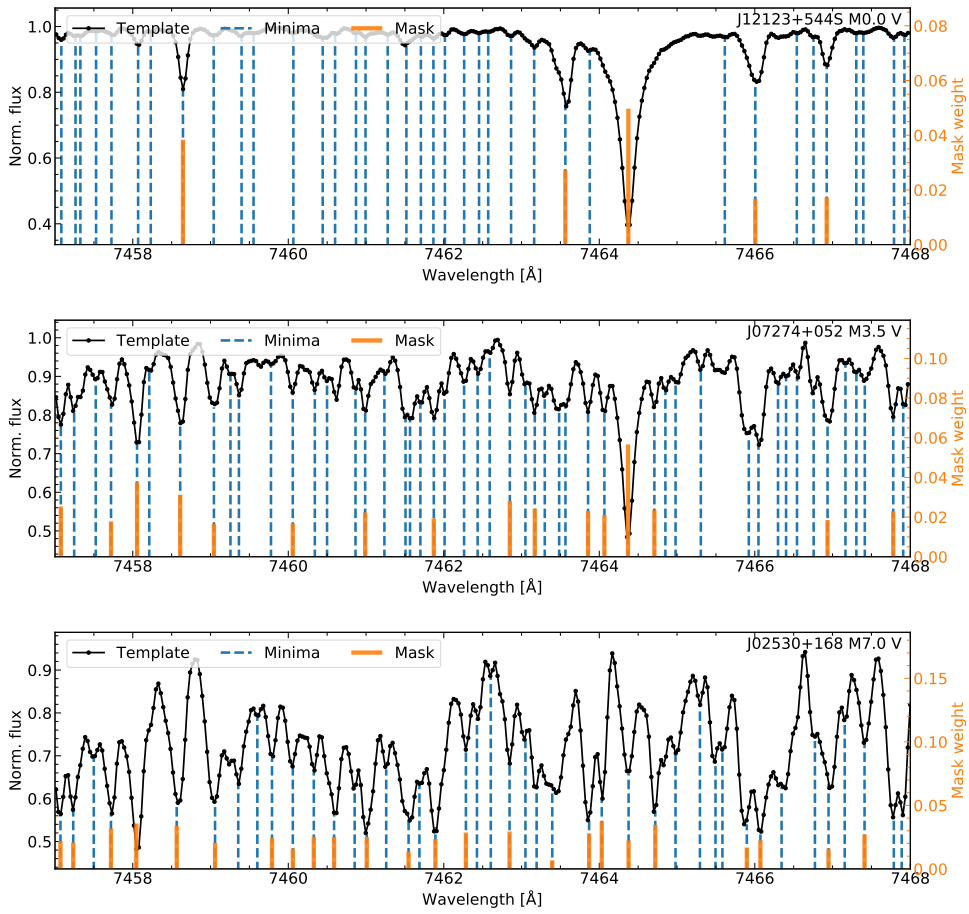

Figure 2.3: Section of a normalised spectrum template used to build masks (solid black data points and line), minima found in the template (dashed blue line), and mask containing the minima selected based on some conditions (solid orange lines) for three stars of different spectral type and low $v \sin i$: HD 238090 (M0.0 V; GJ 458A, Karmn J12123+544S; *top panel*), Luyten's star (M3.5 V; GJ 273, Karmn J07274+052; *middle panel*), and Teegarden's star (M7.0 V; Karmn J02530+168; *bottom panel*). The three targets are Doppler-shifted to the same reference frame.

obtained from the CCF. We used models with solar metallicity $[\mathrm{Fe/H}] = 0.0$, surface gravity $\log g = 5.00$, and effective temperature closest to the one of the star whose observations we used to build the template obtained from Schweitzer et al. (2019).

2.4 CCF and parameter computation

2.4.1 Spectrum preparation: Flux and wavelength correction

As before, we assumed that we have a high-resolution echelle spectrum, which is divided into different orders, and each order consists of a list of data points. One data point represents all of the detector pixels summed perpendicular to the dispersion

direction, with a central wavelength and a flux value.

The CARMENES science spectrum is extracted relative to the spectrum of a flat lamp taken during the daily calibrations (Zechmeister, Anglada-Escudé, and Reiners, 2014). We divided the spectrum flux by an instrument response function (provided by the standard CARMENES reduction pipeline together with the reduced spectrum) to remove the SED of the flat lamp. Due to the way the spectrum was extracted, its flux values do not reflect the S/N of the original image. To weigh each order according to its original S/N, we rescaled the flux of each order so that its mean counts are equal to the square of the original S/N. When other spectral extraction pipelines are used (e.g. HARPS DRS, Mayor et al., 2003), the extracted spectral orders need to be corrected for the blaze response of the spectrograph grating. In addition, we applied a small correction to ensure a constant overall spectral energy distribution and thus minimise biases arising from different extinction values, for example (Berdiñas et al., 2016). These rescaling values were calculated from the spectrum with a higher S/N in the time series. By doing this, we altered the original S/N of the orders, but we avoided systematic biases in the CCFs.

In the bluest orders of the CARMENES VIS channel, the blue end of the order is noisier than the rest of the wavelengths. We found that removing the first 200-300 pixels improves the RV precision obtained.

We also Doppler-shifted the spectrum to correct for the barycentric motion of the Earth and any instrumental drift measured so that the RV shift derived from the spectrum comes solely from the star. In doing so, the centre of the CCF is always located close to the absolute RV of the target.

2.4.2 Mask preparation: Line selection for spectra at different epochs

When computing the CCF of a series of observations of a target taken at different times of the year, we need to make sure that we are using exactly the same mask lines at each epoch to avoid measurement biases. Since the stellar spectrum shifts across the detector during the year according to the relative velocity between the observed star and the Earth, the lines at the detector edges are not always visible. Therefore, to make sure that we were using exactly the same mask lines at any epoch, we removed the mask lines with wavelengths smaller than the wavelength of the blue cutoff plus the maximum BERV of the target observations, and all the lines with a wavelength larger than the red cutoff minus the maximum BERV. Furthermore, since we displaced the mask across the spectrum to compute the CCF, some mask lines appear and disappear at the order cutoffs depending on the Doppler shift applied to the mask. So we also removed the lines that, depending on the mask position, do not always fall within the spectral order limits. In other words, for each order, we only kept the mask lines that

are between $\lambda_{\rm min}$ and $\lambda_{\rm max}$

$$\lambda_{\rm min} = \lambda_1 \left({\rm BERV}_{\rm max} - v_{\rm min}\right)/c \qquad (2.3)$$
$$\lambda_{\rm max} = \lambda_n \left(-{\rm BERV}_{\rm max} - v_{\rm max}\right)/c,$$

where λ_1 and λ_n are the minimum and maximum wavelength of the order, respectively, ${\rm BERV}_{\rm max}$ is the maximum barycentric shift of the observations considered, $v_{\rm min}$ and $v_{\rm max}$ are the minimum and maximum shift applied to the mask (i.e. the CCF velocity range), and c is the speed of light.

When creating a mask from observations of a specific star, we already removed the stellar lines that fall on regions affected by tellurics at any time of the year. However, telluric lines overlap with different stellar lines depending on the absolute radial velocity of the star. One needs to further remove the mask lines that can be affected by tellurics if the absolute velocities of the star used to create the mask and the target star are different. We followed the same procedure as carried out when excluding regions during the mask creation process (Sect. 2.3.2, we broadened the telluric features by the maximum BERV of the target observations and removed the mask lines that overlap with them). Additionally, we needed to take into account the displacement of the mask across the spectrum. Some mask lines overlap with telluric-contaminated regions for some of the Doppler shifts applied, so we also removed them. After this process, we obtained a set of lines per order that, regardless of the Doppler shift applied, are not affected by tellurics and are visible in the spectrum at any epoch.

2.4.3 CCF location in RV space

Prior to computing the CCF of each order, we need to define the RV range and the steps that we use to Doppler-shift the mask, which determine the span and sampling of the CCF. We need to ensure the full coverage of the CCF span (its minimum and part of the wings), but also, we should not extend far into the continuum to save on computing time. To quickly locate the position of the CCF centre in RV space and estimate its width, we computed a test CCF spanning a large RV range of $\sim 200\,{\rm km\,s^{-1}}$, using coarse steps of $\sim 1\,{\rm km\,s^{-1}}$ in the spectral order with the highest S/N. When both the target's absolute RV and $v \sin i$ are known, this first step can be skipped.

The sampling of the CCF velocity grid should be given by the average pixel size in velocity units, Δv, which can be obtained from the resolving power R of the instrument and the pixel sampling per spectral element. The resolving power at a given wavelength λ can be expressed as λ divided by the minimum difference that can be distinguished at this wavelength, $\delta\lambda$, which is typically the size of a spectral element. By applying

Table 2.2: Average pixel sampling per spectral element (SE), resolving power, and pixel size in velocity units.

Instrument	Sampling s [pix/SE]	Resolving power	RV step [$\mathrm{m\,s^{-1}}$]
CARMENES VIS	2.5	94 600	1268
CARMENES NIR	2.8	80 400	1332

Notes. Sampling and resolving power from Quirrenbach et al. (2018).

the Doppler equation, we get the size of a spectral element in velocity units δv

$$R = \frac{\lambda}{\delta\lambda} = \frac{c}{\delta v} \Rightarrow \delta v = \frac{c}{R} \Rightarrow \Delta v = \frac{c}{R \cdot s}, \tag{2.4}$$

where c is the speed of light. By dividing this quantity by the average pixel sampling per spectral element, s, we get the size of a pixel in velocity units Δv, which gives us the step size by which we have to shift the mask. The average values for the CARMENES VIS and NIR arms are shown in Table 2.2. Another way to find this step size is to directly compute the average width of each spectrum pixel in velocity units. It is important to use the correct sampling to ensure that the CCF flux reflects the actual number of photons of the spectrum and, therefore, its S/N. This is used to estimate the statistical uncertainty on the RV. For example, if we were using a denser sampling (smaller RV steps), we would count the flux in the same pixels more than once, resulting in biased RV errors.

By using this RV step, we obtain a well-sampled CCF for which a Gaussian fit provides its minimum, width and depth, with their corresponding uncertainties. However, this type of sampling is not sufficiently dense to measure the bisector correctly and compute the BIS. For this, we used a denser sampling of $\sim 250\,\mathrm{m\,s^{-1}}$. As with the RV, in order to estimate the uncertainty of the BIS, we needed to use the CCF computed with the correct sampling so that it is consistent with the original S/N of the spectrum (see Sect. 2.4.6.3 for details).

2.4.4 CCF computation details

The calculation of the CCF as a function of the Doppler-shift v was performed by applying Eq. 2.1 to each of the spectral orders separately. The product of the two signals, that is, the spectrum and mask, was computed in pixel space, so both the spectrum and mask have to be expressed in pixel units. Since we did not rebin or merge the spectral orders, each data point (wavelength and flux) corresponds to one pixel, so the spectrum is already in pixel space. The values of each data point correspond to the centre of the pixel. Our mask lines are Dirac δ functions (zero width) expressed in wavelength, so we mapped each one to the corresponding position in the

spectral order, interpolating between the wavelengths of the spectral pixels. We then gave each of them a width of 1 pixel by adding or subtracting 0.5 pixels to the central value to obtain the pixel boundaries. In this way, we transformed our δ mask lines into bins of 1-pixel width.

As expressed in Eq. 2.1, if a spectrum pixel overlaps (totally or partially) with a mask line (non-zero region of the mask), we multiply the value of the flux in that pixel by the value of the mask line weight, thus taking the fraction of the pixel overlapping by the mask into account. If the overlap is not exact, we do not take the flux value of the centre of the pixel. Instead, we linearly interpolate the flux between consecutive pixels, and take the interpolated flux value at the centre of the overlap region between the pixel and the mask. In this way, we obtain a smoother CCF profile and still maintain the observed number of photons.

We computed the CCF on spectral orders that have been corrected for the blaze function of the echelle spectrograph to avoid biases due to the blaze slope. However, this does not take into account the difference in S/Ns along the order, from lower S/N edges to a peak S/N at the centre. Thus, a blaze-corrected spectrum does not preserve the flux and, therefore, its CCF does not immediately reflect the original S/N of the spectrum, which we need in order to estimate the uncertainty of the RV estimate. To correct for this, we should multiply all the pixels of an spectral absorption line by the value of the blaze function at the centre of the line. In this way, we approximately recover the original flux of the line without reintroducing the biasing effects caused by the slope of the blaze. However, since we did not know exactly which pixels correspond to a line in the spectrum, we instead multiplied the mask lines by the corresponding blaze value.

2.4.5 Final co-added CCF

We co-added the CCFs of the individual orders to obtain a final CCF that represents the full spectrum. Since we computed the order CCFs using the same RV grid, we could directly sum the flux at each RV step

$$\mathrm{CCF}(v) = \sum_o \mathrm{CCF}_o(v), \tag{2.5}$$

where $\mathrm{CCF}_o(v)$ is the CCF of order o and $\mathrm{CCF}(v)$ is the final co-added CCF.

Depending on the instrument and the star observed, not all the orders contain the same number of useable lines or have a sufficient S/N. For the CARMENES observations, some orders are severely affected by tellurics, which is reflected in a low number of lines in the mask and poor CCFs. Furthermore, for very late M dwarfs, the bluest orders show a markedly degraded S/N. The CCFs of very low S/N orders ($\mathrm{S/N} \leq 10$)

or orders with few usable lines ($\leq$ 10 lines) do not significantly contribute to the final CCF and may actually be counterproductive. Our tests show that discarding such poor orders may improve the profile of the final CCF, in the sense of obtaining better precision on the derived parameters.

We did not need to apply any weight to the CCFs of the different orders because the flux level of each of them is already proportional to the S/N of the original spectrum order, the number of lines used, and their quality, which are the parameters that we would use to asses the quality and, therefore, weight of each CCF. However, the final flux also reflects the values of the mask line weights. These weights depend on the RV-content of each line, but the absolute values are arbitrary and should not affect the final flux of the CCF. Therefore, we applied a normalisation. We only considered the mask lines that actually contributed to the co-added CCF, that is, the lines kept after removing telluric-contaminated regions and order ends of the orders used in the co-adding. We computed the average of the weights of these mask lines and divided the flux of the co-added CCF by it. In this way, the flux of the CCF reflects the true flux of the pixels used (scaled according to their RV-content) and the absolute weight of the mask lines is irrelevant.

2.4.6 CCF parameters and errors

To study the CCF profile, we fitted a Gaussian function to the central region (from maximum to maximum; see Fig. 2.4) of the co-added CCF. From this function, we derived the RV shift of the spectrum with respect to the mask, the FWHM, and the contrast of the CCF profile. We also analysed its asymmetry by studying its bisector. Here, we describe the estimation of these four parameters and their uncertainties.

2.4.6.1 CCF minimum: RV

We estimated the velocity difference between the observed spectrum and the mask as the position of the minimum of the best Gaussian fit to the CCF. For time-series RV work, we are interested in the relative velocities and, therefore, the differential values between the target and the mask are already appropriate. An intuitive method in order to estimate the RV uncertainty would be to use the formal error of the fit. However, the CCF is not a perfect Gaussian function as it represents the convolution of thousands of lines with different profiles. Therefore, the formal error of the fit overestimates the true uncertainty as the Gaussian model is not adequate. To obtain a realistic value for the uncertainty, we consider the total RV content in the CCF assuming photon noise. The capability of the CCF in providing a precise measure of the RV depends on its steepness and depth. A high S/N, deep, and narrow CCF is much more constraining than a low S/N, shallow, and wide CCF. In turn, this is defined by the S/N of the original spectrum by the number of lines used and by their profiles. Descriptions of

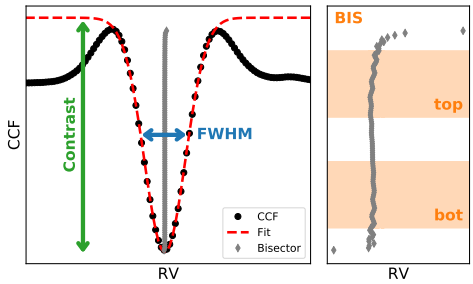

Figure 2.4: Illustration of the CCF activity parameters measured in this work. We plotted a typical CCF of an M dwarf (black dots) and the best Gaussian fit (red dashed line) together with the FWHM and contrast derived from the fit (*left*). We also plotted the bisector of the CCF (grey diamonds) and a zoom to the central region of the CCF to show the bisector shape (*right*). We indicate the top and bottom regions used to compute the BIS.

the estimation of photon-limited errors in RV measurements from spectral lines or CCFs can be found in Butler et al. (1996), Bouchy, Pepe, and Queloz (2001), and Boisse et al. (2010), for example. Here we detail the procedure we followed, which is based on the methodologies of the previous references.

The first step is to compute the uncertainty of the flux on each sampling point of the CCF of each order. This uncertainty is propagated from the uncertainties of the individual pixels that are added when computing the CCF. We consider that the uncertainty on the flux of a pixel x in the spectral order o is given by its photon noise $\sigma_{\mathrm{PN},x}$ and readout noise RON as follows:

$$\sigma^2_{f_{ox}} = (\sigma_{\mathrm{PN},x})^2 + \mathrm{RON}^2 = f_{ox} + \mathrm{RON}^2. \tag{2.6}$$

Assuming Poissonian statistics, the photon noise of the pixel x is calculated as the square root of the total flux in the pixel, f_{ox}, where we use the flux value before rescaling the orders to a constant overall spectral energy distribution, that is, the value representing the observed S/N.

The uncertainty of the CCF of order o at velocity v, $\mathrm{CCF}_o\,(v)$, is then the square root of the quadratic sum of the uncertainties of all the pixels used when computing the CCF at that velocity. For partial pixels, the flux is weighted by the fraction of pixel that overlaps with the line l, which is similar to Eq. 2.1

$$\sigma^2_{\mathrm{CCF},o}\,(v) = \sum_{l=1}^{m} \sum_{x=1}^{n} \sigma^2_{f_{ox}} \Delta_{xl}\,(v)\,. \tag{2.7}$$

When computing the CCF of spectra extracted with a blaze function, the flux of pixel x is also normalised to the original flux level by multiplying it by the interpolated blaze value, corresponding to the pixel of the mask line l, so that the photon noise reflects

the original S/N of the data. This is the same process as with the spectrum (see Section 2.4.4).

The uncertainty of each RV sampling point of the co-added CCF, $\sigma^2_{\mathrm{CCF}}(v)$, is given by the quadratic sum of the uncertainties of all the orders used

$$\sigma^2_{\mathrm{CCF}}(v) = \sum_o \sigma^2_{\mathrm{CCF},o}(v), \tag{2.8}$$

which is the error propagation of Eq. 2.5.

From the value of the uncertainty of the CCF flux ($\sigma_{\mathrm{CCF}}(v)$, the error on the y-axis), we estimate the velocity uncertainty of each CCF point ($\sigma(v)$, the x-axis of the CCF) by using the derivative of the CCF as

$$\sigma(v) = \sigma^2_{\mathrm{CCF}}(v) \left(\frac{\mathrm{dCCF}(v)}{\mathrm{d}v} \right)^{-1}. \tag{2.9}$$

The uncertainty of the final RV is then given by the velocity errors of all the points of the CCF

$$\sigma_{\mathrm{RV}} = \left(\sqrt{\sum_v \frac{1}{\sigma(v)^2}} \right)^{-1}. \tag{2.10}$$

For this procedure to provide realistic uncertainties, it is essential to employ the CCF sampled in RV steps corresponding to the average pixel size.

2.4.6.2 CCF profile variations: FWHM and contrast

To determine the width of the CCF, we used the FWHM of the best-fit Gaussian, which is measured in velocity units (typically $\mathrm{km\,s^{-1}}$). The contrast of the CCF is the amplitude of the Gaussian divided by its baseline level. We inverted the sign of the amplitude, which is negative, and multiplied it by 100 so that the contrast values are positive and given in a percentage. We considered the formal errors of the fit as the uncertainties for these two quantities.

2.4.6.3 CCF profile variations: Bisector (asymmetry)

To quantify the asymmetry in the CCF, we used the standard bisector inverse slope (BIS) as defined in Queloz et al. (2001). We measured the bisector of the CCF in the same interval in which we fitted the Gaussian, that is, the range comprised within the maxima at each side of the global minimum. We linearly interpolated the CCF profile and took the mid points between the left and right side profiles at about 100 different evenly spaced depths. This yields the bisector as a function of the depth d

$$\mathrm{Bisector}(d) = \Big(v(\mathrm{CCF}_{\mathrm{left}} = d) + v(\mathrm{CCF}_{\mathrm{right}} = d) \Big) / 2, \tag{2.11}$$

where $v(\mathrm{CCF}_{\mathrm{left}} = d)$ and $v(\mathrm{CCF}_{\mathrm{right}} = d)$ are the interpolated velocities at depth d at the left and right sides of the CCF. We then consider the following two regions: one at the top of the CCF, from 90 to 60% of the baseline level, and one at the bottom, from 40 to 10% (see orange regions in Fig. 2.4). We computed the average RV of the points in these two regions, and the difference between them, $\mathrm{RV}_{\mathrm{top}}$ and $\mathrm{RV}_{\mathrm{bot}}$, yields the value of the BIS

$$\begin{aligned} \mathrm{BIS} &= \mathrm{RV}_{\mathrm{top}} - \mathrm{RV}_{\mathrm{bot}} \\ &= \langle \mathrm{Bisector}(d) \rangle_{d=60-90\%} - \langle \mathrm{Bisector}(d) \rangle_{d=10-40\%}. \end{aligned} \tag{2.12}$$

As mentioned above, using the CCF computed with the correct RV sampling (i.e. where the RV steps are the size of the average pixel width in velocity units) does not allow us to correctly measure the bisector. Instead, we used a CCF computed with a denser sampling, with steps of 250 $\mathrm{m\,s^{-1}}$.

Regarding the uncertainty, since the BIS is computed from the (interpolated) points of the CCF, we started with the velocity uncertainties of each point of the CCF as computed above (Sect. 2.4.6.1). As was done with the CCF flux when computing the bisector, we linearly interpolated the RV errors of the actual CCF data points to the ~ 100 points, corresponding to the evenly spaced depths used to define the bisector. For each bisector point, the error $\sigma_{\mathrm{bisector}}(d)$ comes from the interpolated uncertainties at each side of the CCF by error propagation of Eq. 2.11. We then computed the uncertainty on the top and bottom regions of the bisector as the mean of all the points considered in each region divided by the squared root of the number of points n_{top} or n_{bot}

$$\begin{aligned} \sigma_{\mathrm{top}} &= \langle \sigma_{\mathrm{Bisector}}(d) \rangle_{d=60-90\%} / \sqrt{n_{\mathrm{top}}} \\ \sigma_{\mathrm{bot}} &= \langle \sigma_{\mathrm{Bisector}}(d) \rangle_{d=10-40\%} / \sqrt{n_{\mathrm{bot}}}. \end{aligned} \tag{2.13}$$

Finally the BIS uncertainty is the square root of the quadratic sum of the uncertainties on the top and bottom regions

$$\sigma(\mathrm{BIS}) = \sqrt{\sigma_{\mathrm{top}}^2 + \sigma_{\mathrm{bot}}^2}. \tag{2.14}$$

2.5 Application to the CARMENES survey

2.5.1 Sample

We followed the procedure explained in the previous sections to build a set of masks using CARMENES survey observations to compute the CCFs for most of the targets in the sample. The CARMENES survey sample (Alonso-Floriano et al., 2015; Cortés-Contreras et al., 2017; Reiners et al., 2018b; Schweitzer et al., 2019) includes about 350

M dwarfs of subtypes from M0.0 to M9.0. Most of the targets are early and mid M dwarfs, and only less than 20 stars have a spectral type equal or later than M6.0. Most of the stars have low projected rotational velocities, $v \sin i \leq 10\,\mathrm{km\,s^{-1}}$, although some show $v \sin i$ values of a few tens of $\mathrm{km\,s^{-1}}$. The sample includes both inactive and active stars for early and mid spectral types, while most of the late spectral type targets show high levels of activity.

In total, we computed CCF profiles and parameters of 323 targets in the VIS, excluding those with $v \sin i \gtrsim 60\,\mathrm{km\,s^{-1}}$ and spectroscopic binary systems (already studied in Baroch et al., 2018). In the NIR, we computed CCFs for 305 targets. Since there is less RV content in the NIR than in the VIS, we could not get reliable masks and CCFs for the faintest targets and the ones with $v \sin i \gtrsim 25\,\mathrm{km\,s^{-1}}$; we therefore excluded them from this analysis. We used different masks for targets of different spectral types, but this is especially the case for targets of different $v \sin i$. In the following, we explain the tests we performed to select the final set of masks used for different types of targets, which we divide into slow and fast rotators.

2.5.2 Slowly-rotating stars

For each spectral subtype (M0.0 V to M0.5 V, M1.0 V to M1.5 V, etc.), we selected the objects with the highest S/N to build the best possible template. This generally corresponds to the brightest objects with the highest number of observations. We restricted this search to targets with low $v \sin i$ ($v \sin i \sim 2\,\mathrm{km\,s^{-1}}$) and low levels of activity. We did this because our early tests show that for targets with larger $v \sin i$, we obtained better results (CCFs with smoother profiles and smaller RV dispersions) when using masks built from observations of a star with also larger rotational velocity, rather than using one of the standard masks obtained with observations of a slowly-rotating star. The masks were built using the selection parameters shown in Table 2.1.

Table 2.3 lists the targets used to create the masks together with the number of co-added observations, the S/N of the template, and the total number of lines of the masks for the CARMENES VIS and NIR spectral ranges. Figure 2.5 shows a histogram of the number of lines of the masks listed in Table 2.3 as a function of wavelength.

We analysed the performance of the different VIS masks on targets of different spectral types. We did this for several targets with low $v \sin i$, low activity levels, and more than 100 observations when possible, since most late spectral type targets are very active and have not been observed that many times. We computed the CCF of these targets with the different masks and studied the CCF profiles and the parameters time series.

Table 2.3: Targets used to build the masks employed to compute the CCFs of the low $v \sin i$ stars with their spectral types, rotational velocities, and magnitudes.

Karmn	Name	Sp. type[a]	$v \sin i$[b] [km s^{-1}]	J[c] [mag]	VIS template # obs	VIS template S/N	VIS mask # lines	NIR template # obs	NIR template S/N	NIR mask # lines
J12123+544S	GJ 458A	M0.0 V	≤ 2.0	6.88	110	1189	2019	105	1423	157
J11033+359	GJ 411	M1.5 V	≤ 2.0	4.20	310	1907	3762	300	2247	166
J19169+051N	GJ 752A	M2.5 V	≤ 2.0	5.58	129	1194	4332	125	1381	201
J07274+052	GJ 273	M3.5 V	≤ 2.0	5.71	733	1090	5334	721	1663	283
J13229+244	GJ 3779	M4.0 V	≤ 2.0	8.73	113	701	5423	110	1022	269
J20260+585	GJ 1253	M5.0 V	≤ 2.0	9.03	183	667	6136	182	991	443
J10564+070	GJ 406	M6.0 V	2.9	7.09	79	517	4382	76	1078	353
J02530+168	Teegarden's star	M7.0 V	≤ 2.0	8.39	245	732	5387	244	1528	389

Notes. We also show the number of observations used to build the templates, the S/N of a reference order (order 82 in the VIS and order 58 in the NIR) and the number of lines of the final mask in the VIS (from order 108 to order 68, 5623–9068 Å) and NIR channels (from order 63 to order 36, 9618–17118 Å).
References. [a] Alonso-Floriano et al. (2015) except J12123+544S, J13229+244, J20260+585 Hawley, Gizis, and Reid (1996). [b] Reiners et al. (2018b). [c] Skrutskie et al. (2006).

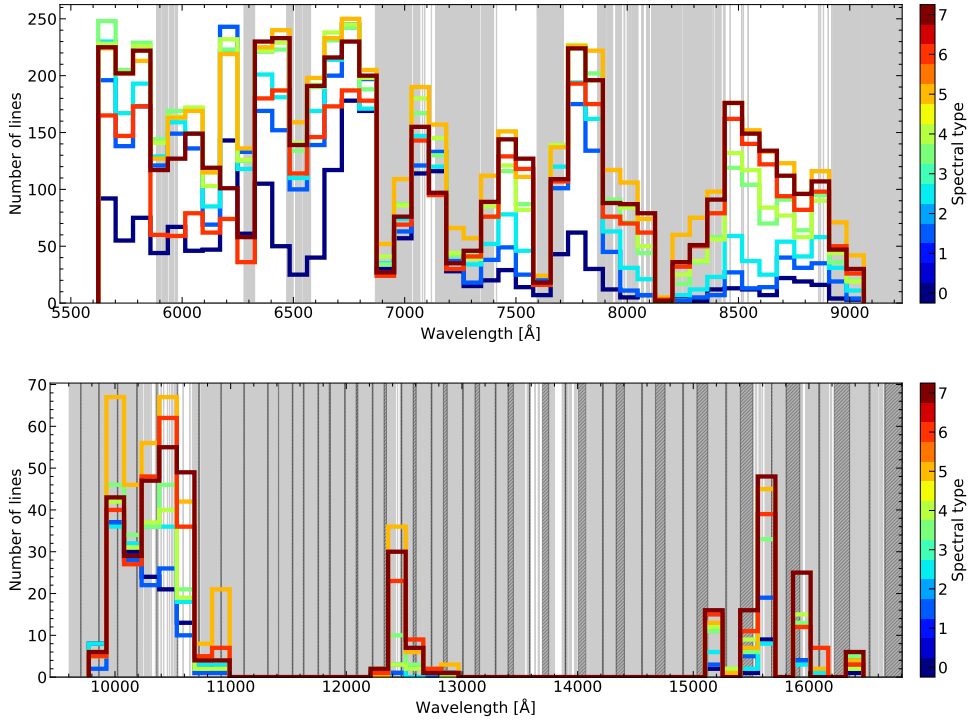

Figure 2.5: Histogram of the line wavelengths of the masks used to compute the CCFs of the low $v \sin i$ targets for the VIS (*top*) and NIR (*bottom*) channels. Different colours correspond to the different spectral types of the targets used to build the masks (see targets and number of lines in Table 2.3). Light grey areas correspond to regions affected by telluric features, which are broadened by ± 30 km s^{-1}. Dark grey hatched areas correspond to regions without spectral information in the CARMENES data, corresponding to gaps between consecutive spectral orders (redwards of 11500 Å), and intra-order gaps in the NIR detector mosaic.

Although they have a different number of lines, we find that for most of the early and mid spectral type stars, from M0 to M6–M7, masks built from early and mid spectral type targets result in smooth CCF profiles and RV time series with similar scatter and modulation. Therefore, we are able to obtain reliable CCF profiles and parameters with a single mask for all early and mid spectral type targets. However, we find that using more than one mask for different spectral subtypes slightly improves the precision of the parameters. We note that different masks result in RV time series with different absolute offsets, with differences of the order of a few tens of $\mathrm{m\,s^{-1}}$, thus showing the difficulty in computing the absolute displacement of a mask.

Regarding the other CCF parameters, they also show similar dispersions and modulations for masks of different spectral types, and their absolute values also seem to depend on the mask used. FWHM mean values can vary by some hundreds of $\mathrm{m\,s^{-1}}$ for masks of a different spectral type showing very similar RV scatters. The same happens with the contrast and the bisector. Contrast mean values can vary by about 10% and bisectors can fluctuate by some tens of $\mathrm{m\,s^{-1}}$. This shows that the same mask must be used if we want to compare CCF parameters.

For early M dwarfs (M0 V−M1 V), the VIS channel CCF has the shape of an absorption line and rather flat wings. The same shape is found in G and K stars (see e.g. Fig. 1 in Mayor and Queloz, 1995). As we move towards later-type stars, the flux level of the CCF continuum decreases and two humps appear at either side of the CCF (such as in Fig. 2.4). The appearance of the two humps and the decreasing continuum are a consequence of the very large density of spectral features in cooler stars. The mask lines are chosen to represent those spectral features that are best defined, that is, showing no obvious blends and asymmetries as well as with a clearer continuum. As the mask slides through the spectrum at different wavelength positions, the density of stellar lines is so high that a number of the mask lines randomly coincide with stellar absorption features. This means that the CCF continuum is depressed. The first CCF flux maximum occurs just before the mask lines enter the stellar absorption lines because all mask lines receive flux from the continuum as the mask is only composed of lines that are well behaved. The second maximum occurs for the same reason just after the mask lines leave the stellar lines. This explains the characteristic shape of the CCF for stars of spectral types later than M1 in the case of the CARMENES VIS spectra. Interestingly, we do not observe this phenomenon in the NIR channel CCFs as the lines in the spectrum are more widely spaced.

2.5.3 Fast-rotating stars

The spectra of stars with high $v \sin i$ values are quite different from those of low $v \sin i$ stars of similar types because their lines are much broader and most of them

become heavily blended. Moreover, line profiles can be affected by distortions due to stellar activity, which is generally stronger in fast rotators. Using one of the 'standard' masks made from a low $v \sin i$ and inactive target for a star with larger $v \sin i$ (from $\sim 3\,\mathrm{km\,s^{-1}}$ up to $\sim 10 - 15\,\mathrm{km\,s^{-1}}$) still delivers a smooth CCF profile. However, the RV dispersion is larger than if we were to use a mask made from an object of $v \sin i$ close to the one of the target star. This would be the case even if the spectral type is not a very good match.

For even faster rotators, using the standard masks results in a CCF profile that shows a global minimum close to the RV value of the target, but mostly this contains noise, with the CCF showing bumps across its profile. The profile becomes noisier as the $v \sin i$ of the star increases up to a point where we are not able to distinguish any minima for the stars with the most extreme $v \sin i$ values ($v \sin i \gtrsim 40\,\mathrm{km\,s^{-1}}$). In using a mask that is also made from a large $v \sin i$ target, the CCF profile becomes less noisy, but we cannot obtain smooth profiles as is the case for slower rotators. When building such a mask, in order to be able to select any line, the FWHM cuts need to be larger than in the low $v \sin i$ case. The resulting masks have fewer lines, only a few hundred, which also impedes obtaining a smooth CCF because of the lower S/N that results from only considering a small number of lines. Another problem is that most of the fast-rotating stars are the ones with the latest spectral types and, therefore, they are fainter and deliver poorer S/N observations. Also, in general, fewer observations are available. All of this implies that the templates have a low S/N. In some extreme cases, we smoothed the templates applying a convolution with a Gaussian profile in order to identify local minima due to bona-fide absorption lines instead of noise features. For stars with $v \sin i \gtrsim 50 - 60\,\mathrm{km\,s^{-1}}$, it becomes unfeasible to identify a large number of lines following our methodology. In all circumstances, and because of the numerous blends, CCF parameters of fast-rotating stars are much less reliable than for slow rotators.

2.5.4 Final masks

In light of these results, we used a grid of masks to compute the CCFs of the CARMENES survey sample. For targets with $v \sin i \leq 4\,\mathrm{km\,s^{-1}}$, we used the standard masks listed in Table 2.3. The procedure is to employ the mask corresponding to the spectral type closest to that of the target. For faster rotators, we used a different set of masks made from targets with larger $v \sin i$ values. We divided the targets according to their $v \sin i$ in bins of approximately $10\,\mathrm{km\,s^{-1}}$, up to $v \sin i \sim 60\,\mathrm{km\,s^{-1}}$ in the VIS, and $v \sin i \sim 30\,\mathrm{km\,s^{-1}}$ in the NIR. For each bin, we selected targets of different spectral types for which we can obtain templates with a sufficiently high S/N and build the masks. We finally obtain one to three masks per $v \sin i$ bin covering different spectral types, depending on target availability.

2.5.5 Comparison between CCF and template-matching RVs

To analyse the performance of the CCF method regarding the precision of the resulting RVs, we compared them with the velocities computed using the standard CARMENES RV pipeline SERVAL (Zechmeister et al., 2018). As mentioned above, SERVAL computes the RV of a series of observations by fitting a high S/N template made from the observations themselves. It matches the template to the observations order-by-order, and the final RV is a weighted average of the RVs of the individual orders. Since it uses a complete spectrum template, it extracts more information than the CCF method, which only uses a subset of the absorption lines.

By default, SERVAL builds the template from the observations of the star that is being analysed, but it is also possible to use a different template built from observations of another star. Using another template gives better results in the case of faint stars or stars with a small number of observations. For the CCFs, we only used masks that were created from high S/N templates, except for a few fast rotators where the templates obtained have an S/N lower than the standard masks for slow rotators. Here, we use the default SERVAL results where a template has been created for each star with its own observations. All of the analysed stars have been observed at least five times.

Aside from using templates of a different S/N, another difference between both methods is the use of different orders to compute the final RV. The RV depends on the spectral region used since there is a chromatic dependence. Also, the RV dispersion appears to be larger in the blue region of the spectral range, where the activity effects are expected to be stronger (see e.g. Tal-Or et al., 2018). Moreover, ground-based observations, such as the CARMENES ones, show regions contaminated with tellurics. Some orders are more affected than others, and they may introduce additional scatter due to unidentified telluric features. In using different sets of orders and in especially removing blue orders in the case of active stars may reduce the RV dispersion. SERVAL uses the VIS orders 108 to 67, except in some faint and late spectral type targets, where about the 20 to 30 bluest orders are omitted. In the CCF VIS data, we used orders 108 to 68. However, between 5 and 10 orders were removed because the masks do not have enough lines to provide a reliable CCF. This is mainly due to the presence of tellurics. We also removed the bluest orders in the case of faint and late-type targets. Using these regions allowed us to obtain better results. In the case of the NIR arm, SERVAL mainly uses about 20 orders, which are not contaminated by tellurics, in the Y and H bands. We chose to use the same orders in the NIR CCFs to avoid telluric contamination.

In Fig. 2.6 we plot the distribution of the RV time series dispersions obtained with the CCF method and with SERVAL's template matching for each of the survey stars analysed in both VIS and NIR channels. We measured the dispersion as the

weighted standard deviation of the RVs, where we used the squared inverse of the RV uncertainties as weights. We corrected the RVs for an instrumental nightly zero-point drift (Trifonov et al., 2018; Tal-Or et al., 2019). These nightly zero-points were calculated using the SERVAL RVs of stars with small variability observed in each night. We used the SERVAL measurements instead of the CCF ones because they are more precise in general. Figure 2.7 shows the correlation of the RV dispersions obtained with the two methods (the same quantities as in Fig. 2.6) for the analysed stars.

In the VIS channel, the RV dispersions of all the stars show a similar distribution for RVs calculated with SERVAL and CCFs. Although, in general, the scatter is slightly larger in the latter case. This is what we expected because the template matching technique used by SERVAL takes all of the spectral regions into account, rather than the regions around a set of some selected lines as the CCF does. Thus SERVAL is able to extract more RV information from the spectra.

For the NIR data, we obtain much larger dispersions than SERVAL in general. This may be caused by the low number of mask lines used (see Table 2.3), which in turn is due to a large number of regions containing tellurics in the NIR range. Not having enough lines in the mask results in CCFs with a low S/N and less precise parameters. We note that the NIR CCF results are not as optimised as in the VIS case, which is the one we used to perform most of our tests due to its better precision compared to the NIR. A different choice of parameters, both in the mask creation (different line selection values) and the CCF computation (different pixel and order masking) processes may lead to improved results. In the same vein, we expect the RV precision to be improved by using telluric-corrected spectra as presented in Nagel et al. (submitted).

There are some cases in which the dispersion of the CCF RVs is smaller than for SERVAL. This occurs for stars where the template has a poorer S/N, that is, in the case of faint stars or stars with a small number of observations. In Fig. 2.8, we plot the ratio of the RV dispersions obtained with SERVAL and with the CCFs as a function of the number of observations co-added to build the SERVAL template for each star. We see that for the VIS data, the ratio is larger (which means lower dispersions for the CCF RVs compared to SERVAL RVs) in the case of stars with less than 10–20 observations. Late spectral type targets, which are faint, also show a large ratio. In these cases, instead of using a template made from the observations of the target itself, which is the default in SERVAL, we used a high S/N template built from observations of a similar star. We obtain RVs that are more precise and that show smaller scatter compared to the results of the default template.

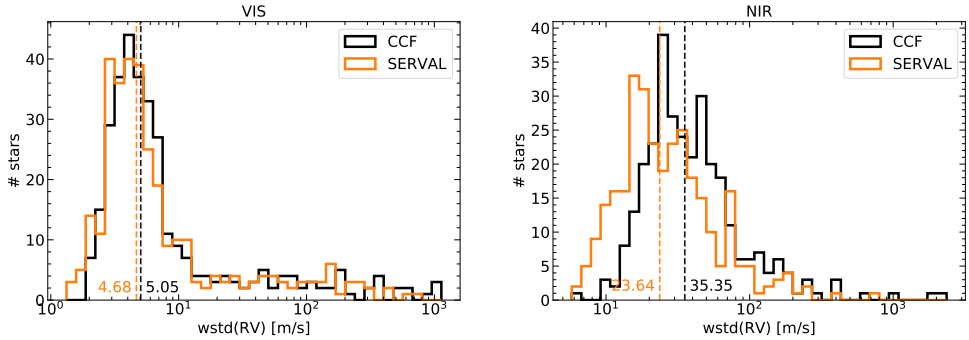

Figure 2.6: Time series RV dispersions (weighted standard deviations) obtained with the CCF (black) and with SERVAL (orange) in the VIS (*left*) and NIR (*right*) channels. The dashed lines show the median of each distribution.

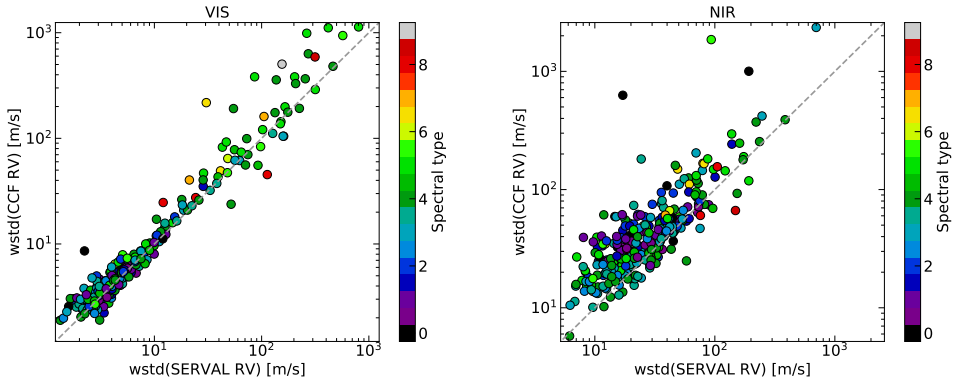

Figure 2.7: Comparison of the time series RV dispersions (weighted standard deviation) obtained with the CCF and SERVAL methods, in the VIS (*left*) and NIR (*right*), which are colour-coded with spectral type. The grey dashed line indicates the one-to-one relation.

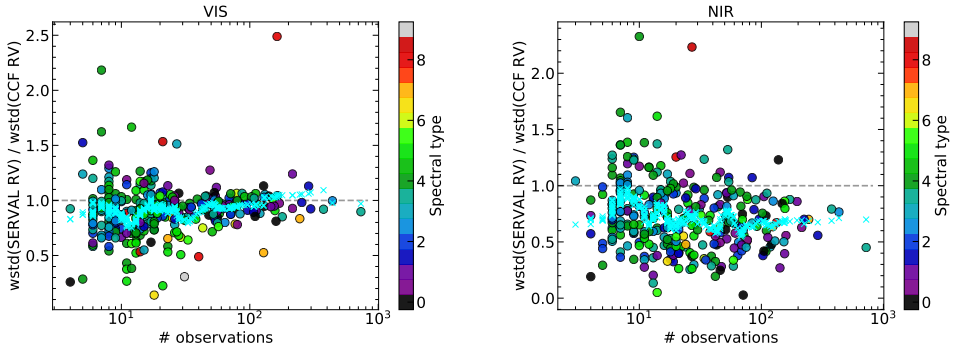

Figure 2.8: Ratio of the SERVAL and CCF RV dispersions (weighted standard deviations) as a function of the number of observations co-added by SERVAL to build the template, in the VIS (*left*) and NIR (*right*) channels, which are colour-coded with the stellar spectral type. The cyan crosses show the moving average of the data computed over windows of 20 data points.

2.5.6 Activity analysis

To show an example of the CCF activity indicators (FWHM, contrast, BIS), in Figs. 2.9 and 2.10, we plot the RV time series, together with the three activity indicators, for an active star in the CARMENES survey sample, YZ CMi (GJ 285, Karmn J07446+035), corresponding to observations obtained with the VIS and NIR channels, respectively. YZ CMi is an active mid M dwarf (spectral type M4.5 V, Reid, Hawley, and Gizis, 1995) with a projected rotation velocity of $v \sin i \simeq 4\,\mathrm{km\,s^{-1}}$ (Reiners et al., 2018b) and a rotation period of $P_{\mathrm{rot}} \simeq 2.78\,\mathrm{d}$ (Díez Alonso et al., 2019).

It shows a large-amplitude modulation in the RV of a few hundreds of $\mathrm{m\,s^{-1}}$ peak-to-peak in both channels due to stellar activity. Both VIS and NIR data show similar behaviour. The BIS is the indicator that shows the clearest correlation with the RVs. Both parameters show a similar modulation in the phase-folded plot but in opposite phase, and the correlation plot shows a strong anti-correlation, with a Pearson's correlation coefficient of about –0.9. This anti-correlation was first observed by Queloz et al. (2001) and has since been observed in several stars for which the RV modulation contains a signal caused by stellar activity (e.g. Bonfils et al., 2013, reported correlations in several M dwarfs). We also observed such anti-correlations in other active M dwarf stars from the CARMENES sample. The behaviour of the BIS is similar to the one observed for the chromatic index of YZ CMi, which is a measure of the variation of the RV with the wavelength (Tal-Or et al., 2018; Zechmeister et al., 2018).

The FWHM and the contrast also show a modulation at the stellar rotation period; although, it is not as clear as the BIS one. The correlation of these two parameters with RV is not very clear either, but there is some loop shape in which the data points follow the stellar rotation phase. This was already observed for another activity indicator, the differential line width, which is a parameter that measures variations in the stellar line width compared with a stellar template (again see Zechmeister et al., 2018).

This example shows the value of the CCF parameters to be reliable activity indicators. These activity proxies, together with other photospheric and chromospheric indicators of activity, are being used in several projects that include CARMENES observations to study stellar activity and to help distinguish between planetary and activity-related signals in RV time series. These projects include both M-dwarf data taken under the CARMENES survey program (Schöfer et al., submitted; Kaminski et al., 2018; Luque et al., 2018; Reiners et al., 2018a; Lalitha et al., 2019; Nagel et al., 2019; Perger et al., 2019) as well as open time observations of other cool stars (Luque et al., 2019a; Pallé et al., 2019). We observe that the indicators in different stars display notable differences depending on the spectral type and activity level of the stars, which

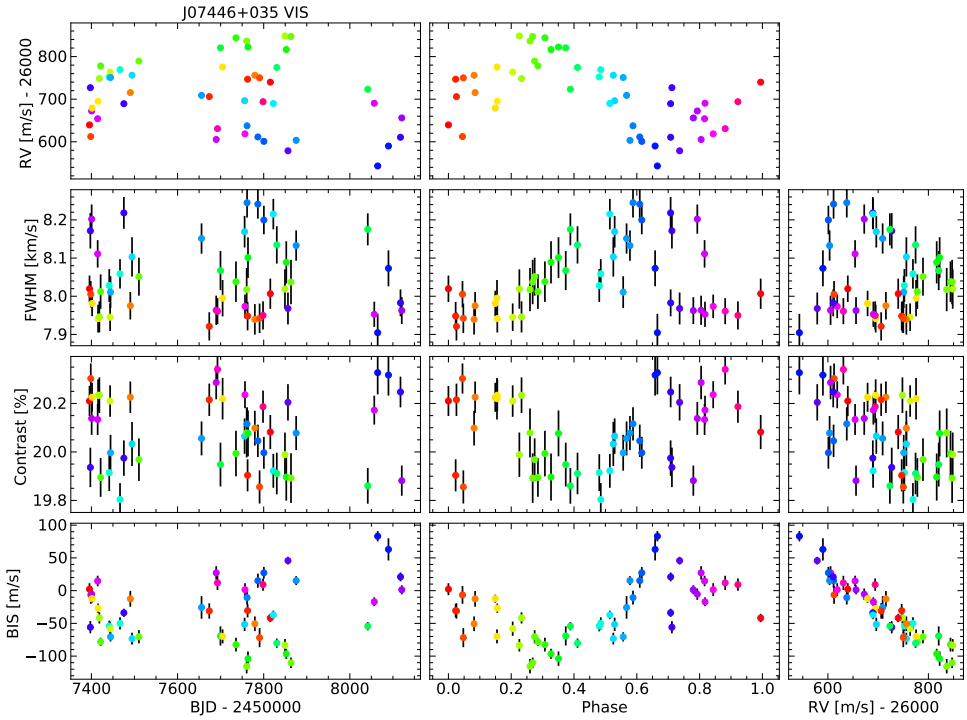

Figure 2.9: Time series of the four parameters derived from the CCF for the star YZ CMi in the VIS channel. We show RV, FWHM, contrast, and BIS (*from top to bottom*) as a function of barycentric Julian Date (*left*), phase of the rotation period (*middle*), and also plot the correlation of the activity indicators with the RV (*right*). The data points are coloured according to the stellar rotation phase.

we study more in depth in the following chapter.

2.5.7 Absolute RVs

We estimated absolute RVs of the CARMENES survey targets by using the RV values derived from the CCFs. Absolute RVs are necessary to determine stellar space motions and to carry out studies of galactic kinematics and dynamics. Since our template masks are calibrated against PHOENIX spectra, our CCF RVs are appropriate to determine the true offset of the wavelengths from their reference values. The radial velocity that we measured from the wavelength shifts of the absorption lines is displaced from the true motion of the stellar barycentre due to several effects (Lindegren and Dravins, 2003). For cool dwarfs, the dominant effects are the gravitational redshift that the photons experience as they escape the potential well, which is created by the mass of the star, and the convective shift due to the motion of hot and cold material in the stellar photosphere. Therefore, apart from the RV that was directly derived from the CCF measurements, we also need to take these effects into account. To compute the

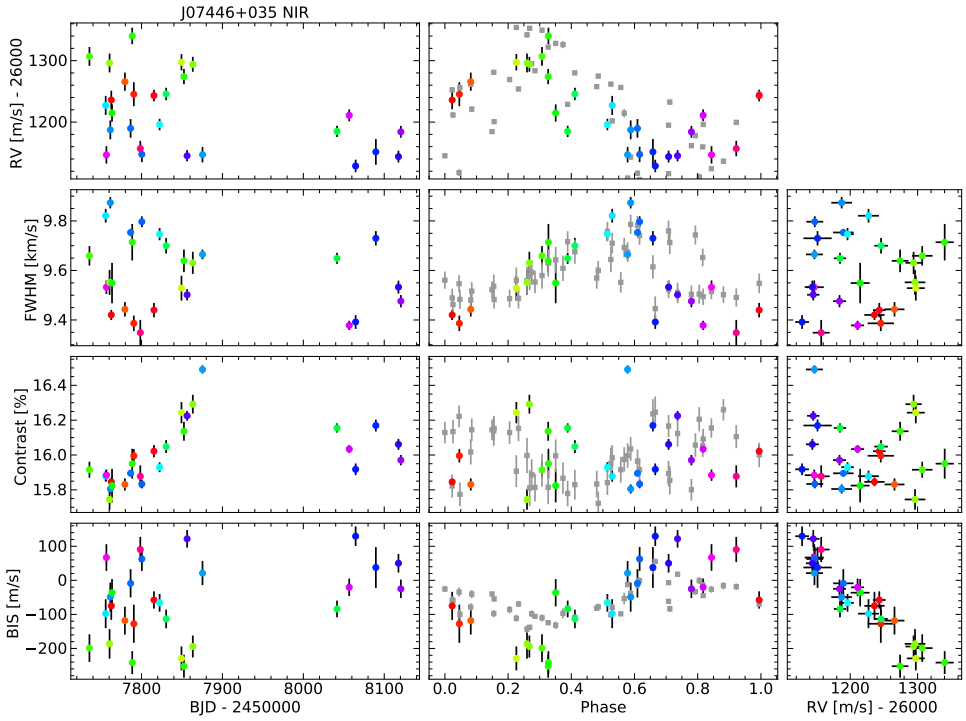

Figure 2.10: Same as Figure 2.9, but for the NIR channel. In the phase-folded plots (*central panels*), we also plotted the VIS data as grey squares, which are shifted to the mean of the corresponding NIR parameter, to compare the amplitude of the modulation.

absolute RVs of the CARMENES survey stars, $\mathrm{RV_{abs}}$, we followed

$$\mathrm{RV_{abs}} = \mathrm{RV_{CCF}} + v_{\mathrm{grav}} + v_{\mathrm{conv}}, \tag{2.15}$$

where $\mathrm{RV_{CCF}}$ is the RV directly derived from the CCF measurements, v_{grav} is the gravitational shift of the star, and v_{conv} is the convective shift of the stellar photosphere.

We computed $\mathrm{RV_{CCF}}$ as the weighted mean of the RV time series of each target. Ideally, we would add in the model of each time series signals from companions and stellar activity on top of the RV zero point. For simplicity, we ignored those effects, which are mostly short-term (and therefore averaged out in long time series) and at the $\mathrm{m\,s^{-1}}$ level. Exceptions include single-lined spectroscopic binaries with long periods where the system velocity has not been established yet. Double-lined spectroscopic binaries in the sample were not considered here; Baroch et al. (2018) already provided absolute RVs for them. We used the nightly zero-point corrected VIS data and removed the observations without drift correction (except in stars without any instrumental drift estimation). We estimated the uncertainty arising from the dispersion of the different RV measurements of each star, σ_{CCF}, as their weighted standard deviation

divided by the square root of the number of measurements.

A systematic error source when estimating the absolute RV shift is the zero-point of the CCF masks. As explained in Sect. 2.3.4.3, in order to transform the masks to an absolute reference, we cross-correlated them with PHOENIX synthetic models, which we assumed to have a zero offset, and we also used the RV derived from the best-fit Gaussian to the CCF to correct the mask shift. There is uncertainty as to the mask zero-point, $\sigma_{\rm mask}$, because of mismatches between the mask and the model lines. To measure this uncertainty, we used the formal error of the Gaussian fit, which has typical values of $\sim 30\,{\rm m\,s^{-1}}$ for a mask made from low $v \sin i$ targets, and it increases by some tens of $\rm m\,s^{-1}$ for the fastest rotators.

The gravitational redshift of a photon escaping from the surface of a star of mass M and radius R is given by

$$v_{\rm grav} = \frac{GM}{cR}, \tag{2.16}$$

where G is the gravitational constant and c is the speed of light. We used this equation with stellar mass and radius values from Schweitzer et al. (2019) to estimate the gravitational redshift, and we assumed the uncertainties derived by error propagation from Eq. 2.16.

The net velocity shift due to convective motions in the photosphere is more difficult to quantify. In the Sun, the effect of the upward motion of the granules and the downward motion of the intergranular lanes results in a net average blueshift of about $400\,{\rm m\,s^{-1}}$. However, the exact value depends on the characteristics of the line used, such as the line strength, the excitation potential, or the formation depth in the atmosphere. There is also a limb effect: The value of the net shift changes from the centre to the limb of the solar disc (Löhner-Böttcher et al., 2019). For other cool stars, 3D hydrodynamical atmosphere models that compute the convective shift using several lines in a specific wavelength range (Allende Prieto et al., 2013), as well as observations of specific spectral lines (Meunier et al., 2017), also show a dependence of the convective shift on the line or lines used. In particular, lines at shorter wavelengths experience larger blueshifts than those at longer wavelengths, and shallower lines (formed deeper in the atmosphere) are also more blueshifted than stronger lines. The effective temperature of the star also affects the convective shift (Bauer et al., 2018) from blueshift values of $500\,{\rm m\,s^{-1}}$ for early G-type stars decreasing until values of $100\,{\rm m\,s^{-1}}$ for late K-type stars. The blueshift also decreases with the metallicity, the surface gravity, and the activity level of the star.

We found neither theoretical nor observational studies that delved into the effects of convective blueshift in M dwarfs. Therefore, we extrapolated the results obtained for earlier spectral type stars. We expect the convective shift in M dwarfs to be small since

they have lower effective temperatures and can have large levels of activity. There even seems to be evidence of a reversed convection pattern, showing a convective redshift instead of a blueshift (Kürster et al., 2003; Baroch et al., 2020). Due to the difficulty in estimating a value for the convective shift $v_{\rm conv}$ for our target stars, we assumed it to be zero with an uncertainty $\sigma_{\rm conv}$ of 100 m s^{-1}.

The final absolute RV values, RV$_{\rm abs}$, obtained using Eq. 2.15, are shown in Table A.1 in Appendix A. The RV$_{\rm abs}$ uncertainties are the quadratic sum of the following four sources of error that we considered: the error of the RV measurements dispersion $\sigma_{\rm CCF}$, the error from the gravitational redshift $\sigma_{\rm grav}$, 100 m s^{-1} to account for the uncorrected convective shift $\sigma_{\rm conv}$ (which for most targets is the dominating one), and the error of the zero-point of the mask $\sigma_{\rm mask}$

$$\sigma^2_{\rm abs} = \sigma^2_{\rm CCF} + \sigma^2_{\rm grav} + \sigma^2_{\rm conv} + \sigma^2_{\rm mask}. \tag{2.17}$$

The same table also contains the average RV from the CCF measurements, RV$_{\rm CCF}$ (which already includes the correction of the mask zero-point), together with the combined uncertainty of the RV scatter $\sigma_{\rm CCF}$ and the mask zero-point $\sigma_{\rm mask}$ given by their quadratic sum. We also list these two uncertainties separately. Finally, we also give the gravitational redshift estimates together with their uncertainties.

2.6 Summary

We present a procedure to build weighted binary masks, compute CCFs of high-resolution echelle spectra with these masks, and derive RVs and the following standard CCF activity indicators: FWHM, contrast, and BIS. In order to build the masks, we used a stellar spectrum template built from observations and we selected the mask lines based on the profile of the local minima present in it.

We applied these methods to the CARMENES survey sample, which is a set of more than 300 nearby M dwarfs. By using CARMENES observations of the brightest and most frequently observed targets, we created several masks covering the different spectral subtypes and rotational velocities of the stars in the sample. We then used these masks to compute CCFs of the whole sample. Our tests show that the CCF parameters depend on the mask used, and they tend to be more precise if the mask was built from observations of a star with similar characteristics as the target. We found that the most important parameter to select a mask was the rotational velocity; results were more sensitive to this than to the spectral subtype of the mask. For fast rotators, the absorption lines in the spectrum become severely blended, so the number of mask lines that we were able to select decreases from a few thousand of the lowest $v \sin i$ masks to only a few hundred, making the CCF and its parameters much less

reliable. Moreover, fast rotators tend to be active stars, so their line profiles are affected by deformations due to activity features on the stellar surface, which add noise to the results.

We compared the RVs derived from the CCF method with the ones obtained with the standard CARMENES pipeline `SERVAL`, which performs a fit of the observation with a spectrum template obtained by co-adding the observations themselves. As expected, `SERVAL` generally performs better than the CCF because it is able to exploit more information from the whole spectrum, while the CCF only uses the region around a set of a few selected lines. However, in some cases, the scatter was smaller in the CCF RVs than in `SERVAL`. This happened in faint stars or stars with few observations, where the template employed by `SERVAL` has a low S/N, while the CCF uses masks built from high S/N templates.

We show the behaviour of the CCF activity indicators of YZ CMi, which is an active mid-type M dwarf that displays a large modulation due to activity in its RV time series. We found that the BIS shows a clear anti-correlation with the RVs in a similar way as the chromatic index. On the other hand, the FWHM and contrast show a more complicated correlation with the RVs, but if we consider the stellar rotation phase of the signals, both parameters show phase-shifted correlations.

Finally, we estimated the absolute RVs of the CARMENES sample stars using the CCF RVs and discuss the main sources of shifts that affect the M-dwarf spectra. This includes the redshift caused by the gravitational potential of the star and the shift due to convective motions in the photosphere.

In conclusion, even though other algorithms allow us to obtain more precise RVs in the case of cool stars, the CCF method still offers a fast and straightforward way of obtaining RVs by simply cross-correlating the observed spectrum with a mask, which is a simple model of the absorption lines in the spectrum. Moreover, we can compute different indicators related to stellar activity from the CCF profile, which have proven to be valuable when studying activity-related signals in RV time series.

Chapter 3

Activity indicators across M dwarfs

3.1 Introduction

To study stellar activity, especially magnetic activity such as spots and faculae, we rely on a variety of activity indicators obtained from the same stellar spectra used to extract RVs, which probe activity in different ways. Common examples are measurements of the flux in the core of chromospheric lines, such as the Ca II H&K or Hα lines, parametrisations of the cross-correlation function (CCF) profile, or chromatic changes in the RVs measured with the so-called chromatic index (CRX). In the next section (Sect. 3.2) we provide an overview of some of the most common spectroscopic indicators. These indicators are affected by the activity of the star, but not by the presence of possible planetary companions. Consequently, they are useful, and often necessary, to distinguish between the planetary or stellar origin of the periodic signals found in the RVs. Nowadays, most planetary detections should be accompanied by an assessment of stellar activity. Nevertheless, as mentioned in Sect. 1.2.5, exoplanet detections have often been challenged by further analyses of the activity of the host stars (e.g. Queloz et al., 2001; Desidera et al., 2004; Bonfils et al., 2007; Huélamo et al., 2008; Boisse et al., 2009; Figueira et al., 2010; Hatzes, 2013; Haywood et al., 2014; Santos et al., 2014; Robertson et al., 2015; Rajpaul, Aigrain, and Roberts, 2016), which reflects the difficulty in finding the true origin of an RV modulation.

Correlations of activity indicators with the RVs, or the presence of the same periodic signal in both the RV and the indicators, suggest the existence of activity-driven variations in the RVs. Indicators such as asymmetry measurements of the CCF bisector inverse slope (BIS) or the CRX have been observed to show linear correlations with the RVs, however, this is not the case for, e.g., the full-width-at-half-maximum (FWHM) of the CCF or indicators derived from chromospheric lines in late-type stars. This does not mean that these indicators are not correlated with the RVs, but rather, they often show a more complicated relation, usually due to being out of phase with the RVs (e.g. Santos et al., 2014; Perger et al., 2017). Usually, indicators display signals at the stellar

rotation period or some of its harmonics (Boisse et al., 2011), but because of differential rotation, the signals may not be exactly at these frequencies. Complex active region patterns on the stellar surface also alter the frequencies seen in the periodograms. Moreover, signals observed in indicators that trace different types of activity, e.g., activity on the photosphere or the chromosphere, do not have to exactly match.

On top of all these difficulties, the behaviour of the activity indicators in different stars displays notable differences. Some stars may show activity-related signals in only some of them but not in others, while in a different set of stars, the 'useful' indicators may be different. Also, the presence of complex active regions can cause the appearance of activity signals at different multiples of the true stellar rotation period on some of the indicators, but not on others (see e.g. Schöfer et al., submitted).

There are a number of studies focusing on the temporal variability experienced by common indicators, the correlations between them, and their relation with RV measurements on relatively large sets of stars. The temporal evolution of RVs and activity indicators is usually studied through a periodogram analysis, which can be used to estimate stellar rotation periods. Suárez Mascareño et al. (2015, 2017) studied temporal variations on timescales comparable to the stellar rotation periods of RVs and the chromopheric Ca II H&K and the Hα lines. The authors analysed a sample of $\sim$ 50 relatively quiet (periods ranging from $\sim$ 10 to 150 d) late-F to mid-M stars observed as part of the HARPS planet-hunting programme (Mayor et al., 2003). They were able to identify periodicities related to the stellar rotation period in most of the sample stars in indicators derived from both lines and the RVs, which highlights the importance of a good characterisation of stellar activity even for quiet stars. Suárez Mascareño et al. (2018) further expanded the two previous works with a similar study of $\sim$ 70 early M dwarfs observed with HARPS-N within the HADES RV programme (Affer et al., 2016). Using the indicators previously mentioned, as well as the FWHM of the CCF, they estimated rotation periods in about half of the sample stars, and identified activity-induced signals in the RVs in a quarter of all the stars.

To perform a periodogram analysis, having a minimum number of observations is essential to detect any significant signal. If that is not the case, it is also possible to study activity by looking for correlations between the RVs and the indicators. Tal-Or et al. (2018) performed such a study in the CARMENES GTO sample of M dwarfs, focusing on stars with large variability in the RVs (RV scatter $\geq 10\,\mathrm{m\,s^{-1}}$), the so-called RV-loud sample. Exoplanet detection becomes more difficult in stars with large RV variability and high activity levels, so most of the RV-loud stars were only observed for about 11 epochs and discarded afterwards, because the main goal of the GTO programme is to detect planets. For this reason, a study of the correlations between the RVs and the indicators was performed. Of the $\sim$ 30 stars in the sample, about a third

show significant anti-correlations between the RVs and the CRX, while for another 20 %, there was a marginal detection of an anti-correlation. For the Hα line and the differential line width (DLW, an indicator that measures changes in the width of the absorption lines), the authors exclude the existence of linear correlations with the RVs, although more complex relations could exist (as shown in e.g. Zechmeister et al., 2018).

Also within the CARMENES sample, Schöfer et al. (2019) computed and studied the temporal variability and the correlations of chromospheric indicators and photospheric absorption band indices in almost the whole sample, over 300 M dwarfs. They identified 15 stars (out of the 133 stars with known rotation period larger than 1 d) where there was a significant signal related to the rotation period in more than two indicators. The indicators that were most likely to vary with the stellar period were the ones measured from the Hα and the Ca IRT-b lines, as well as the ones measured from the photospheric titanium oxide bands at 7050 and 8430 Å.

The aim of this chapter is to study the behaviour of some of these indicators and evaluate their performance when it comes to assess activity signals. We want to see if there is any relation between their performance and the properties of the target stars, with the goal of finding what indicators work best for stars with certain properties. For this purpose, we used indicators from a subsample of CARMENES M dwarfs and studied their time series. In Sect. 3.2 we introduce some of the most commonly used indicators derived from the stellar spectra, some of which we used in the analysis presented here. In Sects. 3.3 and 3.4 we present the subsample of targets selected and the observations and parameters analysed. Sect. 3.5 describes the methodology we followed to analyse the time series data of the stars. In Sects. 3.6 and 3.7 we explain and discuss our results, and we conclude in Sect. 3.8 with a summary of the work presented in this chapter.

3.2 Common spectroscopic activity indicators

3.2.1 Chromospheric lines

A number of spectral lines across the visible and near-infrared spectral ranges have been found to be sensitive to chromospheric activity. Average measurements of their fluxes are used as indicators of the total activity level of the stars, and variations in these measurements with time are related to the rotation of the star and the evolution of its active regions.

In solar-like stars, indices based on the emission in the core of the H and K lines

created by singly ionised calcium, Ca II H&K, at 3969.59 Å and 3934.78 Å[1], have been widely used for chromospheric activity diagnostics. Wilson (1968) presented a survey to measure the fluxes of the Ca II H&K lines in solar-like stars to characterise their activity and search for long-term magnetic cycles. Vaughan, Preston, and Wilson (1978) defined and measured the dimensionless index S in several main sequence stars. This index is proportional to the ratio of the emission flux in the cores of the H and K lines (f_H and f_K), to the flux in two nearby reference bands of continuum emission on the blue and red side of the H and K region (f_B and f_R), $S \propto (f_H + f_K)/(f_B + f_R)$. The value of this index is sensitive to the amount of photospheric flux in the bands, which is highly dependent on spectral type, and also changes for observations obtained with different instruments. To solve this, the S index can be corrected by subtracting the photospheric contribution and normalizing the chromospheric flux of the H and K lines to the bolometric luminosity of the star. This results in the $R'_{\rm HK}$ index, which represents the fraction of bolometric luminosity that the chromosphere emits in the Ca II H&K lines (Middelkoop, 1982; Noyes et al., 1984). The photospheric and bolometric corrections are traditionally well calibrated for FGK-dwarfs. Further extensions of this index have been carried out to account for systematic biases observed in M dwarfs, subgiants, and stars with different metallicities (e.g. Lovis et al., 2011; Suárez Mascareño et al., 2015; Astudillo-Defru et al., 2017a).

M dwarfs emit most of their flux at wavelengths longer than the Ca II H&K lines, so usually other strong, redder chromospheric-sensitive lines are employed to characterise their activity, such as the commonly used Hα line at 6564.60 Å (e.g. Stauffer and Hartmann, 1986; West et al., 2004; Jeffers et al., 2018). This line is halfway between the blue and the red, and therefore, covered by a large number of spectrographs. Studies including both the Ca II H&K and the Hα lines found in general good agreement between the temporal variability of the two lines in a range of cool stars (e.g. Suárez Mascareño et al., 2015). Hα presents a complicated evolution of its line profile with increasing stellar activity. At low activity levels, the line profile becomes deeper as the activity increases, but at some point the line core starts to fill in, eventually going into emission at high levels of activity (Cram and Mullan, 1979). This may lead to ambiguous results, since more active stars can show the same Hα index as less active ones. Its profile also shows clear asymmetries, where the red wing is stronger than the blue one (Fuhrmeister et al., 2018).

There are other lines in the visible and the near-infrared domain that have also been found to be related to chromospheric activity. In the following we focus on the ones covered by CARMENES. The He I D_3 line at 5877.25 Å strongly correlates with Hα (Gizis, Reid, and Hawley, 2002; Schöfer et al., 2019) and is seen in emission if there

[1] Vacuum wavelengths (in air they are at 3968.47 Å and 3933.66 Å). As mentioned previously, throughout this thesis we use vacuum wavelengths rather than air, unless stated otherwise.

is emission in the Na I D doublet at 5891.58 and 5897.56 Å (Houdebine et al., 2009), which is also an indicator of magnetic activity (e.g. Díaz, Cincunegui, and Mauas, 2007). Depending on the absolute RV of the observed star, the Na I D lines can be affected by contamination from emission lines of telluric sodium (Gizis, Reid, and Hawley, 2002; Hanuschik, 2003). They have strong absorption components originated in the photosphere that are sensitive to effective temperature, metallicity and surface gravity, which makes these lines useful to estimate spectral types, metallicities and luminosity classes (e.g. Covey et al., 2007). This strong absorption however also makes it difficult to define pseudo-continuum regions to use as reference to measure the flux of the lines.

Redwards of Hα we find the Ca II infrared triplet lines (Ca IRT, with wavelengths at 8500.35, 8544.44, and 8664.52 Å), which show chromospheric emission in a range of cool active stars of different spectral types and luminosoty classes, including M dwarfs (e.g. Mallik, 1997; Martin et al., 2017). Similarly to the Na I D doublet, the Ca IRT lines also have strong photospheric absorption components sensitive to the stellar parameters (Jones, Alloin, and Jones, 1984; Jorgensen, Carlsson, and Johnson, 1992). Schöfer et al. (2019) shows that for the CARMENES M dwarfs both the Na I D and the Ca IRT have a weaker correlation with the Hα line than the He I D_3, probably because of effects of the photospheric component.

The K I at $\sim$ 7700 Å and the Na I at $\sim$ 8200 Å doublets are also strong features that can trace magnetic activity in cool stars. Both pairs of lines show anticorrelations with Hα in M dwarfs (Kafka and Honeycutt, 2006; Gomes da Silva et al., 2011; Robertson et al., 2016). The Na I doublet is also sensitive to stellar temperature and surface gravity (e.g. Schlieder et al., 2012; Passegger, Wende-von Berg, and Reiners, 2016). They are however contaminated by telluric water (Na) and O_2 (K) lines, and were therefore not studied by Schöfer et al. (2019) for the CARMENES M dwarf sample.

The NIR channel of CARMENES includes the He I λ10833 line and the H Paβ line at 12821.57 Å, which have been observed in emission during flares in M dwarfs (Schmidt et al., 2012), but can be affected by telluric contamination. Schöfer et al. (2019) found unclear correlations between these two features and other lines, which could indicate their low sensitivity to activity. Thanks to its low correlation with activity, the He I λ10833 line delivers unbiased results when performing studies of evaporation in of exoplanet atmospheres (e.g. Nortmann et al., 2018; Salz et al., 2018).

The strength of the lines can be measured by dimensionless indices (I) defined as the ratio of flux around the centre of the line ($f_{\rm line}$) to the flux in reference bandpasses on either sides of the lines ($f_{\rm ref1}$, $f_{\rm ref2}$), $I \propto f_{\rm line} / (f_{\rm ref1} + f_{\rm ref2})$, similar to the S index used in the Ca II H&K line (see e.g. Kürster et al., 2003). Another way to measure the chromospheric activity strength is to compute the equivalent width (EW) of these

lines with respect to a continuum region, or in the case of M dwarfs, with respect to a pseudocontinuum, because their spectra do not show a clear continuum. In this case, the parameter measured is called pseudo-equivalent width (pEW). Usually, before performing the measurements of the pEW, the spectrum of a non-active star of similar properties to the target star is subtracted to the observed spectrum (Young et al., 1989; Montes et al., 1995). This removes the contribution of neighbouring lines and photospheric absorption to obtain only the active-chromosphere contribution to the line. In this case, pEW' is used to indicate the pseudo-equivalent width measured after spectral subtraction.

The EW and the line indices I are closely related, because both quantities measure the integrated flux of the lines (the zeroth moment). The EW has units of wavelength and is normalised to the continuum flux, while the index I is dimensionless and normalised to the flux of reference bands (Zechmeister, Kürster, and Endl, 2009). For an absoprtion line, $EW > 0$ and $0 < I < 1$, and for an emission line, $EW < 0$ and $I > 1$.

3.2.2 Photospheric bands

Molecular absorption bands formed in the photosphere are also used to trace activity, such as the titanium oxide (TiO) bands at ~ 7050 Å and ~ 8430 Å, and the vanadium oxide bands (VO) bands at ~ 7436 Å and ~ 7942 Å (Schöfer et al., 2019), which are sensitive to temperature, and hence, to changes induced by e.g. cool spots. Moreover the TiO bands are also sensitive to magnetic fields (Berdyugina and Solanki, 2002) and to metallicity (e.g. Lépine, Rich, and Shara, 2007). To quantify the activity strength in photospheric bands, usually an index that measures the ratio of the mean fluxes on either side of the band head (f_B, f_R) is used, $index = f_R/f_B$ (Reid, Hawley, and Gizis, 1995; Kirkpatrick et al., 1999; Schöfer et al., 2019).

3.2.3 CCF profile

As mentioned in the previous chapter, average distortions in photospheric absorption lines are reflected in the CCF profile, and can be studied with different parametrisations of the CCF. Common indicators include the asymmetry of the CCF bisector, which can be measured as the difference between the average RV of the upper part and the bottom part (bisector inverse slope, BIS), the CCF FWHM, or its contrast (see Chapter 2).

3.2.4 Chromatic index

The chromatic RV index (CRX), defined in Zechmeister et al. (2018), measures changes in the RV across the observed wavelength range, which are also related to stellar

photospheric activity. Instead of measuring RVs in the complete wavelength range of an observed spectrum, we can divide it in separate wavelength intervals and use those to measure different RVs. In echelle spectrographs such as CARMENES, this comes naturally because the observed spectrum is divided into different echelle orders. Each of these individual RVs can be related to a representative wavelength of the order, such as the average or the central wavelength, which then yields a relation between the RVs and the wavelengths. The formal definition of the CRX uses the natural logarithm of the wavelength $\ln \lambda$ instead of, e.g., the λ or the order number, because in this way, all velocity elements have the same weight (as velocity changes linearly with $\ln \lambda$). The CRX is then defined as the slope of the best fit to the RV as a function of $\ln \lambda$ data, $\mathrm{RV}_o = \alpha + \beta \ln \lambda_o$, where o refers to the order, $\ln \lambda_o$ is the average $\ln \lambda$ of the order, α is an offset, and β is the CRX.

3.2.5 Differential line width

The differential line width (DLW) is another photospheric indicator also recently defined by Zechmeister et al. (2018). It derives from the template-matching scheme `SERVAL` uses to compute RVs presented in the same work, where basically the RV comes from the fit of a spectral template to the observed spectrum. This indicator accounts for differential changes in the line widths of the observed spectrum compared to the spectral template, so it is similar to the FWHM of the CCF, as it traces changes in the average of all the lines. Indicators such as the DLW, the CCF FWHM or contrast can be affected by different instrumental effects such as changes in the instrument profile, sky background (e.g. contamination by light scattered by clouds or the Moon, especially on low S/N observations), or an artificial broadening of the lines due to barycentric motion during a long exposure.

3.3 Targets

We selected targets observed with the CARMENES survey. To make sure that we had sufficient observations to draw conclusions from the time series analysis, we selected targets that had at least 40 observations in the VIS channel, excluding 18 known binaries. This yields a total of 92 stars. This selection criterium would leave out some targets that, in spite of having less than 40 observations, show clear activity-related signals. We performed a preliminary periodogram analysis of the stars with less than 40 observations and also selected those that clearly display significant signals that can be attributed to activity: significant peaks related to the stellar rotation period or, if that is not known or uncertain, the same significant peak in several indicators. This includes 6 additional stars to our set, making a total of 98 targets.

Table 3.1 shows the main properties of the selected stars and the observations

used. To visualise some of these properties, in the next figures we show their statistical distribution. We plot histograms corresponding to the spectral type, stellar mass, average activity level, RV scatter, rotational velocity, rotational period, apparent brightness, and number of observations in Fig. 3.1. Fig. 3.2 shows the correlations between some parameters directly related with stellar activity: average activity level, RV scatter, rotational velocity, and rotational period. Finally, in Fig. 3.3, we show the distribution of the sample stars in an activity-mass parameter space, which we use throughout this chapter to visualise our results. We show the activity level of the selected stars as a function of the stellar mass. The colour and size of the data points show two observational properties: the apparent magnitude measured in the J band, and the number of observations available, respectively. We also show different ranges of the rotation period with different data point markers.

To quantify the average activity level of the stars, we used measurements of the $pEW'(\mathrm{H}\alpha)$, computed as in Schöfer et al. (2019). For each star, these pEW's were measured in a `SERVAL` stellar spectrum template, which is computed by co-adding the different observations of the star (see Sect. 2.3.1 for a short description of the templates), instead of averaging the $pEW'(\mathrm{H}\alpha)$ measurements of individual spectra. Other possible measurements of the activity level of the stars were the average ratio of the Hα line and the bolometric luminosities, $\log(L_{\mathrm{H}\alpha}/L_{\mathrm{bol}})$, or the ratio of X-ray and J-band luminosities, L_X/L_J. However, they were not available for all the stars in the sample, so we opted for using the $pEW'(\mathrm{H}\alpha)$ values. Moreover, the $pEW'(\mathrm{H}\alpha)$ values were measured from the same CARMENES observations that we are using, so they reflect more accurately the activity observed in our data. The mass measurements are computed also from CARMENES observations as in Schweitzer et al. (2019). Both $pEW'(\mathrm{H}\alpha)$ and mass measurements are taken from the latest version of Carmencita at the time of writing, version 096, which contains updated data from Schöfer et al. (2019) and Schweitzer et al. (2019).

The selected stars cover most of the M spectral subtypes, from M0 V to M8 V, plus a late-K type dwarf, but most of them have early and mid M spectral subtype. They also cover a wide range of activity levels, with $pEW'(\mathrm{H}\alpha)$ from ~ 0.2 to -10, however, the majority of stars are considered Hα inactive (70 of them have a $pEW'(\mathrm{H}\alpha) \geq -0.1$, and of these, 42 have $pEW'(\mathrm{H}\alpha) \geq 0$).

Regarding the other properties related with the stellar activity, most of the stars in the sample have low rotational velocities. 66 have $v \sin i \leq 2\,\mathrm{km\,s^{-1}}$, 24 have $v \sin i$ between 2 and 5 $\mathrm{km\,s^{-1}}$, and the other 8 have $v \sin i$ up to $\sim 11\,\mathrm{km\,s^{-1}}$. Stars with larger $v \sin i$ have been observed less than 40 times, which limits the $v \sin i$ of the selected sample. With respect to rotational periods, 61 stars have a previously measured P_{rot}, ranging from $\sim$ 1 to 163 d. Most of these are concentrated towards $\sim$ 3 d (for the

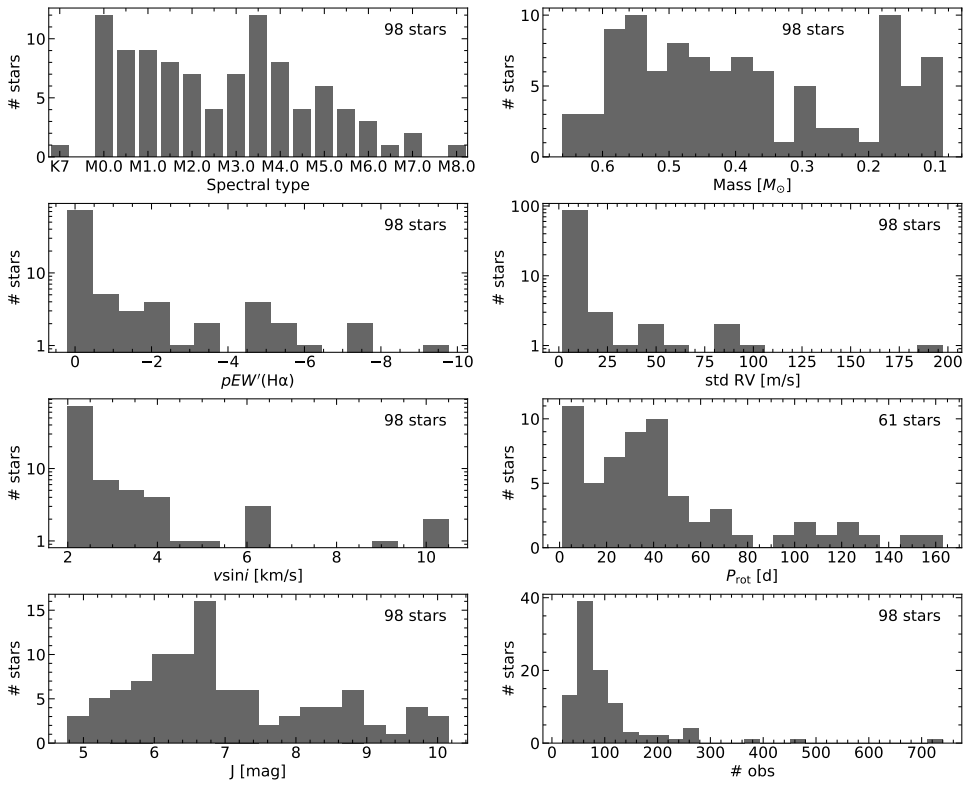

Figure 3.1: Distribution of the spectral type (*top left*), stellar mass (*top right*), mean activity level (measured as the average $pEW'(\mathrm{H}\alpha)$ of the `SERVAL` template, *second row left*), RV scatter (measured as the standard deviation of the `SERVAL` VIS RVs, *second row right*), rotational velocity ($v \sin i$, *third row left*), rotational period (P_{rot}, *third row right*), J magnitude (*bottom left*), and number of observations (#obs, *bottom right*) of the 98 selected stars. Only 61 stars have a known P_{rot}. All values correspond to the ones in Table 3.1.

most active stars, all with $pEW'(\mathrm{H}\alpha) \leq -2$) and $\sim 30 - 40$ d, and only 18 stars have P_{rot} larger than 50 d. Stars with unknown P_{rot} are scattered throughout the activity-mass space. We measured the RV scatter as the standard deviation of the `SERVAL` RVs (std RV). Most of the stars with low activity levels ($pEW'(\mathrm{H}\alpha) > -0.1$) show RV scatter from ~ 1 to $10\,\mathrm{m\,s^{-1}}$, and this increases with activity level, up to values of $\sim 100\,\mathrm{m\,s^{-1}}$. As can be seen in Fig. 3.2, most of these properties are correlated with one another, especially for the stars with the highest levels of activity.

Regarding observational properties, most of the stars are bright (73 stars with $J \lesssim 8$ mag), but some of the ones with the smallest masses are as faint as $J \sim 10$ mag. Almost 70 % of the stars have been observed between 50 and 130 times.

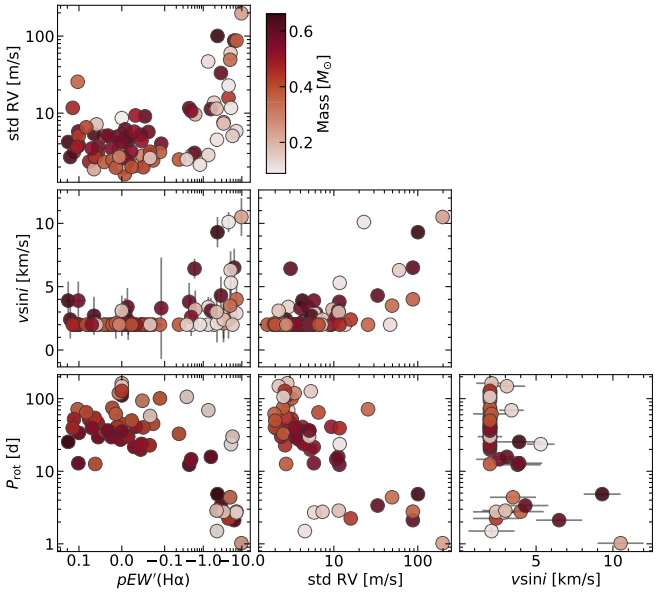

Figure 3.2: Correlations between several properties related to stellar activity (RV scatter std RV, rotational velocity $v \sin i$, rotation period $P_{\rm rot}$, and $pEW'(\mathrm{H}\alpha)$) of the 98 stars in the sample. Data points are colour-coded with the stellar mass. All values correspond to the ones in Table 3.1.

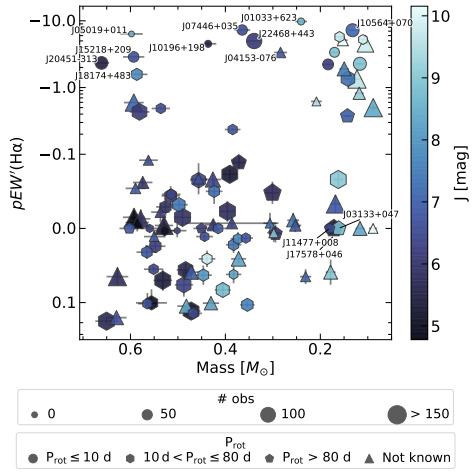

Figure 3.3: Average activity level (measured as the average $pEW'(\mathrm{H}\alpha)$ of the `SERVAL` template) as a function of the stellar mass of the 98 selected stars. The data points are colour-coded according to the target magnitude in the J band, and their size is given by the number of CARMENES VIS observations (with all the stars with more than 150 observations having the same size). The different markers indicate different $P_{\rm rot}$ regimes (circles $P_{\rm rot} \leq 10$ d, hexagons $10 < P_{\rm rot} \leq 80$ d, pentagons $P_{\rm rot} \geq 80$ d, and triangles stars with unknown $P_{\rm rot}$). We have indicated the name of several stars for reference. All values correspond to the ones in Table 3.1.

Table 3.1: Properties of the selected stars. The values are taken from the latest version of the Carmencita database available at the time (version 096). We also show the number CARMENES VIS observations obtained, the number of different nights covered by the observations, their time span, and their RV scatter, measured as the standard deviation (std) of the corrected SERVAL RVs (instrumental drift and nightly average corrected, averaged same-night observations, and linear trend removed).

Karmn	Name	Sp. type[a]	Mass[b] [$M_\odot$]	J[c] [mag]	$v \sin i$ [d] [km s^{-1}]	$P_{\rm rot}$ [e] [d]	$pEW'(\mathrm{H}\alpha)$ [f]	$\log(L_{\mathrm{H}\alpha}/L_{\rm bol})$ [g]	Planet	# obs (# nights)	Span [d]	std RV [m s^{-1}]
J00067-075	GJ 1002	M5.5 V	0.1164 ± 0.0092	8.320 ± 0.019	< 2.0	–	0.0	–	No	91 (91)	1188	2.22
J00183+440	GX And, GJ 15A	M1.0 V*	0.391 ± 0.016	5.30 ± 0.26	< 2.0	45.00 ± 4.40*	-0.0730 ± 0.0070	–	Yes	150 (118)	1441	2.43
J00184+440	GQ And, GJ 15B	M3.5 V	0.168 ± 0.010	6.790 ± 0.024	< 2.0	–	-0.033 ± 0.012	–	No	150 (112)	1446	2.08
J01025+716	Ross 318, GJ 48	M3.0 V	0.488 ± 0.019	6.300 ± 0.034	< 2.0	52.00 ± 2.60	0.076 ± 0.016	–	No	120 (119)	719	2.35
J01026+623	BD+61 195, GJ 49	M1.5 V*	0.515 ± 0.019	6.230 ± 0.021	< 2.0	20.00 ± 0.40	-0.044 ± 0.013	–	Yes	83 (81)	780	5.24
J01033+623	V388 Cas, GJ 51	M5.0 V*	0.241 ± 0.012	8.610 ± 0.027	10.00 ± 1.50	1.020 ± 0.010	-9.770 ± 0.040	-3.5340 ± 0.0017	No	26 (26)	1213	197.35
J01125-169	YZ Cet, GJ 54.1	M4.5 V	0.1418 ± 0.0098	7.260 ± 0.020	3.40 ± 0.80*	69.00 ± 2.40	-1.360 ± 0.020	-4.3400 ± 0.0070	Yes	111 (84)	1081	2.86
J02002+130	TZ Ari, GJ 83.1	M3.5 V:*	0.1497 ± 0.0098	7.510 ± 0.017	< 2.0	–	-1.910 ± 0.025	-4.0670 ± 0.0060	?	92 (91)	1398	13.65
J02222+478	BD+47 612, GJ 96	M0.5 V	0.551 ± 0.020	6.380 ± 0.019	< 2.0	30.00 ± 0.40	0.0550 ± 0.0040	–	Yes	55 (48)	719	3.68
J02442+255	VX Ari, GJ 109	M3.0 V	0.357 ± 0.015	6.750 ± 0.018	< 2.0	39.00 ± 3.70	0.0130 ± 0.0050	–	No	52 (52)	1105	2.08
J02530+168	Teegardens Star	M7.0 V*	0.08857 ± 0.0088	8.390 ± 0.027	< 2.0	–	-0.500 ± 0.050	-5.360 ± 0.040	Yes	150 (240)	1385	2.84
J03133+047	CD Cet, GJ 1057	M5.0 V	0.161 ± 0.010	8.780 ± 0.020	< 2.0	130.0†	0.0	–	Yes	109 (105)	1183	5.31
J03463+262	HD 23453, GJ 154	M0.0 V	0.562 ± 0.020	6.690 ± 0.021	3.30 ± 4.00	–	-0.0920 ± 0.0050	–	No	48 (48)	1332	4.01
J04153-076	omi02 Eri C, GJ 166C	M4.5 V*	0.284 ± 0.014	6.750 ± 0.020	2.10 ± 1.50	–	-3.360 ± 0.028	-3.9460 ± 0.0040	No	53 (47)	725	7.63
J04290+219	BD+21 652, GJ 169	M0.5 V†	0.650 ± 0.024	5.670 ± 0.026	3.90 ± 1.50	25.00 ± 0.30	0.190 ± 0.023	–	No	150 (155)	749	4.22
J04376+528	BD+52 857, GJ 172	M0.0 V‡	0.578 ± 0.020	5.870 ± 0.041	3.40 ± 1.50	–	-0.013 ± 0.013	–	No	126 (119)	971	4.92
J04429+189	HD 285968, GJ 176	M2.0 V	0.501 ± 0.020	6.460 ± 0.024	< 2.0	41.00 ± 0.40	0.0030 ± 0.0090	–	Yes	23 (23)	365	4.22
J04588+498	BD+49 1280, GJ 181	M0.0 V	0.589 ± 0.021	6.920 ± 0.020	< 2.0	–	-0.0540 ± 0.0070	–	No	53 (53)	1422	9.09
J05019+011	1RXS J050156.7+010845	M4.0 V*	0.598 ± 0.024	8.530 ± 0.026	6.50 ± 1.50	2.120 ± 0.020	-6.360 ± 0.019	-3.5800 ± 0.0013	No	19 (19)	1201	87.39
J05314-036	HD 36395, GJ 205	M1.5 V*	0.556 ± 0.033	5.00 ± 0.30	< 2.0	34.00 ± 0.60	0.101 ± 0.019	–	No	94 (89)	804	3.81
J05365+113	V2689 Ori, GJ 208	M0.0 V§	0.581 ± 0.021	6.130 ± 0.023	3.80 ± 1.50	12.00 ± 0.10	-0.432 ± 0.012	-4.540 ± 0.012	No	129 (119)	1105	11.61
J05421+124	V1352 Ori, GJ 213	M4.0 V*	0.231 ± 0.012	7.120 ± 0.021	< 2.0	–	0.065 ± 0.010	–	No	49 (48)	1440	1.88
J06011+595	G 192-013, GJ 3378	M3.5 V	0.257 ± 0.012	7.460 ± 0.023	< 2.0	–	-0.011 ± 0.010	–	No	80 (80)	1404	2.29
J06103+821	GJ 226	M2.0 V	0.415 ± 0.017	6.870 ± 0.023	< 2.0	45.00 ± 1.00	0.0	–	No	55 (55)	1330	3.12
J06105-218	HD 42581 A, GJ 229A	M0.5 V	0.528 ± 0.023	5.100 ± 0.037	< 2.0	27.00 ± 0.20	0.0030 ± 0.0090	–	Yes	50 (50)	1421	3.82

References. [a] Hawley, Gizis, and Reid (1996), except *Alonso-Floriano et al. (2015), †Gray et al. (2006), ‡Gray et al. (2003), §Lépine et al. (2013), ¶Benneke et al. (2017), #Newton et al. (2014), |Riaz, Gizis, and Harvin (2006), **Kirkpatrick, Henry, and McCarthy (1991). [b] Schweitzer et al. (2019), except J20451-313 computed using Mann et al. (2019). [c] Skrutskie et al. (2006). [d] Reiners et al. (2018b), except *Fouqué et al. (2018), †Delfosse et al. (1998b), ‡Martínez-Rodríguez (2014), §López-Santiago et al. (2010), ¶Torres et al. (2006). [e] Díez Alonso et al. (2019), except *Suárez Mascareño et al. (2018), †Newton et al. (2016), ‡Suárez Mascareño et al. (2017), §Morin et al. (2008), ¶Morin et al. (2010), #Suárez Mascareño et al. (2015), |Messina et al. (2011), **Watson, Henden, and Price (2006). [f] Schöfer et al. (2019). [g] Schöfer et al. (2019).

Table 3.1: Continued.

Karmn	Name	Sp. type	Mass [$M_\odot$]	J [mag]	$v \sin i$ [km s^{-1}]	$P_{\rm rot}$ [d]	$pEW'(\mathrm{H}\alpha)$	$\log(L_{\mathrm{H}\alpha}/L_{\rm bol})$	Planet	# obs (# nights)	Span [d]	std RV [m s^{-1}]
J06371+175	HD 260655, GJ 239	M0.0 V[§]	0.456 ± 0.018	6.670 ± 0.024	< 2.0	–	-0.067 ± 0.021	–	No	54 (53)	1401	2.91
J07274+052	Luytens Star, GJ 273	M3.5 V[*]	0.301 ± 0.014	5.710 ± 0.032	< 2.0	90.0 ± 16.0[‡]	-0.048 ± 0.015	–	Yes	150 (203)	1460	2.79
J07403-174	LP 783-002, GJ 283B	M6.0 V	0.08886 ± 0.0087	10.200 ± 0.022	< 2.0	–	0.0	–	No	46 (46)	1089	8.62
J07446+035	YZ CMi, GJ 285	M4.5 V	0.364 ± 0.017	6.580 ± 0.024	4.00 ± 1.50	2.780 ± 0.010	-7.280 ± 0.024	-3.6100 ± 0.0014	No	51 (51)	725	87.37
J08161+013	GJ 2066	M2.0 V[*]	0.444 ± 0.018	6.620 ± 0.026	< 2.0	41.00 ± 0.40	0.0110 ± 0.0070	–	No	47 (45)	1436	2.22
J08413+594	LP 090-018, GJ 3512	M5.5 V	0.1228 ± 0.0094	9.620 ± 0.023	< 2.0	–	-1.340 ± 0.013	-4.4530 ± 0.0040	Yes	150 (163)	1099	46.83
J09143+526	HD 79210, GJ 338A	M0.0 V[*]	0.586 ± 0.025	4.890 ± 0.037	2.90 ± 1.20[†]	–	-0.008 ± 0.012	–	No	69 (69)	1033	6.17
J09144+526	HD 79211, GJ 338B	M0.0 V[*]	0.592 ± 0.023	4.80 ± 0.17	2.30 ± 1.50	–	-0.015 ± 0.010	–	No	150 (152)	1003	4.37
J09561+627	BD+63 869, GJ 373	M0.0 V	0.574 ± 0.020	6.030 ± 0.024	< 2.0	–	-0.0620 ± 0.0060	–	No	69 (65)	817	5.70
J10122-037	AN Sex, GJ 382	M1.5 V	0.526 ± 0.020	5.890 ± 0.021	< 2.0	22.00 ± 0.20	-0.029 ± 0.012	–	No	76 (72)	815	5.75
J10196+198	AD Leo, GJ 388	M3.0 V+[*]	0.436 ± 0.017	5.450 ± 0.027	2.40 ± 1.50	2.23990 ± 0.00060[§]	-4.520 ± 0.040	-3.6140 ± 0.0030	No	26 (13)	26	15.87
J10289+008	BD+01 2447, GJ 393	M2.0 V	0.426 ± 0.017	6.180 ± 0.021	< 2.0	–	-0.0050 ± 0.0070	–	No	69 (67)	1420	1.95
J10482-113	LP 731-058, GJ 3622	M6.5 V[*]	0.1167 ± 0.0096	8.860 ± 0.021	2.10 ± 1.50	1.50 ± 0.20[¶]	-2.270 ± 0.050	-4.630 ± 0.010	No	78 (78)	1388	4.51
J10564+070	CN Leo, GJ 406	M6.0 V[*]	0.132 ± 0.010	7.080 ± 0.024	2.90 ± 0.80[*]	2.7040 ± 0.0030	-7.220 ± 0.080	-3.9820 ± 0.0050	No	78 (73)	816	5.83
J10584-107	LP 731-076	M5.0 V[*]	0.208 ± 0.011	9.510 ± 0.023	3.20 ± 1.50	–	-0.620 ± 0.060	-4.730 ± 0.040	No	39 (39)	1096	9.63
J11000+228	Ross 104, GJ 408	M2.5 V	0.386 ± 0.098	6.310 ± 0.023	< 2.0	–	-0.0070 ± 0.0070	–	No	60 (58)	817	1.61
J11026+219	DS Leo, GJ 410	M1.0 V[§]	0.536 ± 0.019	6.520 ± 0.020	2.60 ± 1.50	15.00 ± 0.20	-0.486 ± 0.013	-4.530 ± 0.012	No	53 (50)	848	10.67
J11054+435	BD+44 2051A, GJ 412A	M1.0 V[*]	0.372 ± 0.015	5.540 ± 0.019	< 2.0	100.00 ± 0.30[*]	-0.0890 ± 0.0090	–	No	111 (107)	816	3.13
J11302+076	K2-18	M2.5 V[¶]	0.439 ± 0.018	9.760 ± 0.028	< 2.0	36.00 ± 0.30	0.041 ± 0.011	–	Yes	63 (62)	431	5.05
J11417+427	Ross 1003, GJ 1148	M4.0 V	0.354 ± 0.015	7.610 ± 0.018	< 2.0	72.00 ± 5.10	0.108 ± 0.010	–	Yes	80 (80)	1194	25.54
J11476+786	GJ 445	M3.5 V	0.253 ± 0.012	6.720 ± 0.024	< 2.0	–	-0.0040 ± 0.0090	–	No	61 (60)	1450	2.49
J11477+008	FI Vir, GJ 447	M4.0 V	0.180 ± 0.011	6.500 ± 0.023	2.10 ± 1.00[*]	160.00 ± 3.00	0.0	–	Yes	56 (53)	1099	2.79
J11511+352	BD+36 2219, GJ 450	M1.5 V[*]	0.456 ± 0.018	6.420 ± 0.020	< 2.0	23.00 ± 1.00	-0.065 ± 0.010	–	No	110 (109)	1266	2.62
J12312+086	BD+09 2636, GJ 471	M0.5 V[§]	0.550 ± 0.021	6.780 ± 0.034	< 2.0	–	0.0110 ± 0.0080	–	No	47 (47)	1250	4.94
J12479+097	Wolf 437, GJ 486	M3.5 V	0.306 ± 0.014	7.200 ± 0.026	< 2.0	–	-0.007 ± 0.014	–	No	45 (44)	1446	2.45
J13299+102	BD+11 2576, GJ 514	M0.5 V	0.490 ± 0.018	5.900 ± 0.018	2.00 ± 0.80[*]	30.00 ± 0.90[‡]	-0.015 ± 0.012	–	No	150 (220)	1461	2.36
J13457+148	HD 119850, GJ 526	M1.5 V	0.472 ± 0.020	5.180 ± 0.037	< 2.0	52.00 ± 1.70[#]	0.1340 ± 0.0090	–	No	150 (209)	816	3.15
J14257+236W	BD+24 2733A, GJ 548A	M0.0 V	0.602 ± 0.021	6.770 ± 0.023	< 2.0	100.0 ± 12.0	0.0	–	No	62 (62)	1291	2.75
J14307-086	BD-07 3856, GJ 553	M0.5 V[‡]	0.630 ± 0.021	6.620 ± 0.021	2.40 ± 1.50	–	0.168 ± 0.014	–	No	92 (92)	1252	2.69
J14321+081	LP 560-035	M6.0 V[#]	0.153 ± 0.010	10.100 ± 0.024	6.30 ± 1.50	–	-5.110 ± 0.070	-4.1320 ± 0.0060	No	58 (54)	926	59.95
J15218+209	OT Ser, GJ 9520	M1.5 V	0.593 ± 0.022	6.610 ± 0.021	4.30 ± 1.50	3.370 ± 0.010	-2.880 ± 0.018	-3.7660 ± 0.0028	No	53 (43)	1002	33.21
J16167+672N	EW Dra, GJ 617B	M3.0 V	0.472 ± 0.019	6.910 ± 0.021	< 2.0	–	0.059 ± 0.010	–	No	93 (91)	1461	2.73

Table 3.1: Continued.

Karmn	Name	Sp. type	Mass [$M_\odot$]	J [mag]	$v \sin i$ [km s^{-1}]	$P_{\rm rot}$ [d]	$pEW'(\mathrm{H}\alpha)$	$\log(L_{\mathrm{H}\alpha}/L_{\rm bol})$	Planet	# obs (# nights)	Span [d]	std RV [m s^{-1}]
J16167+672S	HD 147379, GJ 617A	M0.0 V*	0.627 ± 0.023	5.780 ± 0.019	2.70 ± 1.50	–	0.065 ± 0.012	–	Yes	150 (173)	1461	5.39
J16303-126	V2306 Oph, GJ 628	M3.5 V	0.294 ± 0.014	5.950 ± 0.024	< 2.0	120.00 ± 1.00	0.007 ± 0.012	–	Yes	92 (92)	1290	3.42
J16555-083	vB 8, GJ 644C	M7.0 V*	0.1049 ± 0.0093	9.780 ± 0.029	10.00 ± 0.80*	–	-4.540 ± 0.060	-4.4040 ± 0.0060	No	128 (115)	899	22.81
J16581+257	BD+25 3173, GJ 649	M1.0 V	0.514 ± 0.020	6.450 ± 0.021	< 2.0	24.00 ± 0.10	-0.0460 ± 0.0070	–	Yes	55 (34)	399	4.36
J17303+055	BD+05 3409, GJ 678.1 A	M0.0 V	0.537 ± 0.019	6.240 ± 0.020	< 2.0	–	-0.022 ± 0.013	–	No	55 (54)	905	3.18
J17378+185	BD+18 3421, GJ 686	M1.0 V	0.426 ± 0.017	6.360 ± 0.023	< 2.0	–	-0.0660 ± 0.0070	–	Yes	105 (101)	1060	3.16
J17578+046	Barnards Star, GJ 699	M3.5 V*	0.172 ± 0.010	5.240 ± 0.020	3.10 ± 1.20*	150.00 ± 0.10#	0.0	–	Yes	150 (442)	1379	2.20
J18051-030	HD 165222, GJ 701	M1.0 V	0.450 ± 0.017	6.160 ± 0.019	< 2.0	130.00 ± 3.20#	0.0	–	No	56 (54)	924	2.61
J18174+483	TYC 3529-1437-1	M2.0 V|	0.587 ± 0.022	7.770 ± 0.017	3.10 ± 1.00*	16.00 ± 0.10	-1.580 ± 0.012	-4.0340 ± 0.0040	No	70 (70)	1001	11.28
J18198-019	HD 168442, GJ 710	K7 V†	0.593 ± 0.021	7.080 ± 0.029	6.40 ± 0.78‡	–	-0.6	–	?	134 (132)	847	3.05
J18346+401	LP 229-017, GJ 4063	M3.5 V	0.424 ± 0.018	7.180 ± 0.019	< 2.0	40.00 ± 0.80	-0.050 ± 0.017	–	No	70 (70)	1360	1.99
J18482+076	G 141-036	M5.0 V*	0.170 ± 0.011	8.850 ± 0.024	2.40 ± 1.50	2.760 ± 0.010	-3.370 ± 0.020	-3.9960 ± 0.0026	No	47 (47)	1148	7.33
J18498-238	V1216 Sgr, GJ 729	M3.5V|	0.184 ± 0.011	6.220 ± 0.018	3.00 ± 1.50	2.870 ± 0.010	-2.220 ± 0.018	-4.0010 ± 0.0040	?	56 (56)	367	11.44
J18580+059	BD+05 3993, GJ 740	M0.5 V	0.559 ± 0.020	6.240 ± 0.019	< 2.0	35.00 ± 0.30	0.0	–	No	34 (33)	517	4.20
J19169+051N	V1428 Aql, GJ 752A	M2.5 V*	0.484 ± 0.019	5.580 ± 0.030	< 2.0	46.00 ± 0.20	0.0560 ± 0.0090	–	Yes	129 (127)	622	3.01
J19169+051S	V1298 Aql (vB 10), GJ 752B	M8.0 V*	0.1102 ± 0.0090	9.910 ± 0.025	5.30 ± 0.90*	24.00 ± 0.30	-5.240 ± 0.090	-4.4630 ± 0.0080	No	48 (48)	1175	11.72
J19346+045	BD+04 4157, GJ 763	M0.0 V**	0.564 ± 0.019	6.710 ± 0.019	3.90 ± 1.50	13.00 ± 0.80	0.104 ± 0.017	–	No	53 (50)	1116	5.78
J20260+585	Wolf 1069, GJ 1253	M5.0 V	0.162 ± 0.010	9.030 ± 0.039	< 2.0	58.00 ± 0.40	-0.066 ± 0.010	–	No	150 (258)	1255	2.62
J20305+654	GJ 793	M2.5 V	0.385 ± 0.016	6.740 ± 0.021	< 2.0	33.00 ± 0.50	-0.235 ± 0.010	–	No	53 (53)	1147	2.50
J20336+617	GJ 1254	M4.0 V	0.383 ± 0.016	8.290 ± 0.027	< 2.0	13.00 ± 0.70	0.062 ± 0.012	–	No	47 (47)	1213	2.70
J20451-313	AU Mic, GJ 803	M0.5 V|	0.661 ± 0.016	5.440 ± 0.017	9.30 ± 1.20§	4.840 ± 0.040|	-2.3	–	Yes	75 (39)	88	100.41
J20533+621	HD 199305, GJ 809A	M1.0 V§	0.529 ± 0.019	5.430 ± 0.029	< 2.0	–	-0.0040 ± 0.0090	–	No	150 (159)	1401	2.62
J21164+025	LSPM J2116+0234	M3.0 V§	0.430 ± 0.017	8.220 ± 0.032	< 2.0	–	0.1020 ± 0.0060	–	No	83 (83)	1036	5.05
J21221+229	TYC 2187-512-1	M1.0 V§	0.498 ± 0.019	7.400 ± 0.018	< 2.0	41.00 ± 1.70	-0.0320 ± 0.0060	–	No	94 (93)	1293	9.34
J21348+515	Wolf 926, GJ 4205	M3.0 V	0.446 ± 0.018	8.040 ± 0.019	< 2.0	54.00 ± 1.50	0.063 ± 0.013	–	No	71 (71)	1103	2.70
J22021+014	BD+00 4810, GJ 846	M0.5 V*	0.548 ± 0.021	6.200 ± 0.023	< 2.0	30.00 ± 0.10	0.0240 ± 0.0050	–	No	77 (76)	1121	3.48
J22057+656	G 264-018 A, GJ 4258	M1.5 V	0.482 ± 0.019	8.420 ± 0.023	< 2.0	–	0.113 ± 0.011	–	No	91 (91)	839	3.66
J22096-046	BD-05 5715, GJ 849	M3.5 V	0.468 ± 0.019	6.510 ± 0.024	< 2.0	39.00 ± 6.30#	0.145 ± 0.019	–	Yes	61 (59)	1250	11.71
J22114+409	1RXS J221124.3+410000	M5.5 V*	0.160 ± 0.010	9.720 ± 0.020	< 2.0	30.00 ± 1.30	-5.740 ± 0.050	-3.8210 ± 0.0040	No	55 (55)	712	5.07
J22115+184	Ross 271, GJ 851	M2.0 V	0.565 ± 0.022	6.720 ± 0.037	< 2.0	36.00 ± 0.20	0.0320 ± 0.0090	–	No	68 (66)	1231	5.11
J22125+085	Wolf 1014, GJ 9773	M3.0 V	0.372 ± 0.016	8.280 ± 0.021	< 2.0	–	0.0410 ± 0.0060	–	No	98 (98)	1286	2.32
J22137-176	LP 819-052, GJ 1265	M4.5 V	0.178 ± 0.011	8.960 ± 0.029	< 2.0	–	0.059 ± 0.017	–	Yes	89 (73)	782	7.15

Table 3.1: Continued.

Karmn	Name	Sp. type	Mass [$M_\odot$]	J [mag]	$v \sin i$ [km s^{-1}]	$P_{\rm rot}$ [d]	$pEW'(\mathrm{H}\alpha)$	$\log(L_{\mathrm{H}\alpha}/L_{\rm bol})$	Planet	# obs (# nights)	Span [d]	std RV [m s^{-1}]
J22252+594	G 232-070, GJ 4276	M4.0 V	0.406 ± 0.017	8.740 ± 0.027	< 2.0	65.00 ± 2.10	0.083 ± 0.010	–	No	103 (103)	774	6.55
J22468+443	EV Lac, GJ 873	M3.5 V	0.339 ± 0.015	6.110 ± 0.030	3.50 ± 1.50	4.380 ± 0.030	-4.980 ± 0.021	-3.6500 ± 0.0018	No	107 (86)	701	49.36
J22565+165	HD 216899, GJ 880	M1.5 V	0.532 ± 0.020	5.360 ± 0.020	< 2.0	40.00 ± 0.20	0.070 ± 0.014	–	No	150 (371)	1464	3.48
J23216+172	LP 462-027, GJ 4333	M4.0 V	0.383 ± 0.016	7.390 ± 0.029	< 2.0	75.00 ± 0.70	0.022 ± 0.011	–	No	65 (65)	1187	2.47
J23351-023	GJ 1286	M5.5 V	0.1180 ± 0.0093	9.150 ± 0.021	< 2.0	–	-0.821 ± 0.015	-4.6650 ± 0.0080	No	71 (71)	1266	2.14
J23381-162	G 273-093, GJ 4352	M2.0 V	0.374 ± 0.016	7.810 ± 0.018	$2.10 \pm 1.20^{*}$	62.0^{**}	0.0140 ± 0.0090	–	No	54 (54)	1189	1.96
J23419+441	HH And, GJ 905	M5.0 V*	0.1428 ± 0.0098	6.880 ± 0.026	< 2.0	110.00 ± 6.00	-0.375 ± 0.014	-4.950 ± 0.016	No	99 (97)	1383	2.51
J23492+024	BR Psc, GJ 908	M1.0 V	0.396 ± 0.016	5.830 ± 0.023	< 2.0	$50.00 \pm 3.50^{*}$	-0.023 ± 0.014	–	No	150 (202)	1453	2.00
J23505-095	LP 763-012, GJ 4367	M4.0 V	0.298 ± 0.014	8.940 ± 0.039	< 2.0	–	0.006 ± 0.012	–	No	47 (47)	1189	2.71

3.4 RVs and activity parameters

To analyse the presence of activity signals, we used RVs and several activity indicators derived from the CARMENES VIS observations. We describe these parameters in the following paragraphs.

3.4.1 RVs

In our preliminary work we analysed VIS RVs computed with the template-matching pipeline `SERVAL` (Zechmeister et al., 2018) and with the CCF method, computed as described in Chapter 2. Both datasets have been corrected for barycentric motions, secular acceleration, instrumental drifts, and nightly-zero points (Trifonov et al., 2018; Tal-Or et al., 2019). As previously studied in Chapter 2, we observed that the CCF RVs do not always exactly match the ones obtained with `SERVAL`, and in general, they show more scatter. In some cases, this leads to less clear periodograms. For this reason, in the following analysis, we decided to only use the `SERVAL` RVs.

3.4.2 Activity indicators

Regarding the activity indicators, we analysed the FWHM, contrast, and BIS of the CCF, computed as explained in Chapter 2. We also used the CRX values computed by the `SERVAL` pipeline from the RVs obtained for the different spectral orders, and the DLW (both parameters as defined in Zechmeister et al., 2018).

To probe chromospheric activity, we used measurements of the core emission flux of the Hα and the Ca IRT lines. We analysed both their index I computed by `SERVAL` (Zechmeister et al., 2018) and pseudo-equivalent width pEW' computed as in Schöfer et al. (2019). We observe that, for the four lines, the two types of measurements show in general a similar behaviour. Therefore, to simplify our analysis, we decided to only use one of the two, the index I. In the following, instead of using, for instance, $I_{\mathrm{H}\alpha}$ for the index of Hα, we refer to this measurement simply as 'Hα' for the Hα line, and as 'Ca IRT-a', 'Ca IRT-b', and 'Ca IRT-c' for the three lines of the Ca IRT.

3.5 Time series analysis

3.5.1 Generalised Lomb-Scargle periodogram

The usual procedure to analyse which periodic signals are present in unevenly-sampled data is to use the Lomb-Scargle (LS) periodogram algorithm (Lomb, 1976; Scargle, 1982). It is an extension of the classical periodogram (Schuster, 1898) used to estimate the Fourier power spectrum of a signal observed with uniform sampling. Also, it is equivalent to performing a least-squares fit of a sinusoid to the data for a range of

frequencies f, and computing the periodogram power from the goodness-of-fit at each frequency.

In particular, we used the generalised Lomb-Scargle (GLS) periodogram[2] (Zechmeister and Kürster, 2009), which, following the least-squares interpretation, accounts for an offset or a floating mean in the sinusoid model

$$y(t; f, A_f, \phi_f, c_f) = A_f \sin\left(2\pi f \left(t - \phi_f\right)\right) + c_f, \tag{3.1}$$

where A_f is the amplitude of the sinusoid, ϕ_f the phase, and c_f the offset. The standard LS periodogram assumes that the observed data are already centered about the mean of the real unknown signal, i.e., that both the mean of the observations and the mean of the real signal are the same. This may not be true when the observations do not have a full phase coverage of the signal, which can lead to biased periodograms. Adding an offset parameter to the model makes the algorithm more robust to these effects. Moreover, the GLS also has the possibility of accounting for different weights of the measurements. For each frequency f, the sinusoid is minimised with respect to the parameters A_f, ϕ_f and c_f

$$\chi^2(f) = \sum_n \left(\frac{y_n - y(t_n; f)}{\sigma_n}\right)^2, \tag{3.2}$$

where y_n are the n observations with errors σ_n, assumed to be Gaussian. For each frequency, we can obtain the minimum χ^2, i.e. the χ^2 value given by the best model, $\check{\chi}^2(f)$. The periodogram power P is then constructed as a measure of the goodness-of-fit for each model, $\check{\chi}^2(f)$, with respect to the constant, non-varying reference model $\check{\chi}^2_0$

$$P(f) = \frac{1}{2}\left(\check{\chi}^2_0 - \check{\chi}^2(f)\right), \tag{3.3}$$

so that a larger power indicates a better fit.

We applied the standard least-squares normalisation, in which the values of the periodogram are normalised by the residuals of the data around the constant reference model $\check{\chi}^2_0$

$$P_{\mathrm{norm}}(f) = \frac{\check{\chi}^2_0 - \check{\chi}^2(f)}{\check{\chi}^2_0}. \tag{3.4}$$

By doing so, the periodogram power P goes from $0 \leq P \leq 1$.

We sampled frequencies going from the inverse of the time span of the measurements of each star, $1/T$, until 1 d, since the shortest known P_{rot} of the sample stars is

[2]It has also been called floating-mean periodogram (Cumming, Marcy, and Butler, 1999), or date-compensated discrete Fourier transform (Ferraz-Mello, 1981), and Zechmeister and Kürster (2009) showed that it is equivalent to the "spectral significance" used in Reegen (2007).

~ 1 d. The width of the peaks is approximately proportional to the inverse of the time span of the observations, $1/T$, so a too coarse grid could result in missing peaks. We used a frequency grid that approximately oversamples each peak with 10 points. In this way, we make sure to recover all significant peaks without adding a significant amount of computing time.

For each of the selected stars, we computed the GLS periodogram of the time series of the RVs and the activity indicators mentioned in section 3.4. In each time series, we discarded observations with low S/N (in general S/N < 5, except for J23064-050, the least bright star, for which all the observations have low S/N). We also removed outliers (values that deviate from their average by more than 3 times their standard deviation, i.e. 3σ clipping), and data points with large error bars (also applying a 3σ clipping on the uncertainties), to avoid including in the analysis observations obtained during flaring events, which can strongly affect the measured RVs and spectroscopic indicators (see e.g. Reiners, 2009).

All the data sets were corrected for long-term trends (we fitted them with a linear model and subsequently removed it), to avoid biases due to long-term magnetic cycles or wide-orbit sub-stellar companions. Some of the stars in the sample are known to host planets. We did not remove the planetary signals, so the RV periodograms may reflect those signals, alongside the activity ones, if any. We also averaged all measurements taken on the same night.

3.5.2 Detection of activity-related signals

Periodograms reflect the convolution of the power spectrum of the true signals present in the data with a particular window function, determined by the specific observing pattern of the data. This means that each frequency f can show an alias at $f + nf_W$, where n is an integer, and f_W represents a strong feature in the window function. For ground-based observations, this typically results in 1-day and 1-year aliases. Harmonics of a specific frequency f can appear for periodic signals that are not strictly sinusoidal and have power at higher harmonics mf, where m is a positive integer. These harmonics can also suffer aliasing effects due to the window function. Moreover, every peak at a frequency f has a corresponding peak at a frequency $-f$, and both peaks in the positive and negative frequency domain are subject to aliasing. In general, aliases can appear at frequencies $f_{\rm alias} = |mf + nf_W|$ (VanderPlas, 2018).

A common way to assess the significance of the power of the periodogram peaks is the false alarm probability (FAP), which measures the probability of having a peak of a given minimum height, assuming that the data consists only of Gaussian noise with no periodic component. Since there is no analytical method to compute the FAP of a specific peak in a given periodogram, it is usually determined through

bootstrap simulations or analytical approximations. Bootstrap simulations compute the periodogram on random resamplings of simulated data that keep the same observation times as the original data. It is an accurate but computationally expensive method. Baluev (2008) proposed an analytical approximation (based on statistics of extreme values for stochastic processes) that gives an upper limit to the FAP (or a lower limit to the significance). This limit is derived for alias-free periodograms, i.e. for datasets with window functions with little structure (simple observational patterns), but it has also been proven to be valid in the case of more complex window functions (more realistic observation times). In our analysis, we used the method proposed by Baluev (2008) to evaluate FAP levels in the periodograms.

Therefore, we looked for significant signals related to the activity of the star, taking into account the presence of aliases and harmonics of the true periods contained in the data. Specifically, we looked for significant peaks at the rotation period of the stars, $P_{\rm rot}$, and its first two harmonics, $\frac{1}{2}P_{\rm rot}$ and $\frac{1}{3}P_{\rm rot}$. From previous analyses, we knew that it was frequent to find significant peaks at the 1-day alias of the $P_{\rm rot}$, so we also looked for peaks at the regions around the 1-day aliases of the $P_{\rm rot}$ and its first two harmonics. For stars with unknown $P_{\rm rot}$, we looked for signals at common frequencies in the RVs and the indicators. If we found a significant peak in two or more different indicators, we assumed it was related to the activity of the star.

3.5.3 Examples

In this section we show the time series and periodograms of 5 stars as some representative examples of the analysis performed.

3.5.3.1 Clear signal at known $P_{\rm rot}$: J07446+035 (YZ CMi, GJ 285)

J07446+035 is a mid M dwarf (M4.5 V) with some the largest levels of activity in the sample ($pEW'(\mathrm{H}\alpha) \sim -7$). It has a $P_{\rm rot}$ of 2.78 d and has been observed 51 times with CARMENES. This is a clear example of an active star with a very significant activity-related signal present both in the RVs and most of the activity indicators. In Fig. 3.4 we show the time series of the RVs and the indicators, the data folded at $P_{\rm rot}$, the correlation of the indicators with the RV, and the periodogram of each parameter.

From the phase-folded plots, we see that, except for the chromospheric lines, the rest of the parameters show a more or less sinusoidal modulation with $P_{\rm rot}$. As mentioned in the previous chapter (Sect. 2.5.6), the CRX and BIS are in anti-phase with the RVs, and show a linear anti-correlation. The phase of the DLW, FWHM, and contrast seems to be not aligned with that of the RVs, and hence show a more complex correlation.

The periodograms of the RVs, CRX, DLW and the three CCF parameters all show significant signals at $P_{\rm rot}$, and a smaller but still significant signal at 1.56 d, which

corresponds to the 1-day alias of the signal at $P_{\rm rot}$. The two highest peaks of the Hα periodogram are at $P_{\rm rot}$ and its daily alias, but they are not significant nor clearly above the rest of the peaks. The Ca IRT lines do not show any clear peak. We do not observe any significant power at $\frac{1}{2}P_{\rm rot}$ nor its alias in any of the parameters. For this star, we conclude that only RV, CRX, DLW, FWHM, contrast and BIS show significant signals at both $P_{\rm rot}$ and its 1-day alias. We also note that for Hα, there is a signal at $P_{\rm rot}$, but with very low significance.

3.5.3.2 Multiple signals related to known $P_{\rm rot}$: J22468+443 (EV Lac, GJ 873)

J22468+443 is another example of a very active (pEW'(Hα) ~ -5) mid M dwarf (M3.5 V) with a short $P_{\rm rot}$ (4.38 d). In this case (Fig. 3.5), the periodogram is more complex, with signals at both $P_{\rm rot}$ and $\frac{1}{2}P_{\rm rot}$ (and their 1-day aliases).

As with J07446+035, CRX and BIS show a linear anti-correlation with RV, while the other parameters show a more complex behaviour. The periodograms of RV, CRX, BIS and FWHM show their highest peak at $\frac{1}{2}P_{\rm rot}$, and another much less significant (FAP < 0.1 %), but still very obvious peak at $P_{\rm rot}$. On the contrary, DLW and contrast show their highest peak at $P_{\rm rot}$, and a much less significant peak at $\frac{1}{2}P_{\rm rot}$. The chromospheric lines have a periodogram with more structure around the peaks. They also display their highest peak at $P_{\rm rot}$, and we observe no significant power at $\frac{1}{2}P_{\rm rot}$. Additionally, DLW, FWHM, and BIS show another significant peak at $\frac{1}{3}P_{\rm rot}$, and RV and CRX also seem to have some power at this period, although much less significant. This is the only star for which we found significant signals at $\frac{1}{3}P_{\rm rot}$.

3.5.3.3 Unknown $P_{\rm rot}$: J17303+055 (BD+05 3409, GJ 678.1 A)

In Fig. 3.6 we show an example of an early M dwarf (M0.0 V) with a low activity level (pEW'(Hα) ~ 0) and unknown $P_{\rm rot}$. RV, DLW, FWHM, contrast and the chromospheric lines show a significant peak at ~ 33.8 d. There is also a significant peak at ~ 1.03 d, its 1-day alias. We chose to attribute the real signal to the long period peak, because this is an inactive star with a low rotational velocity ($v \sin i \leq 2\,{\rm km\,s^{-1}}$). BIS shows significant signals at 17.6 d and 1.06 d, which are close to $\frac{1}{2}P_{\rm rot}$ and its 1-day alias. CRX does not show any significant peak.

3.5.3.4 Clear but non-significant signals: J20451-313 (AU Mic, GJ 803)

J20451-313 is an active (pEW'(Hα) ~ -2), early M dwarf (M 0.5V) with a $P_{\rm rot}$ of 4.84 d, for which a transiting planet has been recently announced (Plavchan et al., 2020). We see clear signals at $P_{\rm rot}$ or $\frac{1}{2}P_{\rm rot}$ (and their 1-day aliases) in the RVs and all the indicators (Fig. 3.7). However, for CRX, DLW, Hα, and Ca IRT-a, the peaks have FAP > 10 %. Since these peaks are clear, isolated, and above the rest of the peaks present in the periodogram, we still consider those as valid activity-related signals.

3.5.3.5 Long $P_{\rm rot}$: J03133+047 (CD Cet, GJ 1057)

The least active stars tend to have long rotation periods that are less well constrained than short ones, which complicates their identification in periodograms. J03133+047 is an example of this. It is an M5.0 V star with a low activity level ($pEW'(\mathrm{H}\alpha) \sim 0$) and a long $P_{\rm rot}$ of $\sim$ 126 d. It hosts a super-Earth orbiting on a 2.29 d orbit (Bauer et al., 2020).

DLW, FWHM, contrast, Hα, and Ca IRT-b show significant, wide peaks around $P_{\rm rot}$ (Fig. 3.8). In this case, we chose the peak closest to the literature $P_{\rm rot}$ value as the activity-related signal. These range from 137 to 148 d, depending on the indicator. The other indicators show some power close to $P_{\rm rot}$, but it is less clear and not significant. RV also shows some excess power close to $P_{\rm rot}$ and $\frac{1}{2}P_{\rm rot}$. The power at $P_{\rm rot}$ becomes significant if the 2.29 d planetary signal is removed from the RV measurements (see Bauer et al., 2020).

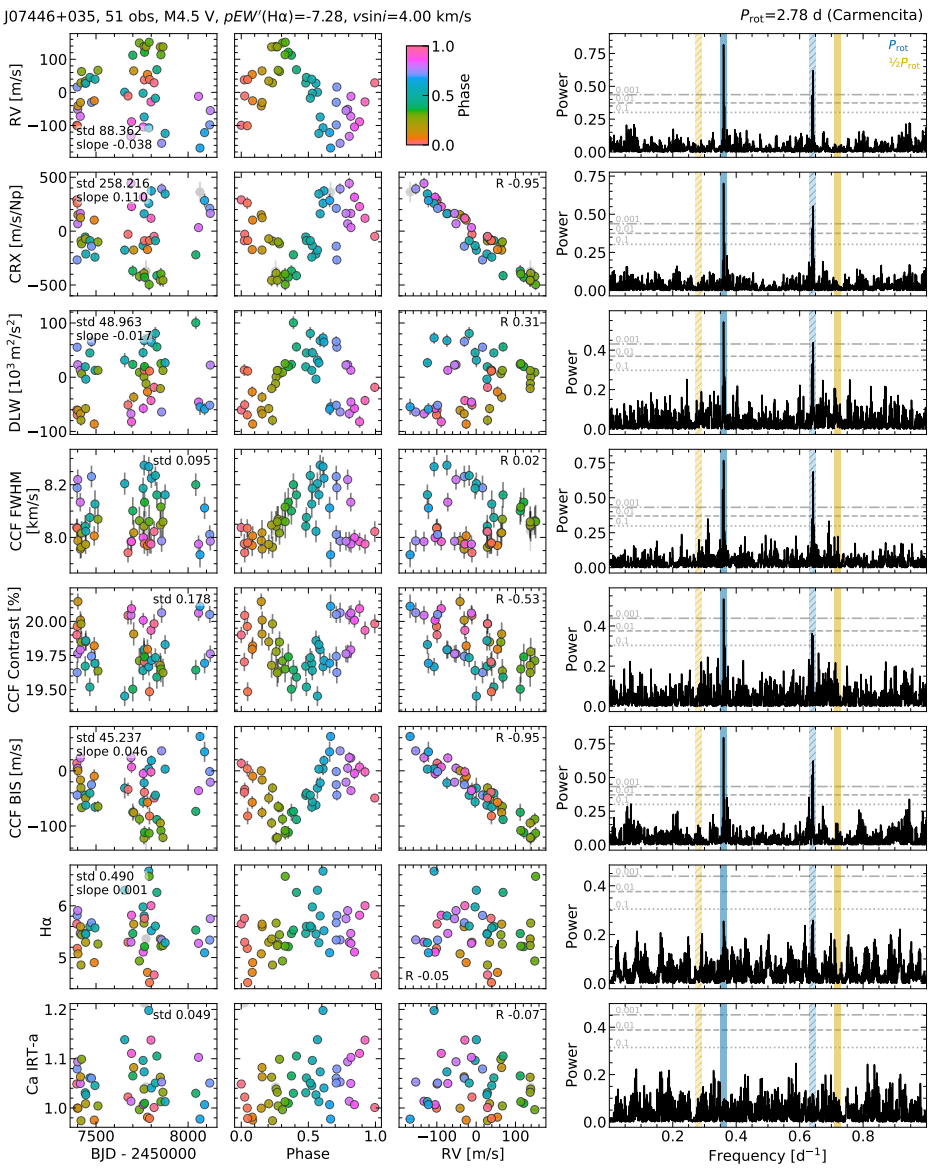

Figure 3.4: RV and indicators time series (*left*), data folded at $P_{\rm rot}$ (*middle left*), correlation with the RV (*middle right*), and periodogram (*right*) of J07446+035. The parameters are, from *top* to *bottom*: corrected `SERVAL` RV, CRX, DLW, CCF FWHM, contrast, and BIS, Hα index, and Ca IRT-a index (we only show the first line because the other two show a very similar time series and periodogram with no significant signal). Each time series has been corrected for a linear trend, and the periodograms are computed on nightly-averaged observations. Data points are colour-coded with the rotation phase, and outliers not considered are marked in grey (some outliers may be outside the data range shown). The text in the time series panels shows the standard deviation of the data (std) and the slope of the linear trend that has been subtracted from the data (only slopes with absolute values ≥ 0.001). The text in the correlation panels indicates the Pearson's correlation coefficient of the data (R). In the periodogram panels, horizontal grey lines indicate the FAP level at 10 (dotted), 1 (dashed) and 0.1 % (dotted dashed), and coloured shaded regions indicate the location of $P_{\rm rot}$ (blue), half $P_{\rm rot}$ (yellow), and their 1-day aliases (lighter hatched regions).

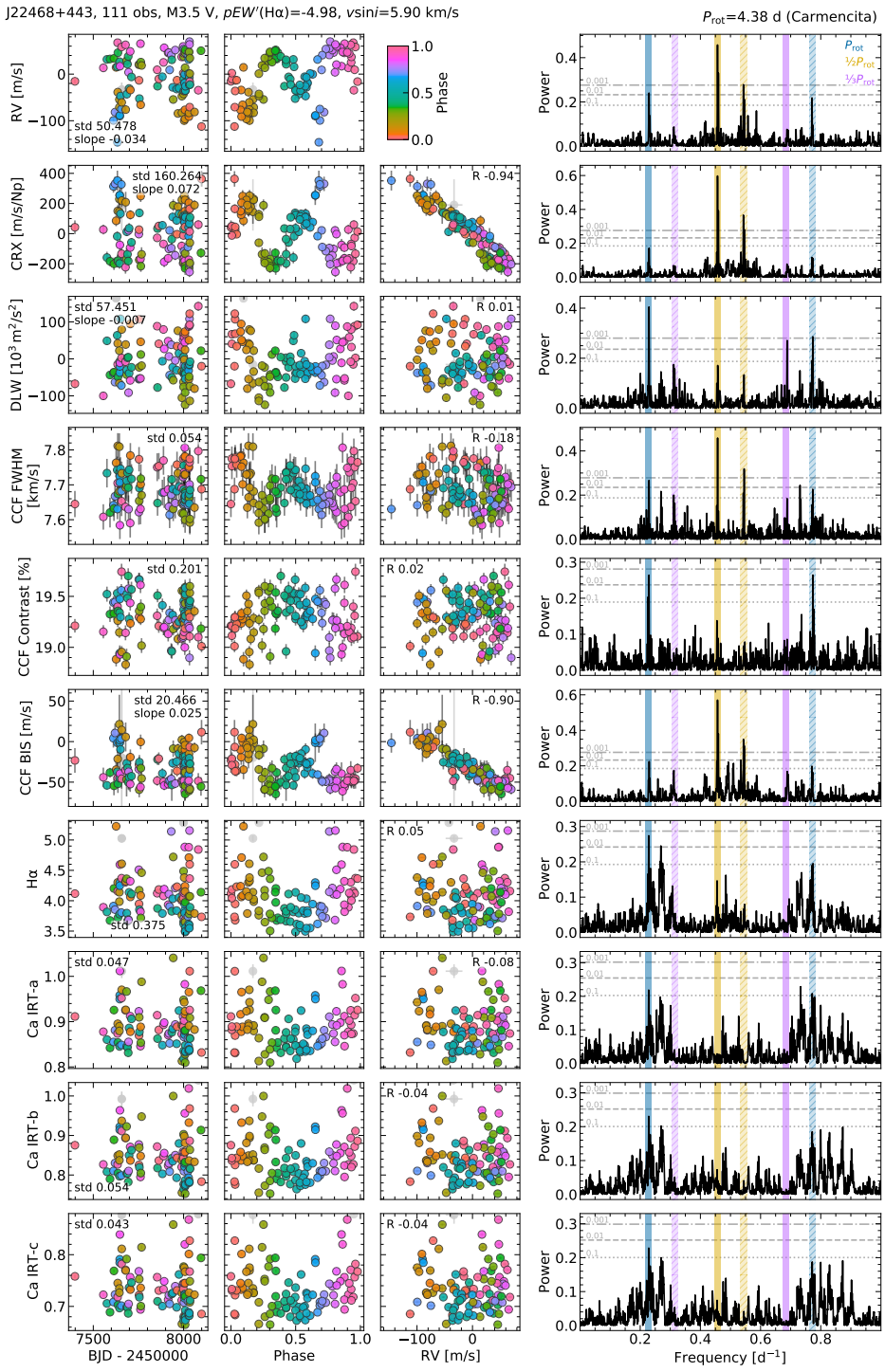

Figure 3.5: Same as Fig. 3.4, but for J22468+443. We now add the Ca IRT-b and -c data because they show significant signals. In the periodogram panels, we add a purple shaded region around $\frac{1}{3}P_{\rm rot}$ (and its corresponding 1-day alias indicated by a hatched purple region).

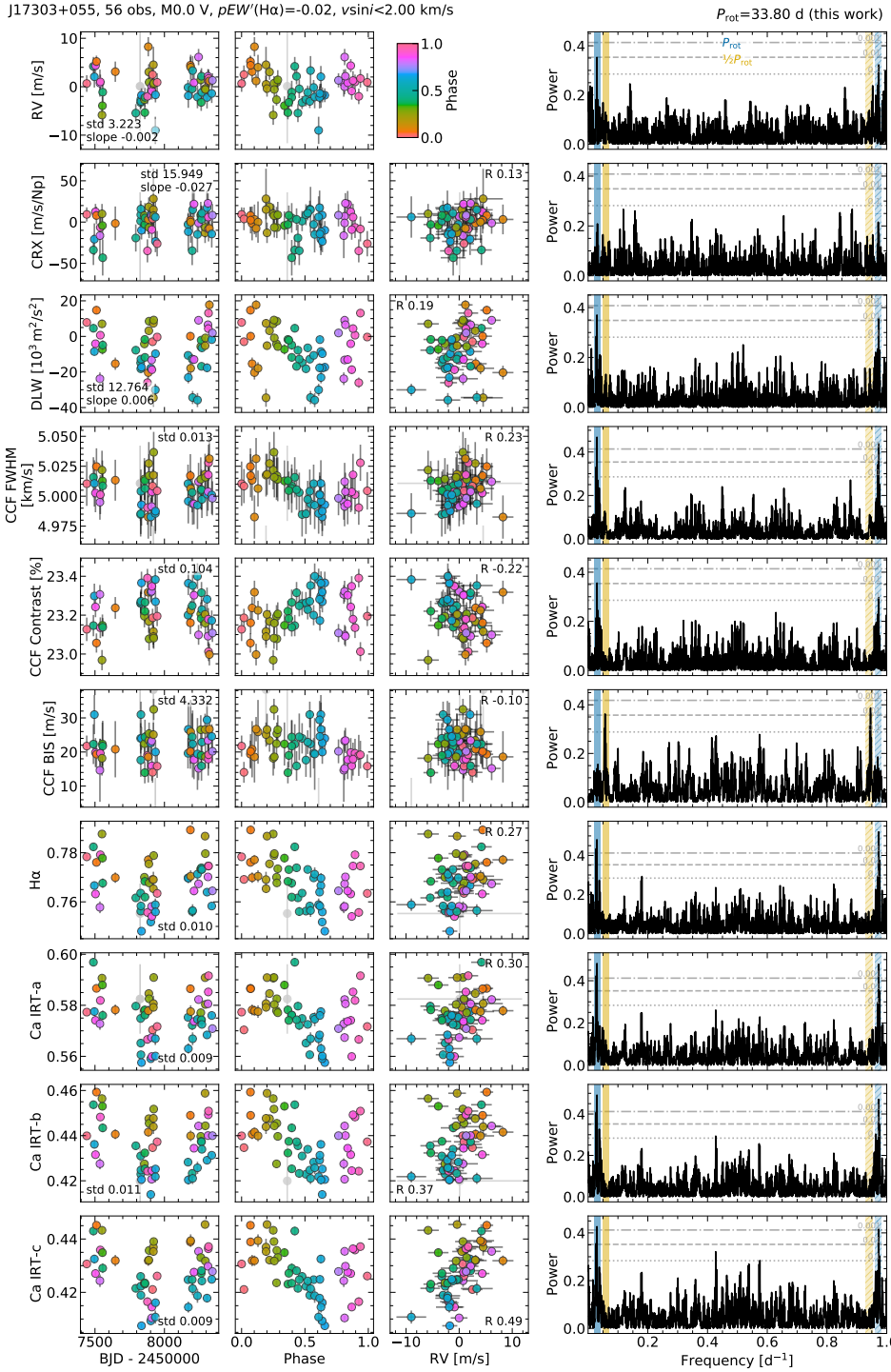

Figure 3.6: Same as Fig. 3.4, but for J17303+055.

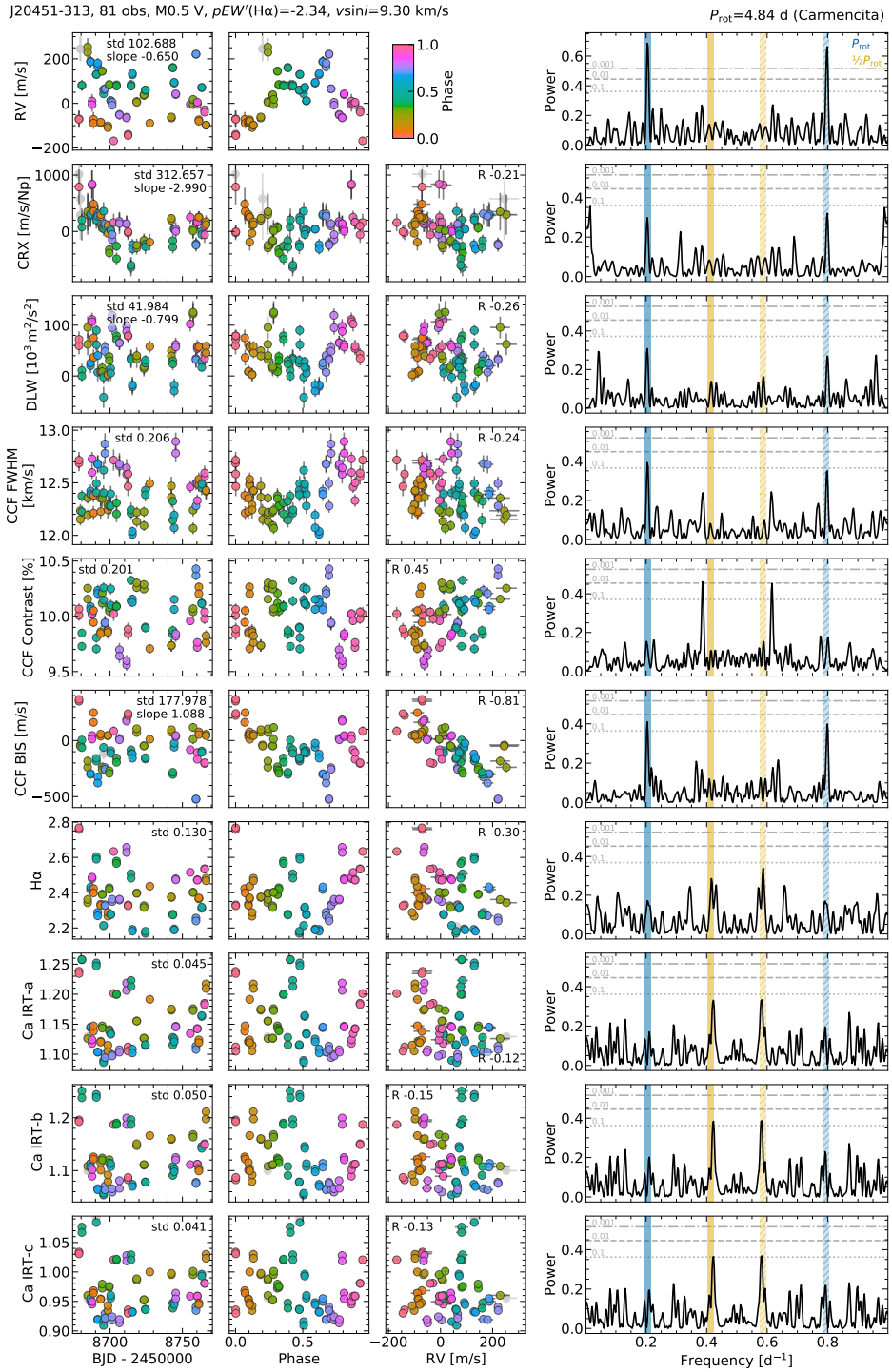

Figure 3.7: Same as Fig. 3.4, but for J20451-313.

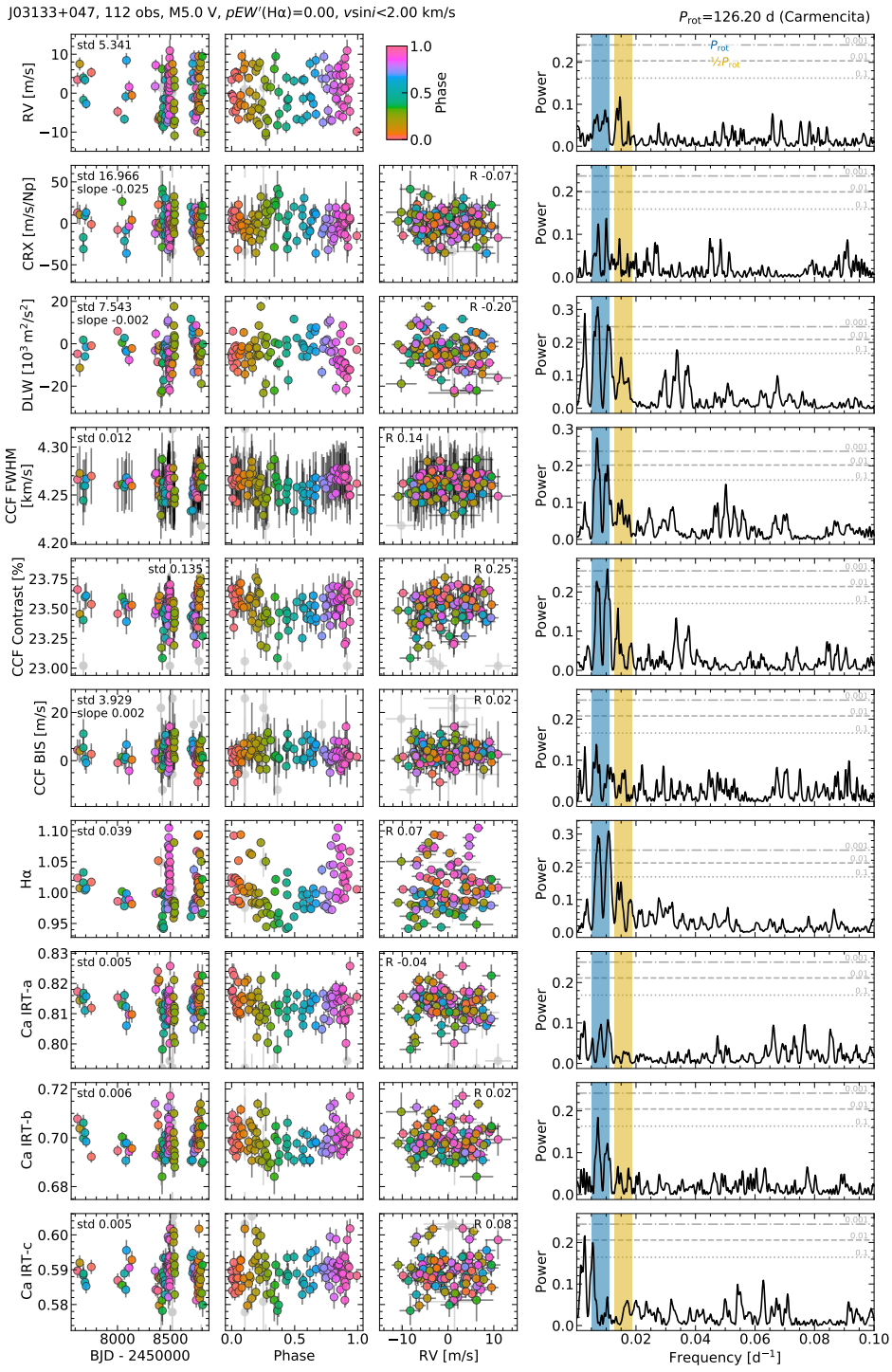

Figure 3.8: Same as Fig. 3.4, but for J03133+047. In this case, the periodogram shows a zoom in at the low frequency range, where we find activity-related peaks (the planetary companion shows a clear significant peak in the RVs at 2.29 d $= 0.44\,\mathrm{d}^{-1}$, not shown here).

3.6 Results

In Table 3.2, we show a summary of the results obtained from the periodogram analysis, where we specify the indicators for which we found a significant activity-related signal. Of the initial 98 stars, we find at least one significant (FAP $\leq 10\,\%$) signal in 56 of them, which we show in the table. In Appendix B, we show the specific results obtained for each indicator. Tables B.1 to B.10 contain, one for each parameter (RV, CRX, DLW, FWHM, contrast, BIS, Hα, and Ca IRT-a,b,c), the periods and FAP of the significant peaks that we identified as being related to stellar activity. Specifically, we show the values of the peaks at $P_{\rm rot}$, $\frac{1}{2}P_{\rm rot}$ and their 1-day aliases (we do not show the values corresponding to $\frac{1}{3}P_{\rm rot}$ because we only found significant signals for J22468+443, see Sect. 3.5.3.2).

To visualise which indicators show a modulation due to activity depending on the properties of the stars, we plot a summary of the results in Fig. 3.9. Each panel corresponds to the results obtained for one of the parameters analysed (RVs and the nine activity indicators). All the panels show the average activity level of the selected stars in the y-axis as a function of their mass in the x-axis. We used the same quantities as in the above Fig. 3.3: average $pEW'(\mathrm{H}\alpha)$ measured from a template of the CARMENES observations themselves from Schöfer et al. (2019), and masses from Schweitzer et al. (2019). In all the panels, each data point corresponds to one of the 98 selected stars. If a star was found to show an activity-related signal in the periodogram of a given indicator, then the star is represented with a filled marker in the panel of that indicator. On the contrary, if the periodogram did not show a clear peak that we could attribute to activity, the star is represented with a cross. For many stars, we found more than one peak related to activity (at $P_{\rm rot}$, its harmonics, or 1-day aliases). In the panels, we show the properties of the highest peak, i.e., the one with the smallest FAP. Different symbols indicate at which frequency the highest peak was found, and their size correspond to the FAP of that peak, with larger sizes indicating smaller FAPs. Finally, the data points are colour-coded according to the semi-amplitude of the sinusoid corresponding to that peak. This type of representation allow us to see how the different indicators behave depending on the mass and activity level of the stars.

RV

Of the 56 stars for which we find a signal in any parameter, 44 show significant (FAP $\leq 10\,\%$) activity signals in the RVs (25 % of them have signals with FAP $\leq 0.1\,\%$). In the upper left panel of Fig. 3.9, we see how they are located in the activity-mass space. Most of the high-mass stars (mass $\gtrsim 0.4 - 0.3\,\mathrm{M}_\odot$) with large levels of activity ($pEW'(\mathrm{H}\alpha) \lesssim -0.1$, stars on the top left corner of the plot), show significant (FAP $\leq 0.1\,\%$) activity signals at $P_{\rm rot}$. The only exceptions are J22468+443, for which

Table 3.2: Parameters that show an activity-related signal with FAP $\leq$ 10 % (parameters in bold-face indicate FAP $\leq$ 0.1 %) of the 56 stars for which we find any detection. We also show the mass and $pEW'(\mathrm{H}\alpha)$ values for reference (same as in Table 3.1).

Karmn	Mass [$M_\odot$]	$pEW'(\mathrm{H}\alpha)$	Detection
J00183+440	0.391 ± 0.016	-0.0730 ± 0.0070	RV, Hα, **Ca IRT-b**, Ca IRT-c
J01025+716	0.488 ± 0.019	0.076 ± 0.016	**RV**, CRX, **DLW**, **FWHM**, Hα, Ca IRT-a, **Ca IRT-b,c**
J01026+623	0.515 ± 0.019	-0.044 ± 0.013	RV, FWHM, BIS, Hα, **Ca IRT-a,b,c**
J01033+623	0.241 ± 0.012	-9.770 ± 0.040	RV, CRX
J01125-169	0.1418 ± 0.0098	-1.360 ± 0.020	RV, **DLW**, **FWHM**, **Contr.**
J02002+130	0.1497 ± 0.0098	-1.910 ± 0.025	**RV**, CRX, DLW, FWHM, **Contr.**, BIS, Hα, Ca IRT-c
J02222+478	0.551 ± 0.020	0.0550 ± 0.0040	RV, **DLW**, Hα, Ca IRT-a, **Ca IRT-b,c**
J02530+168	0.08857 ± 0.0088	-0.500 ± 0.050	**DLW**, **FWHM**, **Contr.**
J03133+047	0.161 ± 0.010	0.0	**DLW**, **FWHM**, Contr., Hα, Ca IRT-b
J03463+262	0.562 ± 0.020	-0.0920 ± 0.0050	Hα, Ca IRT-a,b,c
J04153-076	0.284 ± 0.014	-3.360 ± 0.028	**RV**, **CRX**, **BIS**, Hα
J04290+219	0.650 ± 0.024	0.190 ± 0.023	**RV**, **DLW**, FWHM, BIS, Hα, **Ca IRT-a,b,c**
J04376+528	0.578 ± 0.020	-0.013 ± 0.013	RV, **DLW**, FWHM, BIS, **Ca IRT-a,b**, Ca IRT-c
J04429+189	0.501 ± 0.020	0.0030 ± 0.0090	Hα, Ca IRT-a, **Ca IRT-b**, Ca IRT-c
J04588+498	0.589 ± 0.021	-0.0540 ± 0.0070	**RV**, DLW, **BIS**, Hα, **Ca IRT-a,b,c**
J05019+011	0.598 ± 0.024	-6.360 ± 0.019	**RV**, **CRX**, **BIS**
J05314-036	0.556 ± 0.033	0.101 ± 0.019	**RV**, CRX, **DLW**, Contr., Hα, **Ca IRT-a,b,c**
J05365+113	0.581 ± 0.021	-0.432 ± 0.012	**RV**, DLW, **FWHM**, **BIS**, Hα, **Ca IRT-a,b,c**
J07274+052	0.301 ± 0.014	-0.048 ± 0.015	RV
J07446+035	0.364 ± 0.017	-7.280 ± 0.024	**RV**, **CRX**, **DLW**, **FWHM**, **Contr.**, **BIS**
J08413+594	0.1228 ± 0.0094	-1.340 ± 0.013	**DLW**, **FWHM**, Hα, Ca IRT-b,c
J09143+526	0.586 ± 0.025	-0.008 ± 0.012	**RV**, **DLW**, FWHM, BIS, Hα, **Ca IRT-a,b,c**
J09144+526	0.592 ± 0.023	-0.015 ± 0.010	**RV**, **DLW**, Hα, **Ca IRT-a,b,c**
J09561+627	0.574 ± 0.020	-0.0620 ± 0.0060	**RV**, DLW, FWHM, Hα, **Ca IRT-a,b,c**
J10122-037	0.526 ± 0.020	-0.029 ± 0.012	RV, Hα, Ca IRT-a,b, **Ca IRT-c**
J10196+198	0.436 ± 0.017	-4.520 ± 0.040	**RV**, **CRX**
J10482-113	0.1167 ± 0.0096	-2.270 ± 0.050	RV, **DLW**
J10564+070	0.132 ± 0.010	-7.220 ± 0.080	**RV**, **CRX**, DLW
J10584-107	0.208 ± 0.011	-0.620 ± 0.060	**RV**, CRX
J11026+219	0.536 ± 0.019	-0.486 ± 0.013	RV, CRX, BIS
J11302+076	0.439 ± 0.018	0.041 ± 0.011	**RV**, Hα, **Ca IRT-a,b,c**
J11511+352	0.456 ± 0.018	-0.065 ± 0.010	**RV**
J13299+102	0.490 ± 0.018	-0.015 ± 0.012	**RV**
J15218+209	0.593 ± 0.022	-2.880 ± 0.018	**RV**, CRX, Contr., BIS
J16167+672S	0.627 ± 0.023	0.065 ± 0.012	**RV**, **DLW**, Contr., Hα, **Ca IRT-a,b,c**
J16555-083	0.1049 ± 0.0093	-4.540 ± 0.060	RV, **DLW**, **FWHM**, **Contr.**, BIS
J16581+257	0.514 ± 0.020	-0.0460 ± 0.0070	Hα, Ca IRT-a, **Ca IRT-b**, Ca IRT-c
J17303+055	0.537 ± 0.019	-0.022 ± 0.013	RV, DLW, **FWHM**, Contr., BIS, Hα, **Ca IRT-a,b**, Ca IRT-c
J17378+185	0.426 ± 0.017	-0.0660 ± 0.0070	RV, CRX, **DLW**, FWHM, Hα, **Ca IRT-a,b,c**
J17578+046	0.172 ± 0.010	0.0	**DLW**, **FWHM**, BIS, Hα
J18174+483	0.587 ± 0.022	-1.580 ± 0.012	RV, CRX, DLW, BIS, Hα, Ca IRT-a, **Ca IRT-b**, Ca IRT-c
J18198-019	0.593 ± 0.021	-0.6	**RV**, **DLW**, FWHM, Hα, **Ca IRT-a,b,c**
J18498-238	0.184 ± 0.011	-2.220 ± 0.018	RV, CRX, **DLW**, FWHM, Contr., **BIS**
J18580+059	0.559 ± 0.020	0.0	**DLW**, Hα, **Ca IRT-a,b,c**
J19346+045	0.564 ± 0.019	0.104 ± 0.017	**DLW**, FWHM, Contr., BIS, Hα, **Ca IRT-a,b,c**
J20305+654	0.385 ± 0.016	-0.235 ± 0.010	Hα
J20451-313	0.661 ± 0.016	-2.3	**RV**, FWHM, Contr., BIS, Ca IRT-b,c
J21164+025	0.430 ± 0.017	0.1020 ± 0.0060	**FWHM**, Hα, **Ca IRT-a,b,c**
J21221+229	0.498 ± 0.019	-0.0320 ± 0.0060	**DLW**, **FWHM**, Contr., Hα, **Ca IRT-a,b,c**
J22021+014	0.548 ± 0.021	0.0240 ± 0.0050	RV, Hα, Ca IRT-a,b,c
J22057+656	0.482 ± 0.019	0.113 ± 0.011	**RV**, **CRX**
J22114+409	0.160 ± 0.010	-5.740 ± 0.050	RV, **FWHM**, Contr.
J22115+184	0.565 ± 0.022	0.0320 ± 0.0090	RV, **DLW**, FWHM, **Contr.**, Hα, Ca IRT-a, **Ca IRT-b,c**
J22468+443	0.339 ± 0.015	-4.980 ± 0.021	RV, **CRX**, **DLW**, FWHM, Contr., BIS, Hα, Ca IRT-a,b,c
J22565+165	0.532 ± 0.020	0.070 ± 0.014	**RV**, **DLW**, **FWHM**, **Contr.**, Hα, **Ca IRT-a,b,c**
J23492+024	0.396 ± 0.016	-0.023 ± 0.014	**RV**, **FWHM**, Hα

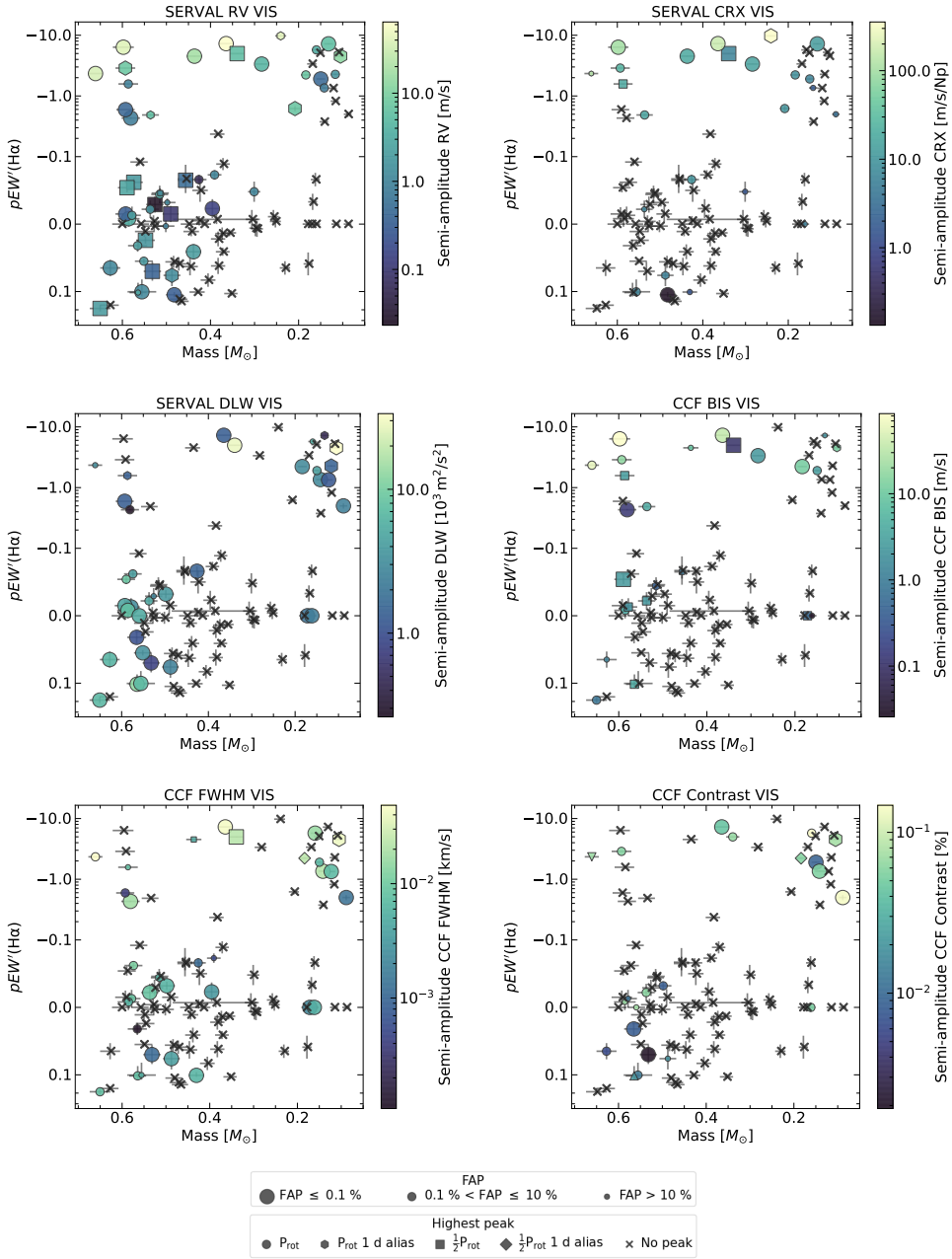

Figure 3.9: Activity detections on the 98 selected stars for the 10 parameters analysed (*left* to *right*, *top* to *bottom*: RV, CRX, DLW, BIS, FWHM, contrast, on this page, and Hα, Ca IRT-a, b and c, on the next one). Stars are shown as a function of their average activity level (measured as the average pEW'(Hα) of the `SERVAL` template) and mass. Different markers represent the signal with the smallest FAP identified in the periodogram of each star (circles correspond to $P_{\rm rot}$, hexagons to $P_{\rm rot}$ 1-day alias, squares to $\frac{1}{2}P_{\rm rot}$, diamonds to $\frac{1}{2}P_{\rm rot}$ 1-day alias, and crosses indicate that no activity-related peak was found). Data point sizes indicate the FAP value of the corresponding peak (larger size means smaller FAP), and are colour coded as a function of the semi-amplitude of the best-fitting sinusoid to the corresponding period. Continues on the next page.

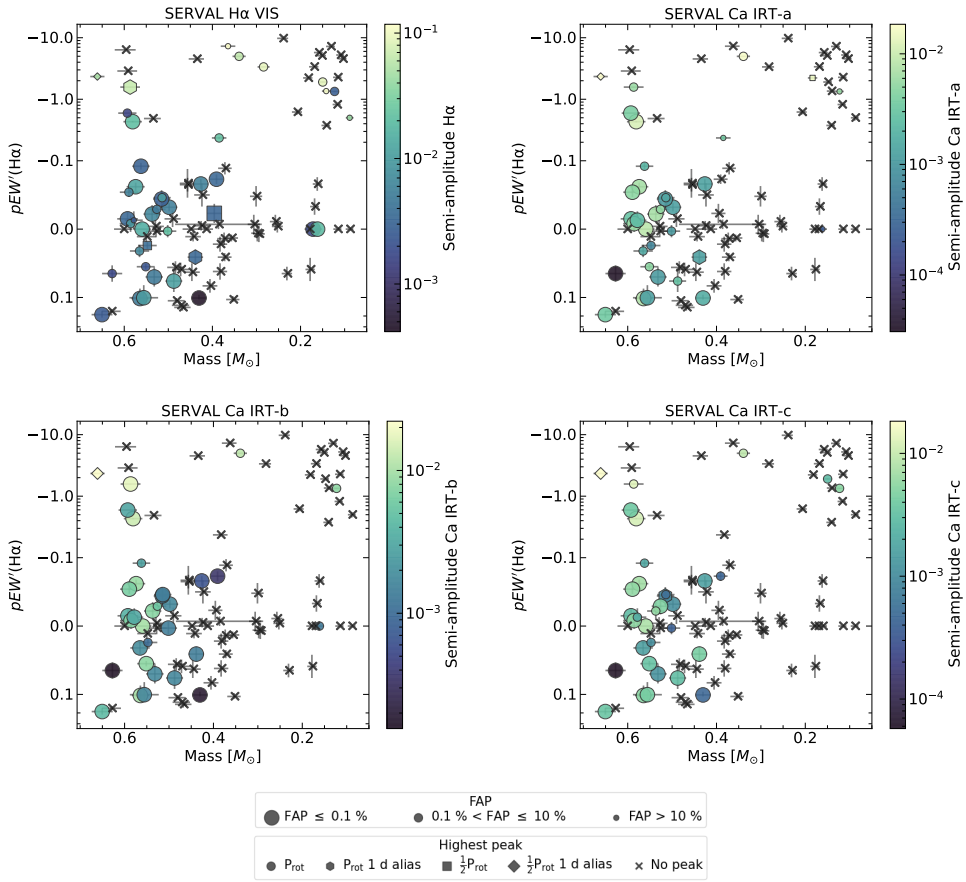

Figure 3.9: Continued.

its most significant peak is at $\frac{1}{2}P_{\rm rot}$ (see Sect. 3.5.3.2), and J15218+209, which shows its highest peak at the 1-day alias of $P_{\rm rot}$. Other two stars show slightly less significant signals ($0.1\,\% < {\rm FAP} \leq 10\,\%$) at $P_{\rm rot}$ and its 1-day alias (J18174+483 and J11026+219, respectively). Some of the less massive (mass $\lesssim 0.4 - 0.3\,{\rm M}_{\odot}$) but active stars ($pEW'({\rm H}\alpha) \lesssim -0.1$, top right corner of the plot), also show clear signals (with FAPs from ≤ 0.1 to $10\,\%$) at either $P_{\rm rot}$ or its 1-day alias, but for seven stars, we do not observe any significant signal in the periodogram. Six of those seven are some of the faintest stars in the sample ($J \lesssim 8\,{\rm mag}$, see Fig. 3.3), and the seventh one (J23419+441), has a long $P_{\rm rot}$, of $\sim 106\,{\rm d}$. Regarding the low-level activity stars ($pEW'({\rm H}\alpha) \gtrsim -0.1$), less than half of the high-mass ones (mass $\gtrsim 0.4 - 0.3\,{\rm M}_{\odot}$, bottom left corner of the plot) show clear signals at either $P_{\rm rot}$ or $\frac{1}{2}P_{\rm rot}$. In the low-mass regime (mass $\lesssim 0.4 - 0.3\,{\rm M}_{\odot}$, bottom right corner of the plot), almost none of the stars show any signal.

CRX and BIS

For CRX and CCF BIS (right panels in the first and second rows of Fig. 3.9), most of the detections correspond to the most active stars, especially in the high-mass regime. In the active and low-mass regime, the situation is similar as in the RVs: more than half of the stars (including some of the faintest ones) do not show any significant signal. There are some detections for the stars in the low-activity regime, but they are in general much less significant.

DLW and FWHM

DLW and CCF FWHM (left panels in the second and third rows of Fig. 3.9) show some significant detections across all the activity levels and masses. In the high-activity regime ($pEW'(\mathrm{H}\alpha) \leq -0.1$), they show significant detections, mostly at P_{rot} and its 1-day alias, for some of the lowest-mass (mass $> 0.3\,\mathrm{M}_{\odot}$) stars (six with FAP $\leq 0.1\,\%$), for which CRX and BIS do not show signals. For the more massive ones, they show signals in about half of the stars (four of them with FAP $\leq 0.1\,\%$). For the low-activity, high-mass stars, we find significant detections, mostly at P_{rot}, in less than half of the stars, in general common to the ones with RV detections. The low-activity, low-mass stars, do not show any signals, as happened with the RVs, except for two stars, J03133+047 (CD Cet) and J17578+046 (Barnard's star). These two stars also show significant peaks in the Hα indicator, but not in the Ca IRT lines.

Contrast

CCF contrast (third row, right panel of Fig. 3.9) shows a similar behaviour to CCF FWHM, but with slightly lower number of detections and with lower significance.

Chromospheric lines

In the chromospheric indicators (bottom panels of Fig. 3.9), we find significant peaks especially in the high-mass low-activity regime, where most of the stars with detections coincide with the ones that have detections in the RV. About half of the high-activity, high-mass stars also show some activity-related peaks. In the high-activity, low-mass regime, 1 to 4 active stars, depending on the chromospheric line, show peaks with very low significance (FAP $> 10\,\%$), and, except for the two stars mentioned above for DLW and FWHM (J03133+047 and J17578+046), none of the low-activity, low-mass stars show any signal. In general, the four lines show similar results. Differences in the detections could be due to the Ca IRT lines being affected by a photospheric component, or telluric contamination, which affect the targets to varying degrees, depending on their absolute RV (Schöfer et al., 2019).

3.7 Discussion

3.7.1 Performance of the indicators as a function of stellar activity and mass

Given their similar behaviour discussed before, we can approximately group the indicators into 3 categories: (1) CRX and BIS, which trace chromaticity, (2) DLW and FWHM, which trace changes in the width of the stellar absorption lines, and (3) Hα and Ca IRT lines, which are both proxies of chromospheric emission. We do not include the contrast because its results were similar to the FWHM and DLW but less significant in general. We also grouped the 56 stars for which we find at least an activity-related signal into four subsets, depending on their activity level (high, $pEW'(\mathrm{H}\alpha) \leq -0.1$, or low, $pEW'(\mathrm{H}\alpha) > -0.1$), and their mass (high, $\geq 0.4\,\mathrm{M}_\odot$, or low, $< 0.4\,\mathrm{M}_\odot$). In the four panels of Fig. 3.10, we show the performance of these three groups of indicators, together with the detections in the RVs, for each of the four subsets of stars. In each panel, the bins correspond to the four subsets of stars, and the colours and numbers indicate how many of them show a significant (FAP $\leq 10\,\%$) activity signal. As in Fig. 3.9, we selected the activity-related peak with smallest FAP. Fig. 3.11 shows the same but we restricted the signals to those with FAP $\leq 0.1\,\%$.

RV

In the RVs, we find significant (FAP $\leq 10\,\%$) signals in most of the stars (more than 75 % of them, especially in the high activity regime), except for the low-mass, low-activity ones, where only 60 % (the three stars with the highest mass in the bin) show a signal. The total numbers decrease if we only consider signals with FAP $\leq 0.1\,\%$, but the proportion of stars with signals within bins remains similar (i.e. we find more detections for the most active, highest mass stars, and significantly less for the least active, lowest mass ones).

CRX and BIS

As noted above, CRX and BIS are effective activity tracers for the stars showing the highest levels of activity, especially for the ones with the highest mass, where 75 % (6 of 8) of stars in the high-mass high-activity subset show a signal with FAP $\leq 10\,\%$. If we restrict the FAP to values $\leq 0.1\,\%$, the number of stars with signals decreases, especially for the high-activity high-mass subset, where only the two most active stars (25 %) show a signal with enough significance. For the low-activity stars, they only show clear signals for 5 of the total 33 stars, all of them in the high-mass regime. Only one of these stars has a signal with FAP $\leq 0.1\,\%$.

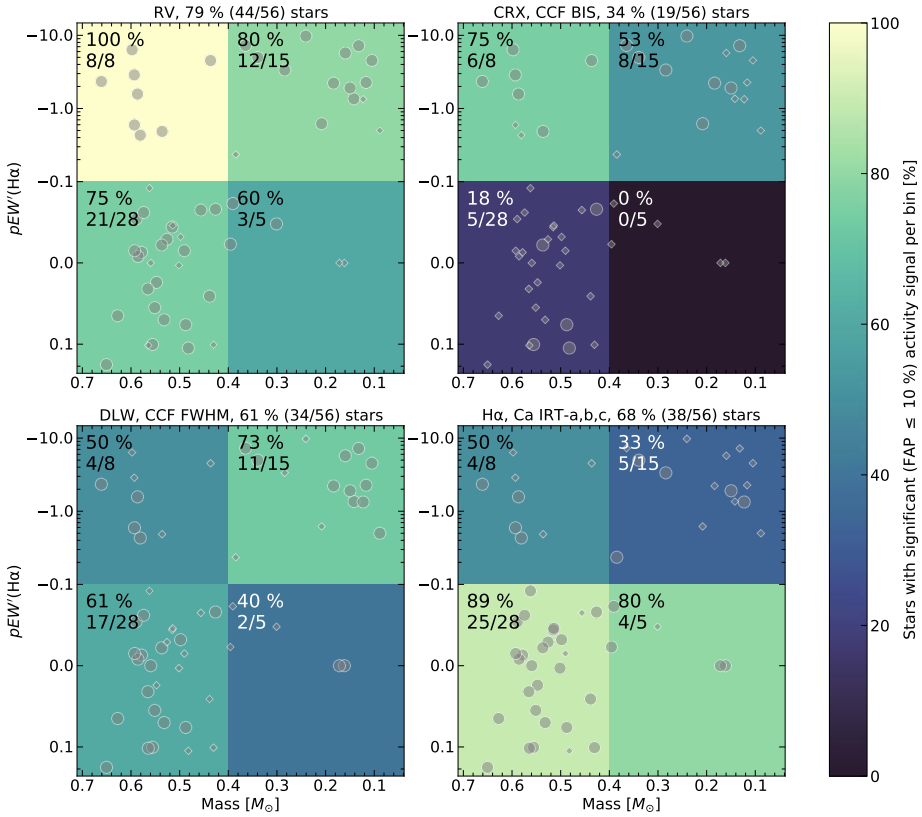

Figure 3.10: Number of stars with activity detections in RV (*top left*), CRX and BIS (*top right*), DLW and FWHM (*bottom left*), and chromospheric lines Hα and Ca IRT-a,b,c (*bottom right*). The stars are divided into four bins, depending on their average activity level and mass (axis are the same as in Fig. 3.9). The colours of each bin indicate the number of stars (in percentage) for which we found an activity-related signal with FAP $\leq 10\,\%$. The text in each bin also shows that percentage, together with the absolute fraction of stars that have such a detection. The title of each panel shows the same numbers, but for all the stars (i.e. for the four bins together). Grey data points indicate the position of the 56 stars considered in the activity-mass space, with large dots representing the stars with a detection in the specific indicator, and small diamonds, stars with no detection.

Chromospheric lines

Chromospheric lines show the opposite behaviour as CRX and BIS. We find significant (FAP $\leq 10\,\%$) signals in most (almost $90\,\%$) of the stars with low activity levels, and in less than half of the most active ones. The signals in all but one of the low activity stars have FAP $\leq 0.1\,\%$, but in the high activity regime, this only occurs for 3 of the most massive stars. Regarding the mass, these indicators perform slightly better for the most massive stars, similarly to RV, and CRX and BIS.

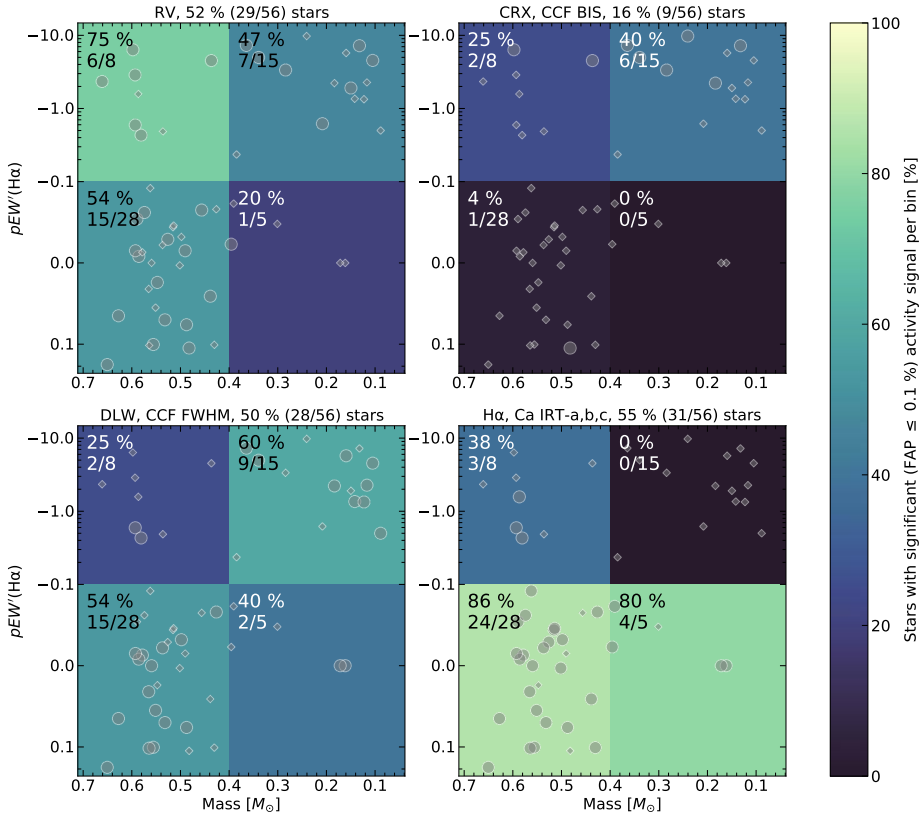

Figure 3.11: Same as Fig. 3.10, but for signals with FAP $\leq 0.1\,\%$.

DLW and FWHM

For DLW and FWHM, we find that they perform better for the high-activity, low-mass stars, with signals with FAP $\leq$ 10 % in 73 % of them (and of these, still 60% have FAP $\leq 0.1\,\%$). None of the other indicators has that many significant signals in such regime. For the other three subsets of stars, they show significant signals for about half of the stars: 50 % for the high-activity high-mass stars, 61 % for the low-activity high-mass stars, and 40 % for the low-activity low-mass ones. These numbers slightly decrease if considering FAP $\leq$ 0.1 %, but the proportion between subsets remains more or less constant.

Overview

About half of the stars in the sample show clear activity signals in the RVs, especially the most active ones. Of the different indicators analysed, we find that they behave differently depending on the mass and activity level of the target star. CRX and BIS work best for the most active stars, while the chromospheric lines Hα and Ca IRT are the most effective in tracing activity in stars with lower activity levels. DLW and

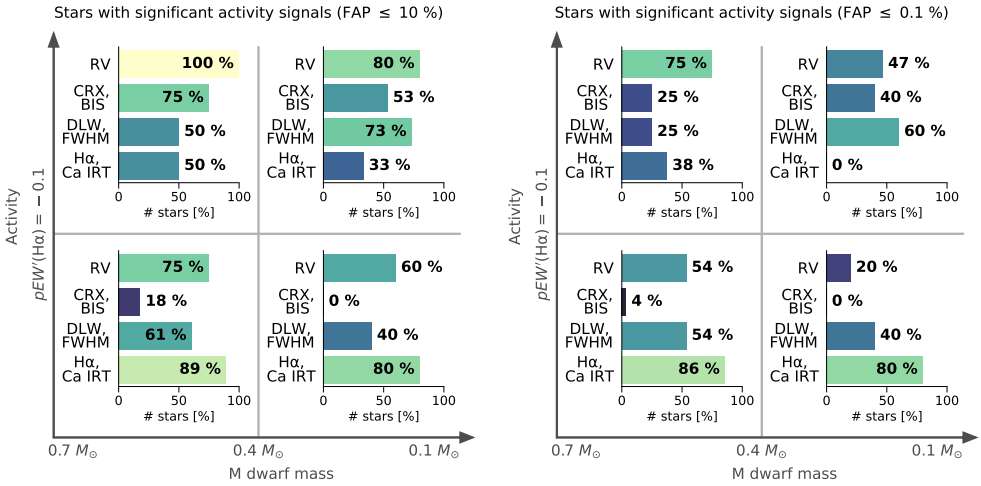

Figure 3.12: Number of stars (% of the total 56 stars with at least a signal) with activity detections on the different groups of indicators, divided in 4 groups according to the activity level ($pEW'(\mathrm{H}\alpha)$ higher or lower than -0.1) and mass (higher or lower than $0.4\,\mathrm{M}_\odot$) of the star. The *left panel* corresponds to signals with FAP $\leq 10\,\%$, and *right* one, to signals with FAP $\leq 0.1\,\%$.

FWHM behave similarly in all mass and activity regimes, but are especially useful for the most active and least massive stars.

In other words (see Fig. 3.12), 50 to 75 % of stars with the highest levels of activity tend to show signals (FAP $\leq 10\,\%$) in photospheric indicators (CRX, BIS, DLW, and FWHM), depending on the mass regime. For the most massive stars, CRX and BIS work best, with signals in about 75 % of the stars. The other photospheric indicators (DLW and FWHM) and the chromospheric lines (Hα and Ca IRT) show signals in 50 % of these stars. For the least massive stars, the most effective indicators are DLW and FWHM, with signals in almost 75 % of the stars, followed by CRX and BIS, with signals in about 50 % of them. Only a third of these stars show signals in the chromospheric lines, all of them with large FAPs.

Regarding stars with low activity levels, most of them ($\sim 90\,\%$ in the high-mass regime, and 80 % in low-mass one) show activity signals in chromospheric indicators. About half of them ($\sim 60\,\%$ high-mass, and 40 % low-mass stars) also show signals in DLW and FWHM. Finally, CRX and BIS indicators are not effective in tracing activity in these low activity stars, with detections in only $\sim 20\,\%$ of the most massive stars (most of them with relatively large FAPs), and none in the low-mass regime.

These results clearly show the need to use different indicators to assess the presence of activity depending on the characteristics of the target star. Failing to use the adequate indicators may result in planetary detections that are actually false positives. It follows that it is possible to rule out the existence of planets that have only been cross-checked with a limited set of indicators (e.g. Tuomi et al., 2019; Feng et al., 2020). To show a

specific example, Tuomi et al. (2019) claim the existence of two planets in the very active ($pEW'(\mathrm{H}\alpha) \sim -7.2$), late-type (M6.0 V) star J10564+070 (CN Leo, GJ 406) based on RV data obtained with the HARPS (Mayor et al., 2003, 23 observations) and HIRES (Vogt et al., 1994, 41 observations) high-resolution spectrographs. One of the claimed planet candidates is a hot super-Earth in a ~ 2.68 d period orbit. The analysis of different spectroscopic activity indicators, CCF BIS and FWHM from the HARPS data, Ca II H&K S-index from both HARPS and HIRES, and photometric time series from ASAS (Pojmanski, 1997), results in no significant periodicities related to the planet orbital period. Therefore, the authors conclude that the 2.68 d signal has no stellar origin. However, we have just seen that in active and low-mass stars such as this one, indicators like the chromospheric lines tend to not show activity signals, and other indicators like CRX and BIS, or DLW and FWHM work better. In this case, CARMENES observations (see Fig. 3.13) show a clear and strong (FAP $< 10^{-13}$) signal at 2.71 d in the CRX data, an indicator that was not analysed in Tuomi et al. (2019), and that clearly points at a stellar origin for this signal. There are weaker activity-related periodicities in DLW and BIS, and none in chromospheric lines. Moreover, Díez Alonso et al. (2019) identified the rotation period of the star to be of ~ 2.7 d from photometric time series. Overall, these findings strengthen the idea that a lot of caution should be exercised when vetting RV planetary candidates, and that a complete activity indicator analysis needs to be performed.

3.7.2 Detection biases

In this analysis, we tried to select stars with enough observations so that, if their activity indicators contain information related to their rotation, which has timescales of days, they could be identified in the data sets using a periodogram analysis. Despite that, there are still several reasons explaining why we may not observe signals in some of the stars.

Of the 98 initial stars selected, we find activity-related signals in 56 of them. In Fig. 3.14 we show the average activity of the stars and their mass, as a function of their brightness and number of observations, and we indicate for which stars we found a detection (with FAP $\leq 10\,\%$) in any of the indicators. In general, stars with for which we find no detections have low levels of activity, and are distributed across the entire mass range. Of the 70 stars in the low-activity regime ($pEW'(\mathrm{H}\alpha) \gtrsim -0.1$), 53 % (37 stars) show no detection in any parameter. This number decreases if we focus only on the lowest mass stars (mass $\lesssim 0.3\,\mathrm{M}_\odot$). In the low-mass low-activity regime, only 3 stars show a detection: J07274+052 (Luyten's star), J17578+046 (Barnard's star), and J03133+047 (CD Cet). They are well studied stars with planetary companions (see Astudillo-Defru et al., 2017b; Ribas et al., 2018; Bauer et al., 2020, respectively) and long rotation periods ($P_{\mathrm{rot}} \gtrsim 100$ d). Since the main aim of the CARMENES survey is

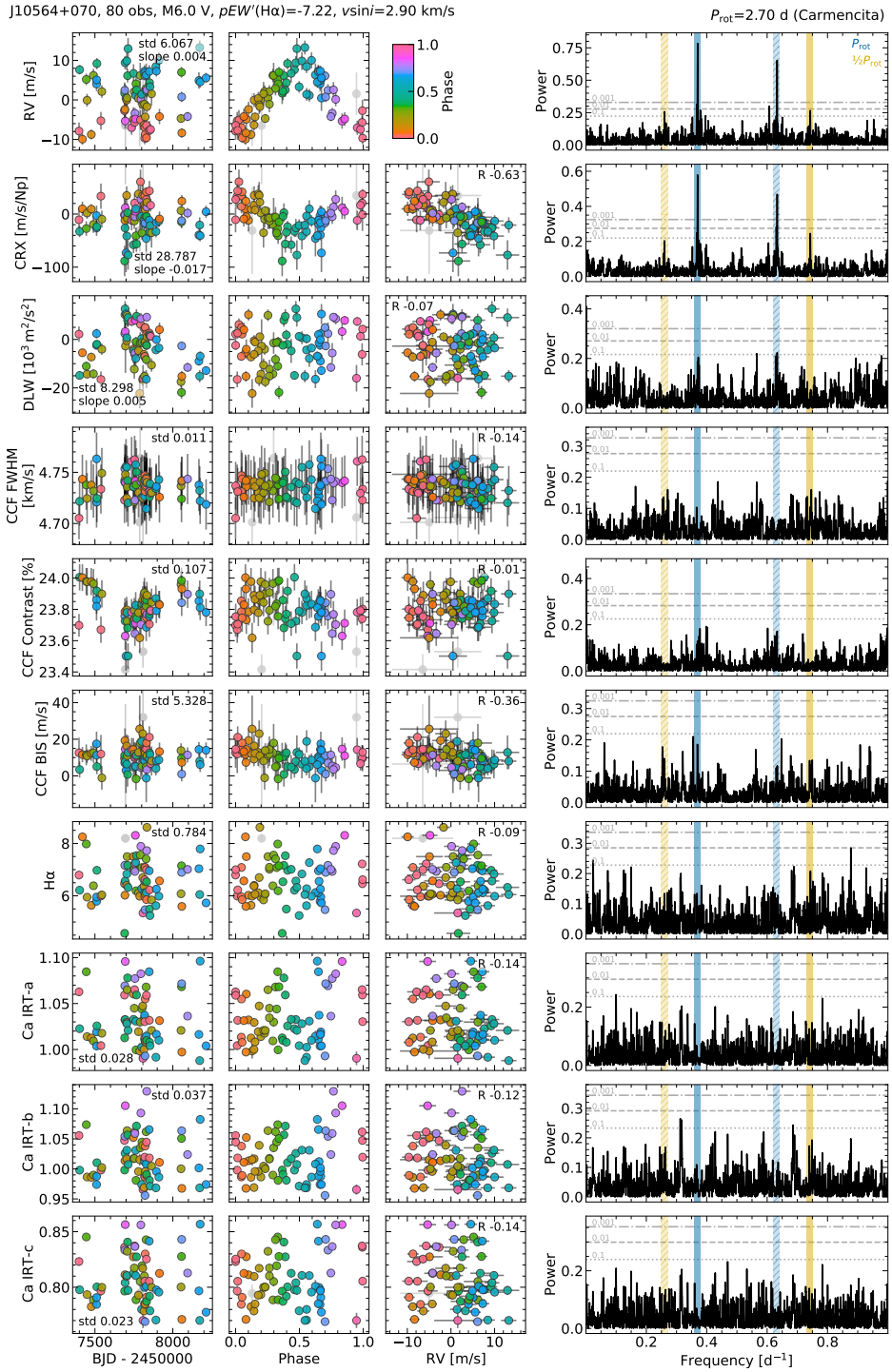

Figure 3.13: Same as Fig. 3.4, but for J10564+070 (CN Leo, GJ 406).

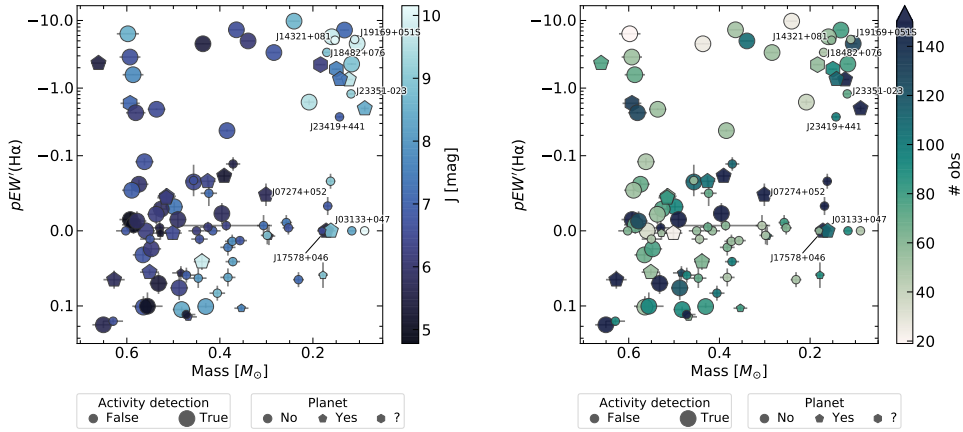

Figure 3.14: *Left*: Average activity level ($pEW'(\mathrm{H}\alpha)$) as a function of the mass of the 98 sample stars, colour-coded with the J magnitude. Large data points indicate that a signal related to the activity of the star was found in at least one parameter, while small data points indicate non-detections. Stars with no known planetary companions are indicated with dots, while stars with confirmed or candidate planetary companions are indicated with pentagons and hexagons, respectively. *Right*: Same as in the *left panel* but colour-coded with the number of observations (nobs) instead of the J magnitude.

to find and characterise exoplanets, these stars have been observed more times than the other stars in that region, which could explain why we have a detection and not for the other stars with similar characteristics. Of the most active stars ($pEW'(\mathrm{H}\alpha) < -0.1$, 28 stars), only 18 % (5 stars) show no detections (J14321+081, J18482+076, J19169+051S, J23351-023, J23419+441). They are low-mass ($\leq 0.17\,\mathrm{M}_\odot$) stars, and 4 of them are at the faintest end of the sample ($J \geq 8.8$ mag), which implies less precise measurements. The fifth star (J23419+441) is brighter ($J \sim 6.9$) but shows a large P_{rot} (~ 106 d). They have between 47 and 99 observations.

Clearly, for the least active stars, signals induced by activity can be below the noise of our measurements, making them impossible to detect. Also, stars with lower activity levels show longer rotation periods. In general, the observations of each star in the sample cover relatively large time spans, of ~ 1000 d, and most of the stars have been observed between 50 and 130 times. However, in stars with long P_{rot}, this may not be sufficient to cover densely enough the rotation modulation so that a significant signal appears in the periodogram. Another observational constraint is the apparent brightness of the stars, which results in observations with lower S/N. Therefore, activity signals could be hidden in the noise. The faintness of some stars at the low-mass end of the sample could be difficulting activity detections, and the combination of a relatively small number of observations and long rotation periods could be a problem when looking for activity signals in the least active stars.

The average activity level of the stars is not constant with time, it increases and

decreases, related to a long-period magnetic cycle. Some of the stars could have been observed at a low-activity phase of the cycle, which would decrease the level of the activity signals, making them more difficult to detect. Also, some stars have groups of observations separated by several months, and we could be merging epochs with very different activity levels, which could also reduce the significance of the signals.

The inclination of the stars with respect to our line of sight also plays a role on the total amplitude of the activity signals. In stars with nearly pole-on inclination, visible active regions do not appear and disappear abruptly as the star rotates. This results in smaller-amplitude modulations, which again makes them more difficult to detect. However, pole-on configurations are unlikely, and statistically should only occur for a small number of stars.

The distribution of active regions also affects the amplitude of activity modulations. Similarly to the case of a pole-on configuration, stars with an homogeneous distribution of active regions display signals with smaller amplitudes. Complex activity patterns on the stellar surface may induce signals that are not exactly at $P_{\rm rot}$, but at its harmonics (e.g. Boisse et al., 2011), although we tried to account for that. Stars can also have differential rotation, which can make the activity modulations to not be seen exactly at $P_{\rm rot}$. Also, active regions could have short life-spans. Rapid changes in the activity surface patterns could hamper the detection of a coherent signal related to $P_{\rm rot}$.

3.7.3 RV jitter - activity relation

Next, we study the RV scatter of the 98 stars in the sample. The left panel in Fig. 3.15 shows the relation between the RV scatter (std RV) and the average activity level (measured as the average $pEW'(\mathrm{H}\alpha)$) of the 98 stars in the sample. We also indicate the stellar mass, the presence of planetary companions, and if we detected any kind of activity-related signal in any of the parameters studied. Fig. 3.16 shows the same but instead of the mass we indicate the number of observations of each star. We did not remove RV variations induced by planetary companions, so the RV scatter of stars identified as having planets is only an upper limit to the RV variation caused by activity.

High activity stars

In the high activity regime ($pEW'(\mathrm{H}\alpha) \leq -0.1$, 28 stars), we observe that the RV scatter increases with the average activity level of the stars, covering values from $\sim 2\,\mathrm{m\,s^{-1}}$ to more than $100\,\mathrm{m\,s^{-1}}$. 12 of these 28 stars have RV scatter $\lesssim 10\,\mathrm{m\,s^{-1}}$. They correspond mostly to low-mass stars (11 of them, i.e. 90 %, have masses $< 0.4\,\mathrm{M_\odot}$). In the other 16 stars with std RV $> 10\,\mathrm{m\,s^{-1}}$, the mass distribution is approximately equally divided between low (9 stars, 6 %, with mass $< 0.4\,\mathrm{M_\odot}$) and high (7, 4 %, with $\geq 0.4\,\mathrm{M_\odot}$).

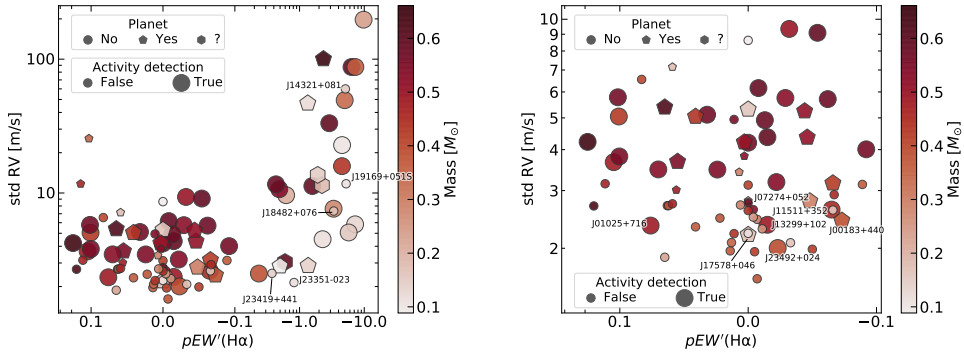

Figure 3.15: *Left*: RV scatter (std RV) as a function of the average activity level ($pEW'(\mathrm{H}\alpha)$) of the 98 stars in the sample, colour-coded with the stellar mass. Stars with no known planetary companions are indicated with dots, while stars with confirmed or candidate planetary companions are indicated with pentagons and hexagons, respectively. Large data points correspond to the 56 stars for which we find an activity-related signal in any of the indicators, and small data points, stars with no detection. *Right*: Zoom in on the stars with small std RV and low activity levels. Data points colour, shape and size are the same as in the *left panel*.

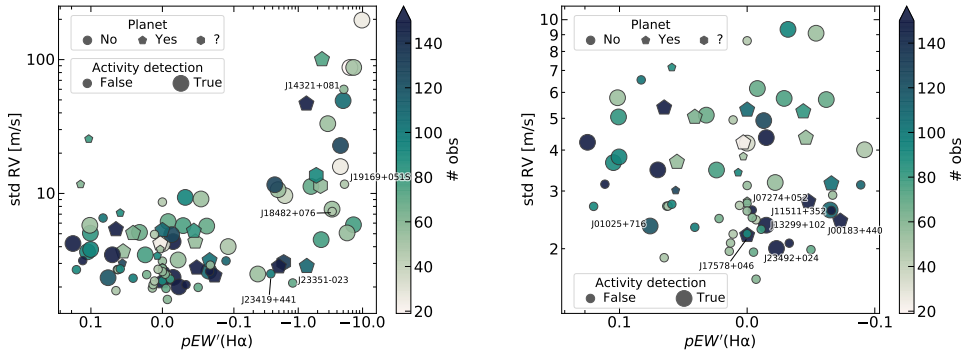

Figure 3.16: Same as Fig. 3.15, but colour-coded with the number of observations.

For most of these 28 stars, we were able to identify an activity-related signal in at least one of the indicators, but, as mentioned above, there are 5 stars with no detections (J14321+081, J18482+076, J19169+051S, J23351-023, J23419+441). They have low mass, are faint, or have a long P_{rot}, which could impact on the possibility of detecting a signal. From Fig. 3.9 (top left), we also see that the RV semi-amplitudes of the stars for which we find signals are, in general, large ($\gtrsim 10\,\mathrm{m\,s^{-1}}$).

Low activity stars

In the low-activity regime ($pEW'(\mathrm{H}\alpha) > -0.1$, 70 stars), most of the stars have low RV scatter, $\leq 10\,\mathrm{m\,s^{-1}}$. There are two outliers, J11417+427 and J22096-046, with larger RV scatter, which contain the modulation due to large planetary companions (see e.g. Butler et al., 2006; Trifonov et al., 2018, respectively). The right panels of 3.15 and 3.16 show a zoom in into the low activity region. Here, about a third of the stars have low

mass (25 stars with mass $< 0.4\,M_\odot$) and two thirds are high mass stars (45 stars with mass $\geq 0.4\,M_\odot$). As occurs with the high-activity regime, we observe a gradient of the stellar mass with the RV scatter: lower RV scatter values correspond in general to the lowest mass stars, while most of the highest mass stars show larger RV scatter. Specifically, of the 32 stars with RV scatter $\leq 3\,m\,s^{-1}$, 19 ($\sim 60\,\%$) have mass $< 0.4\,M_\odot$, while in the 38 stars with RV scatter $> 3\,m\,s^{-1}$, only 6 ($\sim 16\,\%$) have mass $< 0.4\,M_\odot$.

This difference in RV scatter between high- and low-mass M dwarfs could hint at varying manifestations of activity or different dynamo mechanisms. In stars with masses as low as $\sim 0.4 - 0.3\,M_\odot$, magnetic fields are thought to be maintained through an $\alpha\Omega$-dynamo, in which shearing forces in the tachocline, the region between the radiative and the convective zones, seem to play in important role. Stars with lower masses, however, are fully convective and therefore have no tachocline, so a different dynamo mechanism should maintain the magnetic fields observed in them.

Regarding activity detections, we identify signals in almost half (33 of the 70 stars, 47 %) of these low-activity stars. Most of the stars with detections have RV scatter $> 3\,m\,s^{-1}$ (26 of the total of 38 stars, $\sim 70\,\%$). In the group of stars with RV scatter $\leq 3\,m\,s^{-1}$, only 7 of the 32 stars ($\sim 20\,\%$) show reliable detections (J01025+716, J17578+046, J13299+102, J23492+024, J07274+052, J11511+352, and J00183+440). These 7 stars all have a large number of observations, ≥ 110 (5 of them with > 200 observations), while the majority of the rest of stars with std RV $\leq 3\,m\,s^{-1}$ and no detections have been observed significantly less (17 of the other 25 stars, $\sim 70\,\%$, have < 60 observations). All of the 7 stars with detections show clear activity signals in their RVs (except for J17578+046, one of the stars with a planet). For 3 of them (J07274+052, J11511+352, and J13299+102), the only activity signal found is in the RVs.

Overview

In summary, our sample stars with low activity levels ($pEW'(H\alpha) > -0.1$) show RV scatter from ~ 2 to $10\,m\,s^{-1}$, while for active stars, the scatter can reach values one order of magnitude larger. The RV scatter in the active stars increases with the average activity level, and most active stars show clear signals. Nevertheless, we identify activity signals in almost half of the inactive stars, especially in the ones with the largest RV scatters (std RV $> 3\,m\,s^{-1}$).

In both active and inactive stars, the stellar mass shows a gradient with RV jitter. Stars with the lowest RV scatters tend to be those with the lowest masses, and stars with larger scatter correspond to the most massive ones. This relation suggest that there could be different activity manifestations and dynamo processes between M dwarfs with high and low mass. A relevant implication of these results is that, since lower-mass stars (in general, late-type M dwarfs) show the lowest RV jitter, they are better targets

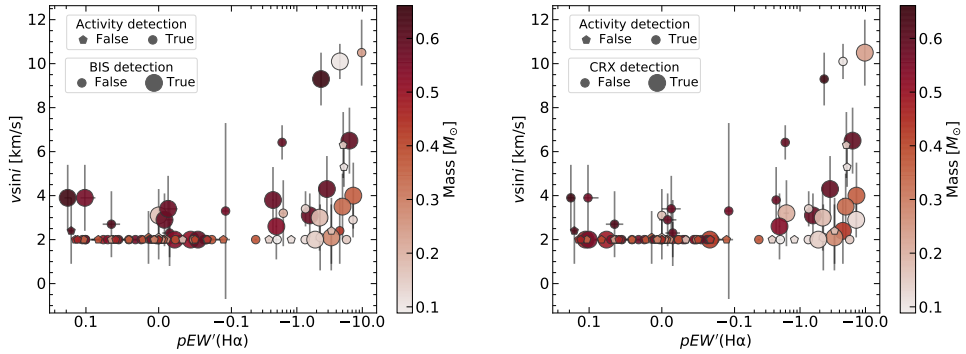

Figure 3.17: *Left*: Rotational velocity ($v \sin i$) as a function of the average activity level ($pEW'(\mathrm{H}\alpha)$) of the 98 stars in the sample, colour-coded with the stellar mass. Stars with activity-related signals (FAP $\leq 10\,\%$) in any of the parameters are shown with dots, and stars with no detections with pentagons. For the stars with detections, large dots indicate a detection (FAP $\leq 10\,\%$) in the BIS. *Right*: Same as the *left panel* but for the CRX instead of the BIS.

for planetary searches than more massive (earlier-type) M dwarfs, independently of their activity level.

3.7.4 $v \sin i$- activity relation and BIS performance

In several works, measurements derived from the CCF bisector have been found to show significant variations related to activity in fast rotating stars, but do not provide significant information in slow rotators (Saar and Donahue, 1997; Bonfils et al., 2007; Desort et al., 2007). In Fig. 3.2 we saw that the $v \sin i$ of the sample stars increases with the average activity level $pEW'(\mathrm{H}\alpha)$ in the high-activity regime. The results presented here show that activity modulation in BIS increases with the average $pEW'(\mathrm{H}\alpha)$ (Fig. 3.9). Given this behaviour of BIS with $pEW'(\mathrm{H}\alpha)$, we then could expect some correspondence between the detections in BIS and $v \sin i$.

Fig. 3.17 (left) shows the $v \sin i$ of the 98 sample stars as a function of the average activity level $pEW'(\mathrm{H}\alpha)$, where we indicate the ones that show an activity signal in any of the parameters, and also the ones with a detection in BIS. About 60 % of the stars with $v \sin i > 2\,\mathrm{km\,s^{-1}}$ and an activity detection in any parameter, show a significant detection in BIS (16 out of 26 stars), while for the slower rotators, this number is of only about 13 % (4 out of 30 stars). This seems to agree with the fact bisector measurements are usually found to be useful in fast rotators, and not in slowly rotating stars.

If instead of BIS we consider the stars with detections in CRX, the other indicator that we find to behave in a similar way as BIS, we obtain similar results (Fig. 3.17 right panel). About 45 % of the stars with $v \sin i > 2\,\mathrm{km\,s^{-1}}$ and detection in at least one of the parameters, show a significant detection in CRX (12 out of 26 stars), and about 16 % of the slowest rotators show a signal (5 out of 30 stars).

If we focus on the low-activity regime ($pEW'(\mathrm{H}\alpha) > -0.1$), most of the stars have very low $v \sin i$, $\leq 2\,\mathrm{km\,s^{-1}}$, but there are ~ 10 stars with larger $v \sin i$ values, up to $\sim 4\,\mathrm{km\,s^{-1}}$. Half of these outliers show significant signals in BIS (although all with low FAP, see Fig. 3.9), but none in the CRX. This could indicate that BIS is more sensitive to activity variations in relatively fast rotating stars than CRX, at least in the low-activity regime.

3.8 Summary

We looked for activity-related periodicities in a sample of 98 M dwarfs observed with CARMENES. We performed a periodogram analysis on the time series of their RVs and nine activity indicators: CCF FWHM, contrast and BIS, the CRX derived from the RVs, the DLW derived from the template matching method used to compute the RVs, and indices measured from four chromospheric lines, Hα and Ca IRT.

Of the initial sample of 98 stars, we find that 56 of them show a signal that we attribute to activity in at least one of the ten parameters analysed. Most of these 56 stars show an activity signal in the RVs. CRX and BIS are the most effective (i.e. they show an activity-related signal) for the most active stars in our sample (stars with $pEW'(\mathrm{H}\alpha) \lesssim -0.1$), and are not effective in the low-activity regime ($pEW'(\mathrm{H}\alpha) \gtrsim -0.1$). Low-activity stars tend to be slow rotators, which agrees with the fact that BIS is usually found to fail in tracing activity in such stars. For the chromospheric lines, we observe the opposite behaviour. Low-activity stars show a larger number of signals in these indicators than the most active ones. However, chromospheric lines are still more effective in the high-activity regime than CRX or BIS on the low-activity one. DLW and FWHM are similarly effective for all the stars, but especially for the high-activity, low-mass (mass $\lesssim 0.4\,\mathrm{M_\odot}$) ones, performing better than any other indicator.

This implies that not all activity indicators can efficiently trace stellar activity for all kinds of stars. Activity in the most active stars tends to be detected in photospheric indicators. CRX and BIS work best for the active, high-mass (mass $\gtrsim 0.4\,\mathrm{M_\odot}$) stars, followed by DLW and FWHM, and chromospheric lines. In active, low-mass stars, the most efficient indicators are DLW and FWHM, followed by CRX and BIS. Chromospheric lines are only effective in a small subset of such stars. Most low-activity stars show activity signals in chromopheric indicators, and about half of them also show signals in DLW and FWHM. CRX and BIS are not good activity tracers in these stars. From these results it is clear that, when assessing the planetary origin of an RV signal, is it key to take into account the adequate activity indicators, depending on the characteristics of the target star. Failing to do so may lead to the detection of false positives.

Stars for which we find no activity detection are located mainly in the low-activity regime, where they account for about half of the sample. In the high-activity regime, stars with no detection are a minority and correspond to faint, low-mass targets. The fact that we are not able to detect any activity signal in these stars could be because these signals are weaker than our measurement precision (in the case of the stars with low activity levels), that, due to complex or changing active region patterns, the signals are not sinusoids, or observational constraints (observations not covering the rotation phase well enough so that a significant peak appears in the periodogram, or low S/Ns).

We also studied the activity of the stars as a function of their RV scatter. As expected, the RV jitter increases with the average activity level of the stars, especially in the high-activity regime, where the RV scatter (std RV) can reach values as high as $\sim 100\,\mathrm{m\,s^{-1}}$. In the low-activity regime, it has values smaller than $\sim 10\,\mathrm{m\,s^{-1}}$. In general, lower RV scatters correspond to stars with no detections. We observe that, both in low- and high-activity regimes, stars with lower RV scatters are the ones with lower mass, which could indicate different activity regime (i.e. dynamo). This also means that late-type M dwarfs could be better candidates for planetary searches than their earlier type siblings.

Overall, this study highlights the fact that, depending on the properties of the star considered, different indicators of stellar activity will behave differently. We find that, in a sample of M dwarfs with a relatively large range of masses and activity levels, each type of indicator performs better (is more effective in tracing activity signals) in specific ranges of mass and activity. Therefore, analyses such as the one presented here can be used as a guide when studying activity signals in spectroscopic observations. Nevertheless, the effectiveness of the indicators depends on several factors, from observational constraints to the specific properties of the stellar active regions, so thorough studies of all the available indicators are desirable.

Chapter 4

Sensitivity to activity of M dwarf spectral lines

4.1 Introduction

The different absorption lines observed in stellar spectra are created by the different components present in the stellar photosphere, which have different sensitivities to temperature, magnetic field strength, and convection velocity. These are parameters affected by photospheric stellar activity features: spots and faculae possess strong magnetic fields that inhibit convective motions and change the temperature in these regions. We therefore expect that changes in these parameters due to stellar activity will affect the profile of different absorption lines in different ways, depending on the sensitivity of the lines to these parameters. Line profile changes affect not only RV measurements used to study exoplanets, but also the determination of stellar parameters and chemical abundances, especially in young, active stars (e.g. Spina et al., 2020).

Usual methods to determine RVs (either by cross-correlation or template-matching schemes) yield a global RV measurement for the full spectrum. This means that these RV measurements average the different asymmetries and shifts experienced by individual lines. Consequently, information related to the different effects of activity on different spectral regions is lost. Some spectroscopic activity indicators are also determined from the entire spectral range of the observations. The cross-correlation function (CCF) full-width-at-half-maximum (FWHM) or bisector asymmetries are measured from a CCF that averages a large number of lines. The chromatic index (CRX) or the differential line width (DLW) also come from a template-matching method that takes into account wide spectral regions at a time. Therefore, as occurs with RVs, the activity information that these indicators contain is also averaged among many absorption lines that may show different activity effects. Other indicators such as the ones measuring the emission from the core of chromospheric lines like the Ca II H&K or

the Hα line, probe activity in the chromosphere, and hence, do not have to be perfectly correlated with the photospheric activity, which is what causes changes in the RVs.

Recently, a number of studies are starting to focus on how line profiles change due to the effects of activity. Davis et al. (2017) used simulations of time-series spectra to study the spectral signatures of spots, faculae, and Doppler shifts induced by planets. By applying a principal component analysis (PCA)[1], they found that the effect of spots and faculae was different on different absorption lines, contrary to what is observed in the case of a planet, for which all the lines are displaced by the same amount. This reflects the fact that absorption lines respond to activity in a non-uniform way.

Several works have found line profile variations correlated with activity indices in HARPS observations (380 – 690 nm, Mayor et al., 2003) in the nearby dwarf α Cen B, a K1 V, a moderately active star that shows a clear activity modulation in its RVs and activity indicators, which led to the false detection of a planet candidate (Dumusque et al., 2012; Rajpaul, Aigrain, and Roberts, 2016). By comparing spectra of high- and low-activity phases of the star, Thompson et al. (2017) were able to identify lines whose profile changes depending on the activity level. The specific morphology of the variations differs on a line-to-line basis, but several lines show depth variations. The pseudo-equivalent widths measured from some of these features are rotationally modulated, and show correlations with the $\log R'_{\rm HK}$ activity index, a robust indicator of activity in early spectral type cool dwarfs. By modelling the observed line profiles, the authors argue that the activity on this star is driven by faculae rather than spots. A similar study made with solar spectra from the HARPS-N solar telescope (Dumusque et al., 2015; Phillips et al., 2016) and images from the Solar Dynamics Observatory (Pesnell, Thompson, and Chamberlin, 2012), further supports this (Thompson et al., 2020). The authors find that profile variations correlate with the $R'_{\rm HK}$ index and faculae-filling factors derived from the SDO images, but the correlation worsens for other chromospheric line indicators such as the Hα.

Wise et al. (2018) also studied line profile variations in HARPS observations of α Cen B and ϵ Eri, a K2 V active star. They found that the depth (or core flux) of about 40 absorption lines is correlated with the S-index derived from the Ca II H&K lines, as well as periodically change with the stellar rotation period. Ning et al. (2019) extended the previous work with an automated method to identify activity-sensitive lines with a Bayesian variable selection method, which accounts for dependencies between lines and uses different activity indicators (S-index, Na I D, Hα, CCF BIS, and FWHM) to trace activity changes in the RVs. Lisogorskyi, Jones, and Feng (2019) used the α Cen B data set to measure equivalent widths and asymmetries and compute their correlation

[1] PCA is a statistical technique that is commonly used to reduce the number of variables or dimensions of a data set with minimal information loss.

with the S-index, finding almost 350 activity-sensitive lines, which include the 40 lines compiled by Wise et al. (2018). Methods such as these could be used to find activity indicators derived from the properties of photospheric absorption lines for stars of other spectral types and for observations at different wavelength ranges.

Instead of studying line profile variations, Dumusque (2018) measured the RV of individual absorption lines present in stellar spectra and correlated them with an activity indicator. As the previous studies, the stars used are early-type cool dwarfs (G1 V to K1 V, including α Cen B) observed with HARPS. In the case of α Cen B, the author used the global RV as the activity indicator, since in principle the RV variation of this star is solely due to activity. Different correlation strengths between the line RVs and the activity indicator are interpreted as the lines having different sensitivities to stellar activity. This work also shows that an accurate selection of the lines used to compute the total RV of a spectrum taking into account the sensitivity of the lines to activity, can result in measurements where the activity signal is mitigated or amplified, depending on the lines selected. Cretignier et al. (2020) continued this work by refining the method used to measure RVs from individual lines and studying the RV relation with the line properties. They show that, in α Cen B, lines with different depths display different effects due to activity; in particular, the RV effect is inversely proportional to the line depth. This agrees with the fact that shallow lines, which are formed deeper in the stellar photosphere, where the convection velocity is larger, are more affected by the inhibition of this convection in the presence of an activity feature, while deep lines, formed in the outer regions of the photosphere, where the convection velocity is lower, show therefore a smaller effect.

All of the aforementioned studies have so far focused on solar-like stars, and did not include M dwarfs. As previously stated, due to their cooler temperatures, M dwarfs display a spectrum with a higher density of features, including atomic lines and molecular bands, where it is difficult to separate individual lines due to blending. Despite that, we know that a method such as the CCF, which uses a mask built from selecting 'individual' lines, is still able to deliver precise RVs, so we expect that it could be possible to study different activity effects on individual lines. Moreover, convective blueshift, which is affected by the presence of active regions, is different in M dwarfs and solar-like stars. Therefore, lines in M dwarf spectra could show different activity-related effects. Inspired by the method proposed in Dumusque (2018), in this chapter we apply a similar approach to CARMENES observations of M dwarfs. In a sample of 6 M dwarfs of early and mid spectral type and different activity levels, we identify and classify lines according to their sensitivity to activity, and use this classification to recompute RVs that are affected by activity to different degrees.

This chapter is structured as follows. In Sect. 4.2, we explain the selection of the

stars that we used. In Sects. 4.3 and 4.4, we present the method followed to determine RVs in individual lines, including our line selection, and how we use those individual line RVs to determine a global RV, respectively. Sect. 4.5 deals with the classification of the lines depending on their sensitivity to activity, and in Sect. 4.6 we make use of this classification to recompute RVs in which the changes induced by activity are removed or enhanced. We compare the lines' sensitivity to activity of the different selected stars in Sect. 4.7. Finally we summarise our findings in Sect. 4.8.

4.2 Targets

We are interested in seeing the effect of activity in individual lines in the spectrum, for different types of stars in the CARMENES sample. Therefore, we select stars of different spectral types and different levels of activity, as measured with their average $pEW'(\mathrm{H}\alpha)$. In Fig. 4.1 we show the mean activity level and the spectral type of a sub-sample of the stars observed with CARMENES. To select the appropriate targets, we considered a set of criteria described next. To be able to properly characterise the individual lines in the spectrum, we limited our targets to bright stars ($\mathrm{J} \leq 9\,\mathrm{mag}$) with low rotational velocity ($v \sin i \leq 7\,\mathrm{km\,s^{-1}}$). We also selected targets for which we had $\gtrsim 20$ observations, which allows us to derive reliable correlations between the RV of the individual lines and the activity indicators. In our early tests, we found that another limiting factor was the RV scatter of the observations. With the method that we used to measure RVs from individual lines, the error on the RV of each line is on average about $300\,\mathrm{m\,s^{-1}}$ for bright targets. If we then average the RV values of about 1000 lines, we have a maximum precision of about $10\,\mathrm{m\,s^{-1}}$ in the RV of each observation. For this reason, we also excluded stars with RV scatter smaller than $15\,\mathrm{m\,s^{-1}}$.

This leaves us with the six targets shown in Table 4.1 (also highlighted in Fig. 4.1). The table shows the main properties of the selected stars together with the number of observations available and their RV scatter. Due to the constrain on the RV scatter, the selected stars have relatively high activity level ($pEW'(\mathrm{H}\alpha) \leq -1.8$, up to $pEW'(\mathrm{H}\alpha) \sim -7$), and only include early and mid spectral types, due to the constraint on the brightness.

4.3 RVs of individual lines

4.3.1 Line selection: CCF mask

We first need to identify and select individual lines in the spectrum. To do that, we made use of the `RACCOON` pipeline that we previously developed to create CCF binary masks (see Chapter 2, Sect. 2.3). As explained before, to select lines, we looked for minima in a `SERVAL` spectral template, characterised them by fitting a Gaussian (as

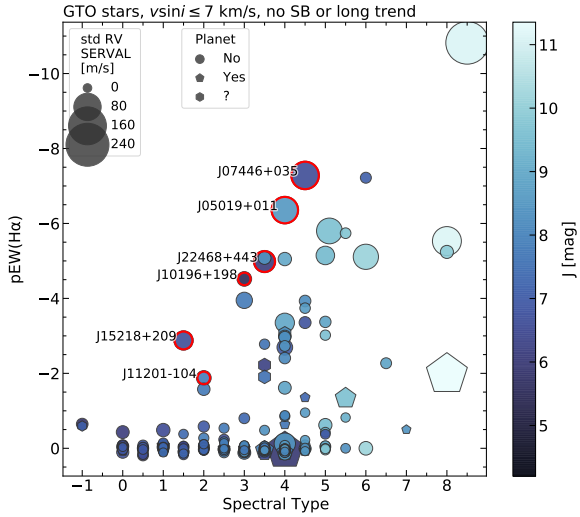

Figure 4.1: Average activity level (measured with the $pEW'(\mathrm{H}\alpha)$) as a function of spectral type of a sub-sample of CARMENES GTO stars. The data points are colour-coded according to the target magnitude in the J band, and their size is given by the SERVAL RV scatter. Stars with no known planetary companions are indicated with dots, while stars with confirmed or candidate planetary companions are indicated with diamonds and squares, respectively. We excluded stars with $v \sin i \geq 7\,\mathrm{km\,s^{-1}}$, known spectroscopic binaries and stars with long term trends that are probably due to high-mass long-period companions. The stars selected for the analysis of this chapter are indicated in red. The $pEW'(\mathrm{H}\alpha)$, spectral type and J magnitude values correspond to the ones in Table 4.1.

in Fig. 2.1), and chose the features with depth, FWHM and contrast between certain cut values. The templates were built with CARMENES survey VIS observations, and the cut values were the same as the ones used for the standard masks (see Table 2.1). We also took into account the position of telluric lines and the varying line position in the CCD due to the barycentric movement of the Earth. In this case, we do not need a binary mask with wavelengths and weights, but are only interested in the wavelengths of the lines, which are given by the minimum of the Gaussian fit.

We used two different line lists, depending on the spectral type of the star. For J15218+209 and J11201-104 (spectral types M1.5 V and M2.0 V, and similar $v \sin i$) we used a line list created from the SERVAL template of J15218+209, with 1712 lines. For the other four stars (spectral types between M3.0 V and M4.5 V, and also similar $v \sin i$), we used a line list obtained from the J07446+035 template, with 2207 lines.

4.3.2 RV computation

Next, for all the available observations of each target, we compute a RV for each of the lines in the line list. There are several ways to do that. To obtain the RV of a specific line l in one of the observed spectra, we could compute its CCF using a single-line mask, or

Table 4.1: Properties of the selected stars. The values are taken from the latest version of the Carmencita database available at the time (version 096). We also show the number CARMENES VIS observations obtained, and their RV scatter, measured as the standard deviation (std) of the corrected `SERVAL` RVs (instrumental drift and nightly average corrected). The stars are sorted with decreasing activity level as measured with their $pEW'(\mathrm{H}\alpha)$.

Karmn	Name	Sp. type[a]	J[b] [mag]	$v \sin i$ [c] [km s^{-1}]	P_{rot} [d]	$pEW'(\mathrm{H}\alpha)$ [e]	$\log(L_{\mathrm{H}\alpha}/L_{\mathrm{bol}})$ [f]	[Fe/H][g]	# obs VIS	std RV [m s^{-1}]
J07446+035	YZ CMi, GJ 285	M4.5 V	6.581 ± 0.024	4.0 ± 1.5	2.78 ± 0.01	-7.281 ± 0.024	-3.6099 ± 0.0014	-	51	88.2
J05019+011	1RXS J050156.7+010845	M4.0 V	8.526 ± 0.026	6.5 ± 1.5	2.12 ± 0.02	-6.356 ± 0.019	-3.5805 ± 0.0013	-0.15 ± 0.16	19	90.3
J22468+443	EV Lac, GJ 873	M3.5 V	6.106 ± 0.030	3.5 ± 1.5	4.38 ± 0.03	-4.983 ± 0.021	-3.6497 ± 0.0018	-0.19 ± 0.16	107	50.2
J10196+198	AD Leo, GJ 388	M3.0 V	5.449 ± 0.027	2.4 ± 1.5	2.2399 ± 0.0006	-4.520 ± 0.040	-3.6140 ± 0.0030	-	26	18.4
J15218+209	OT Ser, GJ 9520	M1.5 V	6.610 ± 0.021	4.3 ± 1.5	3.37 ± 0.01	-2.878 ± 0.018	-3.7657 ± 0.0028	-0.34 ± 0.16	53	36.7
J11201-104	LP 733-099	M2.0 V	7.814 ± 0.026	3.6 ± 1.5	-	-1.877 ± 0.016	-3.9580 ± 0.0040	-0.21 ± 0.16	29	18.3

References. [a] Hawley, Gizis, and Reid (1996), except J05019+011, J10196+198 Alonso-Floriano et al. (2015), J11201-104 Riaz, Gizis, and Harvin (2006). [b] Skrutskie et al. (2006). [c] Reiners et al. (2018b), J10196+198 Kossakowski et al. (in preparation) (computed as in Reiners et al., 2018b). [d] Díez Alonso et al. (2019), except J10196+198 Morin et al. (2008). [e] Schöfer et al. (2019). [f] Schöfer et al. (2019). [g] Schweitzer et al. (2019).

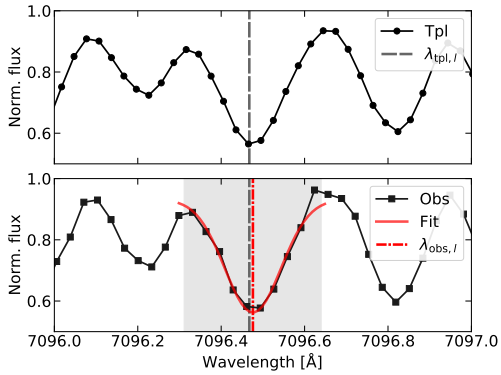

Figure 4.2: RV computation of an individual line. The dashed grey vertical line represents the wavelength of the line l in the line list, as measured in the spectrum template (black dots). The dotted dashed red vertical line represents the wavelength of the line l measured in an observation (black squares) with a Gaussian fit to the line (solid red line). The shaded grey region marks the data points considered in the Gaussian fit to the spectrum.

apply a template matching algorithm using only a small predefined region around the line. We opted for a more straightforward method. First, we obtained the position of the line l in the observed spectrum, $\lambda_{\mathrm{obs},l}$, by fitting a Gaussian to the region around the line in the observed data (similarly to the process of line characterisation when building CCF masks, Sect. 2.3). The line position is given by the minimum of the best fit. Then, we computed the RV of the line as the Doppler shift between the position of the line in the observation, $\lambda_{\mathrm{obs},l}$, and the position of the line in the line list, $\lambda_{\mathrm{tpl},l}$ (i.e. as measured in the template also from a Gaussian fit)

$$\mathrm{RV}_l = c\left(1 - \frac{\lambda_{\mathrm{tpl},l}}{\lambda_{\mathrm{obs},l}}\right), \tag{4.1}$$

where c is the speed of light. We illustrate that in Fig. 4.2. To estimate the uncertainty on the individual RV measurements, we used the formal error of the Gaussian fit. Although we are fitting lines that are not completely Gaussian-shaped, this error gives us an idea of the goodness of the fit for the different lines, which reflects the S/N of the different regions of the observed spectra.

Before performing the fit, to correctly identify the location of the line l in the observed spectrum, we had to correct it for the barycentric Earth RV (BERV), secular acceleration, and instrumental drifts of the observation, as measured by the standard CARMENES pipelines. The spectral region used in the Gaussian fit is constrained by the adjacent local maxima at each side of the line minimum, as measured in the `SERVAL` template (shaded grey area in 4.2). In this way, we made sure to always use the same region around each line. This may not happen if, instead, we measured the maxima in each different observation, because their position could change depending on the S/N, activity effects or tellurics which we may have not considered. For J11201-104, we used the line limits obtained from the template of J15218+209, instead of using its own

template, which did not have a high S/N because the star is faint ($J > 7$ mag) and we did not have a large number of observations available. J05019+011 is one of the faintest stars in our sub-sample ($J > 8$ mag) and has only 19 observations, therefore we also tried to use the line limits from the template of another star, in this case J07446+035. However, for this star, we obtained better results using the line limits obtained from the template of J05019+011 itself, which could be due to the fact that this star has a slightly larger $v \sin i$ than J07446+035.

During the creation of the line list (Sect. 4.3.1), we already took into account the regions contaminated by tellurics affecting the template. However, depending on the absolute RV of the target star and the BERV correction of the target observations, regions different than the ones in the template can be affected by tellurics. Therefore, before computing the RVs, we further removed the affected lines following the steps described in Sect. 2.3.2. In summary, we broadened the features of a telluric mask by the maximum BERV of the observations, and removed from the line list those overlapping, taking into account the absolute RV of the target star.

Since we are using observations of an echelle spectrograph, the observed spectrum is divided into different orders. In some cases, there is an overlap between consecutive orders. For the lines in these overlap regions, we only used the data corresponding to the bluer order of the overlap (that is, the redder part of the order), because in general, we found that the redder part of most of the orders has better S/N than the bluer part.

As an example, in Fig. 4.3 we show, for each line, the scatter of the RVs of all the observations of J07446+035, measured as the weighted standard deviation of the RVs of each epoch. We also show the median RV error of each line. We see that most lines show a scatter close to 300 m s^{-1}, and the typical error in the individual line RV (derived from the Gaussian fit) is also of about 300 m s^{-1}. The lines located at the bluer region of the spectral range, with wavelengths shorter than ~ 6400 Å, are the ones that show a larger RV scatter and error. This happens because the bluer part of the spectral range is where the CARMENES observations have lower S/N, which makes it difficult to correctly identify the lines and measure their RV. We obtain similar values, about $300 - 400$ m s^{-1} for the rest of stars.

4.4 Total RV from the average of individual line RVs

We can compute the average of the RVs of all the individual lines and compare it to the RVs obtained by standard methods that consider all the lines simultaneously, such as the CCF or template matching schemes. In the following, we will refer to the method of computing the total RV by averaging the individual line RVs as the lines average

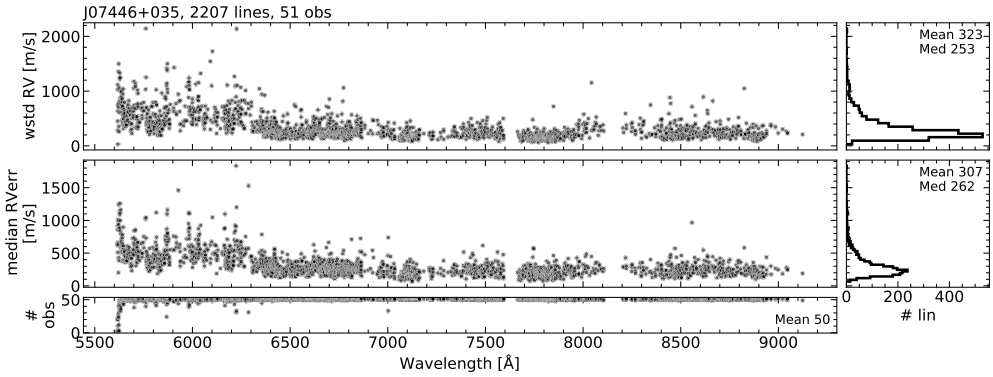

Figure 4.3: RV scatter, median RV error and number of observations used, as a function of the individual line wavelength, for J07446+035.

(LAV) method. Before computing their mean, we discarded some data points. We did not use data points corresponding to bad Gaussian fits to the spectra, which we identified as those with RV errors larger than 1000 m s^{-1} and smaller than 20 m s^{-1}. After removing these data points, we performed a 4 sigma clipping on the RVs of all the lines to discard outliers, in each observation separately. Finally, we discarded lines that did not have a reliable RV measurement in more than 10 observations. This process mainly removed lines in the bluer part of the spectrum, where the S/N is the lower, and weak lines, which can be properly identified and characterised in a co-added spectrum template like the one produced by `SERVAL`, but not in single observations that have much lower S/Ns.

In Figs. 4.4 to 4.9, we show the average RV of all the lines compared to the RV obtained with the CCF method and `SERVAL`, for the active targets under analysis. The masks used to compute the CCFs were the same as the ones used to define the individual line lists. That is, masks created from `SERVAL` templates of J15218+209 (used in the CCF of J15218+209 and J11201-104) and J07446+035 (used in the CCF of J07446+035, J05019+011, J22468+443, and J10196+198). The `SERVAL` RVs of each target are computed using a template made by co-adding the observations of the target itself. We obtain similar RV values for the three different methods (LAV, CCF, and `SERVAL`), but the LAV RVs are in general more similar to the CCF RVs than to the ones obtained with `SERVAL`. This is probably due to the fact that the line list used to compute the individual line RVs is obtained from the mask used in the CCF method, while `SERVAL` considers the entire wavelength domain, not just a set of lines.

There are some observations for which the difference between the average of the individual line RVs and the other two data sets (i.e. CCF and SERVAL RVs) is significantly larger than the rest. These observations are the ones with lower S/N of all the time series. We can observe this difference of S/N in the RV errors of the three data sets, which are significantly larger for these observations, and also, in the number of

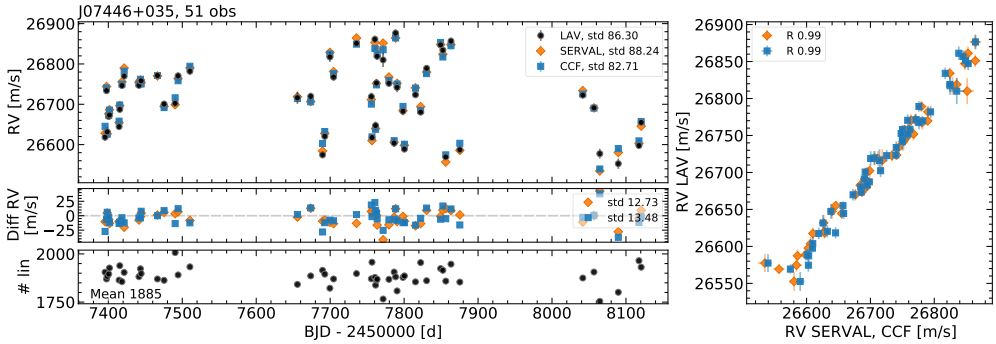

Figure 4.4: *Top left*: RV time series of J07446+035 computed with the average of all the individual line RVs (LAV, black dots), `SERVAL` (orange diamonds), and CCF (blue squares). *Middle left*: Difference between the LAV and the `SERVAL` (orange diamonds) and CCF (blue squares) RVs. *Bottom left*: Number of lines used per observation. *Right*: Correlation between the LAV and the `SERVAL` (orange diamonds) and CCF (blue squares) RVs.

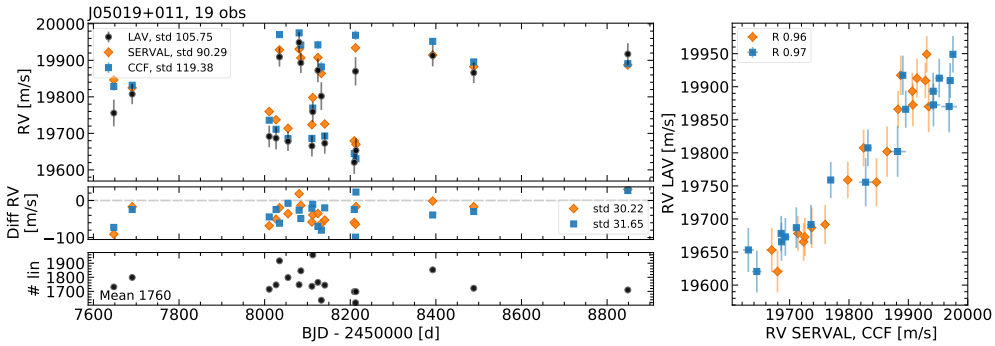

Figure 4.5: Same as 4.4 but for J05019+011.

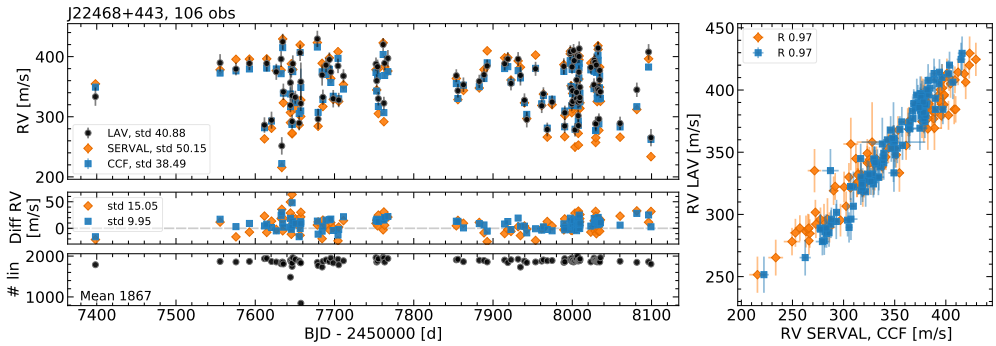

Figure 4.6: Same as 4.4 but for J22468+443.

lines used to compute the average RV, which is significantly lower than for the rest of epochs. This decrease in the number of lines is related to the lower S/N of these observations, which makes it difficult to correctly identify the lines in the observed spectrum and obtain a reliable Gaussian fit of the line. This seems to indicate that computing total RVs by averaging the RVs of individual lines (as computed here) is

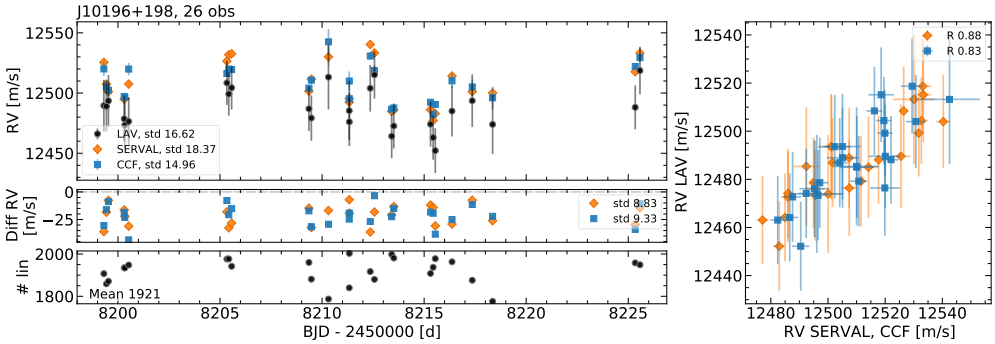

Figure 4.7: Same as 4.4 but for J10196+198.

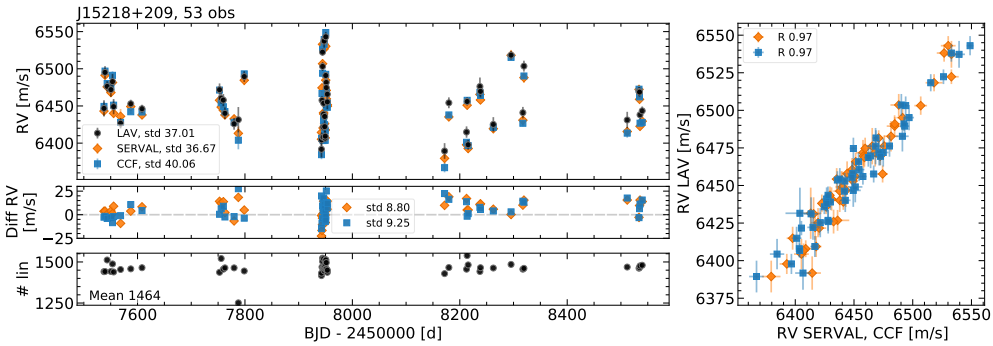

Figure 4.8: Same as 4.4 but for J15218+209.

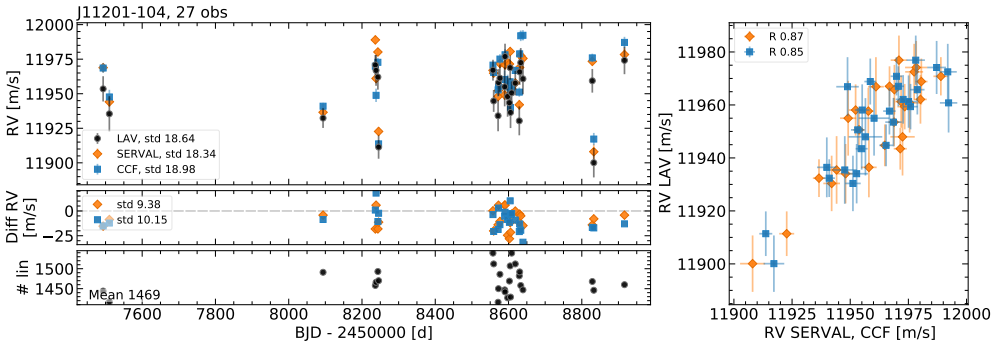

Figure 4.9: Same as 4.4 but for J11201-104.

more sensitive to the S/N of the data than the other two methods. Also, this method needs observations with higher S/N than the other two in order to obtain reliable RVs. In the following analysis, we did not consider these observations with low S/N (specifically, we discarded observations with S/N < 25 to 50 in the CARMENES VIS reference order 36, depending on the average S/N of the different stars).

We also discarded observations with strong flares. Flares add continuum flux over the whole spectrum range, and can be easily identified by an increase in the Hα core emission flux. This change in flux has a strong effect on RVs, introducing drifts of

several hundred m s^{-1} (see e.g. Reiners, 2009). Aside from larger than average $I_{H\alpha}$ or $pEW'(H\alpha)$ values, observations during flares also affect the other activity indicators, which show extreme values in their time series, or clear outliers. Therefore, to avoid RV biases due to strong flares when computing the correlations with the activity indicators, we discarded observations with strong Hα emission by performing a 3 sigma clipping on the $I_{H\alpha}$. We observed that the CCF contrast and the DLW show clear outliers corresponding to strong flare events, but that do not have an $I_{H\alpha}$ large enough to be removed by the sigma clipping procedure. Therefore, we also performed a 3 sigma clipping on the DLW time series.

4.5 Activity effect on individual lines

4.5.1 Correlation between line RV and activity indicators

A way to study how stellar activity affects different lines is to check for correlations between the RV of each individual line and an activity indicator. Strong correlations would indicate that a certain line is highly affected by activity, while no correlation could mean that the line is not very sensitive to activity effects.

We checked the linear correlation between the RVs of the individual lines and several activity indicators: CCF FWHM, contrast, and BIS, and CRX, DLW and $I_{H\alpha}$ computed by `SERVAL`. To quantify the correlations, we computed the Pearson's correlation coefficient, R. A value of R close to 1 indicates a strong linear correlation (or -1, a strong anti-correlation), and R close to 0 indicates no correlation. In Fig. 4.10 we show, as an example, the time series and correlations of two different lines of J07446+035: an 'active' line that shows strong correlations with several activity indicators, $\lambda_{tpl,l} = 6661.25$ Å, and an 'inactive' line, for which we do not observe any clear correlation, $\lambda_{tpl,l} = 7855.92$ Å.

BIS and CRX are known to show clear anti-correlations with the total RV of the spectrum, if it is affected by activity. We also observe a strong anti-correlation with the individual RVs of several lines, such as the example line $\lambda_{tpl,l} = 6661.25$ Å shown here. For the other indicators, we observe some loop-like shapes following the phase of the stellar rotation modulation, as happens with the total RV, but not a clear linear positive or negative correlation. For these indicators, other types of correlations should be investigated.

Aside from activity indicators, we also computed the correlation with the total RV obtained from the CCF (also in Fig. 4.10). In very active stars, where the modulations observed in the total RV are clearly caused by activity, the total RV itself can also be considered an activity indicator. This seems to be the case for the targets under study (but see Sect. 4.6.4 about J10196+198), and, as expected, we see a clear correlation

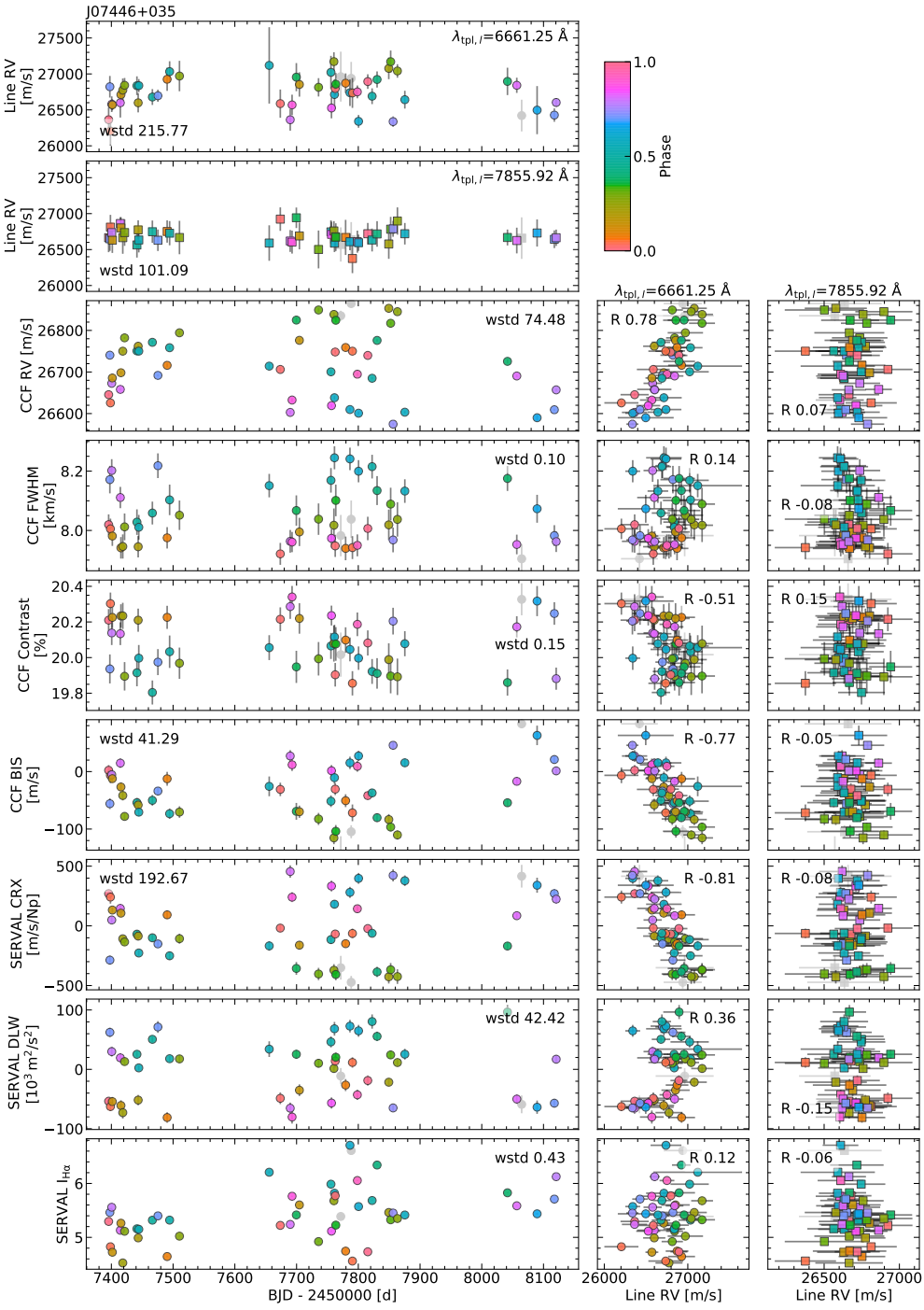

Figure 4.10: Time series RV of an 'active' ($\lambda_{tpl,l} = 6661.25$ Å, *top left*, dots) and 'inactive' ($\lambda_{tpl,l} = 7855.92$ Å, *top left*, squares) line for J07446+035. The panels *below* show the time series of the CCF RV, FWHM, contrast, and BIS, and the CRX, DLW, and $I_{H\alpha}$ computed by `SERVAL` (*left*), together with their correlation with the RV of the individual line (*middle* and *right*). The time series panels show the scatter of the data, computed as their weighted standard deviation (wstd). The correlation panels show the Pearson's correlation coefficient (R). All data points are colour-coded with the stellar rotation phase. Observations removed as explained in Sect. 4.4 are marked in grey.

in the case of several lines. However, if the total RV modulation is not only due to activity, but also to orbiting companions, using RV to find correlations will not be a good choice.

4.5.2 Correlation difference between activity indicators

In the following, we will focus the analysis on the three indicators that show a simple linear correlation with the individual line RVs: total CCF RV, CCF BIS, and SERVAL's CRX. To see if the correlation strength of different lines is consistent within these three activity indicators, we compared the R values obtained for the correlation between the line RVs and the indicators. We plot this comparison in Fig. 4.11 for the six stars studied. We see that for J07446+035, J05019+011, and J22468+443 (the stars with the largest average $pEW'(\mathrm{H}\alpha)$ and largest RV dispersion), the three indicators show similar R distributions and similar values for all the lines, i.e., lines with a strong correlation with CCF RV also show a strong correlation (anti-correlation in these cases) with BIS and CRX. The distribution of R values is not centered at 0, but is displaced towards R $\sim$ 0.2 to 0.3 for the correlation with the total RV (and R ~ -0.2 to -0.3 for BIS and CRX, respectively). Some lines show correlations with R as large as 0.8 for RV (and -0.8 for BIS and CRX).

J10196+198 shows less well-defined correspondence between the R values of the three indicators (i.e. the data points in Fig. 4.11 show a larger spread than in the three previously-discussed stars). This means that the three activity indicators result in correlations of different strength (i.e. different R) for the same line. More lines show R values closer to 0 (the distribution is centered at R $\sim$ 0.1 for RV, and ~ -0.1 to 0.0 for CRX and BIS), with no lines showing very strong correlations (the R values never reach $\sim$ 0.8 for the correlation with RV, or -0.8 for BIS and CRX). By looking at the characteristics of this star, we would expect a similar behaviour as J22468+443, because they have similar spectral types and activity levels ($pEW'(\mathrm{H}\alpha) \sim -4.5$ for J10196+198 and ~ -4.9 for J22468+443). However, the RV scatter is significantly lower for J10196+198 (std RV $= 18\,\mathrm{m\,s^{-1}}$, as opposed to $50\,\mathrm{m\,s^{-1}}$ for J22468+443).

For the earlier type stars, J15218+209 and J11201-104, the three activity indicators also show slightly different correlations for the same line (as in J10196+198, the data points show a relatively large spread). For J15218+209, the most active of the two ($pEW'(\mathrm{H}\alpha) \sim -2.9$, as opposed to -1.9 for J11201-104) and the one with the largest RV scatter (stdRV $= 37\,\mathrm{m\,s^{-1}}$, while J11201-104 shows $18\,\mathrm{m\,s^{-1}}$), the distribution of R values is more displaced towards 'active' values than for J11201-104. That is, the distribution of R is centered at 0.2 for the correlation with RV, and at 0.1 for BIS and CRX. In the case of J11201-104, the distributions are more similar to those of J10196+198, i.e., centered at 0.

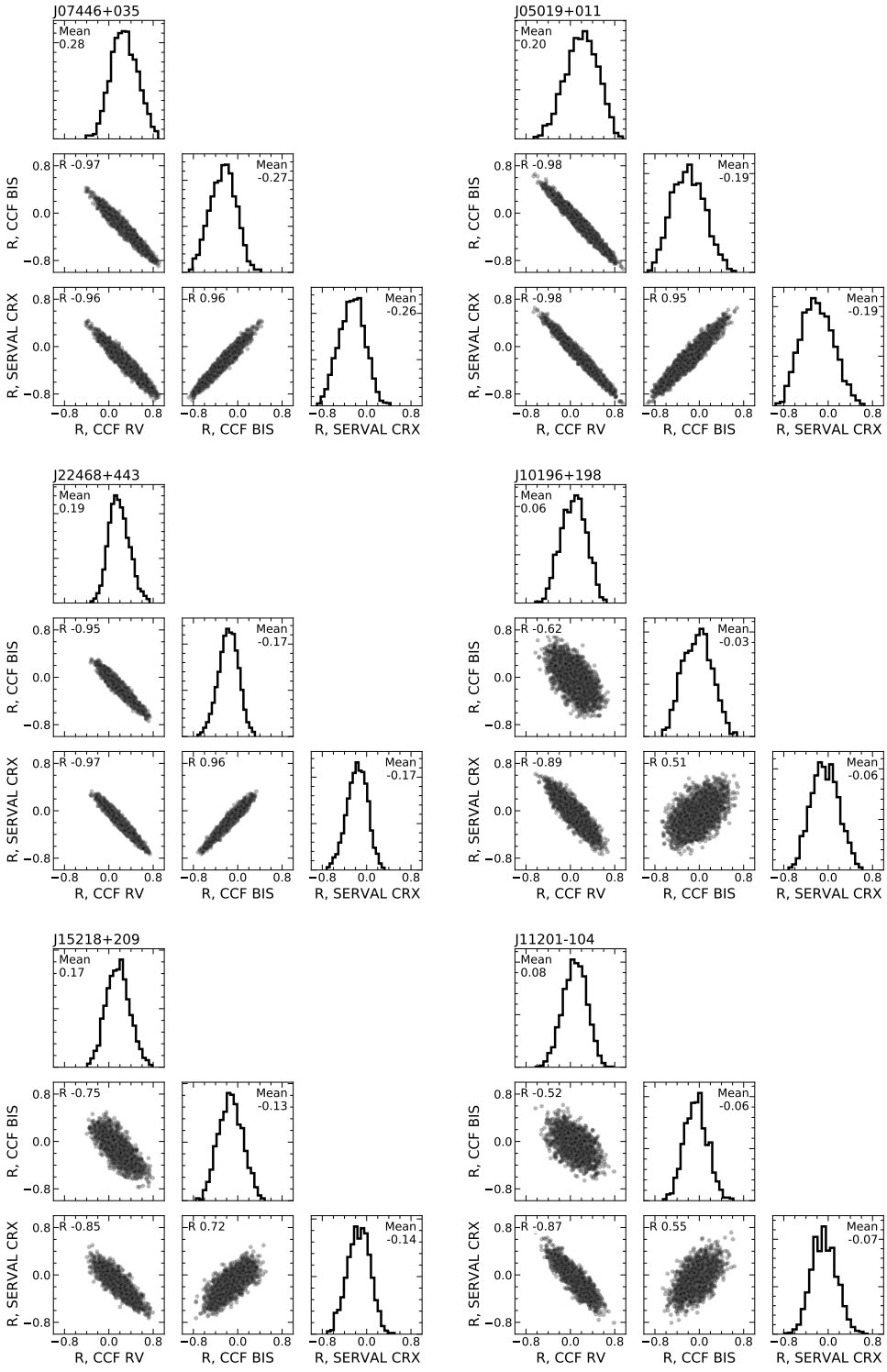

Figure 4.11: Comparison of the R values obtained for the correlation between the line RVs and CCF RV, BIS, and CRX, for J07446+035 (*top left*), J05019+011 (*top right*), J22468+443 (*middle left*), J10196+198 (*middle right*), J15218+209 (*bottom left*), and J11201-104 (*bottom right*). The histogram panels show the mean value of the distribution.

Overall, for the six objects studied here, we observe that the stars with the largest total RV scatter are the ones that show the strongest correlation between the individual line RVs and the activity indicators (i.e. largest values of R). The strength of these correlations seems to be more affected by the total RV scatter of the star than by its average activity level. Moreover, for the stars with the largest RV scatter, the correlation strength of the different lines is similar regardless of the activity indicator used to compute the correlation (CCF RV, BIS or CRX). This dependency on the RV scatter may be due to a bias in the way the correlations are computed. Larger spread in the RV and activity indicator values will result in better defined correlations, if we consider equivalent error bars.

4.5.3 Correlation strength as a function of the line wavelength

Next, we study the distribution of R values as a function of the line wavelength. In Fig. 4.12, we show the distribution of R values of all the lines obtained from the correlations with the three selected indicators (CCF RV, BIS, and CRX) as a function of the line wavelength, for J07446+035. In the same figure, we also show the correlation of the R values with the RV scatter of each line, measured as the weighted standard deviation of the RV of the line in all the observations (wstd RV, as in Fig. 4.3). We see that the distribution of R values is not constant in wavelength. For the three indicators, there are lines with R close to 0 throughout the whole wavelength range, except at $\lambda \sim 6900$ to 7300 Å. The largest value of R increases from short to long wavelengths, peaking for the lines at $\lambda \sim 7000$ to 8000 Å.

Regarding the RV scatter of each line, we see that the lines that show larger scatter are in general located at the bluer part of the wavelength range, where the spectrum has lower S/N. Then, the RV of these lines has larger error bars and is not as precise. All these lines with large RV scatter tend to have correlation strengths of $R \sim 0$. Therefore, due to this lack of correlation with the indicators, the scatter in these lines does not seem to be caused by activity, but rather is an indication of lower RV precision. Also, the R values close to zero do not imply that these lines are not sensitive to activity, but they also indicate the lack of precision in their RV measurement. In conclusion, the R coefficient is biased when the errors of the line RV are large. Fig. 4.12 only shows data of J07446+035, but we observe a similar behaviour for the other five stars.

4.5.4 Active and inactive line selection

The strength of the correlation with the activity indicator allow us to classify the different lines depending on their sensitivity to activity. We have selected several sets of inactive and active lines depending on their R value. We consider as inactive, lines with R values around 0, $|R| \leq R_{cut}$, for several R_{cut} from 0.05 to 0.4. For the active

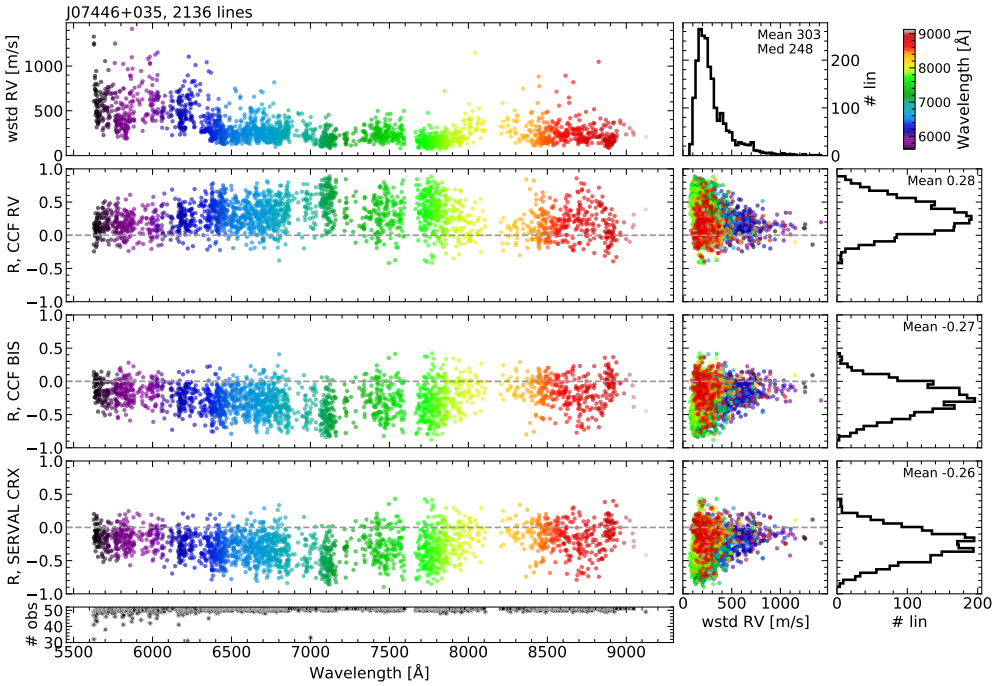

Figure 4.12: RV scatter of each line (computed as the weighted standard deviation of the line RV of all the observations, wstd RV), and Pearson's correlation coefficient R as a function of the wavelength, for the correlation with CCF RV, BIS, and CRX (*top* to *bottom left panels*). All the data points are colour-coded with the wavelength. The *middle panels* show the correlation between the corresponding R and the wstd RV. The histograms on the *right* show the distribution of R. The *top middle* histogram shows the distribution of wstd RV. The *bottom left panel* shows the number of observations used per line.

lines, we selected lines with extreme R values. In the case of the correlation with the total RV, we selected lines with R close to 1, $R > \mathrm{R_{cut}}$, for several positive $\mathrm{R_{cut}}$. For the correlations with BIS and CRX, we expect an anti-correlation if there is a modulation due to activity, so we selected lines with $R < \mathrm{R_{cut}}$, for several negative $\mathrm{R_{cut}}$.

We also selected lines based on their RV scatter. As mentioned above, lines with the largest dispersions have an R close to 0 (Fig. 4.12), probably due to the fact that they do not contain enough RV information to have a precise measurement, and not because they are actually less sensitive to activity. Therefore, in the case of the selection of inactive lines, we also performed some cuts discarding lines with the largest RV scatter (wstd RV).

4.6 Total RV recomputation with selected lines

We used the different sets of selected active and inactive lines to recompute the total RV of each observation. As before, we used the LAV method. In the following, we show the results obtained for the six targets studied. We analyse the change in the

time series RV scatter obtained using different sets of lines, as well as the change of the activity-related signals present in the periodogram of the RVs.

4.6.1 J07446+035 (YZ CMi, GJ 285)

J07446+035 is a mid-type M dwarf and one of the most active stars in our sample. It shows a large RV scatter, of almost 90 m s^{-1}, due to stellar activity. Global RVs and both CRX and BIS show modulations at the stellar rotation period, and these two activity indicators show linear correlations with the RVs (see previous chapter, Fig. 3.4). As mentioned above, for this star we used an initial line list derived from a template of observations of J07446+035 itself, with $\sim$ 2000 lines.

Inactive lines

Fig. 4.13 shows a summary of the time series LAV RV scatter obtained for the different sets of inactive lines tested. As explained above (Sect. 4.5.4), we selected lines based on the strength of the correlation with an activity indicator (R around 0) and on the RV scatter of each line (small wstd RV). The values in the x- and y-axis of the plots indicate the cut values on |R| and wstd RV, respectively, for each set of lines. Then, each data point corresponds to one set of lines, and their colour indicates the RV scatter obtained using the lines in each set. Each panel corresponds to the results obtained using the correlation (R) with one of the three activity indicators considered: total RV, BIS, and CRX.

We observe that, as we decrease the range of the R values of the averaged lines towards zero, and remove lines with large RV dispersions (wstd RV), the scatter of the total RV time series decreases. For the three indicators, the smallest RV scatter occurs when the RVs are computed using lines with $|R| \leq 0.1 - 0.2$ and wstd RV $\lesssim 200$ m s^{-1}, but the scatter is not minimised exactly for the same cuts. For the correlation with the total RV, the scatter becomes $\sim$ 5 times smaller than the initial one, and for the correlation with BIS and CRX, $\sim$ 4 times smaller. This decrease occurs up to a specific point. After that, if we further decrease the maximum |R| and wstd RV of the selected lines, the scatter starts to increase.

To further analyse the recomputed RVs and their modulations, we computed the periodogram of the different RV data sets. Fig. 4.14 shows the LAV RV time series, the number of lines used, and the periodograms obtained for four sets of lines selected using the correlation with the total RV. The different RV data sets shown (top left panel) correspond to the ones obtained with lines having wstd RV $\lesssim 200$ m s^{-1} and four different maximum values of |R|, 0.4, 0.2, 0.1, and 0.05, which include some of the data sets with the smallest time series RV scatter. For comparison, we also show the original RV obtained using all the lines. The panels below show the number of lines averaged to compute each RV data set, for each observation. The histogram on the

right panel shows the distribution of R values, where the coloured regions indicate the different line sets. The bottom panels show the periodograms of the RV data sets of the top panel, with a zoom in on the region around the stellar rotation period. Figs. 4.15 and 4.16 show the same kind of plots but using the correlation with BIS and CRX, respectively. As expected, since for J07446+035 all three indicators show very similar R values for the same lines (as seen in Fig. 4.11), we observe a similar behaviour for the lines selected based on the correlations with the three indicators.

Inspection of these figures shows that, as the RV scatter decreases when restricting the lines used, the power of the periodogram peak at $P_{\rm rot}$ is also reduced. This seems to indicate that, by rejecting lines with large $|\mathrm{R}|$, we are effectively reducing the activity signal present in the RV measurements. If all the lines were equally affected by activity, we would expect the RV scatter to become larger as we restrict the R of the averaged lines. This is because, as we decrease the range of allowed R values, we are decreasing the number of lines used, and hence, we are degrading the precision of the RV measurement. Despite that, since the RV scatter decreases as we reduce the number of lines used, it seems that, for this star, reducing the red noise caused by activity has a larger effect than the increase in white photon noise due to the reduction in RV content, as also found by Dumusque (2018) for α Cen B. We note that some of the smallest RV scatters are obtained using data sets with only ~ 50 lines, less than 3% of the original ~ 2000. With more restrictive cuts, the RV scatter starts to increase. This probably occurs because the number of lines is too small to obtain sufficient precision in the RV measurements, and hence the photon noise dominates. For these sets of lines, the periodogram peak at $P_{\rm rot}$ also becomes less significant, and the highest peak in the periodogram is not related to $P_{\rm rot}$ any more. This could reflect the fact that the RVs of the data sets with the smallest number of lines mostly contain noise.

Active lines

In Figs. 4.17, 4.18, and 4.19 we show the LAV RV time series, number of lines, and periodograms of three sets of active lines, selected using the correlations with the total RV, BIS, and CRX, respectively. The scatter increases significantly as we restrict the minimum value of R towards 1 for the correlation with the total RV, or towards -1 in the case of BIS and CRX, becoming more than 2 times larger for the most extreme sets. This increase could be due to the fact that we are only using the most active lines, but also to an increase in the photon noise, because we are reducing the number of lines used. In all cases, the periodogram shows the highest peak at the stellar rotation period, with similar power. We note that for $\mathrm{R_{cut}} = 0.8$, using 10 to 20 lines (0.5 to less than 1 % of the initial set of lines), depending on the activity indicator, the periodogram still clearly displays a signal due to the stellar rotation, very similar to the periodogram obtained using the ~ 2000 initial lines.

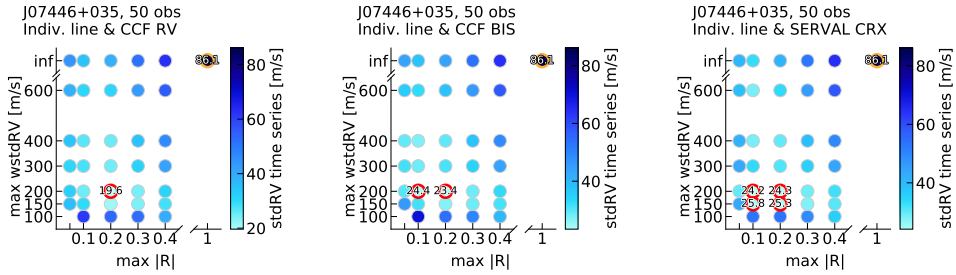

Figure 4.13: LAV RV time series scatter of several sets of inactive lines for J07446+035. The different line sets are selected by limiting the line RV scatter (wstdRV, y-axis) and the strenght of the correlation between the line RV and an activity indicator (Pearson's correlation coeffient R, x-axis). Each data point corresponds to a different set of selected lines. The colour of the data points indicates the scatter of the average RV time series obtained for each line set. We show the results obtained using the correlation with three activity indicators: total RV of the spectrum (*left*), BIS (*middle*), and CRX (*right*). The data points highlighted in red indicate the data sets with the samllest RV time series scatter (values within 10% of the absolute minimum). The data point highlighted in orange indicates the initial data set that uses all lines to compute the RV.

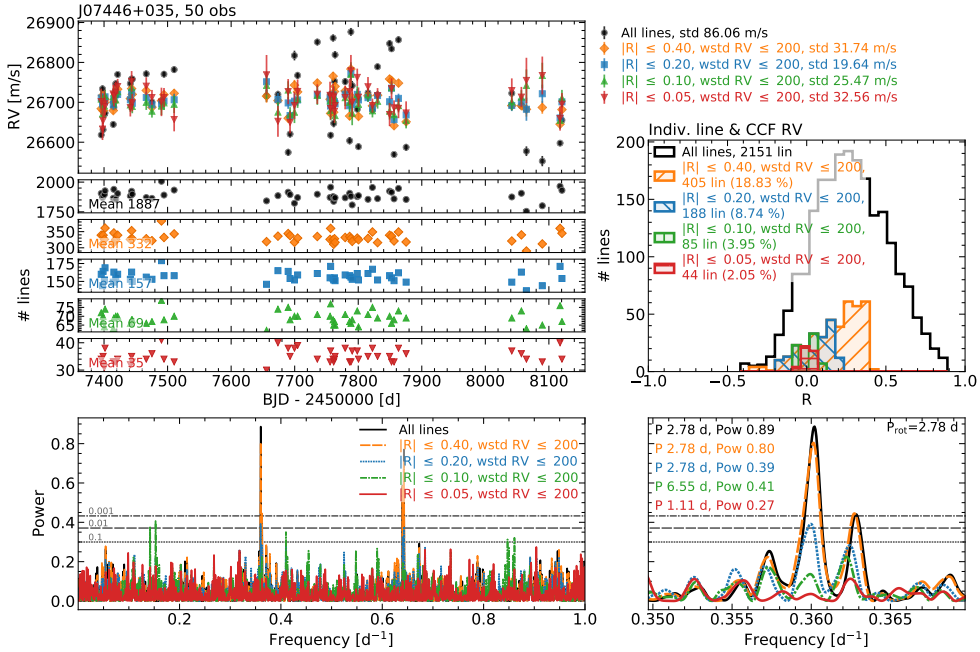

Figure 4.14: *Top left*: LAV RV time series obtained using RVs of selected inactive individual lines (colour), together with the LAV RV time series obtained using all the lines (black). The lines are selected based on the correlation of their RVs with the total spectrum RV, and their RV scatter. *Middle left*: Number of lines used to compute the average RV in each observation, for the different selection of lines used in the *top left panel*. *Top right*: Distribution of the Pearson's correlation coefficient R from the correlation between the individual line RVs and the total spectrum RV. The regions in color indicate the different selection of lines used to compute the RVs of the *top left panel*. *Bottom left*: Periodograms of the RV data sets plotted on the *top left panel*. The horizontal lines correspond to the 0.1, 0.01, and 0.001 FAP levels. *Bottom right*: Zoom in of the periodogram region around the peak corresponding to the rotation period of the star. The text indicates the period and power of the highest peak of each periodogram.

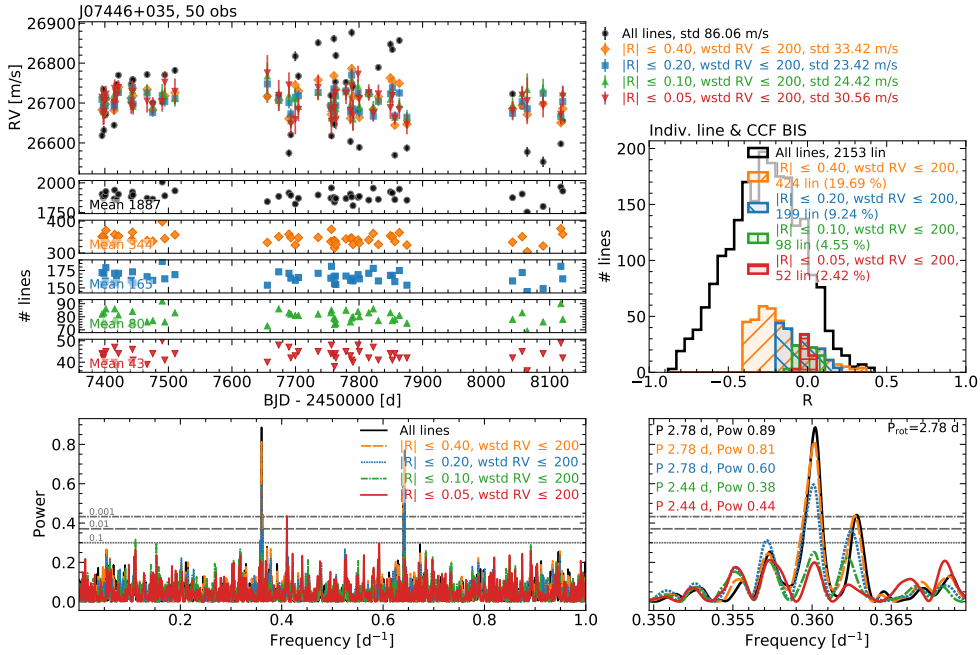

Figure 4.15: Same as Fig. 4.14 but using R values from the correlation between the individual line RVs and CCF BIS.

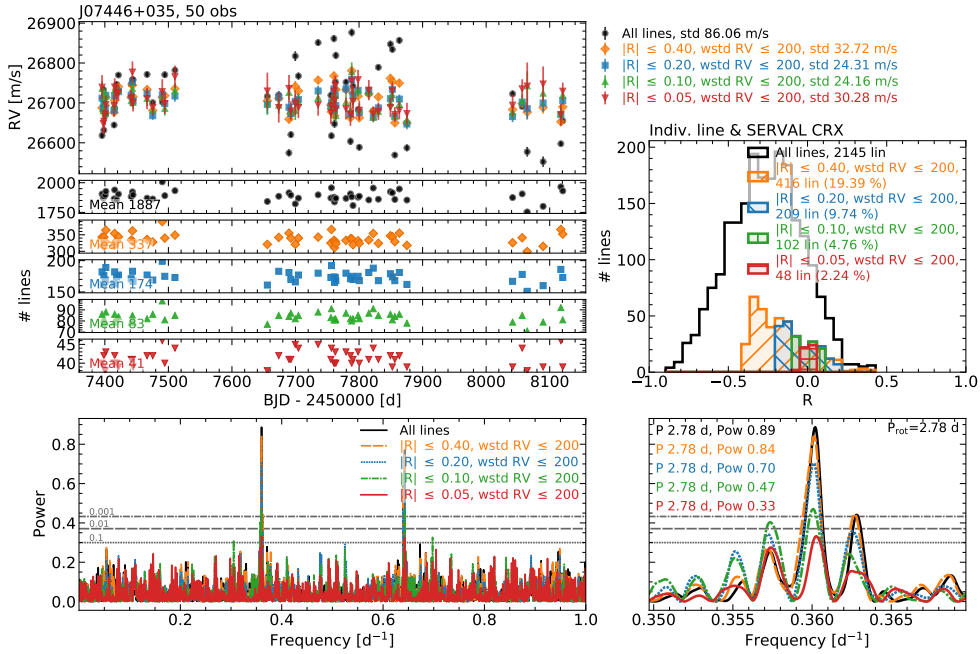

Figure 4.16: Same as Fig. 4.14 but using R values from the correlation between the individual line RVs and CRX.

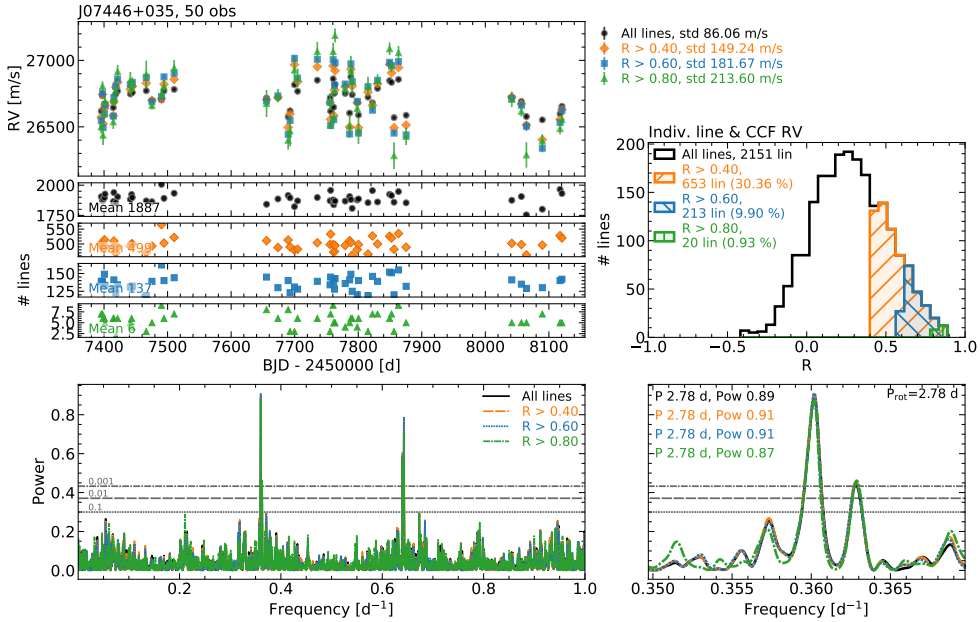

Figure 4.17: Same as Fig. 4.14 but for three sets of active lines.

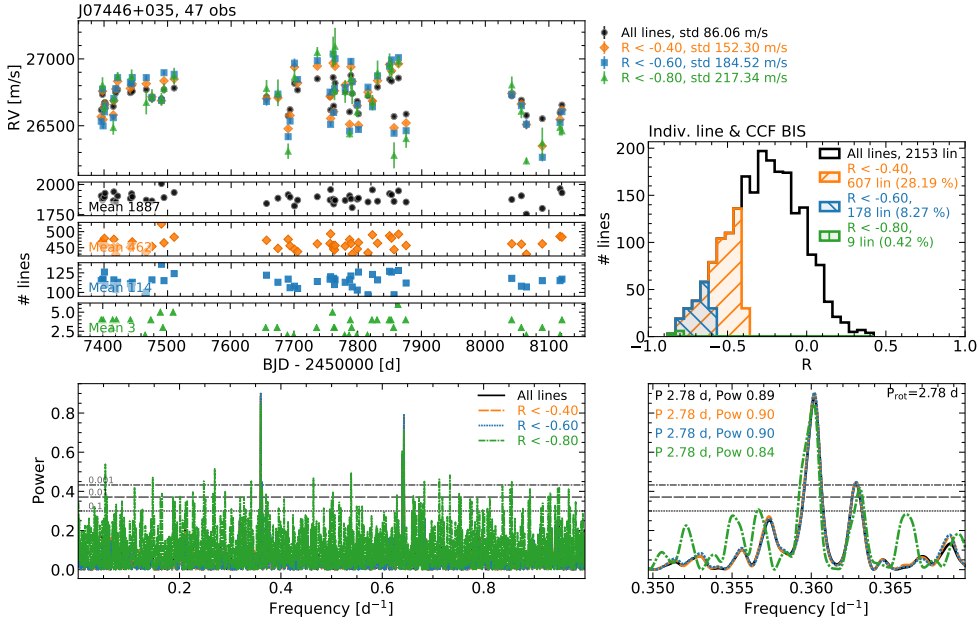

Figure 4.18: Same as Fig. 4.17 but using R values from the correlation between the individual line RVs and CCF BIS.

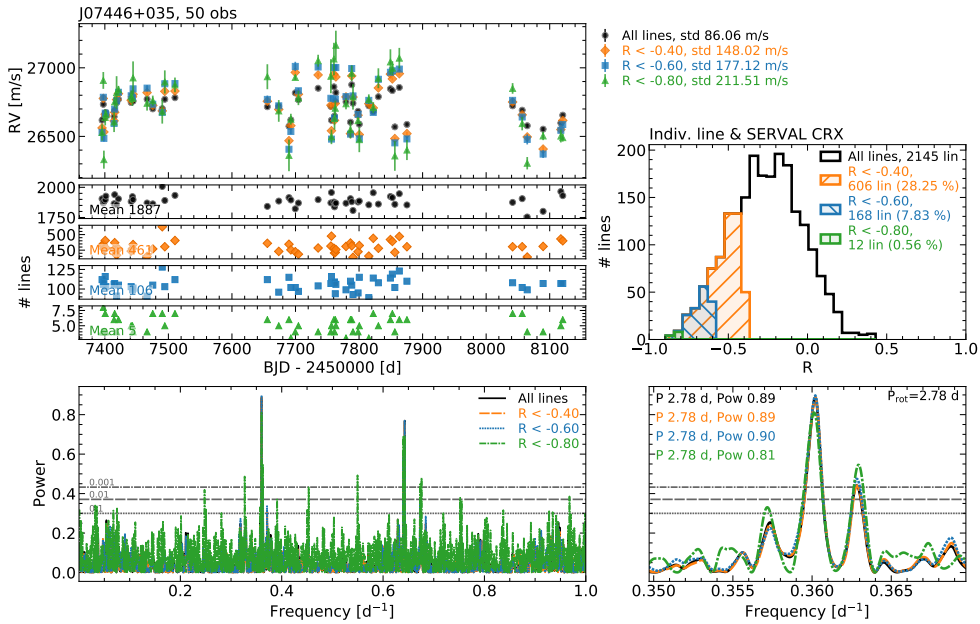

Figure 4.19: Same as Fig. 4.17 but using R values from the correlation between the individual line RVs and CRX.

4.6.2 J05019+011 (1RXS J050156.7+010845)

J05019+011 is also a very active mid M dwarf that shows an initial RV scatter of about 90 m s^{-1} from the SERVAL RVs. The LAV method results in a larger scatter, close to 106 m s^{-1}. We only have 19 observations for this target, but from the activity indicator analysis of the previous chapter we see that, as happens with J07446+035, the global RVs, BIS, and CRX show a significant modulation at the stellar rotation period, and the activity indicators and the RVs are linearly correlated. For this star we also used the line list built from the J07446+035 template.

Inactive lines

As we did for J07446+035, Fig. 4.20 shows the RV scatter obtained for the different sets of inactive lines considered. Figs. 4.21, 4.22, and 4.23 show the RV time series, number of lines, and periodograms of four data sets, obtained using the correlation with the total RV, BIS, and CRX. In this case, the RV scatter is minimised for the data sets that include lines with $|\mathrm{R}| \leq 0.3 - 0.4$ and wstd RV ≤ 300 m s^{-1}, for the correlation with the total RV, BIS, and CRX. The decrease is of ~ 2.5 times compared to the initial set of lines. The periodogram shows a significant peak at 2.09 d, close to but not exactly at P_{rot}, 2.12 d, whose power decreases as we restrict the lines used.

Active lines

Regarding the active lines (Figs. 4.24, 4.25, and 4.26), the RV scatter increases as we restrict the number of lines used, and the periodogram power of the peak at 2.09 d remains significant. Contrary to what happens with J07446+035, the periodogram of the RVs obtained by the average of the lines with RV ≤ 0.80 for the total RV, or RV ≤ -0.80 for BIS and CRX, is less clear than the previous two cuts, and the peak at P_{rot} is not as significant.

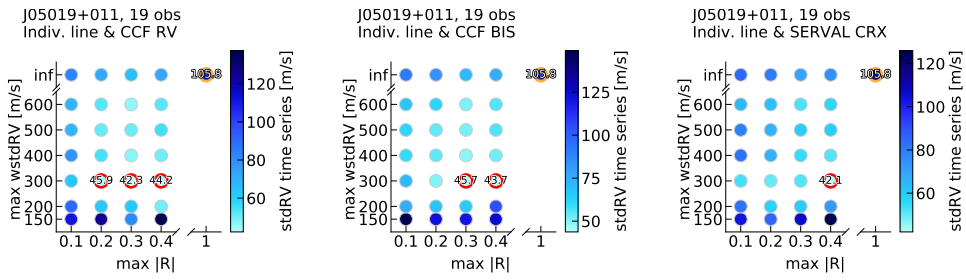

Figure 4.20: Same as Fig. 4.13 but for J05019+011.

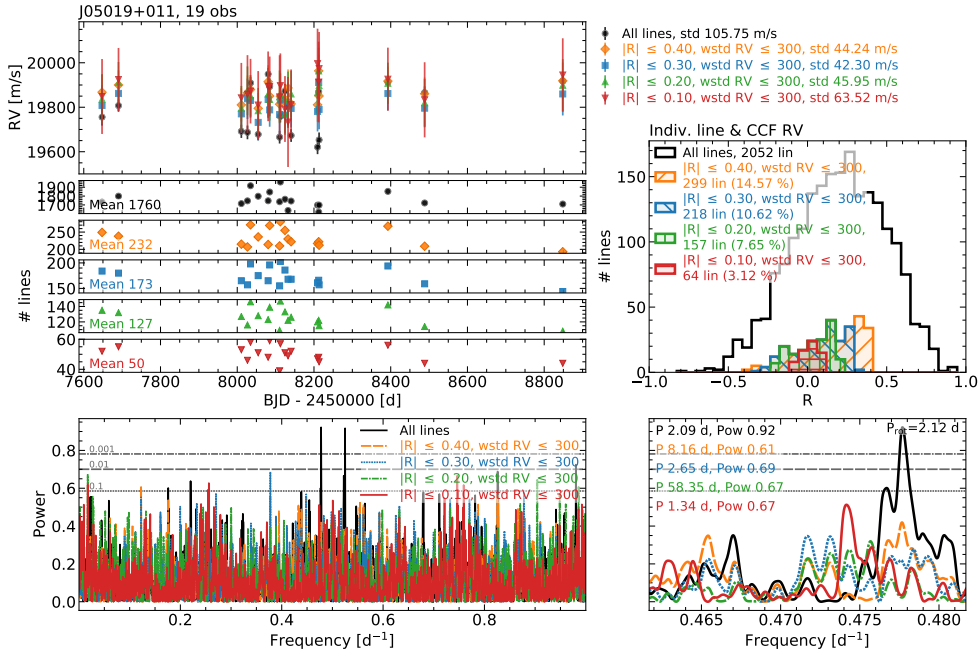

Figure 4.21: Same as Fig. 4.14, but for J05019+011 and lines with RV scatter ≤ 300 m s^{-1}.

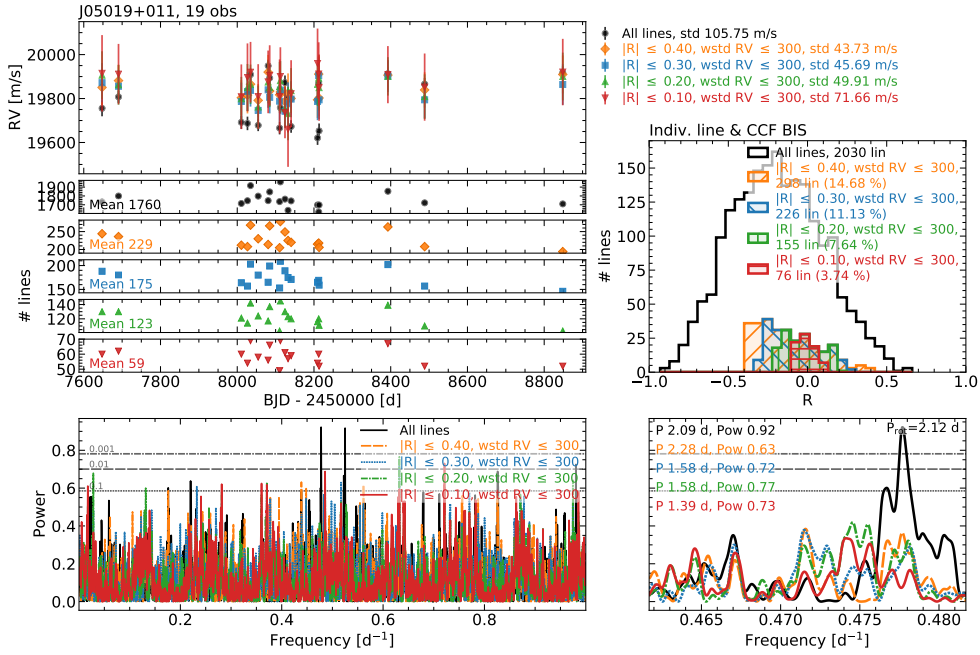

Figure 4.22: Same as Fig. 4.15, but for J05019+011 and lines with RV scatter ≤ 300 m s^{-1}.

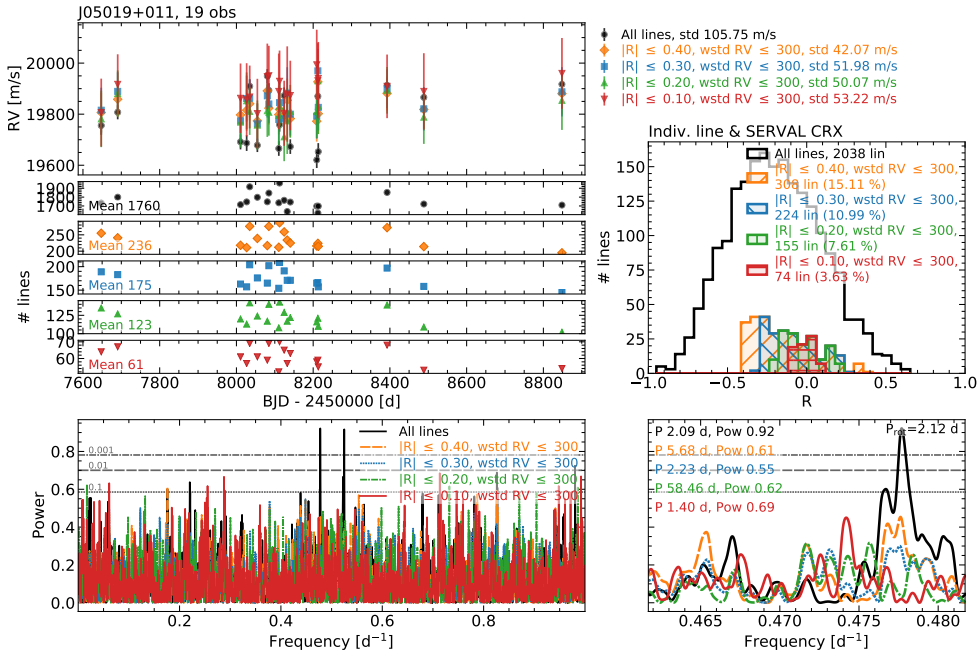

Figure 4.23: Same as Fig. 4.16, but for J05019+011 and lines with RV scatter ≤ 300 m s^{-1}.

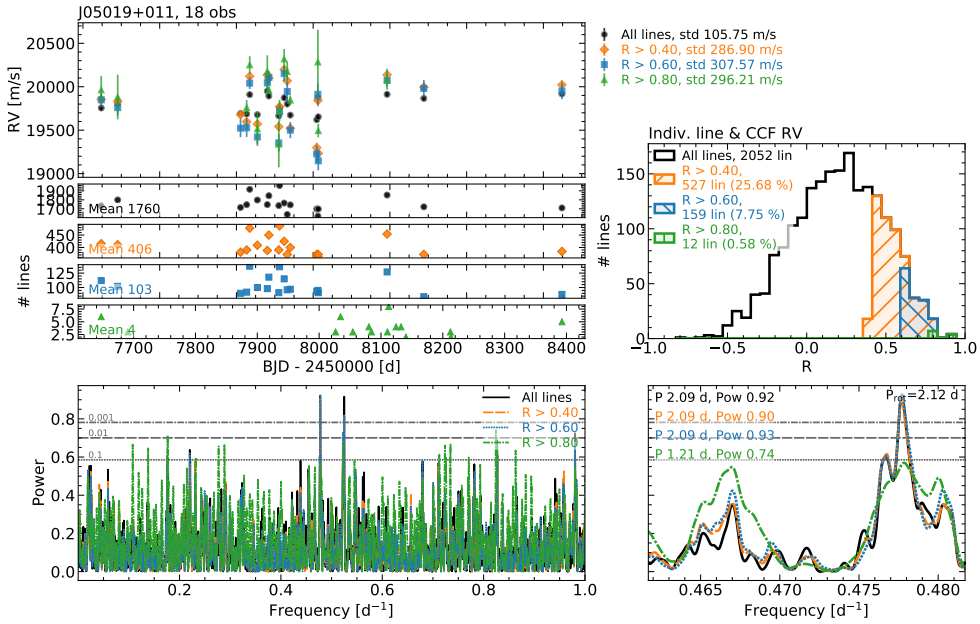

Figure 4.24: Same as Fig. 4.17, but for J05019+011.

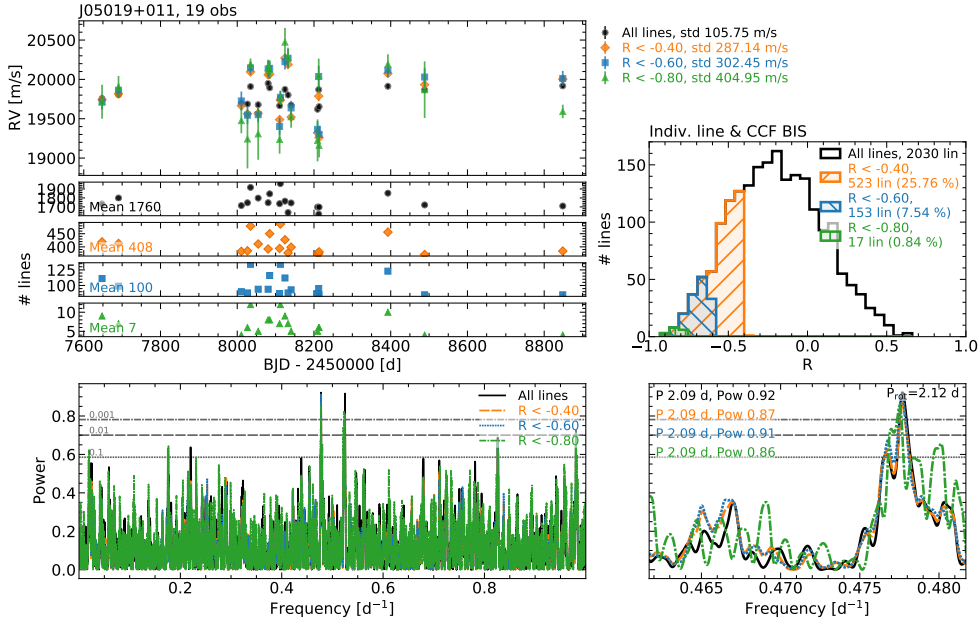

Figure 4.25: Same as Fig. 4.18, but for J05019+011.

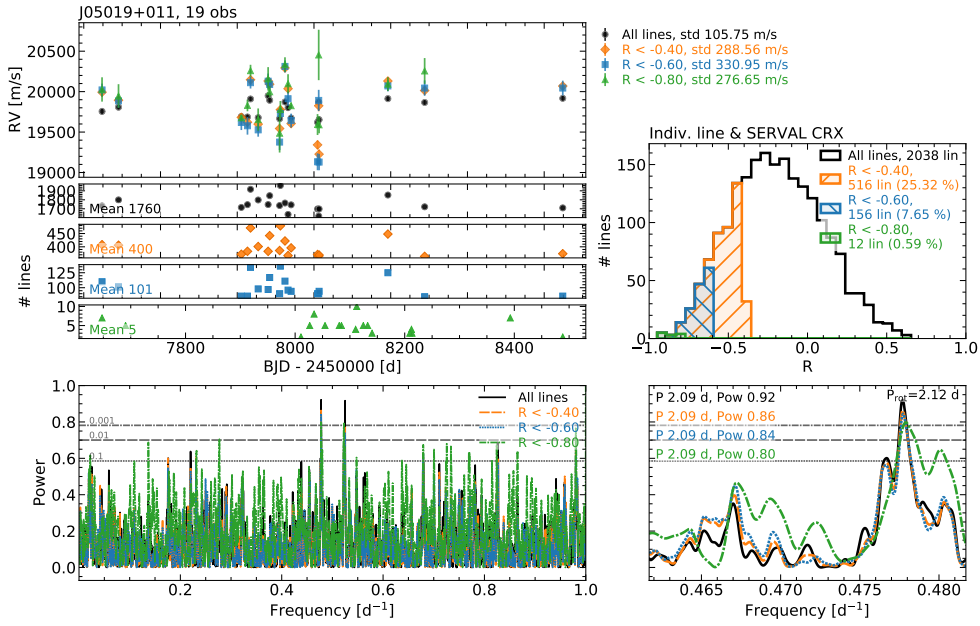

Figure 4.26: Same as Fig. 4.19, but for J05019+011.

4.6.3 J22468+443 (EV Lac, GJ 873)

J22468+443 is a mid M dwarf slightly less active than the two previous targets. CCF and LAV RVs have a scatter of $\sim 40\,\mathrm{m\,s^{-1}}$, about $10\,\mathrm{m\,s^{-1}}$ (1.2 times) smaller than the one obtained with `SERVAL` (Fig. 4.6). In this case, the periodograms of the RVs and the indicators show signals at both $P_{\rm rot}$ and $\frac{1}{2}P_{\rm rot}$, with the strongest signal at $\frac{1}{2}P_{\rm rot}$, and the indicators and the RVs show linear correlations (see previous chapter, Fig. 3.5). We used the line list built from the J07446+035 template. Similarly to the two previous stars, the correlations obtained with the total RV, BIS, and CRX are very similar for all the lines, and hence, we obtain similar results for the three indicators (Fig. 4.11).

Inactive lines

The smallest time series RV scatter occurs when using lines with $|\mathrm{R}| \leq 0.1 - 0.2$ and wstd RV $\lesssim 200 - 400\,\mathrm{m\,s^{-1}}$ (Fig. 4.27). The minimum scatter is of $\sim 18 - 19\,\mathrm{m\,s^{-1}}$, $2.2 - 2.4$ times smaller than the initial $\sim 40\,\mathrm{m\,s^{-1}}$, depending on the indicator. Regarding the activity modulation present in the RVs (Figs. 4.28, 4.29, and 4.30), the periodogram shows a very significant signal at half $P_{\rm rot}$, 2.19 d, and a less significant one at $P_{\rm rot}$, 4.38 d. As we restrict the lines used, the peak at half $P_{\rm rot}$ decreases its power, becoming non-significant for the data sets that result in some of the smallest time series RV scatter (data set with lines with $|\mathrm{R}| \leq 0.1$ and wstd RV $\leq 200\,\mathrm{m\,s^{-1}}$). We see that for some data sets, e.g. the one with lines with $|\mathrm{R}| \leq 0.2$ and wstd RV $\leq 200\,\mathrm{m\,s^{-1}}$, the peak at $P_{\rm rot}$ increases its power, becoming significant.

Active lines

For this star, the strength of the correlations between the individual line RVs and the activity indicators does not reach values as large as $\mathrm{R} = 0.8$, as happens with J07446+035 or J05019+011, so the most restrictive cut performed to select active lines is at $\mathrm{R} > 0.60$ (Figs. 4.31, 4.32, and 4.33). As with the previous stars, the scatter of the RVs increases as we restrict the lines used. The power of the periodogram peak at half $P_{\rm rot}$ slightly increases too. We observe a similar behaviour for the correlations obtained with the three indicators.

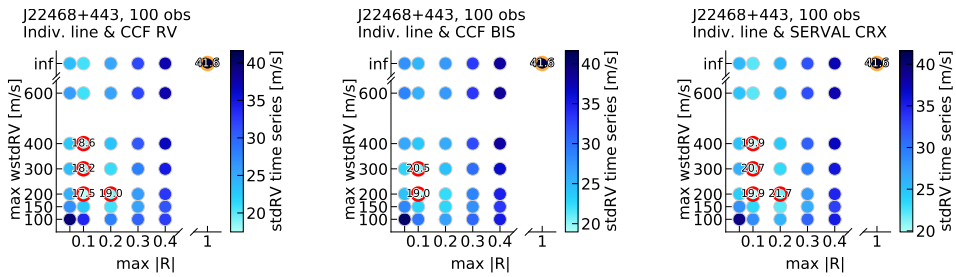

Figure 4.27: Same as Fig. 4.13 but for J22468+443.

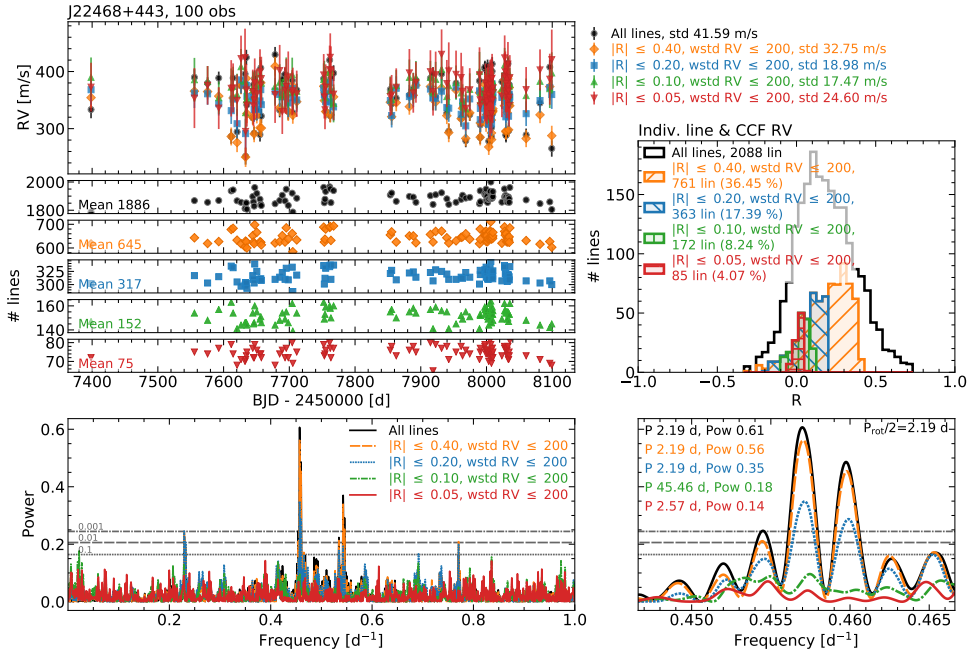

Figure 4.28: Same as Fig. 4.14, but for J22468+443. In this case, the periodogram zoom in on the *right panel* corresponds to half $P_{\rm rot}$, which is the highest peak in total RV periodogram.

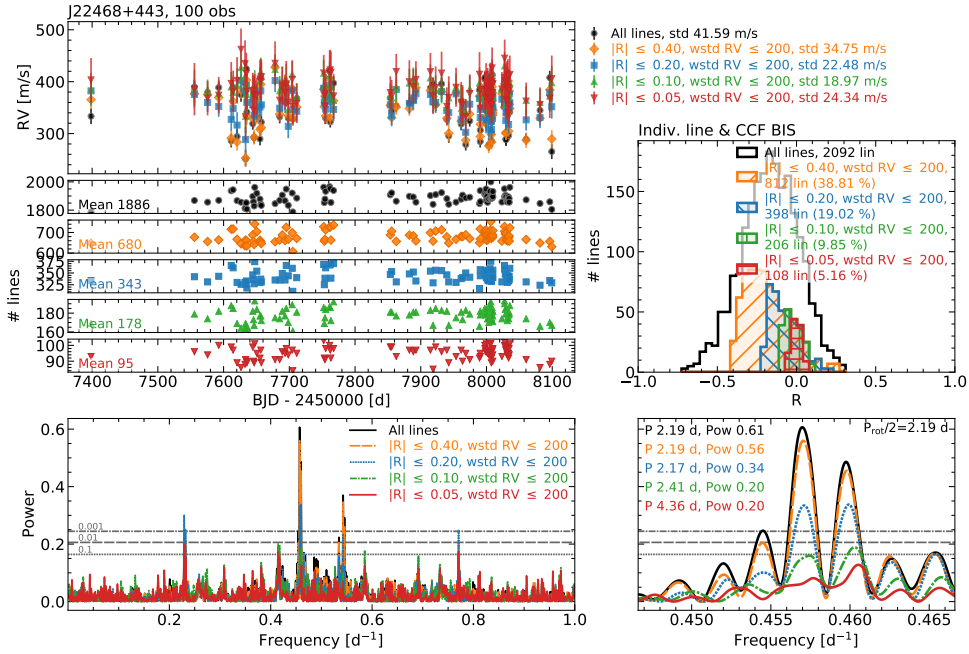

Figure 4.29: Same as Fig. 4.15, but for J22468+443. In this case, the periodogram zoom in on the *right panel* corresponds to half $P_{\rm rot}$, which is the highest peak in total RV periodogram.

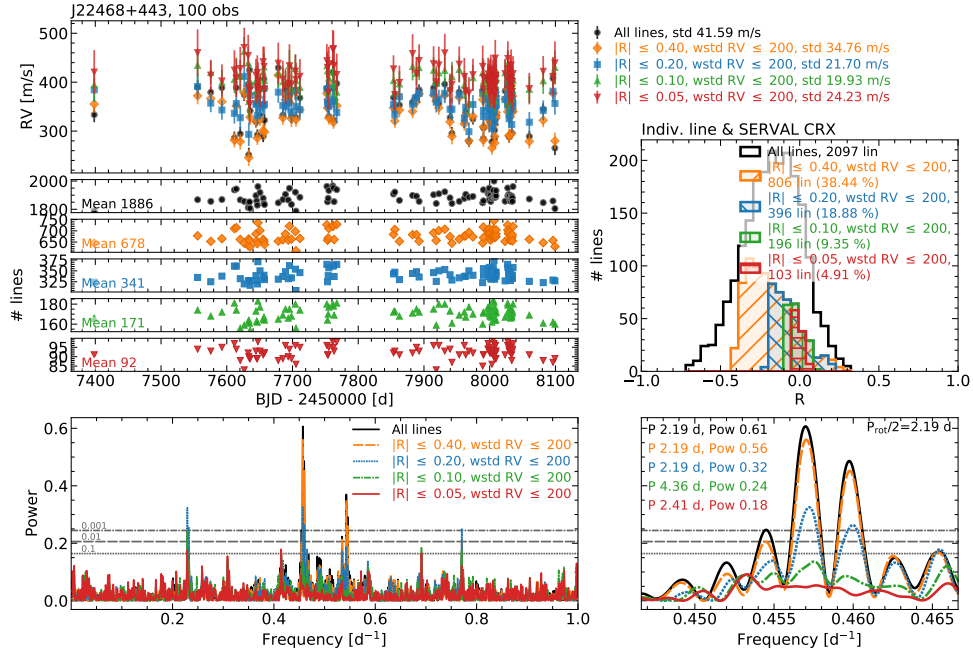

Figure 4.30: Same as Fig. 4.16, but for J22468+43. In this case, the periodogram zoom in on the *right panel* corresponds to half $P_{\rm rot}$, which is the highest peak in total RV periodogram.

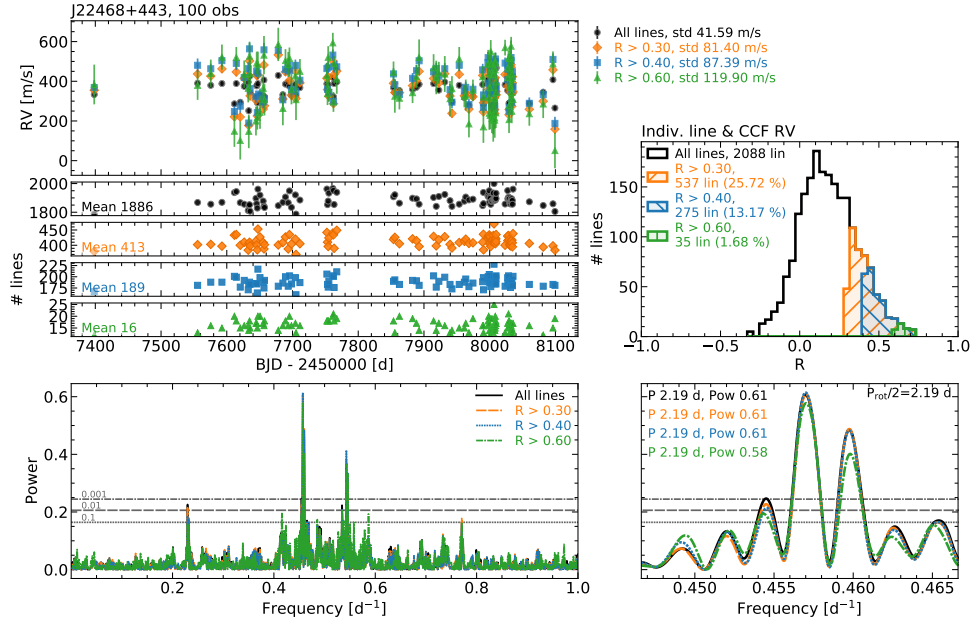

Figure 4.31: Same as Fig. 4.17, but for J22468+443.

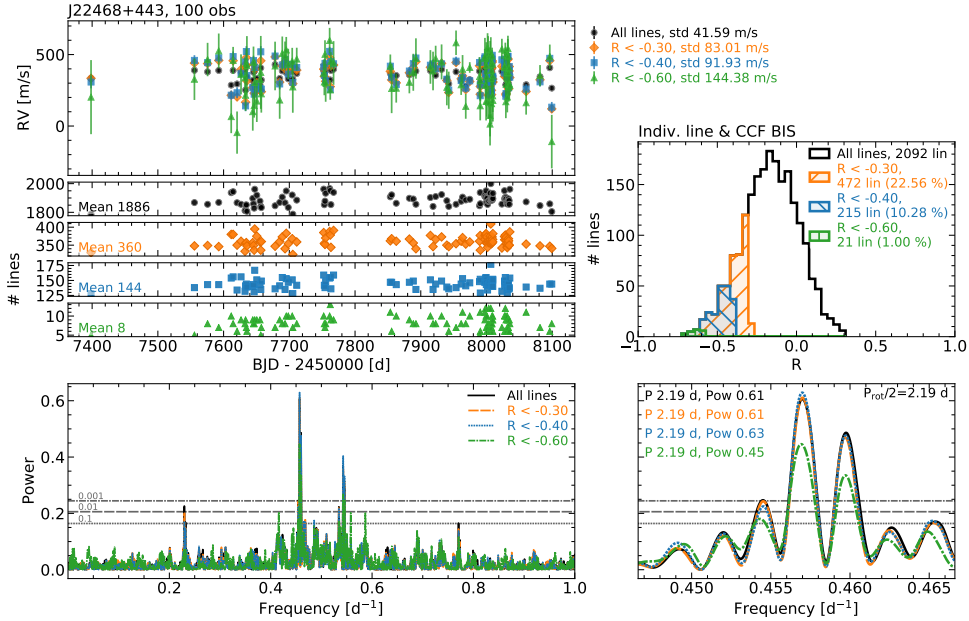

Figure 4.32: Same as Fig. 4.18, but for J22468+443.

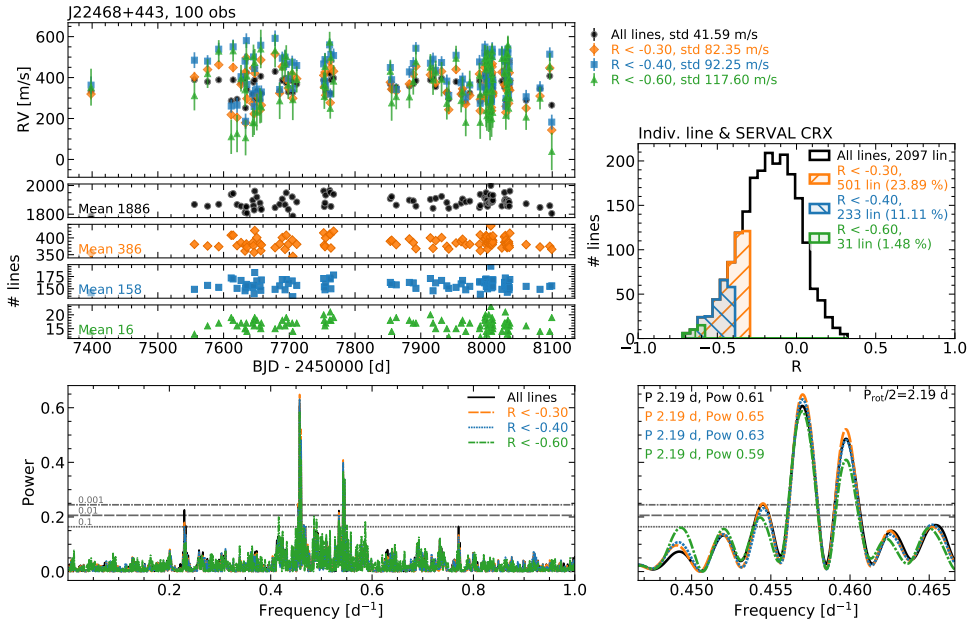

Figure 4.33: Same as Fig. 4.19, but for J22468+443.

4.6.4 J10196+198 (AD Leo, GJ 388)

J10196+198 shows a similar activity level to J22468+443 (similar $pEW'(\mathrm{H}\alpha)$ and $\log(L_{\mathrm{H}\alpha}/L_{\mathrm{bol}})$), but has an RV scatter significantly smaller than J22468+443 or the other two previous stars ($\sim 18\,\mathrm{m\,s^{-1}}$ for J10196+198, while for the previous stars it is $> 50\,\mathrm{m\,s^{-1}}$). The number of observations is relatively small, 26, but from the analysis of the previous chapter, we see that the periodograms of the RVs, BIS, and CRX, show a significant peak the ∼2.24, close to P_{rot}, so the observation number and sampling is enough to observe activity-related modulations.

The different RV amplitudes between J10196+198 and J22468+443 could be caused by different visible spot configurations. J10196+198 has a relatively low spin axis inclination ($i \sim 14°$, Kossakowski et al., in preparation) in comparison to J22468+443 or the previous stars (which have $i \geq 60°$, see e.g. Morin et al., 2008). This close to pole-on inclination could cause any visible co-rotating spots to induce a smaller modulation in the RVs, since they would not abruptly appear and disappear as the star rotates. Also, the photosphere of J10196+198 could be more homogeneously spotted, also inducing smaller RV modulations.

As seen in Sect. 4.5.1, Fig. 4.11, for this star there are no lines whose RV shows a very strong correlation with the activity indicators. The correlation coefficients R do not reach very large values, contrary to what happened with the three previous stars. This means that, by using these correlations, we are not able to identify lines that have a strong contribution to activity. Aside from this, the R values obtained for each line depend on the activity indicator used to compute the correlation. All this could indicate that the correlations that we find do not have much information related to the activity of the star.

This star has been speculated to host an exoplanet with an orbital period similar to the stellar rotation, ∼2.23 d, in a 1:1 spin-orbit resonance (Tuomi et al., 2018), although this claim has been challenged by further studies (Carleo et al., 2020; Robertson et al., 2020). However, since the stellar rotation and the hypothetical planet have the same period, it is difficult to completely rule out the planet existence (Kossakowski et al., in preparation). Since the RVs of this star could potentially contain the signal induced by the presence of an orbiting planet, in this case using the total RV as an activity indicator is not a good choice, because the correlations with the line RVs would not solely reflect the effect of activity.

Inactive lines

As we restrict the lines used to the ones with R closer to 0, we do not see a significant decrease in the RV scatter, but an increase (Fig. 4.34). Only for a few data sets that contain almost the same lines as the initial one, obtained with the correlation with RV

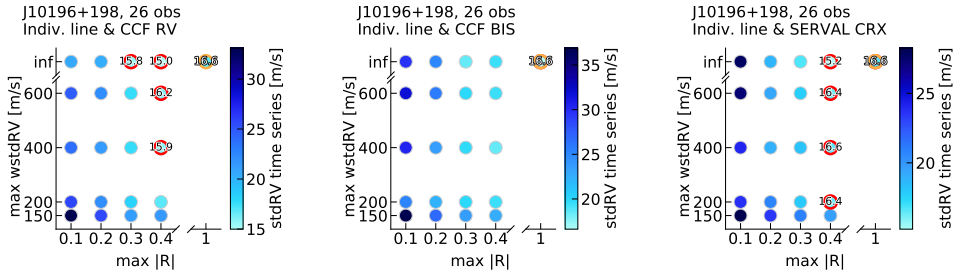

Figure 4.34: Same as Fig. 4.13 but for J10196+198.

and CRX, the scatter decreases, but not significantly (about $1\,\mathrm{m\,s^{-1}}$ less than the initial $16.6\,\mathrm{m\,s^{-1}}$). For the data sets obtained using the correlation with BIS, none shows a decrease in the RV scatter. We note that the initial RV scatter obtained with the LAV method is lower than the one obtained with the SERVAL RVs, $18.4\,\mathrm{m\,s^{-1}}$, but larger than the one obtained with the CCF RVs, $15.0\,\mathrm{m\,s^{-1}}$, which is close to the smallest value obtained with the inactive lines data set.

The periodograms show a peak at the P_{rot} of the star, 2.24 d, which decreases its power as we restrict the lines used (Figs. 4.35, 4.36, and 4.37). This happens for the three indicators, but for the BIS the decrease is smaller than for the total RV and the CRX. Since the RV scatter does not decrease significantly, but remains the same or increases, we attribute this decrease in the significance of the peak at P_{rot} to the increase in photon noise due to the smaller number of lines used in the data sets.

Active lines

As we restrict the line selection to those showing the stronger correlations, we see that the RV scatter increases significantly (Figs. 4.38, 4.39, and 4.40). The activity signal present in the RVs, however, does not remain constant. The peak at P_{rot} shows a decrease in power for the data sets using the lines with the stronger correlations, and even completely disappears in the RV data sets computed using the correlations with BIS. This could indicate that the lines that we identified as active are actually not related to activity, which agrees with the fact that the strength of the correlations between the individual line RVs and the activity indicators were not large (Fig. 4.11).

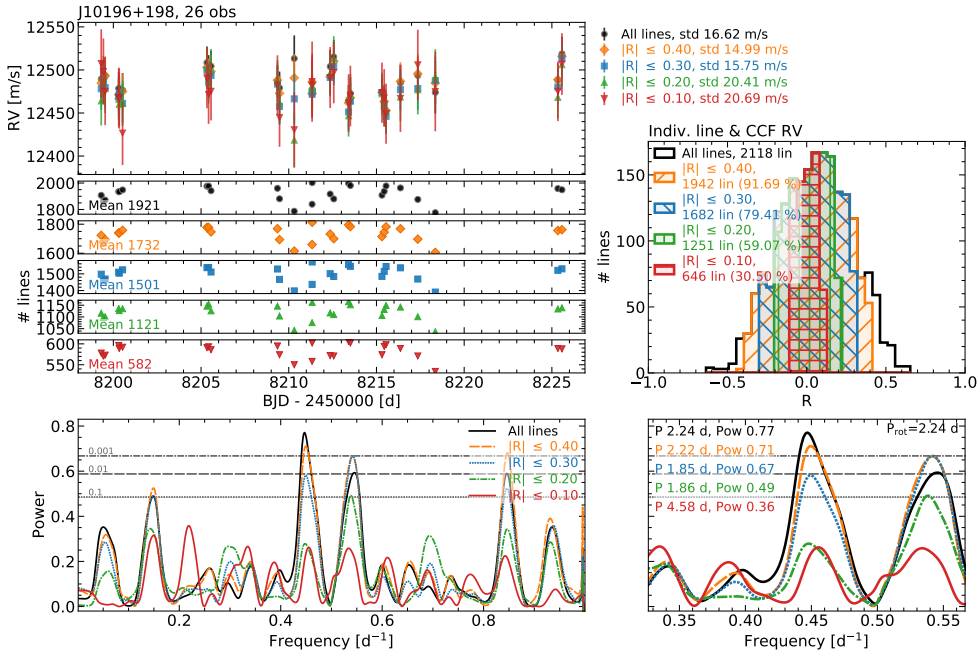

Figure 4.35: Same as Fig. 4.14, but for J10196+198 and lines with no limit on the RV scatter.

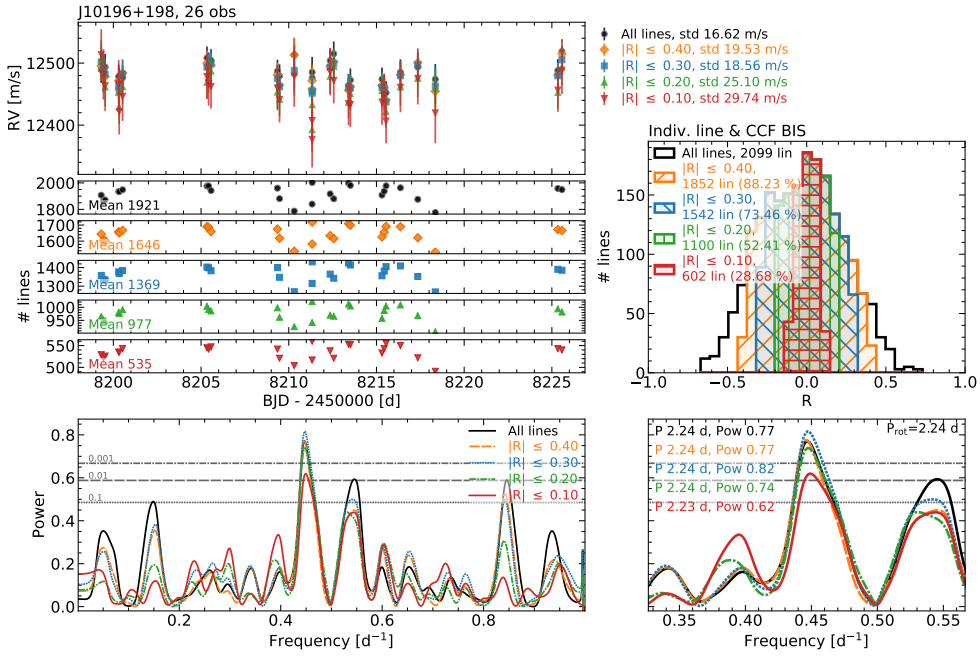

Figure 4.36: Same as Fig. 4.15, but for J10196+198 and lines with no limit on the RV scatter.

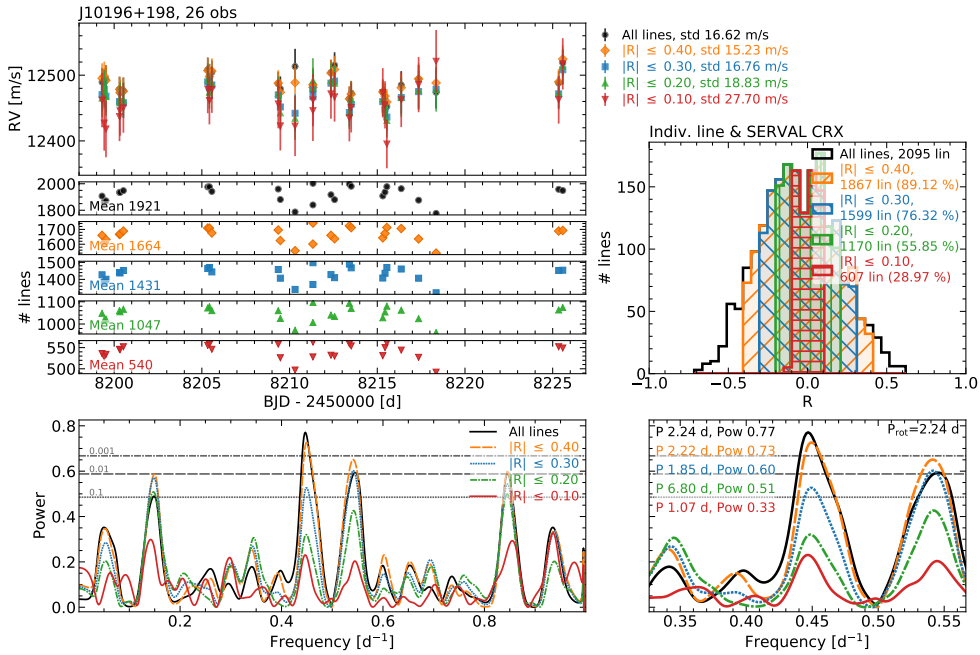

Figure 4.37: Same as Fig. 4.16, but for J10196+198 and lines with no limit on the RV scatter.

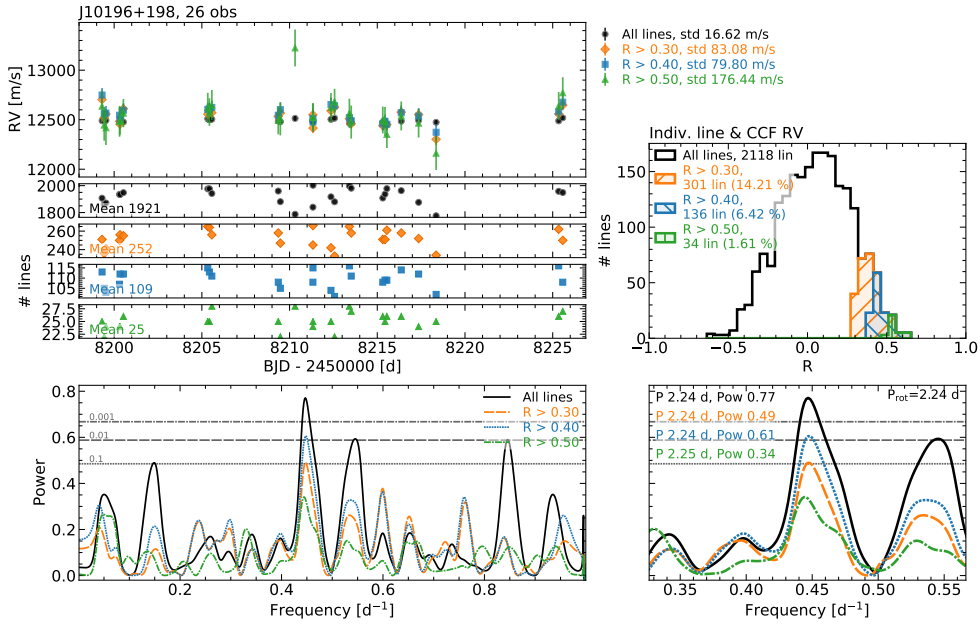

Figure 4.38: Same as Fig. 4.17, but for J10196+198.

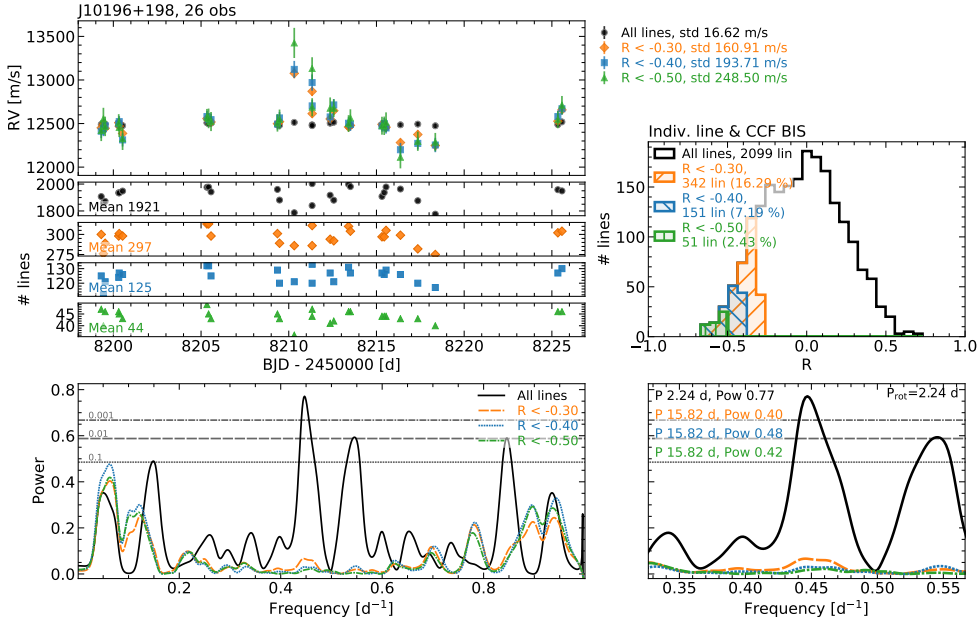

Figure 4.39: Same as Fig. 4.18, but for J10196+198.

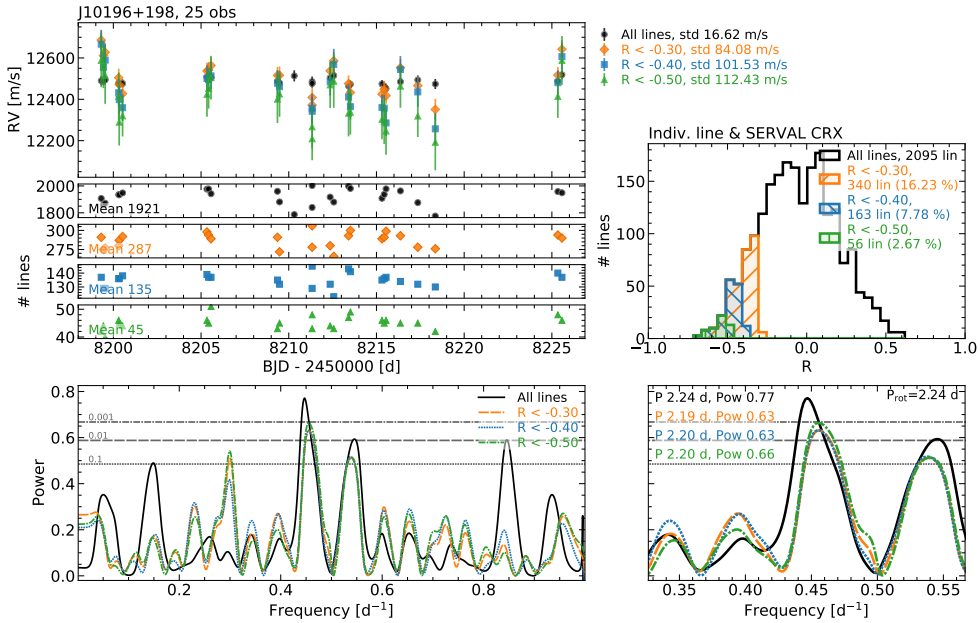

Figure 4.40: Same as Fig. 4.19, but for J10196+198.

4.6.5 J15218+209 (OT Ser, GJ 9520)

J15218+209 is one of the two early M dwarfs analysed. It has a large RV scatter, 37 m s^{-1}. From the previous chapter, we see that the RV, BIS, and CRX periodograms show a peak at $P_{\rm rot}$, 3.37 d, but it is only significant (FAP < 0.1 %) in the case of the RVs. In this case we used the line list built from the J15218+209 template itself.

Inactive lines

The smallest time series RV scatters occurs when using lines with $|\mathrm{R}| \leq 0.1 - 0.2$ and wstd RV $\leq 100 - 300$ m s^{-1} (Fig. 4.41). It reaches values of 13, 19, and 17 m s^{-1}, 2.7, 2.0, and 2.2 times smaller than the initial 37.2 m s^{-1}, for the correlations with the total RV, BIS, and CRX, respectively. The periodogram of the initial data set shows a significant peak at $P_{\rm rot}$, 3.37 d (Figs. 4.45, 4.46, and 4.47). For the data sets computed with the correlations with the total RV and CRX, the $P_{\rm rot}$ peak decreases in power and reaches a FAP of 0.1 for the data set with one of smallest time series RV scatters. For the BIS data sets, the decrease in power is not as clear, and for the data set with the smaller RV scatter, the peak has a similar power as initially.

Active lines

The time series RV scatter increases as we restrict the lines towards the ones with stronger correlations (Figs. 4.45, 4.46, and 4.47). For the data sets obtained with the correlations with the total RV and CRX, the power at the $P_{\rm rot}$ peak remains significant but slightly decreases. For the BIS data sets, the power decreases significantly.

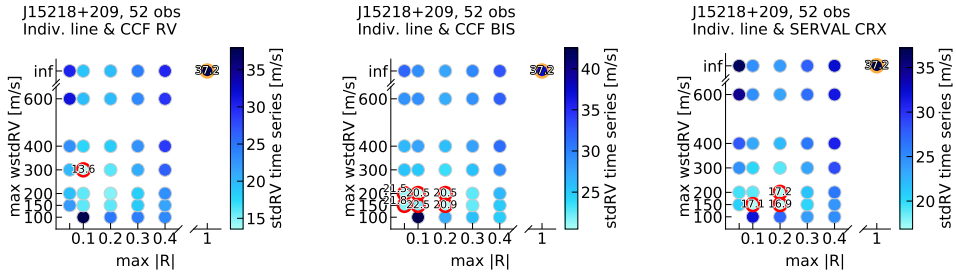

Figure 4.41: Same as Fig. 4.13 but for J15218+209.

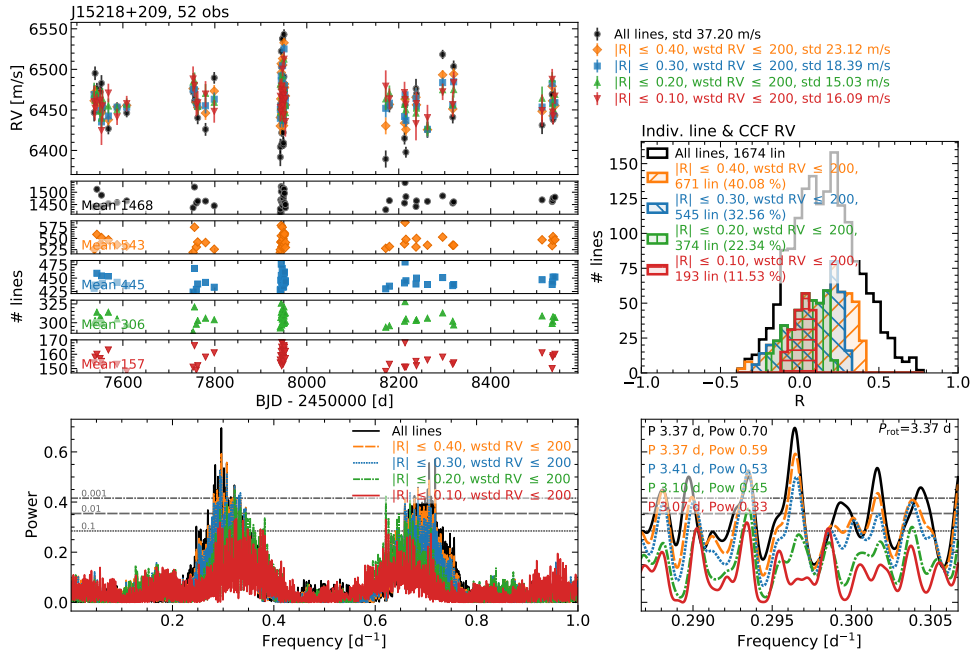

Figure 4.42: Same as Fig. 4.14, but for J15218+209.

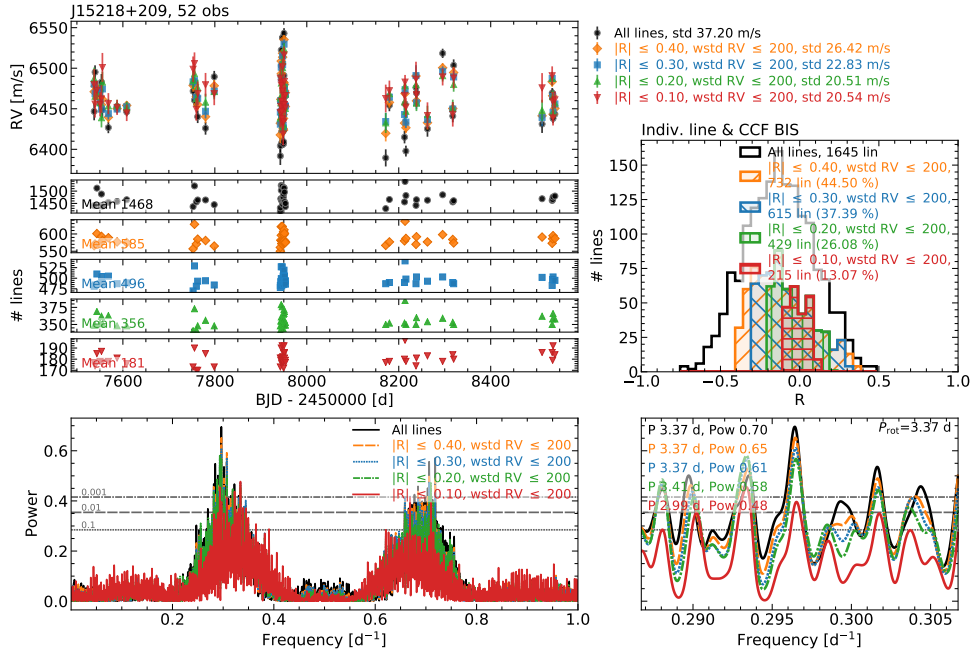

Figure 4.43: Same as Fig. 4.15, but for J15218+209.

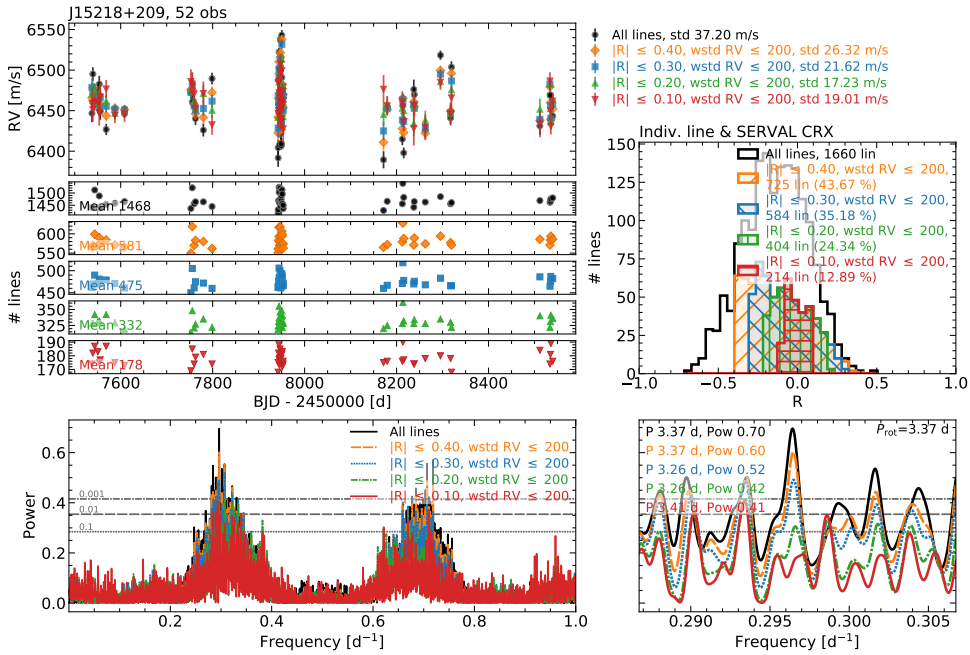

Figure 4.44: Same as Fig. 4.16, but for J15218+209.

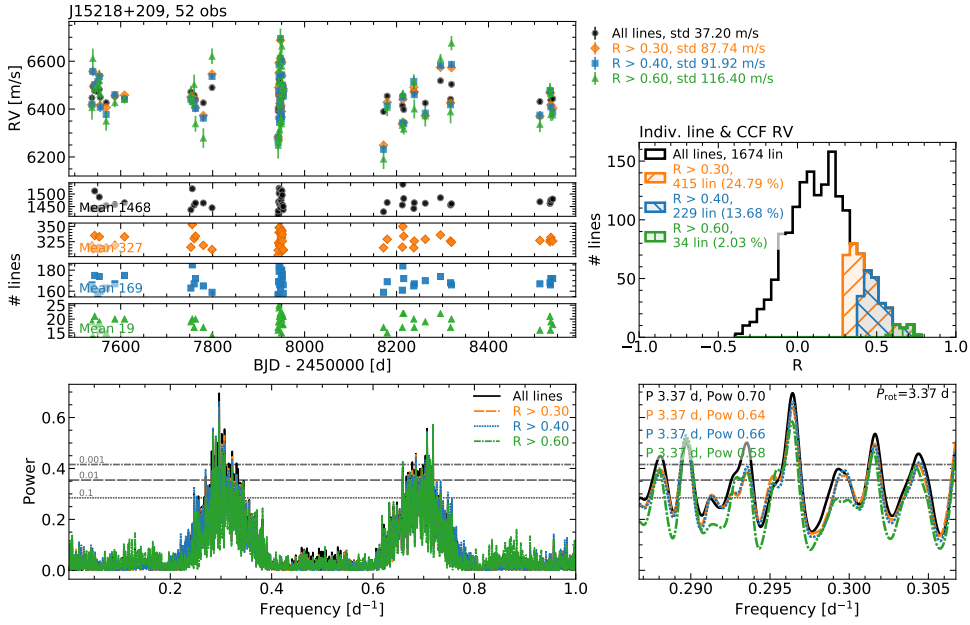

Figure 4.45: Same as Fig. 4.17, but for J15218+209.

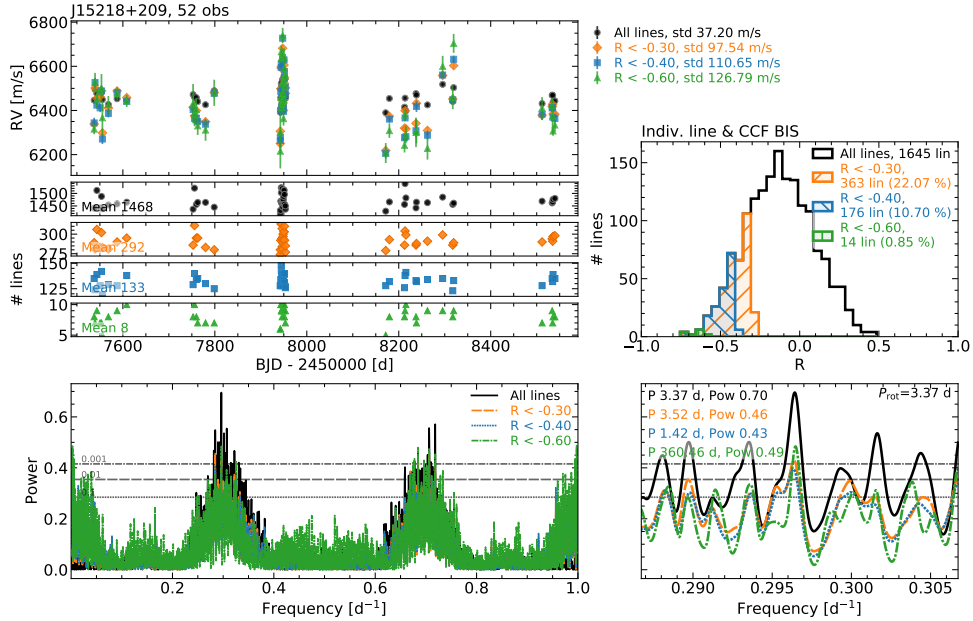

Figure 4.46: Same as Fig. 4.18, but for J15218+209.

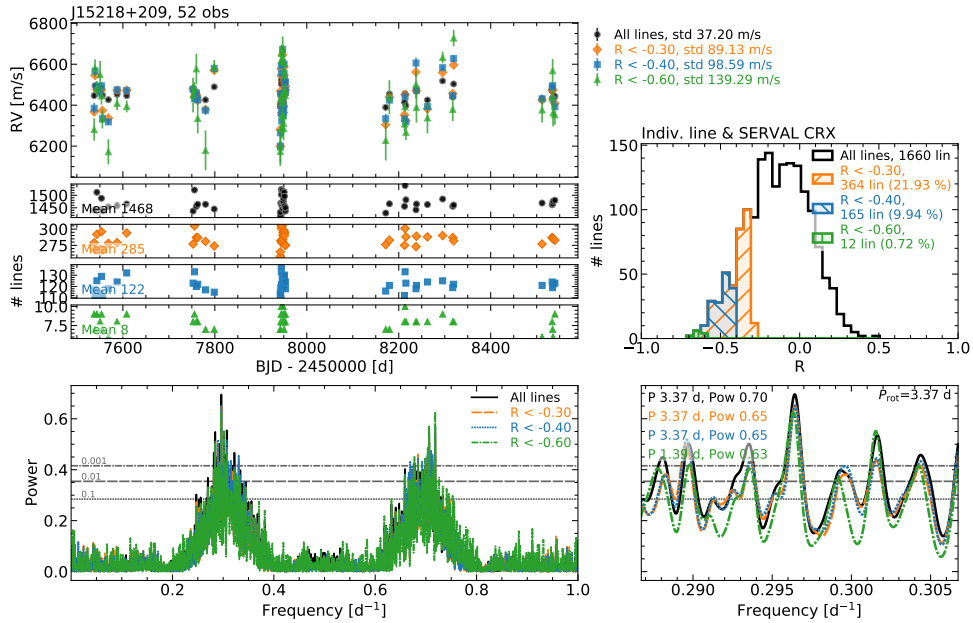

Figure 4.47: Same as Fig. 4.19, but for J15218+209.

4.6.6 J11201-104 (LP 733-099)

J11201-104 is the other early-type star analysed. By looking at the average $I_{H\alpha}$, we see that J11201-104 is less active than J15218+209, and shows a smaller scatter in its RV time series, of about 18 m s^{-1}, in the RVs obtained with SERVAL, the CCF, and the LAV method (Fig. 4.9). We did not include it in our periodogram analysis of the previous chapter because it had a relatively small number of observations (less than 40) and its periodograms did not show any significant signal. CRX and BIS show linear correlations with the RVs, but they are less clear than in the previous stars. For this star, we used the set of lines derived from the J15218+209 template.

Inactive lines

The RV time series with the smallest dispersions are obtained for the data sets with $|R| \leq 0.1 - 0.3$ and wstd RV ≤ 200 m s^{-1} (Fig. 4.48), in the case of the correlations with the total RV and CRX. The scatter decreases from ~ 19 m s^{-1} to ~ 11 m s^{-1} for the RV data sets and to ~ 13 m s^{-1} for the CRX ones, 1.7 and 1.5 time smaller, respectively. In the case of BIS, there are several data sets that show a small scatter close to the minimum one, which is about ~ 15 m s^{-1}, 1.3 times smaller than the initial one. The P_{rot} of this star is not known, and the periodogram does not show any significant peaks (Figs. 4.52, 4.53, and 4.54).

Active lines

Regarding the active lines, the scatter increases significantly, but the periodogram does not shown any significant peaks for any of the data sets used (Figs. 4.52, 4.53, and 4.54).

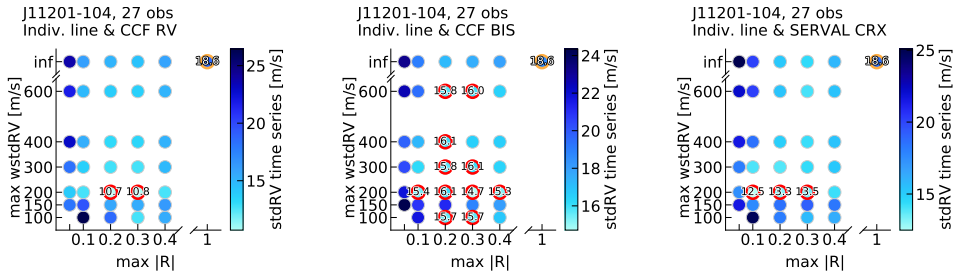

Figure 4.48: Same as Fig. 4.13 but for J11201-104.

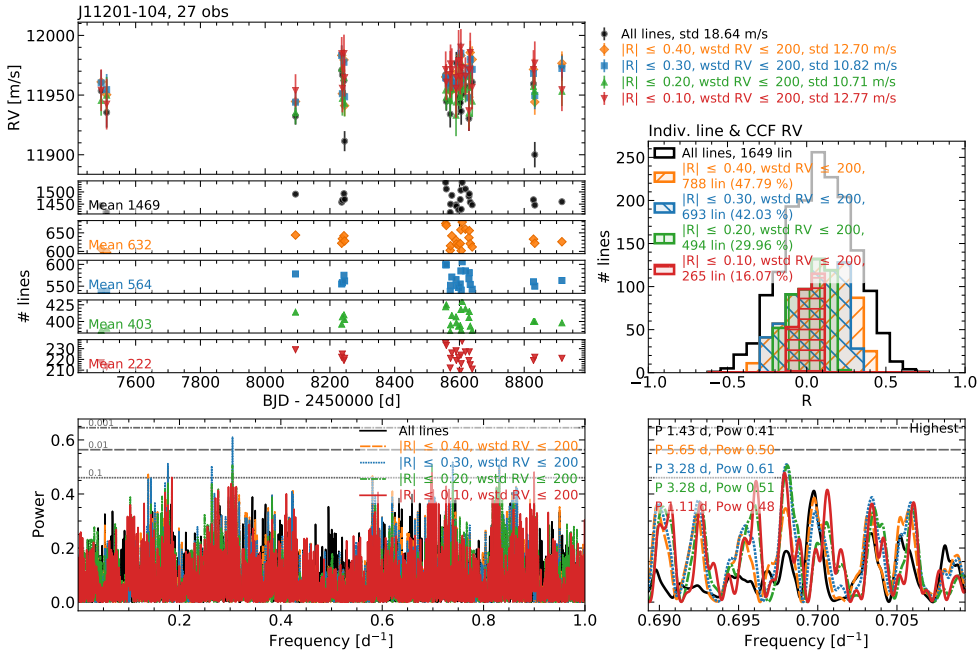

Figure 4.49: Same as Fig. 4.14, but for J11201-104. Since the rotation period of this star is not known, the periodogram zoom in shows the region around the highest peak in the RV time series obtained using the line averages.

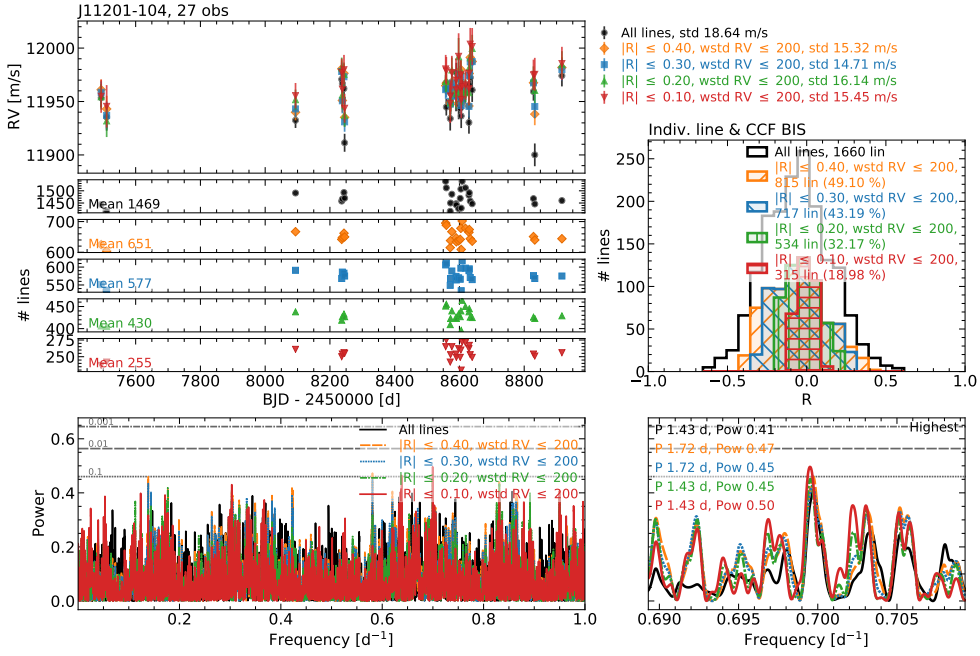

Figure 4.50: Same as Fig. 4.15, but for J11201-104. Since the rotation period of this star is not known, the periodogram zoom in shows the region around the highest peak in the RV time series obtained using the line averages.

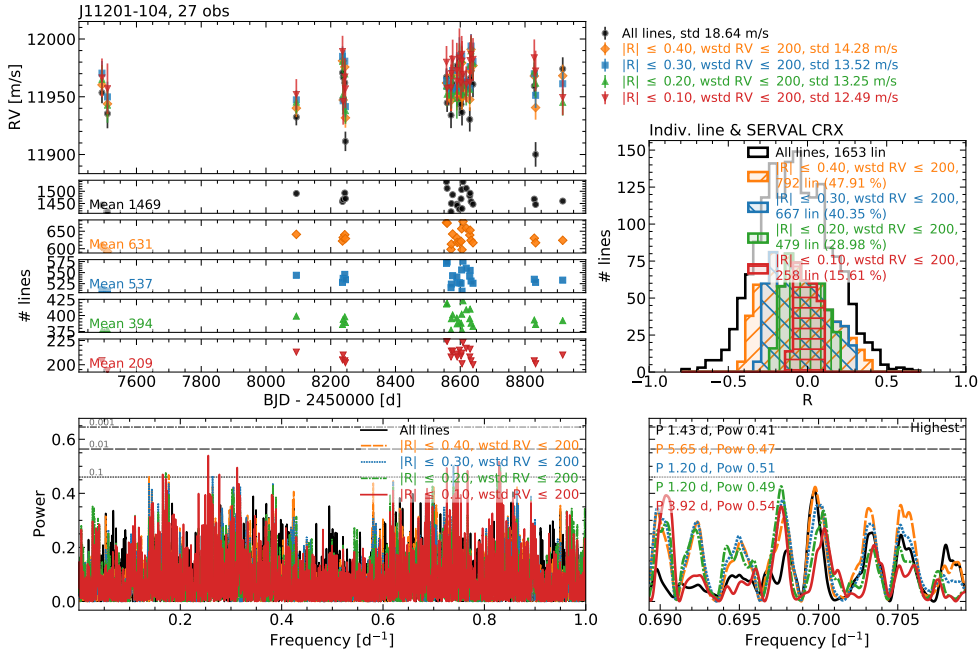

Figure 4.51: Same as Fig. 4.16, but for J11201-104. Since the rotation period of this star is not known, the periodogram zoom in shows the region around the highest peak in the RV time series obtained using the line averages.

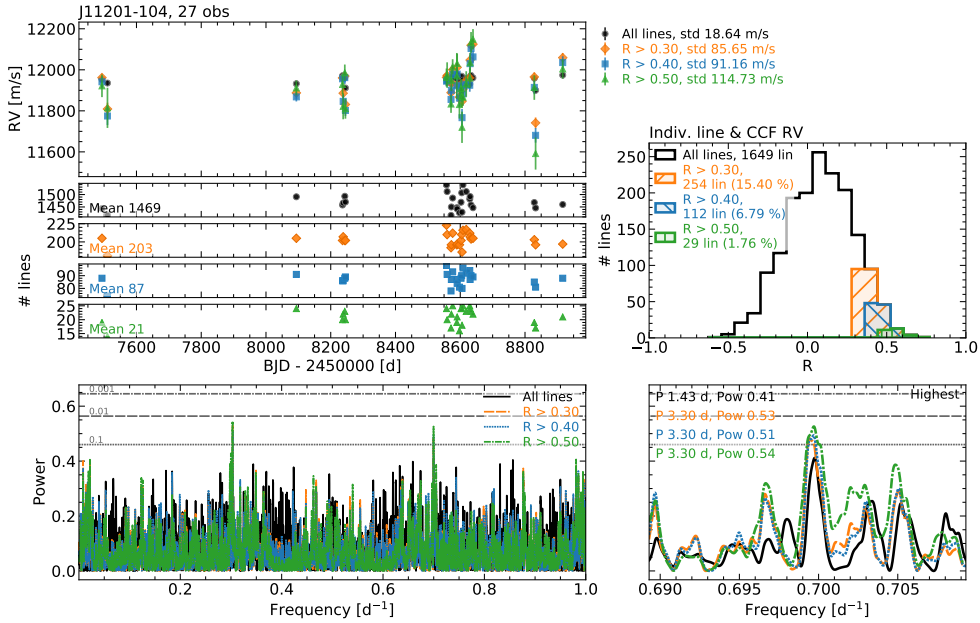

Figure 4.52: Same as Fig. 4.17, but for J11201-104.

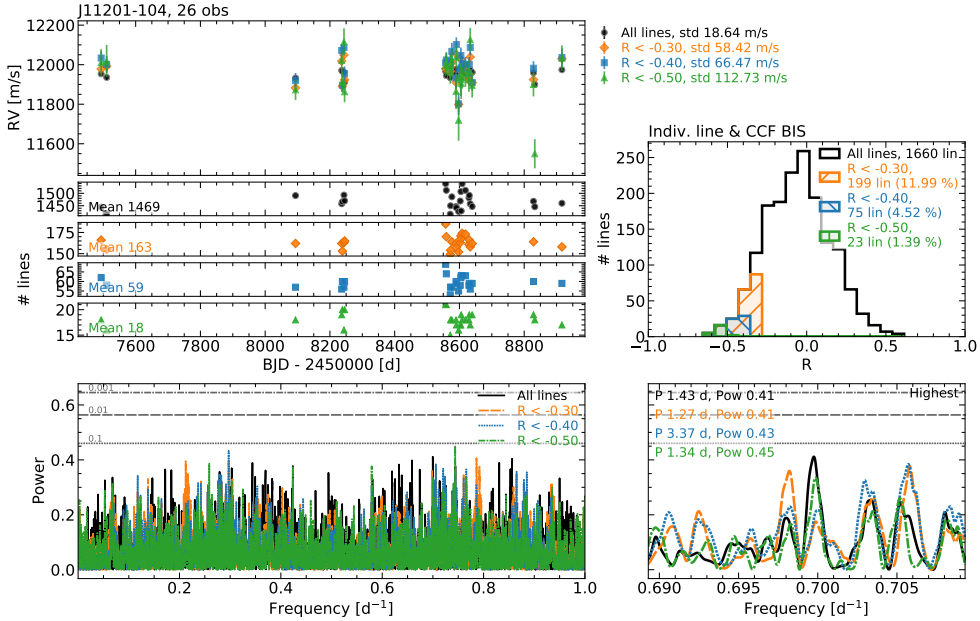

Figure 4.53: Same as Fig. 4.18, but for J11201-104.

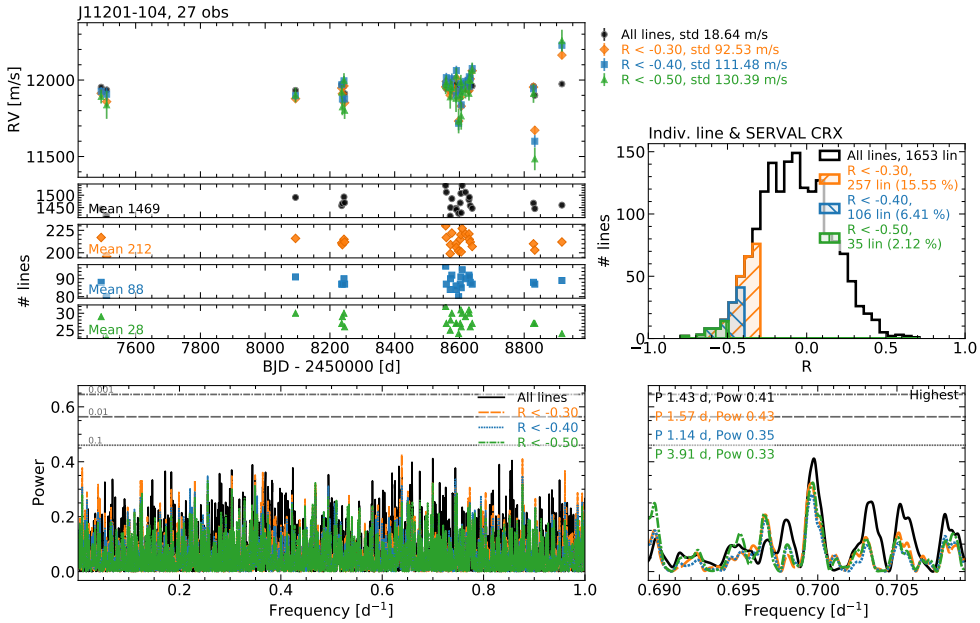

Figure 4.54: Same as Fig. 4.19, but for J11201-104.

4.6.7 Overview of the results

J07446+035, J05019+011, J2246+443, and J15218+209

For four of the six stars analysed, J07446+035, J05019+011, J2246+443, and J15218+209, we see that the total time series LAV RV scatter decreases when restricting the lines used towards those whose RV shows no correlation with the activity indicators ($|R| \sim 0$), and also by removing lines with large RV scatter (limited wstd RV). Also, the activity-related signals in the RV periodogram lose significance. This indicates that the modulation due to activity present in the RVs is mitigated. These four stars are the ones with the largest time series RV scatter, from ~ 37 to $\sim 100\,\mathrm{m\,s^{-1}}$, and the ones whose line RVs show the strongest correlation with the activity indicators.

We observe that there are specific sets of lines for which the time series RV scatter is minimised. These sets change depending on the star and the activity indicator used, but in general, the minimum scatter occurs when using lines with $|R| \lesssim 0.1 - 0.3$ and wstd RV $\lesssim 150 - 300\,\mathrm{m\,s^{-1}}$. For J07446+035, the scatter can be decreased ~ 5 times with respect to the initial one. For the other three stars, the maximum decrease is between ~ 2 and 3 times. The number of lines in the 'best' sets of lines is of ~ 100 to 200 for the mid-type stars J07446+035, J05019+011, and J2246+443, and of ~ 400 for the early-type J15218+209.

Regarding the activity indicators used, for J07446+035, J22468+443, and J15218+209, RVs computed using line sets based on the correlation with the total RV are those that result in the lowest scatter, compared to RVs obtained from line sets based on the correlation with the other two indicators (BIS and CRX). Between BIS and CRX, for J15218+209, the CRX line sets result in smaller RV scatters than those of BIS. For J07446+035 and J22468+443, both BIS and CRX data sets result in similar minimum scatters. For J05019+011, the data sets of the three activity indicators reach similar minimum values.

When using sets of lines in which the conditions are more restrictive than those mentioned above (i.e. sets with less lines), the time series RV scatter starts to increase, probably because the photon noise starts to dominate over the activity-driven variability.

Doing the same but selecting lines that show a strong correlation with an activity indicator ($R \sim 1$ or -1, depending on the activity indicator used), we see that the time series RV scatter increases significantly. This could be due to the fact that we are enhancing the activity signal, but also to the increase in photon noise caused by the decrease in the number of lines (RV content) used. For most of the line sets tested, the activity-related signals in the RV periodograms show similar power as in the periodogram computed from the original RVs. However, for the most restrictive

sets of lines (R $\geq$ 0.6 to 0.8 or -0.6 to -0.8, depending on the indicator), the signal loses significance, which could reflect the fact that the photon noise has increased due to the low number of lines used.

J10196+198

J10196+198 shows similar activity level as J22468+443, however, its initial RV scatter is significantly smaller ($\sim 18\,\mathrm{m\,s^{-1}}$ compared to $\sim 40\,\mathrm{m\,s^{-1}}$ for J22468+443), which may be in part due to the low estimated inclination of the star or to an homogeneously spotted photosphere. The line RVs are less correlated with the activity indicators than in the four previous targets (the correlations between the individual line RVs and the activity indicators show smaller strengths, i.e. R values less close to 1 or -1). The different data sets tested did not result in a significant decrease in RV scatter, probably due to the fact that the correlations between the line RVs and the indicators are not sufficiently strong. The periodogram shows a decrease of power at P_{rot}, probably due to an increase of photon noise in the recomputed RVs. Regarding the data sets of active lines, power at P_{rot} decreases significantly, which agrees with the fact that the correlation between the line RVs and the indicators is not strong. We then also attribute this decrease in power to increasing photon noise.

J11201-104

J11201-104 shows a similar initial scatter as J10196+108 ($\sim 19\,\mathrm{m\,s^{-1}}$) and, as occurs with J10196+198, the correlations between the line RVs and the activity indicators are not strong. Despite that, we observe a decrease in the time series RV scatter for some sets of lines obtained with similar selection criteria as the sets that minimised the scatter in the four stars J07446+035, J05019+011, J2246+443, and J15218+209. The maximum scatter decrease in this case is of ~ 1.7 times the initial one, with a set of about 500 lines. The P_{rot} of this star is not known, and the RV periodogram shows no significant signal.

4.7 Lines in different stars

Next, we investigate if the sensitivities to activity of the different lines (i.e. the R values) are similar in different stars. We performed pairwise comparisons of the stars in two groups: the mid-type stars J07446+035, J05019+011, and J22568+443, which used the same initial line list created from a J07446+035 template, and the early-types J15218+209 and J11201-104, which used the initial line list created from a J15218+209 template. We exclude J10196+198 from this analysis because we were not able to find a set of lines that mitigated the activity signal present in the RVs.

4.7.1 J07446+035 and J05019+011

Fig. 4.55 shows the distribution of R values of J07446+035 and J05019+011 as a function of the line wavelength, together with their correlation. The R values are those obtained from the correlation between the individual line RVs and the total RV. We show the correlation with this indicator as an example, but we obtained similar results for the correlations with CRX and BIS. Of the initial 2207 lines of the J07446+035 line list, we show here 2028 lines, which are those for which we were able to measure a reliable RV for both stars (i.e. after removing those with low S/N and non-common lines due to different overlap with tellurics or order ends). The distribution of R values of J07446+035 is slightly narrower and shifted towards 1 with respect to that of J05019+011. Many of the lines show different R values in the two stars, since there is only a weak correlation between the two sets (R $\sim$ 0.3).

We also indicate the lines selected for the data set for which we obtained the smallest RV scatter: lines with $|R| \leq 0.2$ and wstd RV $\leq 200\,m\,s^{-1}$ for J07446+035, and $|R| \leq 0.3$ and wstd RV $\leq 300\,m\,s^{-1}$ for J05019+011. These data sets have 188 and 218 lines, respectively. Of these, 53 lines are common in both data sets. This represents $24 - 28\,\%$ of the selected lines, and 2.6 % of the initial 2028 lines.

Next, we recomputed the time series RV of each star using the selected lines of the other one, and then, using only the common selected lines. Fig. 4.56 shows the RV time series, lines used, and periodograms of the RVs of J07446+035, computed using those assumptions. We also show the results of the initial data set, using all the lines. The RVs recomputed using the 'best' data set of J05019+011 (blue data points in the figure) have a scatter smaller than the initial one, $\sim 54\,m\,s^{-1}$ compared to $\sim 86\,m\,s^{-1}$, but the periodogram shows a peak at P_{rot} almost as significant as in the initial data set. The RVs recomputed using the 53 common lines (green data points) show a scatter similar to the ones obtained using the 'best' data of J07446+035 (orange data points) but slightly larger, of $\sim 23\,m\,s^{-1}$ compared to $\sim 20\,m\,s^{-1}$, and a periodogram with a peak at P_{rot} with a low significance.

Fig. 4.57 shows the same as Fig. 4.56 but for J05019+011. For the 'best' data set of J07446+035 (orange), the scatter decreases from ~ 106 to $\sim 60\,m\,s^{-1}$, compared with the initial one, and the peak close to P_{rot} decreases in power significantly. The common selected line RVs have a scatter very similar to the one obtained with the 'best' lines of J05019+011 (blue and green), and both periodograms show no significant peaks.

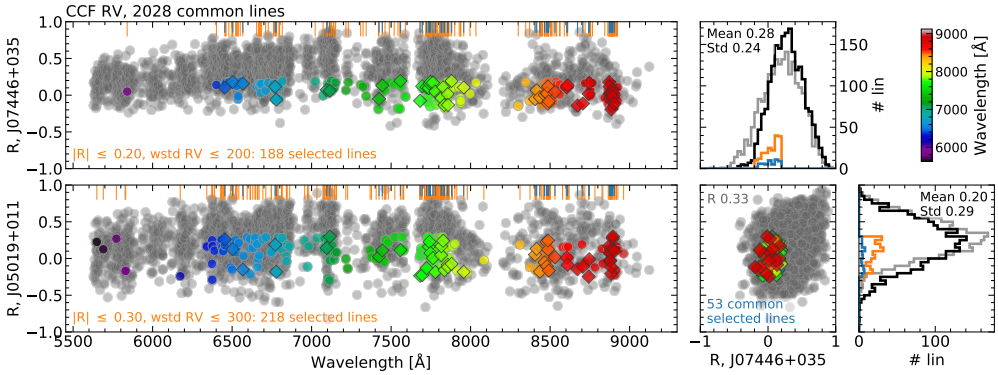

Figure 4.55: Pearson's correlation coefficient R of the lines analysed as a function of their wavelength for J07446+035 (*top left*) and J05019+011 (*bottom left*). Grey dots show lines not selected, coloured dots show lines selected by the specific cut indicated in the orange text, and coloured diamonds indicate selected lines common in both targets. Data points are colour-coded with wavelength. Vertical orange lines at the top of the panels indicate the position of the selected lines, and blue lines indicate those common in both stars. The *bottom middle panel* shows the correlation between J07446+035 and J05019+011 R values. Grey dots show all lines not selected in any of the targets plus lines selected but not common (i.e. grey and coloured dots in the *left panels*), and coloured diamonds indicate selected lines common in both stars (same as in the *left panels*). Histograms at the *right* show the distribution of R values of each star (J07446+035 *top*, J05019+011 *bottom*). The black histogram shows the distribution of all lines, the orange one, lines selected by the cut indicated in the *left panels*, and the blue one, selected lines common in both stars. The grey histogram shows the distribution of all lines for the other star, for comparison.

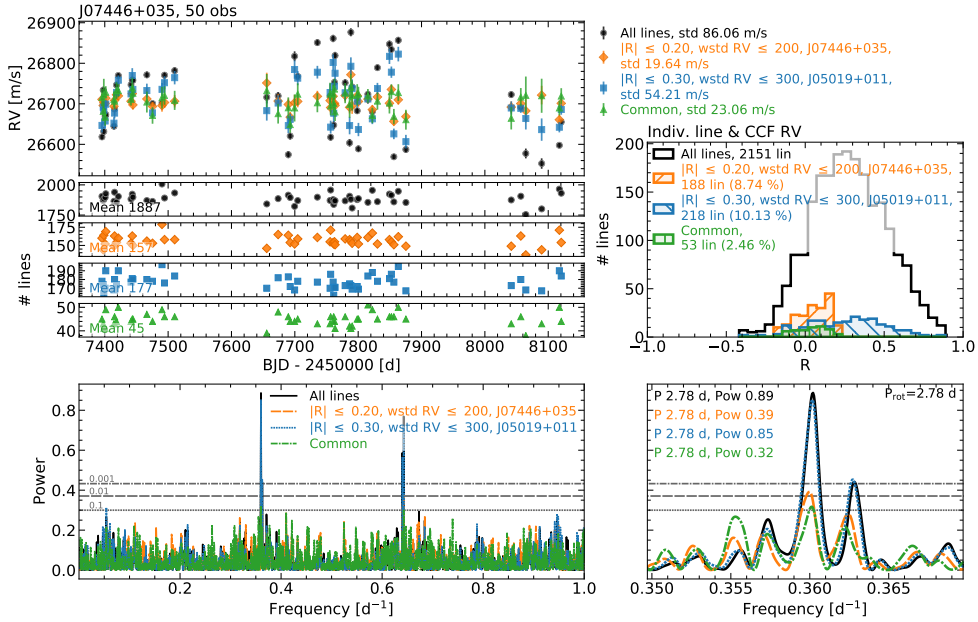

Figure 4.56: Same as Fig. 4.14 but using the following data sets: initial line list (black), lines that minimise the RV scatter of J07446+035 (orange), lines that minimise the RV scatter of J05019+011 (blue) and common lines in the two previous sets (green).

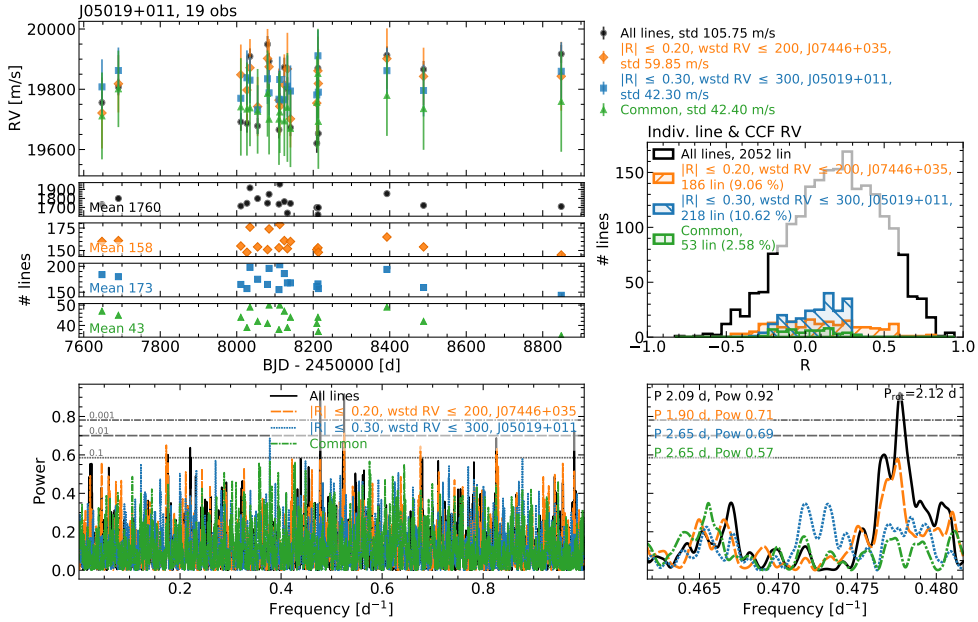

Figure 4.57: Same as 4.56 but for J05019+011.

4.7.2 J07446+035 and J22468+443

Fig. 4.58 shows the distribution R values, obtained from the correlation with the total RV, of J07446+035 and J22468+443 as a function of the wavelength, and their correlation. In this case the R distribution of J07446+035, which is the most active of the two stars, is wider and reaches values closer to 1 than that of J22468+443. The R values of the same lines for the two stars are more similar than for the previous pair of stars (J07446+035 and J05019+011), since now the correlation between the two R data sets is stronger ($R = 0.6$). The cuts yielding the lower RV scatter are $|R| \leq 0.2$ and wstd RV $\leq 200\,\mathrm{m\,s^{-1}}$ for J07446+035 and $|R| \leq 0.1$ and wstd RV $\leq 200\,\mathrm{m\,s^{-1}}$ for J22468+443. This represents 188 lines for J07446+035 and 172 for J22468+443. Of these selected lines, there are 52 common in both stars ($28 - 30\,\%$ of the selected lines, and $2.5\,\%$ of the initial 2052 lines).

Figs. 4.59 and 4.60 show the RV time series and periodograms recomputed using the 'best' set of lines of the other star, and the common selected lines, for J07446+035 and J22468+443, respectively. In both cases, using the line list that minimises the RV scatter of the other star results in a significantly smaller RV scatter than initially, about $1.8 - 2.1$ times smaller. For J07446+035 (blue), this decrease in half is far from the minimum scatter obtained with its own 'best' data set (orange), which is about 4.4 times smaller than the initial one, and the periodogram continues to show a very significant peak at P_{rot}. But for J22468+443 (orange) the decrease is close to the one obtained with its own 'best' data set (blue), which is about 2.4 times smaller, and the periodogram peak at half P_{rot} disappears. Regarding the common selected lines, in both cases the scatter is close to the minimum one obtained with the 'best' data set of each star, and the periodogram does not show significant peaks related to activity.

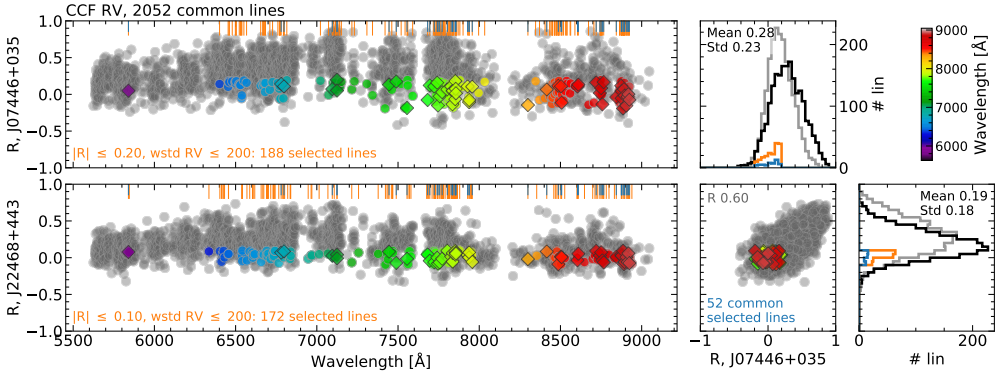

Figure 4.58: Same as Fig. 4.55 but for J07446+035 and J22468+443.

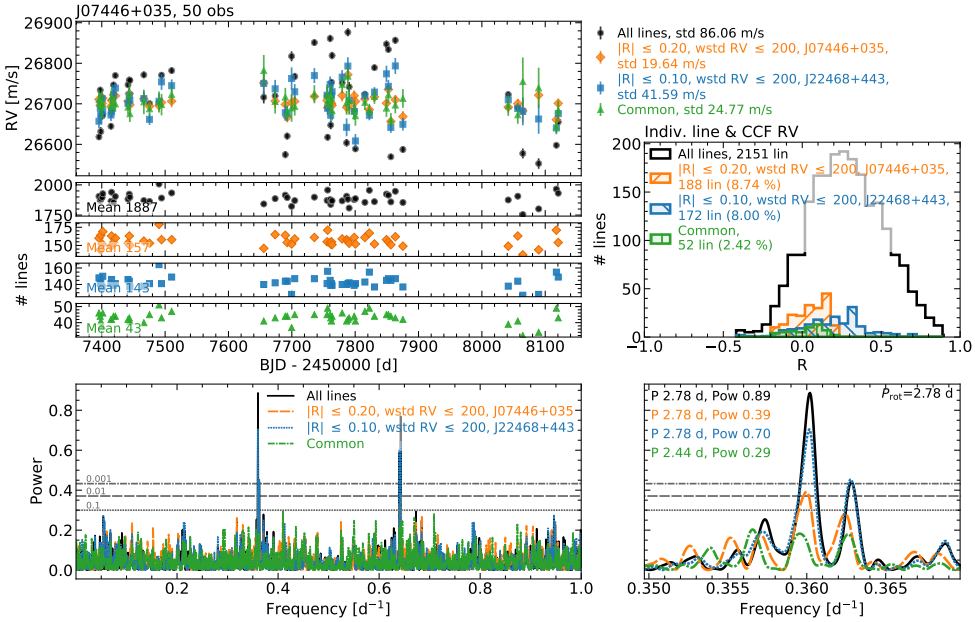

Figure 4.59: Same as 4.56 but using the following data sets: initial line list (black), lines that minimise the RV scatter of J07446+035 (orange), lines that minimise the RV scatter of J22468+443 (blue) and common lines in the two previous sets (green).

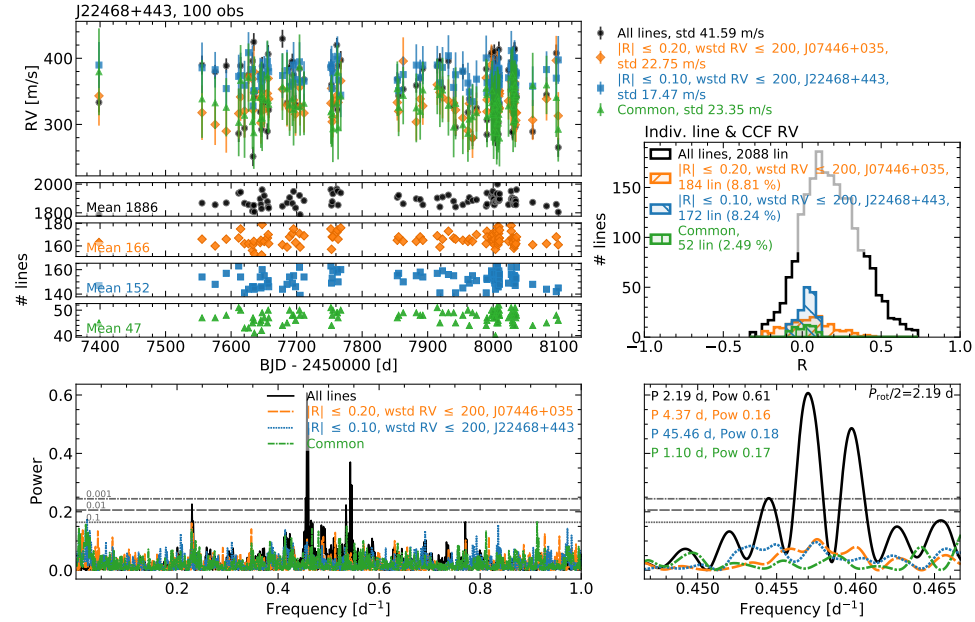

Figure 4.60: Same as Fig. 4.59 but for J22468+443.

4.7.3 J22468+443 and J05019+011

For the pair J22468+443 and J05019+011, the correlation between R values is low (R = 0.3, Fig. 4.61). There are 40 common selected lines, 18 − 23% of the 172 and 218 lines that minimise the RV scatter of the stars, which is 2.0 % of the initial 1963 lines.

For J22468+443, using the 'best' data set of J05019+011 (blue) results in a decrease in the time series RV scatter compared with the initial one (1.4 times smaller), but not as small as the minimum obtained with its own 'best' data set (2.4 times smaller), and the periodogram continues to show a significant peak at half $P_{\rm rot}$, although with less power as initially. For J05019+011, using the 'best' J22468+443 data set (orange) does not decrease the RV scatter significantly (1.2 times smaller compared to 2.5 times smaller for its own best data set), but the periodogram does no longer show a peak at $P_{\rm rot}$. Using the common selected lines, for both stars the RV scatter decreases, but not as much as using their own 'best' data set, and the periodogram does not show any significant peaks.

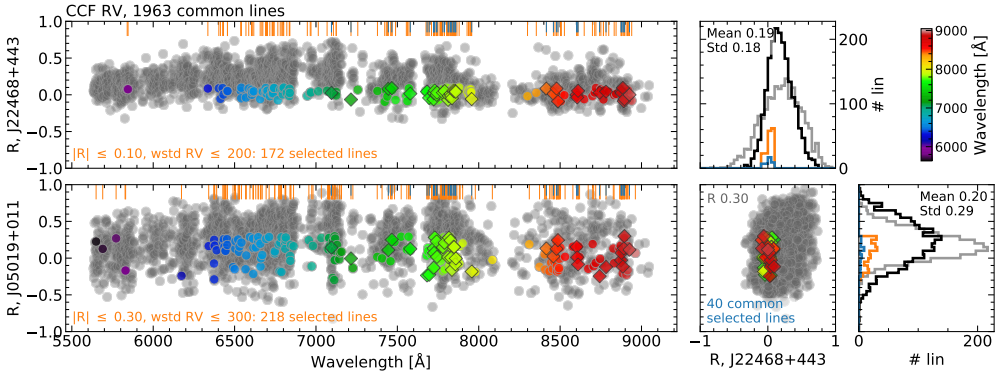

Figure 4.61: Same as Fig. 4.55 but for J22468+443 and J05019+011.

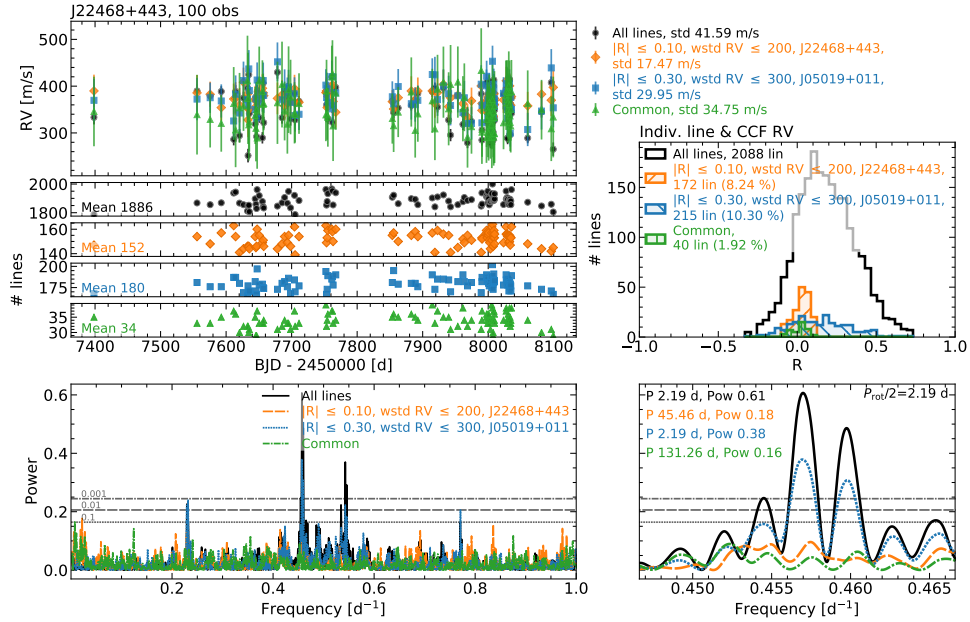

Figure 4.62: Same as 4.56 but for J22468+443 and using the following data sets: initial line list (black), lines that minimise the RV scatter of J22468+443 (orange), lines that minimise the RV scatter of J05019+011 (blue) and common lines in the two previous sets (green).

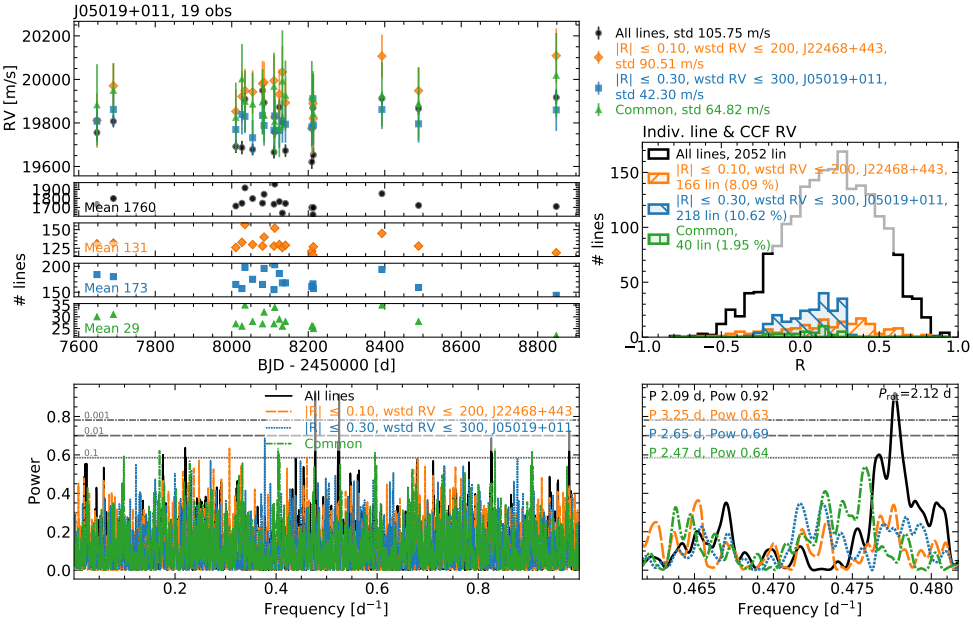

Figure 4.63: Same as 4.62 but for J05019+011.

4.7.4 J15218+209 and J11201-104

For the other pair of stars, J15218+209 and J11201-104, the correlation between R values is even lower than for the mid-type pairs (R $\sim$ 0.2, Fig. 4.64). The selection cuts that result in the smallest RV scatter are $|R| \leq 0.1$ and wstd RV $\leq 300\,\mathrm{m\,s^{-1}}$ for J15218+209 and $|R| \leq 0.2$ and wstd RV $\leq 200\,\mathrm{m\,s^{-1}}$ for J11201-104, which correspond to 355 lines for J15218+209 and 482 lines for J11201-104. Of these, 122 lines are common in both data sets ($25-34\,\%$ of the selected lines, and 7.6 % of the initial 1610 lines).

In both cases, using the 'best' data set of the other star to recompute the RVs results in a time series scatter very similar to the initial one (Fig. 4.65, blue, for J15218+209, and Fig. 4.66, orange, for J11201-104). In the case of J15218+209, the periodogram also looks similar to the original one, with a significant peak at P_{rot}. For J15218+209, the RVs computed with the common selected lines (green) have a scatter smaller than the initial one (1.3 times smaller), but larger than the one obtained using the 'best' line set of the star itself (which was 2.7 times smaller, orange data set). In the case of J11201-104, the scatter of the common selected lines RVs is larger than the original one.

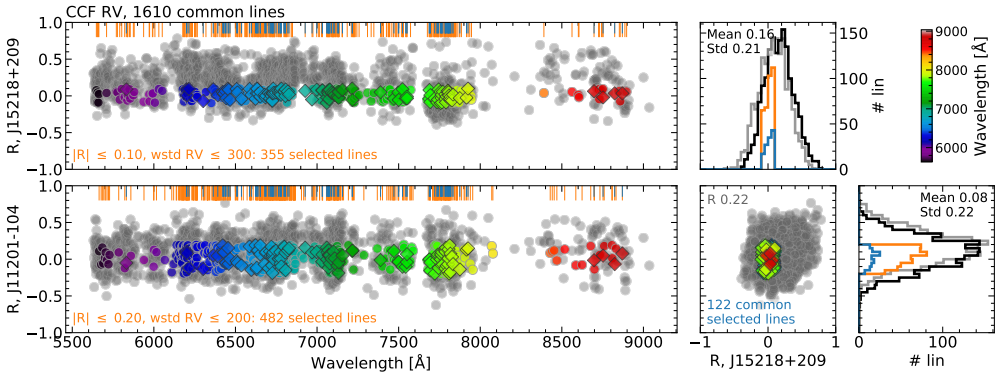

Figure 4.64: Same as Fig. 4.55 but for J15218+209 and J11201-104.

4.7.5 Overview of the results

From this analysis we see that the same lines in different stars show different correlation strengths (i.e. different R values). The R values of the pairs of stars J152918+209 and J11201-104, J07446+035 and J05019+011, and J22468+443 and J05019+011, show weak correlations (R from 0.2 to 0.3), while for the pair J07446+035 and J22468+443, the R values are more similar ($R = 0.6$).

If we focus on the line sets for which the RV activity signal is most strongly mitigated, in general the number of lines common in the star pairs is low. For the pairs of mid-type

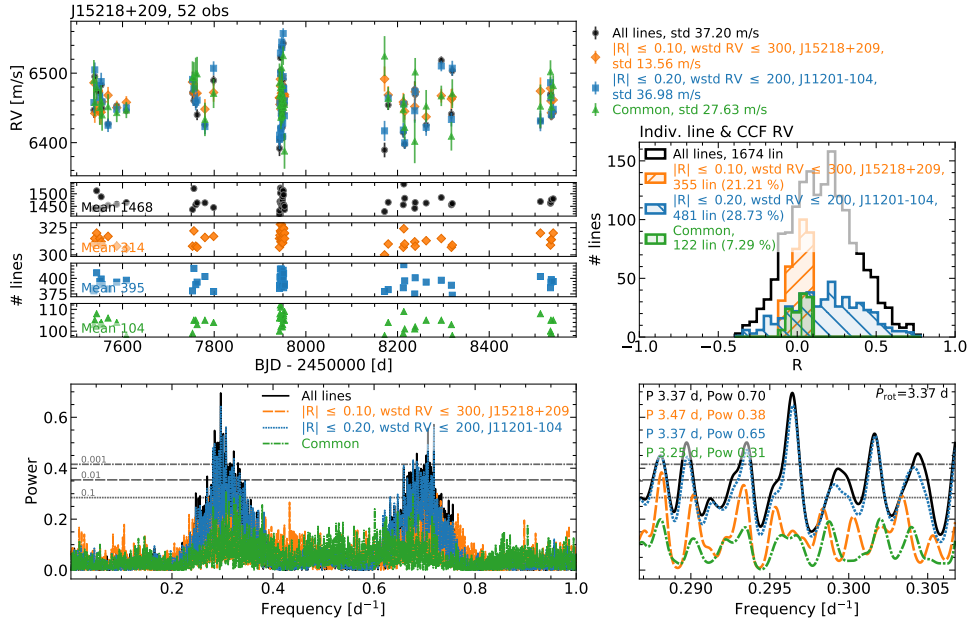

Figure 4.65: Same as 4.56 but for J15218+209 and using the following data sets: initial line list (black), lines that minimise the RV scatter of J15218+209 (orange), lines that minimise the RV scatter of J11201-104 (blue) and common lines in the two previous sets (green).

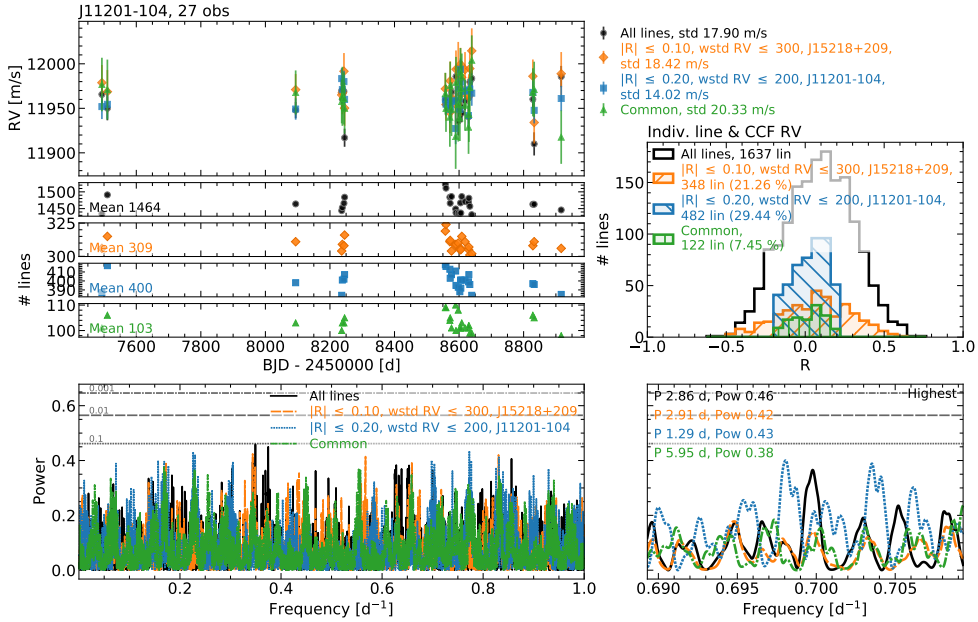

Figure 4.66: Same as Fig. 4.65 but for J11201-104.

targets (J07446+035 and J05019+011, J07446+035 and J22468+443, and J22468+443 and J05019+011), only 2.0 % to 2.6 % of the initial lines are common in the 'best' sets of the respective stars. For the early-type pair (J152918+209 and J11201-104), this number is larger, of almost 8 % (but their 'best' line sets already have a few hundreds of lines more than those of the mid-type stars). These 'common' sets have $\sim$ 50 lines in the case of the mid-type pairs, and 122 lines for the early-type one.

For these pairs of stars, we also used sets of inactive lines based on the correlation of one of the stars to recompute the RVs of the other star. Because of this lack of correspondence between the correlation strength of the same lines in the different stars, this results in small changes in the RV time series. In general, the scatter decreases, but not as much as using a set of inactive lines based on the correlations of the star itself, and the periodogram peaks related to $P_{\rm rot}$ remain significant.

We also recomputed RVs using inactive lines common in the sets that minimised the RV scatter in the two stars of the pair. As mentioned above these sets of common inactive lines have from $\sim$ 50 to 122 lines, depending on the pair of stars, which represents from 18 to 34 % of the lines in the 'best' sets, a significant decrease in the number of lines. In general, using these sets results in RVs and periodograms similar to those obtained using the 'best' set of lines from the star itself, but with slightly larger RV scatters.

The stars in the two groups used here all show high levels of activity, but do not have the exact same properties. The spectral types, rotational velocities, and metallicities are similar but not identical. Based on the results for these stars, we are not able to obtain a general set of lines, even when considering spectral type intervals, for which the effect of activity in the RVs is minimised.

4.8 Summary

In this chapter we have studied activity effects on individual spectral lines in a set of six active early- and mid-type M dwarfs of the CARMENES GTO sample. Specifically, we have analysed the correlation strength between the RV of individual lines, which we selected with the `RACCOON` pipeline, and spectroscopic activity indicators, following a method analogous to that described in Dumusque (2018). Of the different indicators analysed (total RV of the spectrum, CCF FWHM, contrast and BIS, CRX, DLW, and $I_{\rm H\alpha}$), we find that only the total RV, BIS, and CRX show clear linear correlations with the RV of the individual lines.

Using the strength of the correlation, which we measure with the Pearson's correlation coefficient R, we classified the lines according to their sensitivity to activity. We find that the R coefficient is a biased indicator of the correlation with activity when

measurements have low precisions. This is true for lines located at low S/N regions of the spectrum, especially in the bluer region, which leads to large error bars.

We then used different sets of lines to recompute the RV of each observation. With lines that had a strong correlation with the activity indicators, we obtained activity-dominated RVs, while with sets of lines that showed weak correlations, we decrease the effect of activity in the RV. We evaluate the decrease in activity by looking at the total RV scatter and the presence of significant activity-related signals in the RV periodogram. We are able to effectively find lines with different correlation strengths and mitigate the activity effect on the RV of five stars of the sample, J07446+035, J05019+011, J2246+443, J15218+209, and J11201-104. The maximum decrease in RV scatter obtained using sets of inactive lines is of $\sim$ 2 to 5 times the initial one. These sets have of the order of 100 lines, while initially we started with the order of 1000 lines.

We also analysed if the same lines show similar correlation strengths between the RV and the activity indicators in different stars, to see if a set of inactive lines could be generalised for stars with similar characteristics. We made pairwise comparisons of the correlation strength of the mid-type M dwarfs, J07446+035, J05019+011, and J22468+443, and, separately, the early-type M dwarfs, J152918+209 and J11201-104. We find that the same lines in different stars, in general, do not show similar correlation strengths, i.e., there is a different activity dependence for the same lines in different stars, even if the stars are similar. Such lack of consistency could be due to the fact that most absorption features in M dwarf spectra are blended lines rather than well-isolated, single lines. Lines in different stars could be blended to varying degrees, and the combination of the activity-affected profiles of the blended lines could result in different RV variations depending on the specific target star. Further analysis is needed to understand these results.

Using the 'best' set of inactive lines obtained for a specific star to recompute RVs of another target star, even if they have similar properties, is less effective (i.e. results in a less significant reduction of the RV activity signal) than using a line set obtained from the target star itself. Using only the lines common in the 'best' sets results in better results, but, since the number of common lines is very small, the RV scatter is still large, probably due to the fact that noise starts to dominate. Therefore, to achieve the maximum mitigation of activity, it seems that the best strategy is to select lines based on correlations of each individual star.

Chapter 5

Conclusion and future prospects

Stellar activity poses one of the main problems in current radial velocity (RV) surveys that aim at detecting and studying small exoplanets. In this thesis, we have studied the effects of activity in M dwarf spectroscopic measurements obtained with the CARMENES spectrograph as part of the scientific exploitation of its GTO program. In the following, we summarise our main conclusions and comment on how the work presented here could be expanded.

5.1 Summary and conclusions

Radial velocities and activity from cross-correlation with masks

We started this work by developing a procedure to compute RVs and activity indicators using the cross-correlation function (CCF) technique. In this method, the observed spectrum is cross-correlated with a simplified spectral template called weighted binary mask to build an average absorption line profile, the CCF. We provide a detailed description of this technique in Chapter 2. First, we developed a methodology to create weighted binary masks from spectroscopic templates of stars. For such purpose, we used the spectral templates to select absorption lines (which we simply identify as minima in the template, without using any line database) with profiles meeting certain criteria on depth, width, and asymmetry. We then assigned a specific weight based on their RV content to each selected line, considering their depth and width. We also applied the cross-correlation procedure to high-resolution echelle observations such as those obtained with CARMENES or HARPS, including the computation of the CCF with a mask, and the modelling of the CCF profile to extract RVs and standard activity indicators, together with their associated errors. Our methodology was implemented in the code `RACCOON`, which we have made available to the community.

Here, we applied our new CCF methodology to over 300 M dwarfs observed with CARMENES, but it is also suitable to be used in observations of other spectral types observed with similar instruments. We created masks from templates of stars with dif-

ferent M spectral-subtypes and rotational velocities, which cover the full CARMENES M dwarf sample. We computed CCFs of all the stars using these masks, and derived RVs and three parameters related to the average stellar activity effects on the absorption lines: full-width-at-half-maximum (FWHM), contrast, and bisector inverse slope (BIS) of the CCF.

We find that the CCF parameters depend on the mask used, and in general are more precise if the mask is created from a stellar template with similar properties as the target star. We also observe a decrease in the precision of the CCF parameters with the stellar rotation of the star, because lines become increasingly broader and the number of useful lines in the mask drastically falls. Moreover, fast rotators tend to have higher levels of activity, which further affects the line profile introducing deformations biasing the final parameters.

Due to their low effective temperature, the spectrum of M dwarfs contains a large number of atomic and molecular lines which are usually not well isolated and present severe blends. This complicates the process of building cross-correlation masks, because the identification of lines is not as clear as for earlier spectral types. For this reason, other RV computation methods based on matching a whole spectral template to the observations (rather than just a set of lines which are not completely well defined) are usually applied for M dwarfs, such as the `SERVAL` pipeline used in CARMENES. We compared the RVs obtained with the CCF technique implemented here and the ones obtained with the template-matching pipeline `SERVAL`. As expected, in general `SERVAL` performs better than the CCF method because it extracts the RV content of a larger range of the stellar spectrum compared to the CCF, which is focused only on a set of lines. However, in the case of faint stars or stars with a small number of observations, the CCF is able to deliver more precise results than `SERVAL`. This happens because the template used by `SERVAL` is built from the observations of the target star itself, which results in a low signal-to-noise (S/N) template in these cases, while the masks built for the CCF were based on high S/N templates of other stars with similar properties. These results highlight the importance of the template used to compare the spectra against.

Activity indicators across M dwarfs

Stellar activity indicators such as those derived from the CCF are routinely used to identify activity-related signals in the RVs and estimate stellar rotation periods. However, not all indicators trace exactly the same activity effects, and are not always effective in all stars. In Chapter 3, we studied the behaviour of several spectroscopic indicators of stellar activity in a sample of M dwarfs, including the ones we computed from the CCF, to see if there is a common behaviour depending on the properties of the stars. We looked for periodic signals related to the stellar rotation period in the

RVs and spectroscopic activity indicators derived from the CARMENES spectra by analysing the periodograms of their time series.

We find signals related to stellar activity in about half of the stars of our sample (56 out of 98 stars) in all ranges of mass and average activity level. Within this sample of 56 stars, we are able to find a general behaviour for different indicators, depending on the mass and the activity level of the star analysed. The RVs show activity-related signals for most of them, even stars with low levels of activity. The emission flux of the chromospheric lines Hα and the Ca II IRT is especially useful in stars with low activity levels ($pEW'(\mathrm{H}\alpha) \gtrsim -0.1$). The CCF BIS and the chromatic index (CRX) show the opposite behaviour, they better trace activity for the most active stars ($pEW'(\mathrm{H}\alpha) \lesssim -0.1$). Indicators such as the CCF FWHM and the differential line width (DLW, derived from the template matching technique) show a similar behaviour for all the sample of stars, but are the most effective for high-activity, low-mass stars (mass $\lesssim 0.4\,\mathrm{M}_\odot$). Stars with no detections related to activity are mostly those with low levels of activity or very low-mass, faint stars.

Regarding the RV scatter of the observations, as expected, in general small scatters correspond to stars with no detections, although we find activity-related signals in stars with scatters as small as $\sim 2\,\mathrm{m\,s^{-1}}$. We also see a gradient of the stellar mass with the RV scatter: the mass of the stars decreases with the RV scatter, which could indicate some difference in the activity present in high- and low-mass stars. This also implies that late M dwarfs seem to be better suited to planetary searches than earlier-type M dwarfs, given their lower RV scatter.

These results emphasise the importance of considering different indicators of stellar activity when studying the variability of RV measurements. As seen before, using only limited sets of activity indicators can easily lead to interpret as true planet candidates signals that are actually activity-related. Such false positives can be mitigated by using the adequate sets of indicators. Generalisations such as the one presented here as a function of the mass and activity of the star could be used as a starting guide when assessing the impact of activity on spectroscopic measurements, but complete analyses are desired since the presence of activity could also depend on observational constraints or the specific characteristics of the stellar active regions, which so far are mostly unknown in M dwarfs.

Sensitivity to activity of M dwarf spectral lines

Finally, we analysed the effects that stellar activity has on the different lines of the stellar spectrum. The different features present in the spectrum are created by the different components present on the outer layers of the star, which react in different ways to the changes occurring on active regions, i.e., they have different sensitivities to

the temperature, magnetic field, and velocity variations of spots and faculae. Therefore, we expect that different lines in the stellar spectrum will show different sensitivity to stellar activity. In Chapter 4, we studied the sensitivity to activity of different lines in active M dwarfs, and used such information to recompute RVs in which the activity signal is mitigated or enhanced.

First, we used the methodology previously developed in Chapter 2 to create cross-correlation masks to select a set of lines, and computed their individual RV by comparing their centroid with a reference (which we took from a spectral template). To classify the lines according to how sensitive they are to activity variations, we then analysed the correlation between the line RV and an activity indicator. We tested different indicators, and found that the best ones to use were the global RV of the spectrum (if it contains only variability due to activity), CCF BIS, and CRX, because they display linear correlations with the individual line RVs. Moreover, as we saw in Chapter 3, BIS and CRX are some of the most effective indicators in tracing activity in very active stars, as is the case of the stars under analysis here. By selecting lines that show no correlation with the activity indicators (i.e. non-sensitive lines) and recomputing the global RV of each observation, we are able to decrease the RV scatter and the modulation due to activity. Also, we can enhance the activity signal by selecting lines that show strong correlations with the activity indicators. We are able to successfully apply this method to five early- and mid-type active M dwarfs, for which the RV scatter decreases from $\sim$ 2 to 5 times using sets of non-sensitive lines.

We also find that the lines classified as non-sensitive to activity differ from star to star, even for those with similar spectral types and activity levels. Using sets of non-sensitive lines selected for a specific star to recompute RVs of another target results in a less efficient mitigation of the activity signal than if the lines are selected using the target star itself. This indicates that a generalisation of a set of inactive lines achieving the maximum decrease in the activity modulation does not appear to be possible in M dwarfs, and that the best strategy is to select lines based on the data of each specific target star.

5.2 Future prospects

We have seen that stellar activity is present in spectroscopic observations of most M dwarf stars, even quiet ones with low activity levels and small RV variations at the $\mathrm{m\,s^{-1}}$ level. A better understanding of stellar activity and its effects on the observed spectra is therefore necessary if we want to measure unbiased RVs that can be effectively used to discover and characterise small exoplanets, as well as gain insight on the stars themselves. This thesis contributes to the current efforts being done in this direction with a study of the behaviour of different spectroscopic indicators of stellar activity,

and an analysis of the activity effects on the observed spectral lines, which allow us to better comprehend and improve our RV measurements. The research presented here could be extended and improved in several ways, some of which we discuss below.

Accounting for activity during RV extraction

Regarding the way we extract RVs from our observed spectra, we have seen that the reference used to compare the observed spectra against is critical in the final precision and the presence of activity modulations in the derived RVs. Weighted binary masks used to compute CCFs, full spectral templates used in template matching approaches, or just a list of reference wavelengths used to compare their position, all will deliver biased measurements if the stellar activity content of the observations is not taken into account. In Chapter 4, we showed that, in a small sample of active stars with relatively large RV scatters, it is possible to select specific spectral lines to recompute RVs that are affected by stellar activity to varying degrees. The method we used to recompute the global RVs was to simply average the RVs of the selected individual lines, but we could also implement these line selections in the method used to built cross-correlation masks in Chapter 2, or in the templates used in `SERVAL`, to study if these approaches deliver even more precise RVs. By doing this, we could also test if stellar activity indicators such as the ones derived from the CCF or the CRX also vary and show a smaller dependence with the recomputed RV and the activity signals, to further probe the presence of activity.

Improving spectral line RV and expanding activity correlations

We also saw that, for relatively low-activity stars or stars with smaller RV scatters, the method presented in Chapter 4 was not able to distinguish between active and inactive lines, and could not improve RV time series measurements by using subsets of lines. This could be because the precision of the individual line RVs is not good enough to deliver global RV time series with smaller scatters. It is also possible that the correlations with the activity indicators are not reliable, either because of the low precision of the RVs or the indicators, or because of the way we quantify the correlations, which could hamper the classification of lines according to their sensitivity to activity.

As mentioned above, the RV of the individual lines was computed by fitting a Gaussian model to the lines, finding their centroids, and comparing them to a list of reference wavelengths. We know that, in most cases, our lines do not have clear Gaussian profiles, so we expect to obtain more precise individual RVs by fitting other kinds of functions or a model of the spectrum to the region around each individual line. This could improve the precision of individual line RVs, and the reliability of the correlations between the line RVs and the activity indicators, allowing for a better classification of the lines' sensitivity to activity.

With respect to the correlations, to quantify them we used the Pearson's correlation coefficient R, which measures the strength of linear dependencies (proportional changes between variables). We saw that the R coefficient could be biased by the precision of the RV measurements, as it did not provide reliable values in lines with large RV scatters (mainly lines in low-S/N regions). To account for that, we could use different R limits as a function of the local S/N of the spectrum. The relationship between the individual line RVs and the three final indicators used (global RV, CCF BIS and CRX) appears to be linear, but, to further improve the accuracy of the correlations, we could also test if other methods are able to better capture these dependencies, such as the Spearman's rank correlation coefficient. This correlation coefficient assesses the strength of a monotonic relationship between two variables and hence, is not limited to linear dependencies. The other activity indicators investigated (CCF FWHM, contrast, DLW, and chromospheric lines) show clearly non-linear relationships with the individual line RVs. If further methods to quantify this dependencies are studied, these indicators could also be used to assess the sensitivity to activity of the different lines. This could be relevant especially for stars with low levels of stellar activity, for which we saw in Chapter 3 that the emission flux of several chromospheric lines is the most effective indicator to trace stellar activity when performing a periodogram analysis. Also, as mentioned at the end of Sect. 2.2, the different variations on how to quantify the asymmetry in the CCF proposed in the literature could also be explored.

The analysis of the behaviour of the different activity indicators in Chapter 3 could also be extended by studying their correlation with the RVs and their difference in phase. As happens in the case of the individual line RVs, in several stars, only the CCF BIS and the CRX show linear correlations with the total RV, while the other indicators display more complicated relationships, which seem to stem from phase differences (e.g. Santos et al., 2014; Perger et al., 2017).

Exploring spectral line properties

The line selection of Chapters 2 and 4 follows an empirical approach. We initially select minima present in the spectrum based on their profile and then classify the lines according to their correlation with an activity indicator, without any knowledge of the lines origin. We could cross-match the lines selected in our data sets with line databases to study any dependencies between the sensitivity to activity and physical parameters (such as the excitation potential or the element or molecule that originated the line), or directly analyse if the shape of the line profiles (their depth, width or asymmetry) are related to the sensitivity of the lines (see e.g. Wise et al., 2018; Cretignier et al., 2020). A more in depth study of the lines selected could also be applied to the creation of CCF masks (see e.g. Rainer, Borsa, and Affer, 2020).

Near-infrared wavelength range

In the analyses of activity indicators and the activity effects in individual lines performed in Chapters 3 and 4, we only used information from the visible observations taken by CARMENES because in general, we found them to perform better than the measurements taken with the near-infrared arm. After validating these type of analyses with the visible observations, we plan on expanding them by including the simultaneous near-infrared data. This would allow us to evaluate any variations between spectroscopic indicators derived from distinct wavelength ranges, add new chromospheric lines present in the near-infrared, as well as quantify differences between how activity affects stellar lines in a broader wavelength range.

Telluric-corrected spectra

As already mentioned in Chapter 2, another way to improve the precision of our RV measurements would be to use spectra that have been corrected for the telluric features of the Earth's atmosphere (Nagel et al., submitted). Currently, when computing RVs, the regions affected by telluric absorption or emission are simply excluded or downweighted. Therefore, using telluric-free observations would increase the number of useful lines, as well as reduce any possible biases due to telluric contamination for which we did not account for, resulting in better precisions. This is particularly relevant for the near-infrared data, where there is a high presence of telluric contamination.

5.3 Final considerations

The work presented here is a step forward towards resolving the problem of stellar activity in planet searches. We have performed an analysis of the behaviour of spectroscopic activity indicators that give new insight into how activity manifests in different type of stars. Such a study improves the methodology to discriminate between activity and planetary signals, and reduces the detection of false planetary candidates. We have also presented an analysis of the sensitivity to activity of different individual lines in M dwarf stars, which provides a methodology for exploiting the wealth information contained in the stellar spectra. We have shown that it is possible to identify lines that correlate with activity to varying degrees in several active M dwarf stars, and that this information can be used to effectively mitigate or enhance the effect of activity on RV measurements. With the current and next-generation of high-resolution spectrographs reaching increasingly better RV precisions, stellar activity becomes the ultimate obstacle in RV observations. Studies about activity effects on spectroscopic observations such as the ones presented in this thesis will therefore be key in the quest of small Earth-like exoplanets.

Appendix A

Absolute RVs

Table A.1: Absolute RV (RV_{abs}), weighted mean RV from the VIS CCF measurements (RV_{CCF}) and gravitational redshift (v_{grav}).

Karmn	RV_{abs} $[m\,s^{-1}]$	RV_{CCF} $[m\,s^{-1}]$	σ_{CCF} $[m\,s^{-1}]$	σ_{mask} $[m\,s^{-1}]$	v_{grav} $[m\,s^{-1}]$
J00051+457	-1203 ± 107	-561 ± 23	0.52	23	642 ± 31
J00067-075	-40679 ± 113	-40123 ± 20	0.38	20	556 ± 48
J00162+198E	-2242 ± 109	-1625 ± 24	0.69	24	617 ± 35
J00183+440	10849 ± 107	11481 ± 23	0.20	23	632 ± 31
J00184+440	10089 ± 111	10676 ± 25	0.19	25	587 ± 40
J00286-066	-13342 ± 108	-12711 ± 24	0.51	24	631 ± 33
J00389+306	-1261 ± 108	-626 ± 25	0.53	25	634 ± 32
J00570+450	5644 ± 108	6271 ± 25	0.65	25	627 ± 33
J01013+613	6606 ± 108	7237 ± 23	1.07	23	631 ± 32
J01019+541	-5788 ± 168	-5203 ± 128	87.71	93	585 ± 43
J01025+716	606 ± 108	1246 ± 25	0.29	25	640 ± 32
J01026+623	-6945 ± 107	-6304 ± 23	0.56	23	642 ± 30
J01033+623	-7132 ± 131	-6521 ± 77	60.38	47	610 ± 38
J01048-181	10799 ± 111	11373 ± 20	1.12	20	574 ± 44
J01125-169	27271 ± 112	27846 ± 23	0.31	23	574 ± 44
J01339-176	5504 ± 109	6120 ± 24	1.87	24	616 ± 35
J01352-072	8685 ± 237	9335 ± 212	190.67	93	650 ± 33
J01433+043	-26866 ± 108	-26232 ± 23	1.69	23	633 ± 33
J01518+644	-13703 ± 255	-13063 ± 25	0.97	25	640 ± 233
J02002+130	-29411 ± 111	-28832 ± 25	1.93	25	579 ± 42
J02015+637	-85028 ± 109	-84391 ± 25	0.80	25	637 ± 35
J02070+496	18109 ± 108	18735 ± 25	1.12	25	625 ± 33
J02088+494	-10368 ± 123	-9735 ± 64	26.87	58	633 ± 33
J02123+035	-3526 ± 107	-2889 ± 23	0.46	23	637 ± 31
J02222+478	-39154 ± 106	-38511 ± 18	0.63	18	643 ± 30

Notes. The RV_{abs} uncertainty is the quadratic sum of the uncertainties from the RV scatter (σ_{CCF}), the mask zero-point (σ_{mask}), the gravitational redshift (σ_{grav}), and the convective blueshift ($\sigma_{conv} = 100\,m\,s^{-1}$). The uncertainty in RV_{CCF} is the quadratic sum of the scatter and mask zero-points uncertainties, which are also listed separately. The σ_{grav} uncertainty comes from error propagation of Eq. 2.16. See Sect. 2.5.7 for details.

Table A.1: Continued.

Karmn	RV_{abs} $[m\,s^{-1}]$	RV_{CCF} $[m\,s^{-1}]$	σ_{CCF} $[m\,s^{-1}]$	σ_{mask} $[m\,s^{-1}]$	v_{grav} $[m\,s^{-1}]$
J02336+249	-7267 ± 109	-6662 ± 24	2.32	24	605 ± 37
J02358+202	19 ± 108	661 ± 23	0.91	23	642 ± 33
J02362+068	25356 ± 109	25971 ± 24	0.51	24	615 ± 35
J02442+255	29675 ± 108	30304 ± 25	0.37	25	629 ± 33
J02519+224	8501 ± 131	9142 ± 78	51.95	58	640 ± 32
J02530+168	67889 ± 118	68417 ± 28	0.28	28	528 ± 56
J02565+554W	75667 ± 107	76313 ± 23	1.32	23	645 ± 29
J03133+047	27572 ± 110	28156 ± 20	0.76	20	585 ± 42
J03181+382	-5201 ± 107	-4557 ± 23	0.65	23	644 ± 29
J03213+799	-14220 ± 108	-13586 ± 23	0.62	23	634 ± 32
J03217-066	25486 ± 107	26125 ± 23	1.54	23	639 ± 32
J03463+262	34941 ± 105	35585 ± 18	0.55	18	644 ± 28
J03473-019	17235 ± 107	17876 ± 21	6.19	20	641 ± 32
J03531+625	-120947 ± 108	-120319 ± 25	0.74	25	628 ± 33
J04153-076	-44197 ± 109	-43578 ± 24	1.23	24	619 ± 36
J04198+425	20940 ± 132	21486 ± 70	23.46	66	546 ± 49
J04219+213	18174 ± 106	18819 ± 19	5.97	18	645 ± 31
J04225+105	36078 ± 108	36715 ± 25	0.70	25	637 ± 32
J04290+219	-36205 ± 105	-35558 ± 14	0.35	14	647 ± 30
J04311+589	27810 ± 109	28429 ± 24	0.94	24	619 ± 36
J04376+528	33268 ± 105	33913 ± 14	0.45	14	645 ± 28
J04376-110	-7749 ± 107	-7111 ± 23	0.65	23	638 ± 31
J04429+189	25248 ± 107	25889 ± 23	0.96	23	641 ± 32
J04429+214	2171 ± 108	2803 ± 25	1.19	25	632 ± 33
J04472+206	23345 ± 330	23976 ± 312	297.85	93	631 ± 35
J04520+064	-9747 ± 108	-9118 ± 25	0.91	25	629 ± 34
J04538-177	-15460 ± 107	-14826 ± 23	0.71	23	634 ± 32
J04588+498	-34999 ± 106	-34354 ± 18	1.46	18	645 ± 28
J05019+011	19060 ± 110	19706 ± 31	23.35	21	645 ± 33
J05019-069	41378 ± 110	41967 ± 24	1.26	24	589 ± 40
J05033-173	14575 ± 109	15190 ± 25	1.05	25	616 ± 35
J05062+046	18442 ± 130	19083 ± 76	48.50	58	641 ± 33
J05084-210	21563 ± 253	22214 ± 230	222.38	58	650 ± 35
J05127+196	-26001 ± 108	-25365 ± 23	0.62	23	636 ± 32
J05280+096	59697 ± 109	60305 ± 25	0.78	25	608 ± 36
J05314-036	7685 ± 114	8329 ± 23	0.48	23	644 ± 51
J05348+138	36788 ± 108	37416 ± 25	0.57	25	629 ± 33
J05360-076	28462 ± 108	29086 ± 24	0.68	24	625 ± 34
J05365+113	20869 ± 106	21514 ± 18	1.08	18	645 ± 29
J05366+112	20912 ± 109	21530 ± 24	2.68	24	618 ± 35
J05394+406	-6877 ± 118	-6338 ± 29	8.98	28	539 ± 55
J05415+534	1176 ± 107	1818 ± 23	0.60	23	642 ± 29
J05421+124	105065 ± 109	105673 ± 24	0.34	24	608 ± 36
J06000+027	29294 ± 109	29903 ± 25	6.74	24	609 ± 37
J06011+595	1073 ± 109	1687 ± 25	0.34	25	614 ± 35

Table A.1: Continued.

Karmn	RV_{abs} $[m\,s^{-1}]$	RV_{CCF} $[m\,s^{-1}]$	σ_{CCF} $[m\,s^{-1}]$	σ_{mask} $[m\,s^{-1}]$	v_{grav} $[m\,s^{-1}]$
J06024+498	19687 ± 111	20259 ± 20	0.70	20	572 ± 44
J06103+821	-2582 ± 107	-1947 ± 23	0.60	23	635 ± 32
J06105-218	3539 ± 108	4182 ± 18	0.60	18	642 ± 36
J06246+234	-12244 ± 111	-11656 ± 24	1.06	24	587 ± 41
J06318+414	3717 ± 162	4352 ± 123	79.83	93	635 ± 35
J06371+175	-59392 ± 106	-58754 ± 18	0.70	18	638 ± 31
J06396-210	-8039 ± 117	-7426 ± 24	3.77	24	613 ± 55
J06421+035	81557 ± 108	82187 ± 25	0.50	25	630 ± 33
J06548+332	22025 ± 108	22654 ± 25	0.22	25	629 ± 33
J06574+740	-3328 ± 182	-2688 ± 105	87.98	58	641 ± 110
J06594+193	-30072 ± 112	-29510 ± 20	0.76	20	562 ± 47
J07033+346	1415 ± 109	2029 ± 24	4.42	24	613 ± 36
J07044+682	-51400 ± 108	-50766 ± 25	0.94	25	634 ± 33
J07274+052	17274 ± 109	17895 ± 25	0.11	25	622 ± 35
J07287-032	548 ± 108	1180 ± 25	0.84	25	632 ± 32
J07319+362N	-1705 ± 108	-1071 ± 25	1.02	25	634 ± 33
J07353+548	-15901 ± 108	-15270 ± 23	1.22	23	631 ± 32
J07386-212	-29804 ± 109	-29183 ± 25	1.66	25	621 ± 34
J07393+021	18884 ± 106	19529 ± 18	0.65	18	645 ± 29
J07403-174	-29340 ± 119	-28811 ± 32	1.25	32	528 ± 55
J07446+035	26077 ± 111	26707 ± 32	11.35	30	630 ± 36
J07472+503	-15387 ± 116	-14771 ± 47	6.74	47	615 ± 35
J07558+833	7027 ± 119	7642 ± 53	24.29	47	615 ± 36
J07582+413	-21958 ± 109	-21342 ± 25	0.42	25	616 ± 35
J08119+087	13833 ± 111	14416 ± 24	0.67	24	583 ± 42
J08126-215	8065 ± 109	8680 ± 24	0.86	24	615 ± 35
J08161+013	61229 ± 107	61866 ± 23	0.51	23	637 ± 32
J08293+039	21863 ± 108	22504 ± 25	0.91	25	641 ± 31
J08298+267	9372 ± 121	9936 ± 48	10.06	47	564 ± 49
J08315+730	-91460 ± 109	-90841 ± 24	1.16	24	618 ± 35
J08358+680	18234 ± 108	18865 ± 25	0.82	25	630 ± 33
J08402+314	66074 ± 109	66692 ± 25	1.05	25	618 ± 34
J08409-234	86913 ± 108	87547 ± 26	7.84	25	635 ± 33
J08413+594	5560 ± 112	6122 ± 20	3.89	20	561 ± 47
J08526+283	26561 ± 109	27176 ± 24	1.39	24	614 ± 36
J08536-034	-7712 ± 157	-7225 ± 100	90.68	42	487 ± 68
J09003+218	7551 ± 132	8114 ± 71	53.57	47	564 ± 49
J09005+465	1387 ± 110	1989 ± 24	0.98	24	601 ± 38
J09028+680	-25629 ± 109	-25014 ± 24	1.32	24	615 ± 35
J09033+056	-28696 ± 118	-28118 ± 44	33.75	28	578 ± 45
J09133+688	13001 ± 159	13647 ± 25	1.01	25	646 ± 121
J09140+196	12245 ± 109	12885 ± 29	14.98	25	640 ± 32
J09143+526	10041 ± 108	10686 ± 18	0.91	18	645 ± 35
J09144+526	11253 ± 107	11898 ± 18	0.55	18	645 ± 33
J09161+018	-13372 ± 118	-12750 ± 53	23.68	47	622 ± 35

Table A.1: Continued.

Karmn	RV_{abs} $[m\,s^{-1}]$	RV_{CCF} $[m\,s^{-1}]$	σ_{CCF} $[m\,s^{-1}]$	σ_{mask} $[m\,s^{-1}]$	v_{grav} $[m\,s^{-1}]$
J09163-186	13927 ± 107	14566 ± 23	1.59	23	639 ± 32
J09307+003	45245 ± 109	45867 ± 25	1.22	25	622 ± 34
J09360-216	-35459 ± 108	-34833 ± 25	0.79	25	627 ± 34
J09411+132	10519 ± 107	11158 ± 23	0.74	23	639 ± 31
J09423+559	14366 ± 108	14996 ± 25	1.64	25	631 ± 33
J09425+700	6058 ± 108	6699 ± 23	1.36	23	641 ± 32
J09428+700	5718 ± 108	6354 ± 25	1.62	25	636 ± 33
J09439+269	33547 ± 108	34179 ± 25	3.84	25	632 ± 33
J09447-182	7720 ± 109	8337 ± 24	0.44	24	618 ± 35
J09449-123	16332 ± 379	16959 ± 364	352.21	93	627 ± 36
J09468+760	-28735 ± 107	-28094 ± 23	0.94	23	641 ± 30
J09511-123	61213 ± 106	61853 ± 18	0.81	18	641 ± 30
J09561+627	14273 ± 106	14918 ± 18	0.81	18	645 ± 29
J10023+480	-10758 ± 107	-10113 ± 23	1.38	23	645 ± 29
J10122-037	6958 ± 107	7600 ± 23	0.65	23	642 ± 31
J10125+570	-4405 ± 108	-3782 ± 25	0.96	25	623 ± 34
J10167-119	-11454 ± 108	-10813 ± 25	0.99	25	640 ± 32
J10196+198	11650 ± 107	12286 ± 21	4.56	20	636 ± 32
J10251-102	20621 ± 107	21262 ± 23	1.16	23	641 ± 30
J10289+008	7370 ± 108	8005 ± 23	0.31	23	636 ± 32
J10350-094	13693 ± 108	14324 ± 25	0.90	25	631 ± 32
J10360+051	20185 ± 108	20813 ± 25	4.91	25	628 ± 34
J10396-069	2335 ± 108	2973 ± 25	1.35	25	639 ± 32
J10416+376	-2467 ± 109	-1861 ± 24	1.86	24	606 ± 37
J10482-113	1183 ± 117	1740 ± 32	0.71	32	557 ± 51
J10504+331	-60280 ± 154	-59646 ± 112	109.38	24	634 ± 33
J10508+068	-1958 ± 109	-1344 ± 24	0.36	24	614 ± 36
J10564+070	18874 ± 116	19442 ± 32	0.69	32	568 ± 48
J10584-107	10176 ± 109	10778 ± 20	2.72	20	602 ± 38
J11000+228	2256 ± 243	2888 ± 25	0.27	25	632 ± 220
J11026+219	-14881 ± 107	-14238 ± 23	1.55	23	643 ± 29
J11033+359	-85644 ± 112	-85016 ± 23	0.16	23	629 ± 44
J11054+435	67948 ± 108	68578 ± 23	0.36	23	631 ± 32
J11055+435	68605 ± 114	69163 ± 23	1.35	23	558 ± 49
J11110+304W	-16331 ± 107	-15688 ± 23	0.64	23	643 ± 29
J11126+189	30575 ± 107	31218 ± 23	1.15	23	643 ± 31
J11201-104	11382 ± 107	12026 ± 23	4.00	23	643 ± 31
J11289+101	36185 ± 109	36802 ± 25	0.90	25	617 ± 35
J11302+076	-436 ± 108	200 ± 25	0.78	25	637 ± 32
J11306-080	15804 ± 108	16432 ± 25	0.65	25	628 ± 33
J11417+427	-9970 ± 108	-9341 ± 24	2.82	24	629 ± 33
J11421+267	8699 ± 108	9335 ± 25	1.11	25	636 ± 32
J11467-140	19555 ± 108	20196 ± 25	0.54	25	641 ± 31
J11474+667	-10029 ± 112	-9404 ± 36	29.74	20	625 ± 36
J11476+002	5310 ± 109	5938 ± 25	5.84	24	627 ± 35

Table A.1: Continued.

Karmn	RV_{abs} $[m\,s^{-1}]$	RV_{CCF} $[m\,s^{-1}]$	σ_{CCF} $[m\,s^{-1}]$	σ_{mask} $[m\,s^{-1}]$	v_{grav} $[m\,s^{-1}]$
J11476+786	-112578 ± 109	-111965 ± 25	0.44	25	613 ± 36
J11477+008	-31968 ± 110	-31375 ± 24	0.48	24	593 ± 40
J11509+483	-36201 ± 110	-35613 ± 24	0.99	24	588 ± 40
J11511+352	-694 ± 107	-56 ± 23	0.29	23	638 ± 31
J12054+695	4638 ± 108	5260 ± 24	1.49	24	621 ± 34
J12100-150	79580 ± 108	80210 ± 25	0.77	25	630 ± 33
J12111-199	-10005 ± 108	-9376 ± 25	0.85	25	629 ± 33
J12123+544S	-18313 ± 106	-17668 ± 18	0.36	18	645 ± 29
J12156+526	-10192 ± 171	-9548 ± 134	96.72	93	644 ± 33
J12189+111	5105 ± 121	5681 ± 53	24.47	47	576 ± 44
J12230+640	8223 ± 108	8863 ± 25	0.91	25	640 ± 31
J12248-182	50238 ± 108	50853 ± 23	0.68	23	615 ± 34
J12312+086	17945 ± 106	18589 ± 18	0.70	18	643 ± 32
J12350+098	32375 ± 108	33014 ± 25	1.44	25	639 ± 31
J12373-208	8457 ± 108	9092 ± 24	0.87	24	634 ± 33
J12388+116	-5129 ± 108	-4491 ± 25	1.51	25	638 ± 32
J12428+418	-5316 ± 108	-4684 ± 24	3.05	24	632 ± 33
J12479+097	18149 ± 109	18772 ± 25	0.47	25	623 ± 34
J13005+056	-25926 ± 119	-25330 ± 50	16.10	47	596 ± 40
J13102+477	-13033 ± 110	-12446 ± 20	1.26	20	587 ± 41
J13196+333	-12669 ± 107	-12025 ± 23	0.85	23	643 ± 29
J13209+342	-36398 ± 238	-35756 ± 23	0.54	23	642 ± 214
J13229+244	-20177 ± 109	-19560 ± 24	0.67	24	617 ± 35
J13283-023W	-40370 ± 108	-39734 ± 25	1.29	25	637 ± 33
J13293+114	27343 ± 108	27980 ± 25	1.55	25	637 ± 33
J13299+102	13357 ± 106	13997 ± 18	0.22	18	640 ± 30
J13427+332	5834 ± 109	6449 ± 25	0.73	25	615 ± 35
J13450+176	19625 ± 106	20265 ± 18	0.85	18	640 ± 29
J13457+148	14832 ± 108	15471 ± 23	0.21	23	639 ± 34
J13458-179	4008 ± 108	4634 ± 25	0.88	25	627 ± 34
J13536+776	-8208 ± 109	-7591 ± 24	10.59	21	617 ± 36
J13582+125	-10737 ± 109	-10131 ± 25	1.35	25	606 ± 37
J13591-198	-17102 ± 109	-16488 ± 25	5.50	24	615 ± 36
J14010-026	-26785 ± 107	-26144 ± 23	0.71	23	641 ± 30
J14082+805	6416 ± 107	7061 ± 23	1.01	23	645 ± 31
J14152+450	13247 ± 108	13884 ± 25	1.24	25	637 ± 32
J14173+454	2489 ± 123	3108 ± 62	40.20	47	619 ± 36
J14251+518	-11013 ± 108	-10380 ± 25	0.74	25	633 ± 32
J14257+236E	7315 ± 106	7960 ± 18	0.52	18	645 ± 28
J14257+236W	8236 ± 105	8882 ± 18	0.57	18	646 ± 28
J14294+155	6871 ± 107	7512 ± 23	1.65	23	640 ± 31
J14307-086	-23181 ± 105	-22534 ± 18	0.39	18	647 ± 28
J14310-122	-2709 ± 108	-2085 ± 25	1.65	25	624 ± 34
J14321+081	-22601 ± 114	-22021 ± 34	10.17	32	580 ± 44
J14342-125	-2361 ± 109	-1742 ± 24	0.43	24	618 ± 35

Table A.1: Continued.

Karmn	RV_{abs} $[m\,s^{-1}]$	RV_{CCF} $[m\,s^{-1}]$	σ_{CCF} $[m\,s^{-1}]$	σ_{mask} $[m\,s^{-1}]$	v_{grav} $[m\,s^{-1}]$
J14524+123	4760 ± 108	5403 ± 23	2.08	23	643 ± 33
J14544+355	-41692 ± 108	-41063 ± 25	0.88	25	629 ± 33
J15013+055	-6899 ± 108	-6271 ± 25	0.56	25	628 ± 33
J15095+031	-33423 ± 108	-32786 ± 25	1.28	25	637 ± 32
J15194-077	-10284 ± 109	-9662 ± 25	1.32	25	622 ± 34
J15218+209	6071 ± 107	6716 ± 21	4.82	20	645 ± 31
J15305+094	856 ± 121	1434 ± 52	22.09	47	578 ± 45
J15369-141	1475 ± 108	2098 ± 24	0.31	24	623 ± 34
J15499+796	-16902 ± 145	-16285 ± 98	78.70	58	617 ± 38
J15598-082	-18112 ± 107	-17472 ± 23	1.45	23	640 ± 32
J16028+205	5570 ± 109	6182 ± 24	1.06	24	612 ± 36
J16092+093	-45766 ± 108	-45135 ± 25	1.42	25	631 ± 32
J16102-193	-7655 ± 109	-7002 ± 31	20.08	23	653 ± 32
J16167+672N	-19418 ± 108	-18780 ± 25	0.35	25	639 ± 33
J16167+672S	-20011 ± 106	-19364 ± 18	0.43	18	647 ± 30
J16254+543	-14003 ± 108	-13379 ± 23	0.52	23	624 ± 33
J16303-126	-22180 ± 109	-21560 ± 25	0.40	25	621 ± 35
J16313+408	-23752 ± 116	-23156 ± 43	36.36	23	596 ± 41
J16327+126	-33704 ± 108	-33071 ± 25	1.12	25	633 ± 32
J16462+164	17908 ± 108	18544 ± 25	0.42	25	636 ± 32
J16554-083N	14895 ± 110	15498 ± 25	0.69	25	604 ± 37
J16555-083	13863 ± 117	14409 ± 28	3.74	28	546 ± 53
J16570-043	-4575 ± 116	-3963 ± 47	5.69	47	612 ± 36
J16581+257	3350 ± 107	3991 ± 23	0.54	23	642 ± 31
J17033+514	36589 ± 110	37182 ± 24	0.99	24	593 ± 39
J17052-050	33847 ± 107	34485 ± 23	0.55	23	639 ± 31
J17071+215	-51697 ± 108	-51064 ± 25	1.27	25	633 ± 33
J17115+384	-45409 ± 108	-44776 ± 25	0.48	25	632 ± 33
J17166+080	-31559 ± 107	-30925 ± 23	1.59	23	634 ± 32
J17198+417	-20404 ± 108	-19774 ± 25	1.03	25	629 ± 33
J17303+055	-13669 ± 106	-13026 ± 18	0.48	18	643 ± 29
J17338+169	-22504 ± 306	-21873 ± 287	271.31	93	631 ± 38
J17355+616	-16082 ± 106	-15440 ± 18	0.82	18	643 ± 29
J17378+185	-10488 ± 108	-9853 ± 23	0.32	23	636 ± 32
J17542+073	-29236 ± 109	-28614 ± 24	1.85	24	622 ± 35
J17578+046	-111156 ± 110	-110567 ± 20	0.15	20	589 ± 41
J17578+465	-32260 ± 108	-31626 ± 25	1.35	25	633 ± 33
J18022+642	-2219 ± 119	-1627 ± 50	17.49	47	592 ± 41
J18027+375	3091 ± 111	3668 ± 20	0.78	20	577 ± 43
J18051-030	31706 ± 107	32344 ± 23	0.42	23	637 ± 31
J18075-159	-33797 ± 110	-33200 ± 24	2.35	24	596 ± 40
J18131+260	-9239 ± 138	-8612 ± 88	85.23	23	628 ± 34
J18165+048	-54112 ± 110	-53521 ± 20	0.85	20	591 ± 40
J18174+483	-24885 ± 107	-24240 ± 23	1.51	23	645 ± 31
J18180+387E	-397 ± 108	225 ± 25	1.24	25	622 ± 33

Table A.1: Continued.

Karmn	RV_{abs} $[m\,s^{-1}]$	RV_{CCF} $[m\,s^{-1}]$	σ_{CCF} $[m\,s^{-1}]$	σ_{mask} $[m\,s^{-1}]$	v_{grav} $[m\,s^{-1}]$
J18189+661	4779 ± 119	5355 ± 49	12.78	47	576 ± 43
J18221+063	-44585 ± 108	-43965 ± 24	0.57	24	619 ± 34
J18224+620	-14556 ± 112	-13970 ± 24	0.78	24	586 ± 45
J18319+406	-19955 ± 108	-19325 ± 25	1.48	25	630 ± 33
J18346+401	11545 ± 108	12180 ± 25	0.48	25	635 ± 33
J18353+457	-32697 ± 106	-32053 ± 18	1.25	18	645 ± 29
J18356+329	117 ± 215	643 ± 183	157.74	93	526 ± 51
J18363+136	-45944 ± 109	-45321 ± 24	0.95	24	622 ± 35
J18409-133	-33939 ± 107	-33297 ± 23	1.23	23	642 ± 30
J18419+318	-32654 ± 108	-32027 ± 25	2.03	25	628 ± 33
J18480-145	-5412 ± 108	-4780 ± 25	1.09	25	631 ± 32
J18482+076	-35043 ± 110	-34455 ± 20	1.53	20	588 ± 42
J18498-238	-11390 ± 110	-10797 ± 25	2.00	25	594 ± 39
J18580+059	9229 ± 106	9873 ± 18	0.96	18	644 ± 29
J19070+208	31441 ± 108	32064 ± 23	0.65	23	623 ± 33
J19072+208	31207 ± 108	31830 ± 23	0.86	23	623 ± 33
J19084+322	-2606 ± 108	-1979 ± 25	0.97	25	627 ± 33
J19098+176	-14857 ± 110	-14262 ± 24	0.75	24	596 ± 39
J19169+051N	34973 ± 108	35612 ± 25	0.27	25	640 ± 31
J19169+051S	35179 ± 115	35731 ± 28	3.96	28	551 ± 48
J19216+208	3911 ± 110	4519 ± 24	0.86	24	608 ± 39
J19251+283	-41403 ± 267	-40773 ± 25	1.18	25	630 ± 247
J19346+045	-59501 ± 105	-58857 ± 18	0.83	18	644 ± 27
J19422-207	-2702 ± 111	-2094 ± 32	21.55	23	608 ± 37
J19511+464	-13555 ± 122	-12942 ± 60	15.92	58	613 ± 36
J20093-012	-54561 ± 111	-53970 ± 24	13.26	20	591 ± 41
J20260+585	-60631 ± 110	-60047 ± 20	0.26	20	585 ± 42
J20305+654	9694 ± 108	10326 ± 25	0.38	25	632 ± 34
J20336+617	-21816 ± 108	-21184 ± 24	0.55	24	632 ± 33
J20405+154	-60376 ± 110	-59782 ± 24	0.75	24	595 ± 39
J20450+444	-25661 ± 107	-25026 ± 23	0.82	23	635 ± 31
J20525-169	15396 ± 109	16005 ± 24	0.88	24	608 ± 36
J20533+621	-18136 ± 107	-17493 ± 23	0.22	23	642 ± 29
J20556-140S	-142621 ± 110	-142042 ± 20	1.52	20	579 ± 43
J20567-104	34345 ± 108	34984 ± 25	2.19	25	639 ± 32
J21019-063	-15867 ± 108	-15229 ± 25	1.55	25	638 ± 32
J21152+257	-16926 ± 108	-16284 ± 25	1.40	25	642 ± 34
J21164+025	-22946 ± 108	-22310 ± 25	0.78	25	636 ± 32
J21221+229	4713 ± 107	5353 ± 23	1.15	23	641 ± 30
J21348+515	-14760 ± 108	-14122 ± 25	0.37	25	637 ± 32
J21463+382	-83609 ± 110	-83013 ± 24	0.57	24	596 ± 38
J21466+668	-10392 ± 108	-9771 ± 24	0.46	24	621 ± 34
J21466-001	-29165 ± 109	-28548 ± 24	1.25	24	618 ± 35
J22012+283	-3877 ± 175	-3255 ± 139	103.35	93	622 ± 35
J22020-194	-24227 ± 134	-23602 ± 25	1.24	25	625 ± 85

Table A.1: Continued.

Karmn	RV_{abs} $[m\,s^{-1}]$	RV_{CCF} $[m\,s^{-1}]$	σ_{CCF} $[m\,s^{-1}]$	σ_{mask} $[m\,s^{-1}]$	v_{grav} $[m\,s^{-1}]$
J22021+014	17180 ± 106	17823 ± 18	0.66	18	643 ± 32
J22057+656	-47534 ± 107	-46895 ± 23	0.39	23	639 ± 32
J22096-046	-16231 ± 108	-15592 ± 25	2.41	25	639 ± 32
J22114+409	-17462 ± 110	-16878 ± 20	0.85	20	583 ± 42
J22115+184	-52315 ± 107	-51671 ± 23	0.72	23	644 ± 32
J22125+085	7828 ± 108	8459 ± 25	0.58	25	631 ± 33
J22137-176	-25077 ± 110	-24485 ± 24	0.82	24	592 ± 40
J22231-176	-2564 ± 110	-1972 ± 24	2.20	24	591 ± 40
J22252+594	3232 ± 108	3866 ± 24	0.66	24	634 ± 33
J22298+414	1500 ± 109	2114 ± 24	1.22	24	613 ± 35
J22330+093	-7473 ± 107	-6835 ± 23	1.28	23	638 ± 32
J22468+443	-280 ± 110	347 ± 30	3.58	30	627 ± 34
J22503-070	-6778 ± 106	-6135 ± 18	0.57	18	643 ± 29
J22518+317	-3083 ± 117	-2445 ± 50	18.20	47	639 ± 32
J22532-142	-2427 ± 111	-1801 ± 33	22.95	24	625 ± 34
J22559+178	-32880 ± 107	-32238 ± 23	0.93	23	643 ± 29
J22565+165	-28306 ± 107	-27664 ± 23	0.24	23	642 ± 30
J23064-050	-53852 ± 118	-53323 ± 28	3.70	28	529 ± 57
J23216+172	-7400 ± 108	-6769 ± 24	0.48	24	632 ± 33
J23245+578	-34167 ± 107	-33524 ± 23	0.93	23	642 ± 30
J23340+001	-5477 ± 108	-4842 ± 25	0.40	25	635 ± 32
J23351-023	-41614 ± 113	-41056 ± 20	0.68	20	558 ± 48
J23381-162	19840 ± 108	20471 ± 23	0.54	23	631 ± 32
J23419+441	-78648 ± 111	-78073 ± 20	0.44	20	575 ± 44
J23431+365	-3586 ± 109	-2981 ± 24	1.04	24	606 ± 37
J23492+024	-72102 ± 107	-71469 ± 23	0.21	23	633 ± 31
J23505-095	-22492 ± 109	-21871 ± 24	0.67	24	621 ± 35
J23548+385	4746 ± 109	5372 ± 27	11.38	24	626 ± 34

Appendix B

Activity indicators periodogram analysis

Table B.1: Activity-related signals (periods and FAPs) at $P_{\rm rot}$, $\frac{1}{2}P_{\rm rot}$ and their 1 day aliases (1 d a.) found in the periodograms of the SERVAL RVs. We also show literature periods compiled in Carmencita (same references as in Table 3.1). For stars with no known period, we take as $P_{\rm rot}$ the signal with the smallest FAP present in more than one indicator.

Karmn	$P_{\rm rot}$ lit.	$P_{\rm rot}$		$\frac{1}{2}P_{\rm rot}$		$P_{\rm rot}$ 1 d a.		$\frac{1}{2}P_{\rm rot}$ 1 d a.	
	[d]	P [d]	FAP [%]	P [d]	FAP [%]	P [d]	FAP [%]	P [d]	FAP [%]
J00183+440	$45.00 \pm 4.40^{*}$	40.71	0.69	-	-	-	-	-	-
J01025+716	52.00 ± 2.60	50.99	≤ 0.1	-	-	1.02	≤ 0.1	-	-
J01026+623	20.00 ± 0.40	18.89	1.03	9.43	1.26	-	-	1.12	6.12
J01033+623	1.020 ± 0.010	1.08	45.38	-	-	13.67	5.20	-	-
J01125-169	69.00 ± 2.40	80.67	9.56	-	-	-	-	-	-
J02002+130	–	1.95	≤ 0.1	-	-	2.03	≤ 0.1	-	-
J02222+478	30.00 ± 0.40	28.20	2.21	-	-	1.03	9.51	-	-
J04153-076	–	1.80	≤ 0.1	-	-	-	-	-	-
J04290+219	25.00 ± 0.30	25.14	13.49	12.53	≤ 0.1	-	-	-	-
J04376+528	–	16.30	3.08	8.64	11.20	-	-	-	-
J04429+189	41.00 ± 0.40	40.55	18.07	-	-	-	-	-	-
J04588+498	–	-	-	8.97	≤ 0.1	-	-	1.13	20.29
J05019+011	2.120 ± 0.020	2.09	≤ 0.1	-	-	1.91	2.65	-	-
J05314-036	34.00 ± 0.60	34.07	≤ 0.1	-	-	-	-	-	-
J05365+113	12.00 ± 0.10	11.77	≤ 0.1	-	-	1.09	≤ 0.1	-	-
J07274+052	$90.0 \pm 16.0^{\ddagger}$	94.81	0.37	-	-	-	-	-	-
J07446+035	2.780 ± 0.010	2.78	≤ 0.1	-	-	1.56	0.12	-	-
J09143+526	–	16.37	≤ 0.1	-	-	-	-	-	-
J09144+526	–	16.63	≤ 0.1	-	-	-	-	-	-
J09561+627	–	18.69	≤ 0.1	8.93	≤ 0.1	1.06	1.01	-	-
J10122-037	22.00 ± 0.20	21.38	1.91	10.65	≤ 0.1	-	-	-	-
J10196+198	$2.23990 \pm 0.00060^{\S}$	2.24	≤ 0.1	-	-	1.81	≤ 0.1	-	-
J10482-113	$1.50 \pm 0.20^{\P}$	1.52	0.30	-	-	2.90	0.53	-	-
J10564+070	2.7040 ± 0.0030	2.70	≤ 0.1	-	-	1.58	≤ 0.1	-	-
J10584-107	–	4.62	≤ 0.1	-	-	1.27	≤ 0.1	-	-
J11026+219	15.00 ± 0.20	13.96	6.71	-	-	1.08	5.98	-	-

Table B.1: Continued.

Karmn	P_{rot} lit.	P_{rot}		$\frac{1}{2}P_{rot}$		P_{rot} 1 d a.		$\frac{1}{2}P_{rot}$ 1 d a.	
	[d]	P [d]	FAP [%]	P [d]	FAP [%]	P [d]	FAP [%]	P [d]	FAP [%]
J11302+076	36.00 ± 0.30	33.95	≤ 0.1	-	-	1.03	≤ 0.1	-	-
J11511+352	23.00 ± 1.00	23.96	14.13	11.12	≤ 0.1	-	-	-	-
J13299+102	$30.00 \pm 0.90^{\ddagger}$	-	-	15.22	≤ 0.1	-	-	-	-
J15218+209	3.370 ± 0.010	3.37	≤ 0.1	-	-	1.39	≤ 0.1	-	-
J16167+672S	–	20.93	≤ 0.1	-	-	-	-	-	-
J16555-083	–	1.09	0.14	-	-	11.19	≤ 0.1	-	-
J16581+257	24.00 ± 0.10	-	-	12.39	37.13	-	-	-	-
J17303+055	–	33.76	0.84	-	-	-	-	-	-
J17378+185	–	41.25	0.13	-	-	-	-	-	-
J18174+483	16.00 ± 0.10	16.02	0.59	8.11	1.49	-	-	-	-
J18198-019	–	28.53	≤ 0.1	-	-	-	-	-	-
J18498-238	2.870 ± 0.010	2.86	0.35	1.42	0.66	1.53	2.08	3.34	3.35
J19346+045	13.00 ± 0.80	21.09	24.32	-	-	-	-	-	-
J20451-313	4.840 ± 0.040	4.90	≤ 0.1	-	-	1.25	≤ 0.1	-	-
J21221+229	41.00 ± 1.70	40.39	94.16	-	-	-	-	-	-
J22021+014	30.00 ± 0.10	20.76	2.89	10.95	≤ 0.1	-	-	-	-
J22057+656	–	120.47	≤ 0.1	-	-	-	-	-	-
J22114+409	30.00 ± 1.30	31.37	1.86	15.21	3.31	-	-	-	-
J22115+184	36.00 ± 0.20	38.95	2.36	-	-	-	-	-	-
J22468+443	4.380 ± 0.030	4.36	0.68	2.19	≤ 0.1	1.30	2.00	1.84	≤ 0.1
J22565+165	40.00 ± 0.20	38.65	≤ 0.1	18.64	≤ 0.1	-	-	-	-
J23492+024	$50.00 \pm 3.50^{*}$	53.82	≤ 0.1	-	-	-	-	-	-

Table B.2: Same as Table B.1 but for the CRX.

Karmn	P_{rot} lit.	P_{rot}		P_{rot} 1 d a.		$\frac{1}{2}P_{rot}$		$\frac{1}{2}P_{rot}$ 1 d a.	
	[d]	P [d]	FAP [%]	P [d]	FAP [%]	P [d]	FAP [%]	P [d]	FAP [%]
J01025+716	52.00 ± 2.60	50.99	42.41	-	-	1.02	5.62	-	-
J01033+623	1.020 ± 0.010	1.06	0.40	-	-	16.59	≤ 0.1	-	-
J01125-169	69.00 ± 2.40	80.67	12.43	-	-	-	-	-	-
J02002+130	–	1.96	0.79	-	-	2.03	19.09	-	-
J02530+168	–	96.20	73.37	-	-	-	-	-	-
J03133+047	$130.0^{\dagger}$	100.24	25.37	-	-	-	-	-	-
J04153-076	–	1.80	≤ 0.1	-	-	-	-	-	-
J05019+011	2.120 ± 0.020	2.09	≤ 0.1	-	-	1.90	≤ 0.1	-	-
J05314-036	34.00 ± 0.60	31.90	6.91	-	-	-	-	-	-
J07274+052	$90.0 \pm 16.0^{\ddagger}$	96.06	74.09	-	-	-	-	-	-
J07446+035	2.780 ± 0.010	2.78	≤ 0.1	-	-	1.56	0.32	-	-
J10196+198	$2.23990 \pm 0.00060^{\S}$	2.21	≤ 0.1	-	-	1.83	≤ 0.1	-	-
J10564+070	2.7040 ± 0.0030	2.71	≤ 0.1	-	-	1.58	≤ 0.1	-	-
J10584-107	–	4.67	1.34	-	-	1.27	21.50	-	-
J11026+219	15.00 ± 0.20	13.69	1.02	-	-	-	-	-	-
J15218+209	3.370 ± 0.010	3.37	7.60	-	-	1.43	23.63	-	-
J17303+055	–	32.08	72.02	-	-	-	-	-	-

Table B.2: Continued.

Karmn	$P_{\rm rot}$ lit.	$P_{\rm rot}$		$\frac{1}{2}P_{\rm rot}$		$P_{\rm rot}$ 1 d a.		$\frac{1}{2}P_{\rm rot}$ 1 d a.	
	[d]	P [d]	FAP [%]	P [d]	FAP [%]	P [d]	FAP [%]	P [d]	FAP [%]
J17378+185	–	53.81	0.28	-	-	-	-	-	-
J18174+483	16.00 ± 0.10	15.97	61.75	7.96	0.69	-	-	-	-
J18498-238	2.870 ± 0.010	1.43	8.96	-	-	-	-	3.30	18.43
J20451-313	4.840 ± 0.040[|]	4.90	38.98	-	-	1.25	25.14	-	-
J21164+025	–	42.46	39.23	-	-	-	-	-	-
J22057+656	–	120.47	≤ 0.1	-	-	-	-	-	-
J22468+443	4.380 ± 0.030	4.36	17.99	2.19	≤ 0.1	-	-	1.84	≤ 0.1

Table B.3: Same as Table B.1 but for the DLW.

Karmn	$P_{\rm rot}$ lit.	$P_{\rm rot}$		$P_{\rm rot}$ 1 d a.		$\frac{1}{2}P_{\rm rot}$		$\frac{1}{2}P_{\rm rot}$ 1 d a.	
	[d]	P [d]	FAP [%]	P [d]	FAP [%]	P [d]	FAP [%]	P [d]	FAP [%]
J01025+716	52.00 ± 2.60	51.73	≤ 0.1	-	-	1.02	33.48	-	-
J01125-169	69.00 ± 2.40	80.67	≤ 0.1	-	-	-	-	-	-
J02002+130	–	1.95	1.99	-	-	2.05	6.65	-	-
J02222+478	30.00 ± 0.40	28.88	≤ 0.1	-	-	1.03	1.15	-	-
J02530+168	–	97.56	≤ 0.1	-	-	-	-	-	-
J03133+047	130.0[†]	140.81	≤ 0.1	-	-	-	-	-	-
J04290+219	25.00 ± 0.30	25.14	≤ 0.1	-	-	-	-	-	-
J04376+528	–	16.30	≤ 0.1	-	-	-	-	-	-
J04588+498	–	19.19	0.58	-	-	-	-	-	-
J05314-036	34.00 ± 0.60	33.78	≤ 0.1	-	-	-	-	-	-
J05365+113	12.00 ± 0.10	11.43	8.49	-	-	-	-	-	-
J07446+035	2.780 ± 0.010	2.78	≤ 0.1	-	-	1.56	3.58	-	-
J08413+594	–	88.65	≤ 0.1	-	-	-	-	-	-
J09143+526	–	17.48	≤ 0.1	-	-	-	-	-	-
J09144+526	–	16.69	≤ 0.1	-	-	-	-	-	-
J09561+627	–	19.40	0.24	-	-	1.05	6.14	-	-
J10122-037	22.00 ± 0.20	21.16	22.10	-	-	-	-	-	-
J10482-113	1.50 ± 0.20[¶]	1.52	16.85	-	-	2.96	≤ 0.1	-	-
J10564+070	2.7040 ± 0.0030	2.71	28.26	-	-	1.58	7.50	-	-
J16167+672S	–	21.30	≤ 0.1	-	-	-	-	-	-
J16555-083	–	1.09	≤ 0.1	-	-	11.54	≤ 0.1	-	-
J17303+055	–	33.51	0.34	-	-	-	-	-	-
J17378+185	–	37.51	≤ 0.1	-	-	-	-	-	-
J17578+046	150.00 ± 0.10[#]	135.15	≤ 0.1	-	-	-	-	-	-
J18174+483	16.00 ± 0.10	16.66	8.02	-	-	1.06	0.65	-	-
J18198-019	–	28.53	≤ 0.1	-	-	-	-	-	-
J18498-238	2.870 ± 0.010	2.86	≤ 0.1	1.43	40.67	1.53	≤ 0.1	3.31	48.52
J18580+059	35.00 ± 0.30	30.50	≤ 0.1	-	-	-	-	-	-
J19346+045	13.00 ± 0.80	21.75	≤ 0.1	-	-	-	-	-	-
J20451-313	4.840 ± 0.040[|]	4.90	39.30	-	-	1.25	68.65	-	-
J21221+229	41.00 ± 1.70	39.17	≤ 0.1	-	-	-	-	-	-
J22114+409	30.00 ± 1.30	30.69	18.89	-	-	-	-	-	-

Table B.3: Continued.

Karmn	$P_{\rm rot}$ lit.	$P_{\rm rot}$		$\frac{1}{2}P_{\rm rot}$		$P_{\rm rot}$ 1 d a.		$\frac{1}{2}P_{\rm rot}$ 1 d a.	
	[d]	P [d]	FAP [%]	P [d]	FAP [%]	P [d]	FAP [%]	P [d]	FAP [%]
J22115+184	36.00 ± 0.20	37.30	≤ 0.1	-	-	-	-	-	-
J22468+443	4.380 ± 0.030	4.37	≤ 0.1	2.19	19.88	1.29	≤ 0.1	-	-
J22565+165	40.00 ± 0.20	38.65	≤ 0.1	-	-	-	-	-	-

Table B.4: Same as Table B.1 but for the CCF FWHM.

Karmn	$P_{\rm rot}$ lit.	$P_{\rm rot}$		$P_{\rm rot}$ 1 d a.		$\frac{1}{2}P_{\rm rot}$		$\frac{1}{2}P_{\rm rot}$ 1 d a.	
	[d]	P [d]	FAP [%]	P [d]	FAP [%]	P [d]	FAP [%]	P [d]	FAP [%]
J00183+440	$45.00 \pm 4.40^{*}$	42.38	10.03	21.38	38.78	-	-	-	-
J01025+716	52.00 ± 2.60	50.28	≤ 0.1	-	-	1.02	0.55	-	-
J01026+623	20.00 ± 0.40	18.80	1.70	-	-	1.05	0.58	-	-
J01125-169	69.00 ± 2.40	79.48	≤ 0.1	-	-	-	-	-	-
J02002+130	–	1.96	1.29	-	-	2.03	14.83	-	-
J02530+168	–	97.56	≤ 0.1	-	-	-	-	-	-
J03133+047	$130.0^{\dagger}$	144.25	≤ 0.1	-	-	-	-	-	-
J04290+219	25.00 ± 0.30	25.14	3.20	-	-	-	-	-	-
J04376+528	–	15.72	8.03	-	-	-	-	-	-
J05314-036	34.00 ± 0.60	34.36	14.32	-	-	-	-	-	-
J05365+113	12.00 ± 0.10	11.77	≤ 0.1	-	-	-	-	-	-
J07446+035	2.780 ± 0.010	2.78	≤ 0.1	-	-	1.56	1.93	-	-
J08413+594	–	88.65	≤ 0.1	-	-	-	-	-	-
J09143+526	–	16.37	8.73	-	-	-	-	-	-
J09561+627	–	17.79	0.66	-	-	1.06	3.97	-	-
J10196+198	$2.23990 \pm 0.00060^{\S}$	-	-	1.11	15.27	-	-	10.41	34.61
J16555-083	–	1.09	16.69	-	-	11.16	≤ 0.1	-	-
J17303+055	–	33.51	≤ 0.1	-	-	-	-	-	-
J17378+185	–	40.94	1.30	-	-	-	-	-	-
J17578+046	$150.00 \pm 0.10^{\#}$	156.65	≤ 0.1	-	-	-	-	-	-
J18174+483	16.00 ± 0.10	15.97	32.49	-	-	-	-	-	-
J18198-019	–	28.22	6.04	-	-	-	-	-	-
J18498-238	2.870 ± 0.010	2.89	2.13	1.43	2.18	1.53	6.12	3.30	2.02
J19346+045	13.00 ± 0.80	21.86	3.51	-	-	-	-	-	-
J20451-313	$4.840 \pm 0.040^{|}$	4.90	5.00	-	-	1.25	14.34	-	-
J21164+025	–	47.09	≤ 0.1	-	-	-	-	-	-
J21221+229	41.00 ± 1.70	40.14	≤ 0.1	-	-	-	-	-	-
J22114+409	30.00 ± 1.30	30.96	≤ 0.1	-	-	-	-	-	-
J22115+184	36.00 ± 0.20	34.38	1.30	-	-	-	-	-	-
J22468+443	4.380 ± 0.030	4.36	0.19	2.19	≤ 0.1	1.29	1.53	1.83	≤ 0.1
J22565+165	40.00 ± 0.20	38.45	≤ 0.1	-	-	-	-	-	-
J23492+024	$50.00 \pm 3.50^{*}$	53.42	≤ 0.1	-	-	-	-	-	-

Table B.5: Same as Table B.1 but for the CCF contrast.

Karmn	$P_{\rm rot}$ lit.	$P_{\rm rot}$		$P_{\rm rot}$ 1 d a.		$\frac{1}{2}P_{\rm rot}$		$\frac{1}{2}P_{\rm rot}$ 1 d a.	
	[d]	P [d]	FAP [%]	P [d]	FAP [%]	P [d]	FAP [%]	P [d]	FAP [%]
J01025+716	52.00 ± 2.60	57.52	19.03	-	-	-	-	-	-
J01125-169	69.00 ± 2.40	70.19	≤ 0.1	-	-	-	-	-	-
J02002+130	–	1.96	≤ 0.1	-	-	2.03	≤ 0.1	-	-
J02530+168	–	96.20	≤ 0.1	-	-	-	-	-	-
J03133+047	130.0†	147.86	0.42	-	-	-	-	-	-
J04376+528	–	16.52	30.43	-	-	-	-	-	-
J05314-036	34.00 ± 0.60	34.07	0.51	-	-	-	-	-	-
J07446+035	2.780 ± 0.010	2.77	≤ 0.1	-	-	1.56	1.58	-	-
J09143+526	–	17.19	16.65	-	-	-	-	-	-
J15218+209	3.370 ± 0.010	3.79	2.30	-	-	1.40	16.38	-	-
J16167+672S	–	22.00	0.17	-	-	-	-	-	-
J16555-083	–	1.09	≤ 0.1	-	-	11.16	≤ 0.1	-	-
J17303+055	–	33.51	0.70	-	-	-	-	-	-
J18498-238	2.870 ± 0.010	2.86	80.95	1.42	12.42	-	-	3.35	7.28
J18580+059	35.00 ± 0.30	30.50	12.95	-	-	-	-	-	-
J19346+045	13.00 ± 0.80	21.77	2.39	-	-	-	-	-	-
J21221+229	41.00 ± 1.70	38.70	4.78	-	-	-	-	-	-
J22114+409	30.00 ± 1.30	30.43	0.39	-	-	-	-	-	-
J22115+184	36.00 ± 0.20	37.30	≤ 0.1	-	-	-	-	-	-
J22468+443	4.380 ± 0.030	4.37	0.25	2.20	66.45	1.29	22.74	-	-
J22565+165	40.00 ± 0.20	38.65	≤ 0.1	-	-	-	-	-	-

Table B.6: Same as Table B.1 but for the CCF BIS.

Karmn	$P_{\rm rot}$ lit.	$P_{\rm rot}$		$P_{\rm rot}$ 1 d a.		$\frac{1}{2}P_{\rm rot}$		$\frac{1}{2}P_{\rm rot}$ 1 d a.	
	[d]	P [d]	FAP [%]	P [d]	FAP [%]	P [d]	FAP [%]	P [d]	FAP [%]
J01026+623	20.00 ± 0.40	18.27	1.65	-	-	1.05	0.38	-	-
J02002+130	–	1.96	0.16	-	-	2.03	0.76	-	-
J03133+047	130.0†	147.86	33.13	-	-	-	-	-	-
J04153-076	–	1.80	≤ 0.1	-	-	-	-	-	-
J04290+219	25.00 ± 0.30	24.97	0.43	-	-	-	-	-	-
J04376+528	–	16.30	32.79	7.90	1.42	-	-	-	-
J04588+498	–	-	-	8.97	≤ 0.1	-	-	1.13	0.67
J05019+011	2.120 ± 0.020	2.09	≤ 0.1	-	-	1.90	≤ 0.1	-	-
J05365+113	12.00 ± 0.10	11.77	≤ 0.1	-	-	-	-	-	-
J07446+035	2.780 ± 0.010	2.78	≤ 0.1	-	-	1.56	≤ 0.1	-	-
J09143+526	–	16.22	0.60	-	-	-	-	-	-
J10196+198	2.23990 ± 0.00060§	2.22	13.05	-	-	1.82	22.77	-	-
J10564+070	2.7040 ± 0.0030	2.71	33.10	-	-	1.55	18.22	-	-
J11026+219	15.00 ± 0.20	13.69	4.48	-	-	1.08	7.90	-	-
J11511+352	23.00 ± 1.00	-	-	11.45	13.66	-	-	-	-
J15218+209	3.370 ± 0.010	3.45	2.72	-	-	-	-	-	-
J16167+672S	–	20.29	11.83	-	-	-	-	-	-

Table B.6: Continued.

Karmn	P_{rot} lit.	P_{rot}		$\frac{1}{2}P_{rot}$		P_{rot} 1 d a.		$\frac{1}{2}P_{rot}$ 1 d a.	
	[d]	P [d]	FAP [%]	P [d]	FAP [%]	P [d]	FAP [%]	P [d]	FAP [%]
J16555-083	–	1.09	7.62	-	-	11.57	0.38	-	-
J17303+055	–	-	-	17.60	0.52	-	-	10.21	99.35
J17578+046	$150.00 \pm 0.10^{\#}$	-	-	74.11	0.51	-	-	-	-
J18174+483	16.00 ± 0.10	15.97	31.01	8.11	2.04	-	-	-	-
J18498-238	2.870 ± 0.010	2.86	≤ 0.1	1.43	2.86	1.53	0.15	3.30	3.97
J19346+045	13.00 ± 0.80	21.67	5.63	13.05	3.11	-	-	-	-
J20451-313	$4.840 \pm 0.040^{\|}$	4.90	2.95	-	-	1.25	3.96	-	-
J22468+443	4.380 ± 0.030	4.35	1.54	2.19	≤ 0.1	-	-	1.84	≤ 0.1

Table B.7: Same as Table B.1 but for the Hα.

Karmn	P_{rot} lit.	P_{rot}		P_{rot} 1 d a.		$\frac{1}{2}P_{rot}$		$\frac{1}{2}P_{rot}$ 1 d a.	
	[d]	P [d]	FAP [%]	P [d]	FAP [%]	P [d]	FAP [%]	P [d]	FAP [%]
J00183+440	$45.00 \pm 4.40^{*}$	47.40	≤ 0.1	-	-	-	-	-	-
J01025+716	52.00 ± 2.60	50.28	≤ 0.1	-	-	-	-	1.02	≤ 0.1
J01026+623	20.00 ± 0.40	18.89	≤ 0.1	-	-	1.05	≤ 0.1	-	-
J01125-169	69.00 ± 2.40	70.19	25.22	-	-	-	-	-	-
J02002+130	–	1.95	2.58	-	-	2.04	39.57	-	-
J02222+478	30.00 ± 0.40	28.20	5.39	-	-	1.04	6.35	-	-
J02530+168	–	96.20	24.18	-	-	-	-	-	-
J03133+047	$130.0^{\dagger}$	137.54	≤ 0.1	-	-	-	-	-	-
J03463+262	–	10.07	≤ 0.1	-	-	-	-	-	-
J04153-076	–	1.74	3.24	-	-	-	-	-	-
J04290+219	25.00 ± 0.30	25.31	≤ 0.1	-	-	-	-	-	-
J04376+528	–	15.42	25.74	-	-	-	-	-	-
J04429+189	41.00 ± 0.40	39.67	2.79	-	-	-	-	-	-
J04588+498	–	19.19	8.05	-	-	-	-	-	-
J05314-036	34.00 ± 0.60	33.50	≤ 0.1	-	-	-	-	-	-
J05365+113	12.00 ± 0.10	11.79	≤ 0.1	-	-	-	-	-	-
J07446+035	2.780 ± 0.010	2.78	36.83	-	-	-	-	-	-
J08413+594	–	88.65	1.83	-	-	-	-	-	-
J09143+526	–	17.60	0.18	-	-	-	-	-	-
J09144+526	–	16.69	≤ 0.1	-	-	-	-	-	-
J09561+627	–	17.79	≤ 0.1	-	-	1.06	≤ 0.1	-	-
J10122-037	22.00 ± 0.20	21.36	3.70	-	-	-	-	-	-
J11302+076	36.00 ± 0.30	37.49	0.86	-	-	1.02	≤ 0.1	-	-
J16167+672S	–	22.90	1.48	-	-	-	-	-	-
J16581+257	24.00 ± 0.10	22.41	0.28	-	-	-	-	-	-
J17303+055	–	33.76	≤ 0.1	-	-	-	-	-	-
J17378+185	–	40.00	≤ 0.1	-	-	-	-	-	-
J17578+046	$150.00 \pm 0.10^{\#}$	125.32	≤ 0.1	-	-	-	-	-	-
J18174+483	16.00 ± 0.10	15.97	≤ 0.1	-	-	1.07	≤ 0.1	-	-
J18198-019	–	31.59	8.72	-	-	-	-	-	-
J18580+059	35.00 ± 0.30	36.09	≤ 0.1	-	-	-	-	-	-

Table B.7: Continued.

Karmn	$P_{\rm rot}$ lit.	$P_{\rm rot}$		$\frac{1}{2}P_{\rm rot}$		$P_{\rm rot}$ 1 d a.		$\frac{1}{2}P_{\rm rot}$ 1 d a.	
	[d]	P [d]	FAP [%]	P [d]	FAP [%]	P [d]	FAP [%]	P [d]	FAP [%]
J19346+045	13.00 ± 0.80	21.75	≤ 0.1	-	-	-	-	-	-
J20305+654	33.00 ± 0.50	32.77	9.36	-	-	-	-	-	-
J20451-313	4.840 ± 0.040|	-	-	2.40	53.29	-	-	1.70	19.54
J21164+025	–	41.77	≤ 0.1	-	-	-	-	-	-
J21221+229	41.00 ± 1.70	39.90	≤ 0.1	-	-	-	-	-	-
J22021+014	30.00 ± 0.10	-	-	10.65	3.52	-	-	-	-
J22115+184	36.00 ± 0.20	33.81	3.82	-	-	-	-	-	-
J22468+443	4.380 ± 0.030	4.38	0.20	-	-	1.29	9.04	-	-
J22565+165	40.00 ± 0.20	38.05	≤ 0.1	-	-	-	-	-	-
J23492+024	50.00 ± 3.50*	-	-	25.76	≤ 0.1	-	-	-	-

Table B.8: Same as Table B.1 but for the Ca IRT-a.

Karmn	$P_{\rm rot}$ lit.	$P_{\rm rot}$		$P_{\rm rot}$ 1 d a.		$\frac{1}{2}P_{\rm rot}$		$\frac{1}{2}P_{\rm rot}$ 1 d a.	
	[d]	P [d]	FAP [%]	P [d]	FAP [%]	P [d]	FAP [%]	P [d]	FAP [%]
J01025+716	52.00 ± 2.60	59.42	4.07	-	-	-	-	-	-
J01026+623	20.00 ± 0.40	18.89	≤ 0.1	-	-	1.05	≤ 0.1	-	-
J02222+478	30.00 ± 0.40	31.13	2.25	-	-	-	-	-	-
J03133+047	$130.0^{\dagger}$	120.70	98.07	-	-	-	-	-	-
J03463+262	–	10.07	0.23	-	-	-	-	-	-
J04290+219	25.00 ± 0.30	25.14	≤ 0.1	-	-	-	-	-	-
J04376+528	–	15.47	≤ 0.1	-	-	-	-	-	-
J04429+189	41.00 ± 0.40	38.83	0.65	-	-	-	-	-	-
J04588+498	–	19.19	≤ 0.1	-	-	-	-	-	-
J05314-036	34.00 ± 0.60	34.07	≤ 0.1	-	-	-	-	-	-
J05365+113	12.00 ± 0.10	11.79	≤ 0.1	-	-	-	-	-	-
J08413+594	–	87.24	65.71	-	-	-	-	-	-
J09143+526	–	17.54	≤ 0.1	-	-	-	-	-	-
J09144+526	–	16.69	≤ 0.1	-	-	-	-	-	-
J09561+627	–	17.79	≤ 0.1	-	-	1.06	≤ 0.1	-	-
J10122-037	22.00 ± 0.20	21.38	0.11	-	-	-	-	-	-
J11302+076	36.00 ± 0.30	35.05	≤ 0.1	-	-	1.03	≤ 0.1	-	-
J16167+672S	–	22.00	≤ 0.1	-	-	-	-	-	-
J16581+257	24.00 ± 0.10	23.75	0.24	-	-	-	-	-	-
J17303+055	–	33.51	≤ 0.1	-	-	-	-	-	-
J17378+185	–	37.99	≤ 0.1	-	-	-	-	-	-
J18174+483	16.00 ± 0.10	16.07	0.12	-	-	-	-	-	-
J18198-019	–	31.61	≤ 0.1	-	-	-	-	-	-
J18498-238	2.870 ± 0.010	-	-	1.43	17.24	-	-	3.30	20.41
J18580+059	35.00 ± 0.30	36.09	≤ 0.1	-	-	-	-	-	-
J19346+045	13.00 ± 0.80	21.75	≤ 0.1	-	-	-	-	-	-
J20305+654	33.00 ± 0.50	32.77	22.90	-	-	-	-	-	-
J20451-313	4.840 ± 0.040|	-	-	2.37	21.05	-	-	1.72	19.75
J21164+025	–	44.21	≤ 0.1	-	-	-	-	-	-

Table B.8: Continued.

Karmn	$P_{\rm rot}$ lit.	$P_{\rm rot}$		$\frac{1}{2}P_{\rm rot}$		$P_{\rm rot}$ 1 d a.		$\frac{1}{2}P_{\rm rot}$ 1 d a.	
	[d]	P [d]	FAP [%]	P [d]	FAP [%]	P [d]	FAP [%]	P [d]	FAP [%]
J21221+229	41.00 ± 1.70	39.90	≤ 0.1	-	-	-	-	-	-
J22021+014	30.00 ± 0.10	22.06	2.22	-	-	-	-	-	-
J22115+184	36.00 ± 0.20	34.00	1.02	-	-	-	-	-	-
J22468+443	4.380 ± 0.030	4.38	5.06	-	-	1.36	29.18	-	-
J22565+165	40.00 ± 0.20	38.25	≤ 0.1	-	-	-	-	-	-

Table B.9: Same as Table B.1 but for the Ca IRT-b.

Karmn	$P_{\rm rot}$ lit.	$P_{\rm rot}$		$P_{\rm rot}$ 1 d a.		$\frac{1}{2}P_{\rm rot}$		$\frac{1}{2}P_{\rm rot}$ 1 d a.	
	[d]	P [d]	FAP [%]	P [d]	FAP [%]	P [d]	FAP [%]	P [d]	FAP [%]
J00183+440	$45.00 \pm 4.40^{*}$	46.19	≤ 0.1	-	-	-	-	-	-
J01025+716	52.00 ± 2.60	51.73	≤ 0.1	-	-	1.02	≤ 0.1	-	-
J01026+623	20.00 ± 0.40	18.89	≤ 0.1	-	-	1.05	≤ 0.1	-	-
J02222+478	30.00 ± 0.40	31.13	≤ 0.1	-	-	-	-	-	-
J03133+047	$130.0^{\dagger}$	140.81	4.01	-	-	-	-	-	-
J03463+262	–	10.07	0.11	-	-	-	-	-	-
J04290+219	25.00 ± 0.30	25.14	≤ 0.1	-	-	-	-	-	-
J04376+528	–	15.47	≤ 0.1	-	-	-	-	-	-
J04429+189	41.00 ± 0.40	38.83	≤ 0.1	-	-	-	-	-	-
J04588+498	–	19.19	≤ 0.1	-	-	-	-	-	-
J05314-036	34.00 ± 0.60	34.07	≤ 0.1	-	-	-	-	-	-
J05365+113	12.00 ± 0.10	11.79	≤ 0.1	-	-	-	-	-	-
J08413+594	–	87.24	6.98	-	-	-	-	-	-
J09143+526	–	17.54	≤ 0.1	-	-	-	-	-	-
J09144+526	–	16.69	≤ 0.1	-	-	-	-	-	-
J09561+627	–	17.79	≤ 0.1	-	-	1.06	≤ 0.1	-	-
J10122-037	22.00 ± 0.20	21.38	0.11	-	-	-	-	-	-
J11302+076	36.00 ± 0.30	35.63	≤ 0.1	-	-	1.03	≤ 0.1	-	-
J16167+672S	–	22.00	≤ 0.1	-	-	-	-	-	-
J16581+257	24.00 ± 0.10	23.75	≤ 0.1	-	-	-	-	-	-
J17303+055	–	33.51	≤ 0.1	-	-	-	-	-	-
J17378+185	–	36.18	≤ 0.1	-	-	-	-	-	-
J18174+483	16.00 ± 0.10	16.02	≤ 0.1	-	-	-	-	-	-
J18198-019	–	31.70	≤ 0.1	-	-	-	-	-	-
J18580+059	35.00 ± 0.30	36.65	≤ 0.1	-	-	-	-	-	-
J19346+045	13.00 ± 0.80	21.75	≤ 0.1	-	-	-	-	-	-
J20451-313	4.840 ± 0.040	-	-	2.37	5.72	-	-	1.72	5.35
J21164+025	–	41.77	≤ 0.1	-	-	-	-	-	-
J21221+229	41.00 ± 1.70	39.90	≤ 0.1	-	-	-	-	-	-
J22021+014	30.00 ± 0.10	22.06	1.00	-	-	-	-	-	-
J22115+184	36.00 ± 0.20	34.00	≤ 0.1	-	-	-	-	-	-
J22468+443	4.380 ± 0.030	4.38	2.70	-	-	1.30	18.55	-	-
J22565+165	40.00 ± 0.20	38.25	≤ 0.1	-	-	-	-	-	-

Table B.10: Same as Table B.1 but for the Ca IRT-c.

Karmn	$P_{\rm rot}$ lit.	$P_{\rm rot}$		$P_{\rm rot}$ 1 d a.		$\frac{1}{2}P_{\rm rot}$		$\frac{1}{2}P_{\rm rot}$ 1 d a.	
	[d]	P [d]	FAP [%]	P [d]	FAP [%]	P [d]	FAP [%]	P [d]	FAP [%]
J00183+440	$45.00 \pm 4.40^{*}$	46.19	6.52	-	-	-	-	-	-
J01025+716	52.00 ± 2.60	52.48	≤ 0.1	-	-	1.02	9.53	-	-
J01026+623	20.00 ± 0.40	18.98	≤ 0.1	-	-	1.05	≤ 0.1	-	-
J02002+130	–	1.95	4.54	-	-	-	-	-	-
J02222+478	30.00 ± 0.40	28.65	≤ 0.1	-	-	-	-	-	-
J03463+262	–	10.07	0.33	-	-	-	-	-	-
J04290+219	25.00 ± 0.30	25.14	≤ 0.1	-	-	-	-	-	-
J04376+528	–	15.47	0.39	-	-	-	-	-	-
J04429+189	41.00 ± 0.40	38.83	0.64	-	-	-	-	-	-
J04588+498	–	19.19	≤ 0.1	-	-	-	-	-	-
J05314-036	34.00 ± 0.60	33.78	≤ 0.1	-	-	-	-	-	-
J05365+113	12.00 ± 0.10	11.79	≤ 0.1	-	-	-	-	-	-
J08413+594	–	87.24	6.07	-	-	-	-	-	-
J09143+526	–	17.54	≤ 0.1	-	-	-	-	-	-
J09144+526	–	16.69	≤ 0.1	-	-	-	-	-	-
J09561+627	–	17.79	≤ 0.1	-	-	1.06	1.57	-	-
J10122-037	22.00 ± 0.20	21.38	≤ 0.1	-	-	-	-	-	-
J11302+076	36.00 ± 0.30	35.05	≤ 0.1	-	-	1.03	2.22	-	-
J16167+672S	–	22.00	≤ 0.1	-	-	-	-	-	-
J16581+257	24.00 ± 0.10	23.75	0.17	-	-	-	-	-	-
J17303+055	–	33.76	0.11	-	-	-	-	-	-
J17378+185	–	37.99	≤ 0.1	-	-	-	-	-	-
J18174+483	16.00 ± 0.10	16.02	0.15	-	-	-	-	-	-
J18198-019	–	31.61	≤ 0.1	-	-	-	-	-	-
J18580+059	35.00 ± 0.30	36.65	≤ 0.1	-	-	-	-	-	-
J19346+045	13.00 ± 0.80	21.84	≤ 0.1	-	-	-	-	-	-
J20451-313	4.840 ± 0.040	-	-	2.37	9.28	-	-	1.72	8.62
J21164+025	–	44.21	≤ 0.1	-	-	-	-	-	-
J21221+229	41.00 ± 1.70	39.90	≤ 0.1	-	-	-	-	-	-
J22021+014	30.00 ± 0.10	22.06	0.50	-	-	-	-	-	-
J22115+184	36.00 ± 0.20	34.00	≤ 0.1	-	-	-	-	-	-
J22468+443	4.380 ± 0.030	4.38	2.98	-	-	1.30	16.84	-	-
J22565+165	40.00 ± 0.20	38.25	≤ 0.1	-	-	-	-	-	-

Bibliography

Affer, L., Micela, G., Damasso, M., Perger, M., Ribas, I., Suárez Mascareño, A., González Hernández, J. I., Rebolo, R., Poretti, E., Maldonado, J., et al. (2016). "HADES RV Program with HARPS-N at the TNG GJ 3998: An Early M-Dwarf Hosting a System of Super-Earths". *Astronomy & Astrophysics* 593. DOI: 10.1051/0004-6361/201628690.

Allende Prieto, C., Koesterke, L., Ludwig, H.-G., Freytag, B., and Caffau, E. (2013). "Convective Line Shifts for the Gaia RVS from the CIFIST 3D Model Atmosphere Grid". *Astronomy & Astrophysics* 550. DOI: 10.1051/0004-6361/201220064.

Allende Prieto, C., Lambert, D. L., Tull, R. G., and MacQueen, P. J. (2002). "Convective Wavelength Shifts in the Spectra of Late-Type Stars". *The Astrophysical Journal Letters* 566. DOI: 10.1086/339658.

Alonso-Floriano, F. J., Morales, J. C., Caballero, J. A., Montes, D., Klutsch, A., Mundt, R., Cortés-Contreras, M., Ribas, I., Reiners, A., Amado, P. J., et al. (2015). "CARMENES Input Catalogue of M Dwarfs. I. Low-Resolution Spectroscopy with CAFOS". *Astronomy & Astrophysics* 577. DOI: 10.1051/0004-6361/201525803.

Alonso-Floriano, F. J., Snellen, I. A. G., Czesla, S., Bauer, F. F., Salz, M., Lampón, M., Lara, L. M., Nagel, E., López-Puertas, M., Nortmann, L., et al. (2019). "He I λ 10 830 Å in the Transmission Spectrum of HD209458 b". *Astronomy & Astrophysics* 629. DOI: 10.1051/0004-6361/201935979.

Anglada-Escudé, G. and Butler, R. P. (2012). "The HARPS-TERRA Project. I. Description of the Algorithms, Performance, and New Measurements on a Few Remarkable Stars Observed by HARPS". *The Astrophysical Journal Supplement Series* 200. DOI: 10.1088/0067-0049/200/2/15.

Artigau, É., Kouach, D., Donati, J.-F., Doyon, R., Delfosse, X., Baratchart, S., Lacombe, M., Moutou, C., Rabou, P., Parès, L. P., et al. (2014). "SPIRou: The near-Infrared Spectropolarimeter/High-Precision Velocimeter for the Canada-France-Hawaii Telescope". 9147. DOI: 10.1117/12.2055663.

Astudillo-Defru, N., Bonfils, X., Delfosse, X., Ségransan, D., Forveille, T., Bouchy, F., Gillon, M., Lovis, C., Mayor, M., Neves, V., et al. (2015). "The HARPS Search for Southern Extra-Solar Planets. XXXVI. Planetary Systems and Stellar Activity of the M Dwarfs GJ 3293, GJ 3341, and GJ 3543". *Astronomy & Astrophysics* 575. DOI: 10.1051/0004-6361/201424253.

Astudillo-Defru, N., Delfosse, X., Bonfils, X., Forveille, T., Lovis, C., and Rameau, J. (2017a). "Magnetic Activity in the HARPS M Dwarf Sample. The Rotation-Activity Relationship for Very Low-Mass Stars through R'(HK)". *Astronomy & Astrophysics* 600. DOI: 10.1051/0004-6361/201527078.

Astudillo-Defru, N., Forveille, T., Bonfils, X., Ségransan, D., Bouchy, F., Delfosse, X., Lovis, C., Mayor, M., Murgas, F., Pepe, F., et al. (2017b). "The HARPS Search for Southern Extra-Solar Planets - XLI. A Dozen Planets around the M Dwarfs GJ 3138, GJ 3323, GJ 273, GJ 628, and GJ 3293". *Astronomy & Astrophysics* 602. DOI: 10.1051/0004-6361/201630153.

Baluev, R. V. (2008). "Assessing the Statistical Significance of Periodogram Peaks". *Monthly Notices of the Royal Astronomical Society* 385. DOI: 10.1111/j.1365-2966.2008.12689.x.

Baluev, R. V. and Shaidulin, V. S. (2015). "Analytic Models of the Rossiter-McLaughlin Effect for Arbitrary Eclipser/Star Size Ratios and Arbitrary Multiline Stellar Spectra". *Monthly Notices of the Royal Astronomical Society* 454. DOI: 10.1093/mnras/stv2251.

Baran, A. S., Winiarski, M., Siwak, M., Fox-Machado, L., Kozieł-Wierzbowska, D., Krzesinski, J., Dróżdz, M., and Winans, A. (2013). "Mt. Suhora Survey - Searching for Pulsating M Dwarfs. III". *Acta Astronomica* 63.

Baranne, A., Mayor, M., and Poncet, J. L. (1979). "Coravel— A New Tool for Radial Velocity Measurements". *Vistas in Astronomy* 23. DOI: 10.1016/0083-6656(79)90016-3.

Baranne, A., Queloz, D., Mayor, M., Adrianzyk, G., Knispel, G., Kohler, D., Lacroix, D., Meunier, J.-P., Rimbaud, G., and Vin, A. (1996). "ELODIE: A Spectrograph for Accurate Radial Velocity Measurements." *Astronomy & Astrophysics Supplement Series* 119.

Baroch, D., Morales, J. C., Ribas, I., Herrero, E., Rosich, A., Perger, M., Anglada-Escudé, G., Reiners, A., Caballero, J. A., Quirrenbach, A., et al. (2020). "The CARMENES Search for Exoplanets around M Dwarfs. Convective Shift and Starspot Constraints from Chromatic Radial Velocities". *Astronomy & Astrophysics* 641. DOI: 10.1051/0004-6361/202038213.

Baroch, D., Morales, J. C., Ribas, I., Tal-Or, L., Zechmeister, M., Reiners, A., Caballero, J. A., Quirrenbach, A., Amado, P. J., Dreizler, S., et al. (2018). "The CARMENES Search for Exoplanets around M Dwarfs. Nine New Double-Line Spectroscopic Binary Stars". *Astronomy & Astrophysics* 619. DOI: 10.1051/0004-6361/201833440.

Bauer, F. F., Reiners, A., Beeck, B., and Jeffers, S. V. (2018). "The Influence of Convective Blueshift on Radial Velocities of F, G, and K Stars". *Astronomy & Astrophysics* 610. DOI: 10.1051/0004-6361/201731227.

Bauer, F. F., Zechmeister, M., Kaminski, A., Rodríguez López, C., Caballero, J. A., Azzaro, M., Stahl, O., Kossakowski, D., Quirrenbach, A., Becerril Jarque, S., et al. (2020). "The CARMENES Search for Exoplanets around M Dwarfs. Measuring Precise Radial Velocities in the near Infrared: The Example of the Super-Earth CD Cet b". *Astronomy & Astrophysics* 640. DOI: 10.1051/0004-6361/202038031.

Bauer, F. F., Zechmeister, M., and Reiners, A. (2015). "Calibrating Echelle Spectrographs with Fabry-Pérot Etalons". *Astronomy & Astrophysics* 581. DOI: 10.1051/0004-6361/201526462.

Bedding, T. R., Butler, R. P., Kjeldsen, H., Baldry, I. K., O'Toole, S. J., Tinney, C. G., Marcy, G. W., Kienzle, F., and Carrier, F. (2001). "Evidence for Solar-like Oscillations in β Hydri". *The Astrophysical Journal Letters* 549. DOI: 10.1086/319139.

Benneke, B., Werner, M., Petigura, E., Knutson, H., Dressing, C., Crossfield, I. J. M., Schlieder, J. E., Livingston, J., Beichman, C., Christiansen, J., et al. (2017). "Spitzer Observations Confirm and Rescue the Habitable-Zone Super-Earth K2-18b for Future Characterization". *The Astrophysical Journal* 834. DOI: 10.3847/1538-4357/834/2/187.

Berdiñas, Z. M., Amado, P. J., Anglada-Escudé, G., Rodríguez-López, C., and Barnes, J. (2016). "High-Cadence Spectroscopy of M Dwarfs - I. Analysis of Systematic Effects in HARPS-N Line Profile Measurements on the Bright Binary GJ 725A+B". *Monthly Notices of the Royal Astronomical Society* 459.4. DOI: 10.1093/mnras/stw906.

Berdiñas, Z. M., Rodríguez-López, C., Amado, P. J., Anglada-Escudé, G., Barnes, J. R., MacDonald, J., Zechmeister, M., and Sarmiento, L. F. (2017). "High-Cadence Spectroscopy of M-Dwarfs - II. Searching for Stellar Pulsations with HARPS". *Monthly Notices of the Royal Astronomical Society* 469. DOI: 10.1093/mnras/stx1140.

Berdyugina, S. V. and Solanki, S. K. (2002). "The Molecular Zeeman Effect and Diagnostics of Solar and Stellar Magnetic Fields. I. Theoretical Spectral Patterns in the Zeeman Regime". *Astronomy & Astrophysics* 385. DOI: 10.1051/0004-6361:20020130.

Bluhm, P., Luque, R., Espinoza, N., Pallé, E., Caballero, J. A., Dreizler, S., Livingston, J. H., Mathur, S., Quirrenbach, A., Stock, S., et al. (2020). "Precise Mass and Radius of a Transiting Super-Earth Planet Orbiting the M Dwarf TOI-1235: A Planet in the Radius Gap?" *Astronomy & Astrophysics* 639. DOI: 10.1051/0004-6361/202038160.

Boisse, I., Bouchy, F., Hébrard, G., Bonfils, X., Santos, N., and Vauclair, S. (2011). "Disentangling between Stellar Activity and Planetary Signals". *Astronomy & Astrophysics* 528. DOI: 10.1051/0004-6361/201014354.

Boisse, I., Eggenberger, A., Santos, N. C., Lovis, C., Bouchy, F., Hébrard, G., Arnold, L., Bonfils, X., Delfosse, X., Desort, M., et al. (2010). "The SOPHIE Search for Northern Extrasolar Planets: III. A Jupiter-Mass Companion around HD 109246". *Astronomy & Astrophysics* 523. DOI: 10.1051/0004-6361/201014909.

Boisse, I., Moutou, C., Vidal-Madjar, A., Bouchy, F., Pont, F., Hébrard, G., Bonfils, X., Croll, B., Delfosse, X., Desort, M., et al. (2009). "Stellar Activity of Planetary Host Star HD 189 733". *Astronomy & Astrophysics* 495. DOI: 10.1051/0004-6361:200810648.

Bonfils, X., Delfosse, X., Udry, S., Forveille, T., Mayor, M., Perrier, C., Bouchy, F., Gillon, M., Lovis, C., Pepe, F., et al. (2013). "The HARPS Search for Southern Extra-Solar Planets. XXXI. The M-Dwarf Sample". *Astronomy & Astrophysics* 549. DOI: 10.1051/0004-6361/201014704.

Bonfils, X., Mayor, M., Delfosse, X., Forveille, T., Gillon, M., Perrier, C., Udry, S., Bouchy, F., Lovis, C., Pepe, F., et al. (2007). "The HARPS Search for Southern Extra-Solar Planets. X. A m Sin i = 11 M_⊕ Planet around the Nearby Spotted M Dwarf GJ 674". *Astronomy & Astrophysics* 474. DOI: 10.1051/0004-6361:20077068.

Bouchy, F., Pepe, F., and Queloz, D. (2001). "Fundamental Photon Noise Limit to Radial Velocity Measurements". *Astronomy & Astrophysics* 374. DOI: 10.1051/0004-6361:20010730.

Brandt, P. N. and Solanki, S. K. (1990). "Solar Line Asymmetries and the Magnetic Filling Factor". *Astronomy & Astrophysics* 231.

Butler, R. P., Marcy, G. W., Williams, E., McCarthy, C., Dosanjh, P., and Vogt, S. S. (1996). "Attaining Doppler Precision of 3 M S-1". *Publications of the Astronomical Society of the Pacific* 108. DOI: 10.1086/133755.

Butler, R. P., Johnson, J. A., Marcy, G. W., Wright, J. T., Vogt, S. S., and Fischer, D. A. (2006). "A Long-Period Jupiter-Mass Planet Orbiting the Nearby M Dwarf GJ 849*". *Publications of the Astronomical Society of the Pacific* 118.850. DOI: 10.1086/510500.

Butler, R. P., Vogt, S. S., Marcy, G. W., Fischer, D. A., Wright, J. T., Henry, G. W., Laughlin, G., and Lissauer, J. J. (2004). "A Neptune-Mass Planet Orbiting the Nearby M Dwarf GJ 436". *The Astrophysical Journal* 617.1. DOI: 10.1086/425173.

Carleo, I., Malavolta, L., Lanza, A. F., Damasso, M., Desidera, S., Borsa, F., Mallonn, M., Pinamonti, M., Gratton, R., Alei, E., et al. (2020). "The GAPS Programme at TNG. XXI. A GIARPS Case Study of Known Young Planetary Candidates: Confirmation of HD 285507 b and Refutation of AD Leonis b". *Astronomy & Astrophysics* 638. DOI: 10.1051/0004-6361/201937369.

Cegla, H. M., Shelyag, S., Watson, C. A., and Mathioudakis, M. (2013). "Stellar Surface Magneto-Convection as a Source of Astrophysical Noise. I. Multi-Component Parameterization of Absorption Line Profiles". *The Astrophysical Journal* 763. DOI: 10.1088/0004-637X/763/2/95.

Cegla, H. M., Watson, C. A., Shelyag, S., Chaplin, W. J., Davies, G. R., Mathioudakis, M., Palumbo III, M. L., Saar, S. H., and Haywood, R. D. (2018). "Stellar Surface Magneto-Convection as a Source of Astrophysical Noise. II. Center-to-Limb Parameterization of Absorption Line Profiles and Comparison to Observations". *The Astrophysical Journal* 866. DOI: 10.3847/1538-4357/aaddfc.

Cegla, H. M., Watson, C. A., Shelyag, S., Mathioudakis, M., and Moutari, S. (2019). "Stellar Surface Magnetoconvection as a Source of Astrophysical Noise. III. Sun-as-a-Star Simulations and Optimal Noise Diagnostics". *The Astrophysical Journal* 879. DOI: 10.3847/1538-4357/ab16d3.

Cersullo, F., Coffinet, A., Chazelas, B., Lovis, C., and Pepe, F. (2019). "New Wavelength Calibration for Echelle Spectrographs Using Fabry-Pérot Etalons". *Astronomy & Astrophysics* 624. DOI: 10.1051/0004-6361/201833852.

Chabrier, G. and Baraffe, I. (1997). "Structure and Evolution of Low-Mass Stars". *Astronomy & Astrophysics* 327.

Charbonneau, P. (2020). "Dynamo Models of the Solar Cycle". *Living Reviews in Solar Physics* 17.1. DOI: 10.1007/s41116-020-00025-6.

Claudi, R., Benatti, S., Carleo, I., Ghedina, A., Guerra, J., Micela, G., Molinari, E., Oliva, E., Rainer, M., Tozzi, A., et al. (2017). "GIARPS@TNG: GIANO-B and HARPS-N Together for a Wider Wavelength Range Spectroscopy". *European Physical Journal Plus* 132. DOI: 10.1140/epjp/i2017-11647-9.

Coffinet, A., Lovis, C., Dumusque, X., and Pepe, F. (2019). "New Wavelength Calibration of the HARPS Spectrograph". *Astronomy & Astrophysics* 629. DOI: 10.1051/0004-6361/201833272.

Cortés-Contreras, M., Béjar, V. J. S., Caballero, J. A., Gauza, B., Montes, D., Alonso-Floriano, F. J., Jeffers, S. V., Morales, J. C., Reiners, A., Ribas, I., et al. (2017). "CARMENES Input Catalogue of M Dwarfs. II. High-Resolution Imaging with FastCam". *Astronomy & Astrophysics* 597. DOI: 10.1051/0004-6361/201629056.

Cosentino, R., Lovis, C., Pepe, F., Collier Cameron, A., Latham, D. W., Molinari, E., Udry, S., Bezawada, N., Black, M., Born, A., et al. (2012). "Harps-N: The New Planet Hunter at TNG". *Ground-based and Airborne Instrumentation for Astronomy IV* 8446. DOI: 10.1117/12.925738.

Covey, K. R., Ivezić, Ž., Schlegel, D., Finkbeiner, D., Padmanabhan, N., Lupton, R. H., Agüeros, M. A., Bochanski, J. J., Hawley, S. L., West, A. A., et al. (2007). "Stellar SEDs from 0.3 to 2.5 *M*m: Tracing the Stellar Locus and Searching for Color Outliers in the SDSS and 2MASS". *The Astronomical Journal* 134. DOI: 10.1086/522052.

Cram, L. E. and Mullan, D. J. (1979). "Model Chromospheres of Flare Stars. I - Balmer-Line Profiles". *The Astrophysical Journal* 234. DOI: 10.1086/157532.

Cretignier, M., Dumusque, X., Allart, R., Pepe, F., and Lovis, C. (2020). "Measuring Precise Radial Velocities on Individual Spectral Lines. II. Dependance of Stellar Activity Signal on Line Depth". *Astronomy & Astrophysics* 633. DOI: 10.1051/0004-6361/201936548.

Cumming, A., Marcy, G. W., and Butler, R. P. (1999). "The Lick Planet Search: Detectability and Mass Thresholds". *The Astrophysical Journal* 526. DOI: 10.1086/308020.

Davis, A. B., Cisewski, J., Dumusque, X., Fischer, D. A., and Ford, E. B. (2017). "Insights on the Spectral Signatures of Stellar Activity and Planets from PCA". *The Astrophysical Journal* 846. DOI: 10.3847/1538-4357/aa8303.

Del Moro, D., Berrilli, F., Duvall Jr., T. L., and Kosovichev, A. G. (2004). "Dynamics and Structure of Supergranulation". *Solar Physics* 221. DOI: 10.1023/B:SOLA.0000033363.15641.8f.

Delfosse, X., Forveille, T., Mayor, M., Perrier, C., Naef, D., and Queloz, D. (1998a). "The Closest Extrasolar Planet. A Giant Planet around the M4 Dwarf GL 876". *Astronomy & Astrophysics* 338.

Delfosse, X., Forveille, T., Perrier, C., and Mayor, M. (1998b). "Rotation and Chromospheric Activity in Field M Dwarfs". *Astronomy & Astrophysics* 331.

Desidera, S., Gratton, R. G., Endl, M., Claudi, R. U., Cosentino, R., Barbieri, M., Bonanno, G., Lucatello, S., Martinez Fiorenzano, A. F., Marzari, F., et al. (2004). "No Planet around HD 219542 B". *Astronomy & Astrophysics* 420. DOI: 10.1051/0004-6361:20040155.

Desort, M., Lagrange, A.-M., Galland, F., Udry, S., and Mayor, M. (2007). "Search for Exoplanets with the Radial-Velocity Technique: Quantitative Diagnostics of Stellar Activity". *Astronomy & Astrophysics* 473.3. DOI: 10.1051/0004-6361:20078144.

Díaz, R. F., Cincunegui, C., and Mauas, P. J. D. (2007). "The NaI D Resonance Lines in Main-Sequence Late-Type Stars". *Monthly Notices of the Royal Astronomical Society* 378. DOI: 10.1111/j.1365-2966.2007.11833.x.

Díez Alonso, E., Caballero, J. A., Montes, D., de Cos Juez, F. J., Dreizler, S., Dubois, F., Jeffers, S. V., Lalitha, S., Naves, R., Reiners, A., et al. (2019). "CARMENES Input Catalogue of M Dwarfs. IV. New Rotation Periods from Photometric Time Series". *Astronomy & Astrophysics* 621. DOI: 10.1051/0004-6361/201833316.

Donati, J.-F., Kouach, D., Moutou, C., Doyon, R., Delfosse, X., Artigau, E., Baratchart, S., Lacombe, M., Barrick, G., Hébrard, G., et al. (2020). "SPIRou: NIR Velocimetry and Spectropolarimetry at the CFHT". *Monthly Notices of the Royal Astronomical Society* 498. DOI: 10.1093/mnras/staa2569.

Dravins, D. (1982). "Photospheric Spectrum Line Asymmetries and Wavelength Shifts". *Annual Review of Astronomy and Astrophysics* 20. DOI: 10.1146/annurev.aa.20.090182.000425.

Dumusque, X. (2018). "Measuring Precise Radial Velocities on Individual Spectral Lines. I. Validation of the Method and Application to Mitigate Stellar Activity". *Astronomy & Astrophysics* 620. DOI: 10.1051/0004-6361/201833795.

Dumusque, X., Santos, N. C., Udry, S., Lovis, C., and Bonfils, X. (2011a). "Planetary Detection Limits Taking into Account Stellar Noise. II. Effect of Stellar Spot Groups on Radial-Velocities". *Astronomy & Astrophysics* 527. DOI: 10.1051/0004-6361/201015877.

Dumusque, X., Udry, S., Lovis, C., Santos, N. C., and Monteiro, M. J. P. F. G. (2011b). "Planetary Detection Limits Taking into Account Stellar Noise. I. Observational Strategies to Reduce Stellar Oscillation and Granulation Effects". *Astronomy & Astrophysics* 525. DOI: 10.1051/0004-6361/201014097.

Dumusque, X., Glenday, A., Phillips, D. F., Buchschacher, N., Collier Cameron, A., Cecconi, M., Charbonneau, D., Cosentino, R., Ghedina, A., Latham, D. W., et al. (2015). "HARPS-N Observes the Sun as a Star". *The Astrophysical Journal Letters* 814. DOI: 10.1088/2041-8205/814/2/L21.

Dumusque, X., Pepe, F., Lovis, C., Ségransan, D., Sahlmann, J., Benz, W., Bouchy, F., Mayor, M., Queloz, D., Santos, N., et al. (2012). "An Earth-Mass Planet Orbiting α Centauri B". *Nature* 491.7423. DOI: 10.1038/nature11572.

Durney, B. R., De Young, D. S., and Roxburgh, I. W. (1993). "On the Generation of the Large-Scale and Turbulent Magnetic Fields in Solar-Type Stars". *Solar Physics* 145. DOI: 10.1007/BF00690652.

Feng, F., Shectman, S. A., Clement, M. S., Vogt, S. S., Tuomi, M., Teske, J. K., Burt, J., Crane, J. D., Holden, B., Wang, S. X., et al. (2020). "Search for Nearby Earth Analogs .III. Detection of 10 New Planets, 3 Planet Candidates, and Confirmation of 3 Planets around 11 Nearby M Dwarfs". *The Astrophysical Journal Supplement Series* 250. DOI: 10.3847/1538-4365/abb139.

Ferraz-Mello, S. (1981). "Estimation of Periods from Unequally Spaced Observations". *The Astronomical Journal* 86. DOI: 10.1086/112924.

Figueira, P., Marmier, M., Bonfils, X., di Folco, E., Udry, S., Santos, N. C., Lovis, C., Mégevand, D., Melo, C. H. F., Pepe, F., et al. (2010). "Evidence against the Young Hot-Jupiter around BD +20 1790". *Astronomy & Astrophysics* 513. DOI: 10.1051/0004-6361/201014323.

Figueira, P., Santos, N. C., Pepe, F., Lovis, C., and Nardetto, N. (2013). "Line-Profile Variations in Radial-Velocity Measurements. Two Alternative Indicators for Planetary Searches". *Astronomy & Astrophysics* 557. DOI: 10.1051/0004-6361/201220779.

Fischer, D. A., Anglada-Escude, G., Arriagada, P., Baluev, R. V., Bean, J. L., Bouchy, F., Buchhave, L. A., Carroll, T., Chakraborty, A., Crepp, J. R., et al. (2016). "State of the Field: Extreme Precision Radial Velocities". *Publications of the Astronomical Society of the Pacific* 128.964. DOI: 10.1088/1538-3873/128/964/066001.

Fouqué, P., Moutou, C., Malo, L., Martioli, E., Lim, O., Rajpurohit, A., Artigau, E., Delfosse, X., Donati, J.-F., Forveille, T., et al. (2018). "SPIRou Input Catalogue: Global Properties of 440 M Dwarfs Observed with ESPaDOnS at CFHT". *Monthly Notices of the Royal Astronomical Society* 475. DOI: 10.1093/mnras/stx3246.

Fuhrmeister, B., Czesla, S., Hildebrandt, L., Nagel, E., Schmitt, J. H. M. M., Hintz, D., Johnson, E. N., Sanz-Forcada, J., Schöfer, P., Jeffers, S. V., et al. (2019a). "The CARMENES Search for Exoplanets around M Dwarfs. The He I Triplet at 10830 Å across the M Dwarf Sequence". *Astronomy & Astrophysics* 632. DOI: 10.1051/0004-6361/201936193.

Fuhrmeister, B., Czesla, S., Schmitt, J. H. M. M., Jeffers, S. V., Caballero, J. A., Zechmeister, M., Reiners, A., Ribas, I., Amado, P. J., Quirrenbach, A., et al. (2018). "The CARMENES Search for Exoplanets around M Dwarfs. Wing Asymmetries of Hα, Na I D, and He I Lines". *Astronomy & Astrophysics* 615. DOI: 10.1051/0004-6361/201732204.

Fuhrmeister, B., Czesla, S., Schmitt, J. H. M. M., Johnson, E. N., Schöfer, P., Jeffers, S. V., Caballero, J. A., Zechmeister, M., Reiners, A., Ribas, I., et al. (2019b). "The CARMENES Search for Exoplanets around M Dwarfs. Period Search in Hα, Na I D, and Ca II IRT Lines". *Astronomy & Astrophysics* 623. DOI: 10.1051/0004-6361/201834483.

Gabriel, M. and Grossman, A. S. (1977). "The Pulsational Stability of Very Low Mass Stars on the Hydrogen and Deuterium Main Sequences". *Astronomy & Astrophysics* 54.

Getling, A. V. and Brandt, P. N. (2002). "Regular Structures of the Solar Photosphere. (Persistence of the Granular Field and Trenching in the Brightness Relief)". *Astronomy & Astrophysics* 382. DOI: 10.1051/0004-6361:20011762.

Giannattasio, F., Berrilli, F., Consolini, G., Del Moro, D., Gošić, M., and Bellot Rubio, L. (2018). "Occurrence and Persistence of Magnetic Elements in the Quiet Sun". *Astronomy & Astrophysics* 611. DOI: 10.1051/0004-6361/201730583.

Gizis, J. E., Reid, I. N., and Hawley, S. L. (2002). "The Palomar/MSU Nearby Star Spectroscopic Survey. III. Chromospheric Activity, M Dwarf Ages, and the Local Star Formation History". *The Astronomical Journal* 123. DOI: 10.1086/340465.

Gomes da Silva, J., Santos, N. C., Bonfils, X., Delfosse, X., Forveille, T., and Udry, S. (2011). "Long-Term Magnetic Activity of a Sample of M-Dwarf Stars from the HARPS Program. I. Comparison of Activity Indices". *Astronomy & Astrophysics* 534. DOI: 10.1051/0004-6361/201116971.

Gray, D. F. (2009). "The Third Signature of Stellar Granulation". *The Astrophysical Journal* 697.2. DOI: 10.1088/0004-637X/697/2/1032.

Gray, R. O., Corbally, C. J., Garrison, R. F., McFadden, M. T., Bubar, E. J., McGahee, C. E., O'Donoghue, A. A., and Knox, E. R. (2006). "Contributions to the Nearby Stars (NStars) Project: Spectroscopy of Stars Earlier than M0 within 40 Pc-The Southern Sample". *The Astronomical Journal* 132. DOI: 10.1086/504637.

Gray, R. O., Corbally, C. J., Garrison, R. F., McFadden, M. T., and Robinson, P. E. (2003). "Contributions to the Nearby Stars (NStars) Project: Spectroscopy of Stars Earlier than M0 within 40 Parsecs: The Northern Sample. I." *The Astronomical Journal* 126. DOI: 10.1086/378365.

Hall, J. C. (2008). "Stellar Chromospheric Activity". *Living Reviews in Solar Physics* 5. DOI: 10.12942/lrsp-2008-2.

Hall, J. C., Lockwood, G. W., and Skiff, B. A. (2007). "The Activity and Variability of the Sun and Sun-like Stars. I. Synoptic Ca II H and K Observations". *The Astronomical Journal* 133. DOI: 10.1086/510356.

Hanuschik, R. W. (2003). "A Flux-Calibrated, High-Resolution Atlas of Optical Sky Emission from UVES". *Astronomy & Astrophysics* 407. DOI: 10.1051/0004-6361:20030885.

Hathaway, D. H. (2010). "The Solar Cycle". *Living Reviews in Solar Physics* 7. DOI: 10.12942/lrsp-2010-1.

Hatzes, A. P. (2002). "Starspots and Exoplanets". *Astronomische Nachrichten* 323. DOI: 10.1002/1521-3994(200208)323:3/4<392::AID-ASNA392>3.0.CO;2-M.

Hatzes, A. P., Dvorak, R., Wuchterl, G., Guterman, P., Hartmann, M., Fridlund, M., Gandolfi, D., Guenther, E., and Pätzold, M. (2010). "An Investigation into the Radial Velocity Variations of CoRoT-7". *Astronomy & Astrophysics* 520. DOI: 10.1051/0004-6361/201014795.

Hatzes, A. P. (2013). "The Radial Velocity Detection of Earth-Mass Planets in the Presence of Activity Noise: The Case of α Centauri Bb". *The Astrophysical Journal* 770. DOI: 10.1088/0004-637X/770/2/133.

Hawley, S. L., Gizis, J. E., and Reid, I. N. (1996). "The Palomar/MSU Nearby Star Spectroscopic Survey.II.The Southern M Dwarfs and Investigation of Magnetic Activity". *The Astronomical Journal* 112. DOI: 10.1086/118222.

Haywood, R. D., Collier Cameron, A., Queloz, D., Barros, S. C. C., Deleuil, M., Fares, R., Gillon, M., Lanza, A. F., Lovis, C., Moutou, C., et al. (2014). "Planets and Stellar Activity: Hide and Seek in the CoRoT-7 System". *Monthly Notices of the Royal Astronomical Society* 443. DOI: 10.1093/mnras/stu1320.

Haywood, R. D., Collier Cameron, A., Unruh, Y. C., Lovis, C., Lanza, A. F., Llama, J., Deleuil, M., Fares, R., Gillon, M., Moutou, C., et al. (2016). "The Sun as a Planet-Host Star: Proxies from SDO Images for HARPS Radial-Velocity Variations". *Monthly Notices of the Royal Astronomical Society* 457. DOI: 10.1093/mnras/stw187.

Herrero, E., Ribas, I., Jordi, C., Morales, J. C., Perger, M., and Rosich, A. (2016). "Modelling the Photosphere of Active Stars for Planet Detection and Characterization". *Astronomy & Astrophysics* 586. DOI: 10.1051/0004-6361/201425369.

Hintz, D., Fuhrmeister, B., Czesla, S., Schmitt, J. H. M. M., Johnson, E. N., Schweitzer, A., Caballero, J. A., Zechmeister, M., Jeffers, S. V., Reiners, A., et al. (2019). "The CARMENES Search for Exoplanets around M Dwarfs. Chromospheric Modeling of M 2–3 V Stars with PHOENIX". *Astronomy & Astrophysics* 623. DOI: 10.1051/0004-6361/201834788.

Hintz, D., Fuhrmeister, B., Czesla, S., Schmitt, J. H. M. M., Schweitzer, A., Nagel, E., Johnson, E. N., Caballero, J. A., Zechmeister, M., Jeffers, S. V., et al. (2020). "The CARMENES Search for Exoplanets around M Dwarfs. The He I Infrared Triplet Lines in PHOENIX Models of M 2-3 V Stars". *Astronomy & Astrophysics* 638. DOI: 10.1051/0004-6361/202037596.

Hoekzema, N. M., Brandt, P. N., and Rutten, R. J. (1998). "Small-Scale Topology of Solar Atmosphere Dynamics. III. Granular Persistence and Photospheric Wave Amplitudes". *Astronomy & Astrophysics* 333.

Houdebine, E. R., Junghans, K., Heanue, M. C., and Andrews, A. D. (2009). "Observation and Modelling of Main Sequence Star Chromospheres. VIII. High Resolution Observations of M and K Dwarf Chromospheric Lines". *Astronomy & Astrophysics* 503. DOI: 10.1051/0004-6361/200811349.

Huélamo, N., Figueira, P., Bonfils, X., Santos, N. C., Pepe, F., Gillon, M., Azevedo, R., Barman, T., Fernández, M., di Folco, E., et al. (2008). "TW Hydrae: Evidence of Stellar Spots Instead of a Hot Jupiter". *Astronomy & Astrophysics* 489. DOI: 10.1051/0004-6361:200810596.

Husser, T.-O., Wende-von Berg, S., Dreizler, S., Homeier, D., Reiners, A., Barman, T., and Hauschildt, P. H. (2013). "A New Extensive Library of PHOENIX Stellar Atmospheres and Synthetic Spectra". *Astronomy & Astrophysics* 553. DOI: 10.1051/0004-6361/201219058.

Jeffers, S. V., Schöfer, P., Lamert, A., Reiners, A., Montes, D., Caballero, J. A., Cortés-Contreras, M., Marvin, C. J., Passegger, V. M., Zechmeister, M., et al. (2018). "CARMENES Input Catalogue of M Dwarfs. III. Rotation and Activity from High-Resolution Spectroscopic Observations". *Astronomy & Astrophysics* 614. DOI: 10.1051/0004-6361/201629599.

Jones, J. E., Alloin, D. M., and Jones, B. J. T. (1984). "The Infrared CA II Triplet - A Luminosity Indicator for Stellar Population Synthesis". *The Astrophysical Journal* 283. DOI: 10.1086/162325.

Jorgensen, U. G., Carlsson, M., and Johnson, H. R. (1992). "The Calcium Infrared Triplet Lines in Stellar Spectra". *Astronomy & Astrophysics* 254.

Jurgenson, C., Fischer, D., McCracken, T., Sawyer, D., Szymkowiak, A., Davis, A., Muller, G., and Santoro, F. (2016). "EXPRES: A next Generation RV Spectrograph in the Search for Earth-like Worlds". 9908. DOI: 10.1117/12.2233002.

Kafka, S. and Honeycutt, R. K. (2006). "Spectroscopy of Active and Inactive M Dwarfs in Praesepe". *The Astronomical Journal* 132. DOI: 10.1086/506561.

Kaminski, A., Trifonov, T., Caballero, J. A., Quirrenbach, A., Ribas, I., Reiners, A., Amado, P. J., Zechmeister, M., Dreizler, S., Perger, M., et al. (2018). "The CARMENES Search for Exoplanets around M Dwarfs. A Neptune-Mass Planet Traversing the Habitable Zone around HD 180617". *Astronomy & Astrophysics* 618. DOI: 10.1051/0004-6361/201833354.

Kiraga, M. and Stepien, K. (2007). "Age-Rotation-Activity Relations for M Dwarf Stars". *Acta Astronomica* 57.

Kirkpatrick, J. D., Henry, T. J., and McCarthy Jr., D. W. (1991). "A Standard Stellar Spectral Sequence in the Red/near-Infrared - Classes K5 to M9". *The Astrophysical Journal Supplement Series* 77. DOI: 10.1086/191611.

Kirkpatrick, J. D., Reid, I. N., Liebert, J., Cutri, R. M., Nelson, B., Beichman, C. A., Dahn, C. C., Monet, D. G., Gizis, J. E., and Skrutskie, M. F. (1999). "Dwarfs Cooler than "M": The Definition of Spectral Type "L" Using Discoveries from the 2 Micron All-Sky Survey (2MASS)". *The Astrophysical Journal* 519. DOI: 10.1086/307414.

Kossakowski, D., Kürster, M., Trifonov, T., Bauer, F. F., Lafarga, M., Cortés-Contreras, M., Caballero, J. A., Jeffers, S. V., Zechmeister, M., Reiners, A., et al. (in preparation). "The

CARMENES Search for Exoplanets around M Dwarfs. AD Leonis: Stellar Activity Prevails in New CARMENES Data".

Kotani, T., Tamura, M., Suto, H., Nishikawa, J., Sato, B., Aoki, W., Usuda, T., Kurokawa, T., Kashiwagi, K., Nishiyama, S., et al. (2014). "Infrared Doppler Instrument (IRD) for the Subaru Telescope to Search for Earth-like Planets around Nearby M-Dwarfs". 9147. DOI: 10.1117/12.2055075.

Kraft, R. P. (1967). "Studies of Stellar Rotation. V. The Dependence of Rotation on Age among Solar-Type Stars". *The Astrophysical Journal* 150. DOI: 10.1086/149359.

Kürster, M., Endl, M., Rouesnel, F., Els, S., Kaufer, A., Brillant, S., Hatzes, A. P., Saar, S. H., and Cochran, W. D. (2003). "The Low-Level Radial Velocity Variability in Barnard's Star (= GJ 699). Secular Acceleration, Indications for Convective Redshift, and Planet Mass Limits". *Astronomy & Astrophysics* 403. DOI: 10.1051/0004-6361:20030396.

Lafarga, M., Ribas, I., Lovis, C., Perger, M., Zechmeister, M., Bauer, F. F., Kürster, M., Cortés-Contreras, M., Morales, J. C., Herrero, E., et al. (2020). "The CARMENES Search for Exoplanets around M Dwarfs. Radial Velocities and Activity Indicators from Cross-Correlation Functions with Weighted Binary Masks". *Astronomy & Astrophysics* 636. DOI: 10.1051/0004-6361/201937222.

Lagrange, A.-M., Desort, M., and Meunier, N. (2010). "Using the Sun to Estimate Earth-like Planets Detection Capabilities . I. Impact of Cold Spots". *Astronomy & Astrophysics* 512. DOI: 10.1051/0004-6361/200913071.

Lalitha, S., Baroch, D., Morales, J. C., Passegger, V. M., Bauer, F. F., Guillén, C. C., Dreizler, S., Oshagh, M., Reiners, A., Ribas, I., et al. (2019). "The CARMENES Search for Exoplanets around M Dwarfs. Detection of a Mini-Neptune around LSPM J2116+0234 and Refinement of Orbital Parameters of a Super-Earth around GJ 686 (BD+18 3421)". *Astronomy & Astrophysics* 627. DOI: 10.1051/0004-6361/201935534.

Lanza, A. F., Bonomo, A. S., Moutou, C., Pagano, I., Messina, S., Leto, G., Cutispoto, G., Aigrain, S., Alonso, R., Barge, P., et al. (2010). "Photospheric Activity, Rotation, and Radial Velocity Variations of the Planet-Hosting Star CoRoT-7". *Astronomy & Astrophysics* 520. DOI: 10.1051/0004-6361/201014403.

Lanza, A. F., Malavolta, L., Benatti, S., Desidera, S., Bignamini, A., Bonomo, A. S., Esposito, M., Figueira, P., Gratton, R., Scandariato, G., et al. (2018). "The GAPS Programme with HARPS-N at TNG. XVII. Line Profile Indicators and Kernel Regression as Diagnostics of Radial-Velocity Variations Due to Stellar Activity in Solar-like Stars". *Astronomy & Astrophysics* 616. DOI: 10.1051/0004-6361/201731010.

Leighton, R. B., Noyes, R. W., and Simon, G. W. (1962). "Velocity Fields in the Solar Atmosphere. I. Preliminary Report." *The Astrophysical Journal* 135. DOI: 10.1086/147285.

Lépine, S., Hilton, E. J., Mann, A. W., Wilde, M., Rojas-Ayala, B., Cruz, K. L., and Gaidos, E. (2013). "A Spectroscopic Catalog of the Brightest ($J < 9$) M Dwarfs in the Northern Sky". *The Astronomical Journal* 145. DOI: 10.1088/0004-6256/145/4/102.

Lépine, S., Rich, R. M., and Shara, M. M. (2007). "Revised Metallicity Classes for Low-Mass Stars: Dwarfs (dM), Subdwarfs (sdM), Extreme Subdwarfs (esdM), and Ultrasubdwarfs (usdM)". *The Astrophysical Journal* 669. DOI: 10.1086/521614.

Lindegren, L. and Dravins, D. (2003). "The Fundamental Definition of "radial Velocity"". *Astronomy & Astrophysics* 401. DOI: 10.1051/0004-6361:20030181.

Lisogorskyi, M., Jones, H. R. A., and Feng, F. (2019). "Activity and Telluric Contamination in HARPS Observations of Alpha Centauri B". *Monthly Notices of the Royal Astronomical Society* 485.4. DOI: 10.1093/mnras/stz694.

Livingston, W. C. (1982). "Magnetic Fields, Convection and Solar Luminosity Variability". *Nature* 297. DOI: 10.1038/297208a0.

Lo Curto, G., Pasquini, L., Manescau, A., Holzwarth, R., Steinmetz, T., Wilken, T., Probst, R., Udem, T., Hänsch, T. W., González Hernández, J., et al. (2012). "Astronomical Spectrograph Calibration at the Exo-Earth Detection Limit". *The Messenger* 149.

Löhner-Böttcher, J., Schmidt, W., Schlichenmaier, R., Steinmetz, T., and Holzwarth, R. (2019). "Convective Blueshifts in the Solar Atmosphere: III. High-Accuracy Observations of Spectral Lines in the Visible". *Astronomy & Astrophysics* 624. DOI: 10.1051/0004-6361/201834925.

Lomb, N. R. (1976). "Least-Squares Frequency Analysis of Unequally Spaced Data". *Astrophysics and Space Science* 39. DOI: 10.1007/BF00648343.

López-Santiago, J., Montes, D., Gálvez-Ortiz, M. C., Crespo-Chacón, I., Martínez-Arnáiz, R. M., Fernández-Figueroa, M. J., Castro, E. de, and Cornide, M. (2010). "A High-Resolution Spectroscopic Survey of Late-Type Stars: Chromospheric Activity, Rotation, Kinematics, and Age". *Astronomy & Astrophysics* 514. DOI: 10.1051/0004-6361/200913437.

Lovis, C., Dumusque, X., Santos, N. C., Bouchy, F., Mayor, M., Pepe, F., Queloz, D., Ségransan, D., and Udry, S. (2011). "The HARPS Search for Southern Extra-Solar Planets. XXXI. Magnetic Activity Cycles in Solar-Type Stars: Statistics and Impact on Precise Radial Velocities". *arXiv:1107.5325* [*astro-ph*]. arXiv: 1107.5325 [astro-ph].

Luque, R., Nowak, G., Pallé, E., Dai, F., Kaminski, A., Nagel, E., Hidalgo, D., Bauer, F., Lafarga, M., Livingston, J., et al. (2019a). "Detection and Characterization of an Ultra-Dense Sub-Neptunian Planet Orbiting the Sun-like Star K2-292". *Astronomy & Astrophysics* 623. DOI: 10.1051/0004-6361/201834952.

Luque, R., Nowak, G., Pallé, E., Kossakowski, D., Trifonov, T., Zechmeister, M., Béjar, V. J. S., Guillén, C. C., Tal-Or, L., Hidalgo, D., et al. (2018). "The CARMENES Search for Exoplanets around M Dwarfs - The Warm Super-Earths in Twin Orbits around the Mid-Type M Dwarfs Ross 1020 (GJ 3779) and LP 819-052 (GJ 1265)". *Astronomy & Astrophysics* 620. DOI: 10.1051/0004-6361/201833423.

Luque, R., Pallé, E., Kossakowski, D., Dreizler, S., Kemmer, J., Espinoza, N., Burt, J., Anglada-Escudé, G., Béjar, V. J. S., Caballero, J. A., et al. (2019b). "Planetary System around the Nearby M Dwarf GJ 357 Including a Transiting, Hot, Earth-Sized Planet Optimal for Atmospheric Characterization". *Astronomy & Astrophysics* 628. DOI: 10.1051/0004-6361/201935801.

Mahadevan, S., Ramsey, L. W., Terrien, R., Halverson, S., Roy, A., Hearty, F., Levi, E., Stefansson, G. K., Robertson, P., Bender, C., et al. (2014). "The Habitable-Zone Planet Finder: A Status Update on the Development of a Stabilized Fiber-Fed near-Infrared Spectrograph for the for the Hobby-Eberly Telescope". 9147. DOI: 10.1117/12.2056417.

Mallik, S. V. (1997). "The CA II Triplet Lines as Diagnostics of Luminosity, Metallicity and Chromospheric Activity in Cool Stars". *Astronomy & Astrophysics Supplement Series* 124. DOI: 10.1051/aas:1997199.

Mallonn, M., Herrero, E., Juvan, I. G., von Essen, C., Rosich, A., Ribas, I., Granzer, T., Alexoudi, X., and Strassmeier, K. G. (2018). "GJ 1214: Rotation Period, Starspots, and Uncertainty on the Optical Slope of the Transmission Spectrum". *Astronomy & Astrophysics* 614. DOI: 10.1051/0004-6361/201732300.

Mann, A. W., Dupuy, T., Kraus, A. L., Gaidos, E., Ansdell, M., Ireland, M., Rizzuto, A. C., Hung, C.-L., Dittmann, J., Factor, S., et al. (2019). "How to Constrain Your M Dwarf. II. The Mass-Luminosity-Metallicity Relation from 0.075 to 0.70 Solar Masses". *The Astrophysical Journal* 871. DOI: 10.3847/1538-4357/aaf3bc.

Marcy, G. W. and Butler, R. P. (1992). "Precision Radial Velocities with an Iodine Absorption Cell". *Publications of the Astronomical Society of the Pacific* 104. DOI: 10.1086/132989.

Marcy, G. W., Butler, R. P., Fischer, D., Vogt, S. S., Lissauer, J. J., and Rivera, E. J. (2001). "A Pair of Resonant Planets Orbiting GJ 876". *The Astrophysical Journal* 556. DOI: 10.1086/321552.

Marcy, G. W., Butler, R. P., Vogt, S. S., Fischer, D., and Lissauer, J. J. (1998). "A Planetary Companion to a Nearby M4 Dwarf, Gliese 876*". *The Astrophysical Journal Letters* 505.2. DOI: 10.1086/311623.

Marfil, E., Tabernero, H. M., Montes, D., Caballero, J. A., Soto, M. G., González Hernández, J. I., Kaminski, A., Nagel, E., Jeffers, S. V., Reiners, A., et al. (2020). "Stellar Atmospheric Parameters of FGK-Type Stars from High-Resolution Optical and near-Infrared CARMENES Spectra". *Monthly Notices of the Royal Astronomical Society* 492. DOI: 10.1093/mnras/staa058.

Martin, J., Fuhrmeister, B., Mittag, M., Schmidt, T. O. B., Hempelmann, A., González-Pérez, J. N., and Schmitt, J. H. M. M. (2017). "The Ca II Infrared Triplet's Performance as an Activity Indicator Compared to Ca II H and K. Empirical Relations to Convert Ca II Infrared Triplet Measurements to Common Activity Indices". *Astronomy & Astrophysics* 605. DOI: 10.1051/0004-6361/201630298.

Martínez-Rodríguez, H. (2014). "Master Thesis". Universidad Complutense de Madrid.

Martínez-Rodríguez, H., Caballero, J. A., Cifuentes, C., Piro, A. L., and Barnes, R. (2019). "Exomoons in the Habitable Zones of M Dwarfs". *The Astrophysical Journal* 887. DOI: 10.3847/1538-4357/ab5640.

Mayor, M., Pepe, F., Queloz, D., Bouchy, F., Rupprecht, G., Lo Curto, G., Avila, G., Benz, W., Bertaux, J.-L., Bonfils, X., et al. (2003). "Setting New Standards with HARPS". *The Messenger* 114.

Mayor, M. and Queloz, D. (1995). "A Jupiter-Mass Companion to a Solar-Type Star". *Nature* 378. DOI: 10.1038/378355a0.

Messina, S., Desidera, S., Lanzafame, A. C., Turatto, M., and Guinan, E. F. (2011). "RACE-OC Project: Rotation and Variability in the ε Chamaeleontis, Octans, and Argus Stellar Associations". *Astronomy & Astrophysics* 532. DOI: 10.1051/0004-6361/201016116.

Mestel, L. (1968). "Magnetic Braking by a Stellar Wind-I". *Monthly Notices of the Royal Astronomical Society* 138. DOI: 10.1093/mnras/138.3.359.

Meunier, N., Desort, M., and Lagrange, A.-M. (2010). "Using the Sun to Estimate Earth-like Planets Detection Capabilities . II. Impact of Plages". *Astronomy & Astrophysics* 512. DOI: 10.1051/0004-6361/200913551.

Meunier, N., Lagrange, A.-M., and Borgniet, S. (2017). "A New Method of Correcting Radial Velocity Time Series for Inhomogeneous Convection". *Astronomy & Astrophysics* 607. DOI: 10.1051/0004-6361/201630328.

Meunier, N., Lagrange, A.-M., Borgniet, S., and Rieutord, M. (2015). "Using the Sun to Estimate Earth-like Planet Detection Capabilities. VI. Simulation of Granulation and Supergranulation Radial Velocity and Photometric Time Series". *Astronomy & Astrophysics* 583. DOI: 10.1051/0004-6361/201525721.

Meunier, N., Lagrange, A.-M., and Desort, M. (2010). "Reconstructing the Solar Integrated Radial Velocity Using MDI/SOHO". *Astronomy & Astrophysics* 519. DOI: 10.1051/0004-6361/201014199.

Meunier, N., Lagrange, A.-M., Mbemba Kabuiku, L., Alex, M., Mignon, L., and Borgniet, S. (2017). "Variability of Stellar Granulation and Convective Blueshift with Spectral Type and Magnetic Activity. I. K and G Main Sequence Stars". *Astronomy & Astrophysics* 597. DOI: 10.1051/0004-6361/201629052.

Meunier, N., Mignon, L., and Lagrange, A.-M. (2017). "Variability in Stellar Granulation and Convective Blueshift with Spectral Type and Magnetic Activity . II. From Young to Old Main-Sequence K-G-F Stars". *Astronomy & Astrophysics* 607. DOI: 10.1051/0004-6361/201731017.

Middelkoop, F. (1982). "Magnetic Structure in Cool Stars. IV - Rotation and CA II H and K Emission of Main-Sequence Stars". *Astronomy & Astrophysics* 107.

Montes, D., Fernandez-Figueroa, M. J., de Castro, E., and Cornide, M. (1995). "Excess Hα Emission in Chromospherically Active Binaries." *Astronomy & Astrophysics* 294.

Morales, J. C., Mustill, A. J., Ribas, I., Davies, M. B., Reiners, A., Bauer, F. F., Kossakowski, D., Herrero, E., Rodríguez, E., López-González, M. J., et al. (2019). "A Giant Exoplanet Orbiting a Very-Low-Mass Star Challenges Planet Formation Models". *Science* 365.6460. DOI: 10.1126/science.aax3198.

Morin, J., Donati, J.-F., Petit, P., Delfosse, X., Forveille, T., Albert, L., Aurière, M., Cabanac, R., Dintrans, B., Fares, R., et al. (2008). "Large-Scale Magnetic Topologies of Mid M Dwarfs". *Monthly Notices of the Royal Astronomical Society* 390. DOI: 10.1111/j.1365-2966.2008.13809.x.

Morin, J., Donati, J.-F., Petit, P., Delfosse, X., Forveille, T., and Jardine, M. M. (2010). "Large-Scale Magnetic Topologies of Late M Dwarfs*". *Monthly Notices of the Royal Astronomical Society* 407. DOI: 10.1111/j.1365-2966.2010.17101.x.

Nagel, E., Czesla, S., Kaminski, A., Zechmeister, M., Tal-Or, L., Schmitt, J. H. M. M., Ribas, I., Reiners, A., Quirrenbach, A., Amado, P. J., et al. (submitted). "The CARMENES Search for Exoplanets around M Dwarfs. The Template Division Telluric Modeling Technique and Its Application to Opticaland near-Infrared Radial Velocities".

Nagel, E., Czesla, S., Schmitt, J. H. M. M., Dreizler, S., Anglada-Escudé, G., Rodríguez, E., Ribas, I., Reiners, A., Quirrenbach, A., Amado, P. J., et al. (2019). "The CARMENES Search for Exoplanets around M Dwarfs. The Enigmatic Planetary System GJ 4276: One Eccentric Planet or Two Planets in a 2:1 Resonance?" *Astronomy & Astrophysics* 622. DOI: 10.1051/0004-6361/201834569.

Nardetto, N., Mourard, D., Kervella, P., Mathias, P., Mérand, A., and Bersier, D. (2006). "High Resolution Spectroscopy for Cepheids Distance Determination. I. Line Asymmetry". *Astronomy & Astrophysics* 453.1. DOI: 10.1051/0004-6361:20054333.

Newton, E. R., Charbonneau, D., Irwin, J., Berta-Thompson, Z. K., Rojas-Ayala, B., Covey, K., and Lloyd, J. P. (2014). "Near-Infrared Metallicities, Radial Velocities, and Spectral Types for 447 Nearby M Dwarfs". *The Astronomical Journal* 147. DOI: 10.1088/0004-6256/147/1/20.

Newton, E. R., Irwin, J., Charbonneau, D., Berlind, P., Calkins, M. L., and Mink, J. (2017). "The Hα Emission of Nearby M Dwarfs and Its Relation to Stellar Rotation". *The Astrophysical Journal* 834. DOI: 10.3847/1538-4357/834/1/85.

Newton, E. R., Irwin, J., Charbonneau, D., Berta-Thompson, Z. K., Dittmann, J. A., and West, A. A. (2016). "The Rotation and Galactic Kinematics of Mid M Dwarfs in the Solar Neighborhood". *The Astrophysical Journal* 821. DOI: 10.3847/0004-637X/821/2/93.

Ning, B., Wise, A., Cisewski-Kehe, J., Dodson-Robinson, S., and Fischer, D. (2019). "Identifying Activity-Sensitive Spectral Lines: A Bayesian Variable Selection Approach". *The Astronomical Journal* 158.5. DOI: 10.3847/1538-3881/ab441c.

Nortmann, L., Pallé, E., Salz, M., Sanz-Forcada, J., Nagel, E., Alonso-Floriano, F. J., Czesla, S., Yan, F., Chen, G., Snellen, I. A. G., et al. (2018). "Ground-Based Detection of an Extended Helium Atmosphere in the Saturn-Mass Exoplanet WASP-69b". *Science* 362. DOI: 10.1126/science.aat5348.

Nowak, G., Luque, R., Parviainen, H., Pallé, E., Molaverdikhani, K., Béjar, V. J. S., Lillo-Box, J., Rodríguez-López, C., Caballero, J. A., Zechmeister, M., et al. (2020). "The CARMENES Search for Exoplanets around M Dwarfs - Two Planets on Opposite Sides of the Radius Gap Transiting the Nearby M Dwarf LTT 3780". *Astronomy & Astrophysics* 642. DOI: 10.1051/0004-6361/202037867.

Noyes, R. W., Hartmann, L. W., Baliunas, S. L., Duncan, D. K., and Vaughan, A. H. (1984). "Rotation, Convection, and Magnetic Activity in Lower Main-Sequence Stars". *The Astrophysical Journal* 279. DOI: 10.1086/161945.

Oliva, E., Origlia, L., Baffa, C., Biliotti, C., Bruno, P., D'Amato, F., Del Vecchio, C., Falcini, G., Gennari, S., Ghinassi, F., et al. (2006). "The GIANO-TNG Spectrometer". 6269. DOI: 10.1117/12.670006.

Pallé, E., Nowak, G., Luque, R., Hidalgo, D., Barragán, O., Prieto-Arranz, J., Hirano, T., Fridlund, M., Gandolfi, D., Livingston, J., et al. (2019). "Detection and Doppler Monitoring of K2-285 (EPIC 246471491), a System of Four Transiting Planets Smaller than Neptune". *Astronomy & Astrophysics* 623. DOI: 10.1051/0004-6361/201834001.

Parker, E. N. (1955). "Hydromagnetic Dynamo Models". *The Astrophysical Journal* 122. DOI: 10.1086/146087.

Passegger, V. M., Bello-García, A., Ordieres-Meré, J., Caballero, J. A., Schweitzer, A., González-Marcos, A., Ribas, I., Reiners, A., Quirrenbach, A., Amado, P. J., et al. (2020). "The CARMENES Search for Exoplanets around M Dwarfs. A Deep Learning Approach to Determine Fundamental Parameters of Target Stars". *Astronomy & Astrophysics* 642. DOI: 10.1051/0004-6361/202038787.

Passegger, V. M., Reiners, A., Jeffers, S. V., Wende-von Berg, S., Schöfer, P., Caballero, J. A., Schweitzer, A., Amado, P. J., Béjar, V. J. S., Cortés-Contreras, M., et al. (2018). "The CARMENES Search for Exoplanets around M Dwarfs. Photospheric Parameters of Target Stars from High-Resolution Spectroscopy". *Astronomy & Astrophysics* 615. DOI: 10.1051/0004-6361/201732312.

Passegger, V. M., Schweitzer, A., Shulyak, D., Nagel, E., Hauschildt, P. H., Reiners, A., Amado, P. J., Caballero, J. A., Cortés-Contreras, M., Domínguez-Fernández, A. J., et al. (2019). "The CARMENES Search for Exoplanets around M Dwarfs. Photospheric Parameters of Target Stars from High-Resolution Spectroscopy. II. Simultaneous Multiwavelength Range Modeling of Activity Insensitive Lines". *Astronomy & Astrophysics* 627. DOI: 10.1051/0004-6361/201935679.

Passegger, V. M., Wende-von Berg, S., and Reiners, A. (2016). "Fundamental M-Dwarf Parameters from High-Resolution Spectra Using PHOENIX ACES Models. I. Parameter Accuracy and Benchmark Stars". *Astronomy & Astrophysics* 587. DOI: 10.1051/0004-6361/201322261.

Pepe, F., Mayor, M., Galland, F., Naef, D., Queloz, D., Santos, N. C., Udry, S., and Burnet, M. (2002). "The CORALIE Survey for Southern Extra-Solar Planets VII. Two Short-Period Saturnian Companions to HD 108147 and HD 168746". *Astronomy & Astrophysics* 388. DOI: 10.1051/0004-6361:20020433.

Pepe, F., Cameron, A. C., Latham, D. W., Molinari, E., Udry, S., Bonomo, A. S., Buchhave, L. A., Charbonneau, D., Cosentino, R., Dressing, C. D., et al. (2013). "An Earth-Sized Planet with an Earth-like Density". *Nature* 503. DOI: 10.1038/nature12768.

Pepe, F., Cristiani, S., Rebolo Lopez, R., Santos, N. C., Amorim, A., Avila, G., Benz, W., Bonifacio, P., Cabral, A., Carvas, P., et al. (2010). "ESPRESSO: The Echelle Spectrograph for Rocky Exoplanets and Stable Spectroscopic Observations". 7735. DOI: 10.1117/12.857122.

Perger, M., Ribas, I., Damasso, M., Morales, J. C., Affer, L., Suárez Mascareño, A., Micela, G., Maldonado, J., González Hernández, J. I., Rebolo, R., et al. (2017). "HADES RV Programme with HARPS-N at TNG. VI. GJ 3942 b behind Dominant Activity Signals". *Astronomy & Astrophysics* 608. DOI: 10.1051/0004-6361/201731307.

Perger, M., Scandariato, G., Ribas, I., Morales, J. C., Affer, L., Azzaro, M., Amado, P. J., Anglada-Escudé, G., Baroch, D., Barrado, D., et al. (2019). "Gliese 49: Activity Evolution and Detection of a Super-Earth. A HADES and CARMENES Collaboration". *Astronomy & Astrophysics* 624. DOI: 10.1051/0004-6361/201935192.

Pesnell, W. D., Thompson, B. J., and Chamberlin, P. C. (2012). "The Solar Dynamics Observatory (SDO)". *Solar Physics* 275. DOI: 10.1007/s11207-011-9841-3.

Petersburg, R. R., Ong, J. M. J., Zhao, L. L., Blackman, R. T., Brewer, J. M., Buchhave, L. A., Cabot, S. H. C., Davis, A. B., Jurgenson, C. A., Leet, C., et al. (2020). "An Extreme-Precision Radial-Velocity Pipeline: First Radial Velocities from EXPRES". *The Astronomical Journal* 159. DOI: 10.3847/1538-3881/ab7e31.

Phillips, D. F., Glenday, A. G., Dumusque, X., Buchschacher, N., Cameron, A. C., Cecconi, M., Charbonneau, D., Cosentino, R., Ghedina, A., Haywood, R., et al. (2016). "An Astro-Comb Calibrated Solar Telescope to Search for the Radial Velocity Signature of Venus". *Advances in Optical and Mechanical Technologies for Telescopes and Instrumentation II*. Vol. 9912. International Society for Optics and Photonics. DOI: 10.1117/12.2232452.

Plavchan, P., Barclay, T., Gagné, J., Gao, P., Cale, B., Matzko, W., Dragomir, D., Quinn, S., Feliz, D., Stassun, K., et al. (2020). "A Planet within the Debris Disk around the Pre-Main-Sequence Star AU Microscopii". *Nature* 582. DOI: 10.1038/s41586-020-2400-z.

Pojmanski, G. (1997). "The All Sky Automated Survey". *Acta Astronomica* 47.

Queloz, D., Bouchy, F., Moutou, C., Hatzes, A., Hébrard, G., Alonso, R., Auvergne, M., Baglin, A., Barbieri, M., Barge, P., et al. (2009). "The CoRoT-7 Planetary System: Two Orbiting Super-Earths". *Astronomy & Astrophysics* 506. DOI: 10.1051/0004-6361/200913096.

Queloz, D., Henry, G. W., Sivan, J. P., Baliunas, S. L., Beuzit, J. L., Donahue, R. A., Mayor, M., Naef, D., Perrier, C., and Udry, S. (2001). "No Planet for HD 166435". *Astronomy & Astrophysics* 379. DOI: 10.1051/0004-6361:20011308.

Queloz, D. (1995). "Echelle Spectroscopy with a CCD at Low Signal-To-Noise Ratio". *New Developments in Array Technology and Applications* 167.

Quirrenbach, A., Amado, P. J., Caballero, J. A., Mundt, R., Reiners, A., Ribas, I., Seifert, W., Abril, M., Aceituno, J., Alonso-Floriano, F. J., et al. (2016). "CARMENES: An Overview Six Months after First Light". *Ground-Based and Airborne Instrumentation for Astronomy VI*. Vol. 9908. International Society for Optics and Photonics. DOI: 10.1117/12.2231880.

Quirrenbach, A., Amado, P. J., Ribas, I., Reiners, A., Caballero, J. A., Seifert, W., Aceituno, J., Azzaro, M., Baroch, D., Barrado, D., et al. (2018). "CARMENES: High-Resolution Spectra and Precise Radial Velocities in the Red and Infrared". *Ground-Based and Airborne Instrumentation for Astronomy VII*. Vol. 10702. International Society for Optics and Photonics. DOI: 10.1117/12.2313689.

Rainer, M., Borsa, F., and Affer, L. (2020). "Stellar Masks and Bisector's Shape for M-Type Stars Observed in the GAPS Programme with HARPS-N at TNG". *Experimental Astronomy* 49. DOI: 10.1007/s10686-020-09654-z.

Rajpaul, V. M., Aigrain, S., and Buchhave, L. A. (2020). "A Robust, Template-Free Approach to Precise Radial Velocity Extraction". *Monthly Notices of the Royal Astronomical Society*. DOI: 10.1093/mnras/stz3599.

Rajpaul, V., Aigrain, S., Osborne, M. A., Reece, S., and Roberts, S. (2015). "A Gaussian Process Framework for Modelling Stellar Activity Signals in Radial Velocity Data". *Monthly Notices of the Royal Astronomical Society* 452. DOI: 10.1093/mnras/stv1428.

Rajpaul, V., Aigrain, S., and Roberts, S. (2016). "Ghost in the Time Series: No Planet for Alpha Cen B". *Monthly Notices of the Royal Astronomical Society* 456. DOI: 10.1093/mnrasl/slv164.

Rast, M. P. (2003). "The Scales of Granulation, Mesogranulation, and Supergranulation". *The Astrophysical Journal* 597. DOI: 10.1086/381221.

Rayner, J., Tokunaga, A., Jaffe, D., Bonnet, M., Ching, G., Connelley, M., Kokubun, D., Lockhart, C., and Warmbier, E. (2016). "iSHELL: A Construction, Assembly and Testing". 9908. DOI: 10.1117/12.2232064.

Reegen, P. (2007). "SigSpec. I. Frequency- and Phase-Resolved Significance in Fourier Space". *Astronomy & Astrophysics* 467. DOI: 10.1051/0004-6361:20066597.

Reid, I. N. and Hawley, S. L. (2005). "New Light on Dark Stars : Red Dwarfs, Low-Mass Stars, Brown Dwarfs". *New Light on Dark Stars Red Dwarfs, Low-Mass Stars, Brown Stars, by I.N. Reid and S.L. Hawley. Springer-Praxis books in astrophysics and astronomy. Praxis Publishing Ltd, 2005. ISBN 3-540-25124-3*.

Reid, I. N., Hawley, S. L., and Gizis, J. E. (1995). "The Palomar/MSU Nearby-Star Spectroscopic Survey. I. The Northern M Dwarfs -Bandstrengths and Kinematics". *The Astronomical Journal* 110. DOI: 10.1086/117655.

Reiners, A. (2009). "Activity-Induced Radial Velocity Jitter in a Flaring M Dwarf". *Astronomy & Astrophysics* 498. DOI: 10.1051/0004-6361/200810257.

Reiners, A., Ribas, I., Zechmeister, M., Caballero, J. A., Trifonov, T., Dreizler, S., Morales, J. C., Tal-Or, L., Lafarga, M., Quirrenbach, A., et al. (2018a). "The CARMENES Search for Exoplanets around M Dwarfs. HD147379 b: A Nearby Neptune in the Temperate Zone of an Early-M Dwarf". *Astronomy & Astrophysics* 609. DOI: 10.1051/0004-6361/201732165.

Reiners, A., Schüssler, M., and Passegger, V. M. (2014). "Generalized Investigation of the Rotation-Activity Relation: Favoring Rotation Period Instead of Rossby Number". *The Astrophysical Journal* 794. DOI: 10.1088/0004-637X/794/2/144.

Reiners, A., Zechmeister, M., Caballero, J. A., Ribas, I., Morales, J. C., Jeffers, S. V., Schöfer, P., Tal-Or, L., Quirrenbach, A., Amado, P. J., et al. (2018b). "The CARMENES Search for Exoplanets around M Dwarfs. High-Resolution Optical and near-Infrared Spectroscopy of 324 Survey Stars". *Astronomy & Astrophysics* 612. DOI: 10.1051/0004-6361/201732054.

Riaz, B., Gizis, J. E., and Harvin, J. (2006). "Identification of New M Dwarfs in the Solar Neighborhood". *The Astronomical Journal* 132. DOI: 10.1086/505632.

Ribas, I., Tuomi, M., Reiners, A., Butler, R. P., Morales, J. C., Perger, M., Dreizler, S., Rodríguez-López, C., Hernández, J. I. G., Rosich, A., et al. (2018). "A Candidate Super-Earth Planet

Orbiting near the Snow Line of Barnard's Star". *Nature* 563.7731. DOI: 10.1038/s41586-018-0677-y.

Rieutord, M. and Rincon, F. (2010). "The Sun's Supergranulation". *Living Reviews in Solar Physics* 7. DOI: 10.12942/lrsp-2010-2.

Robertson, P., Bender, C., Mahadevan, S., Roy, A., and Ramsey, L. W. (2016). "Proxima Centauri as a Benchmark for Stellar Activity Indicators in the Near-Infrared". *The Astrophysical Journal* 832. DOI: 10.3847/0004-637X/832/2/112.

Robertson, P., Endl, M., Henry, G. W., Cochran, W. D., MacQueen, P. J., and Williamson, M. H. (2015). "Stellar Activity and Its Implications for Exoplanet Detection on GJ 176". *The Astrophysical Journal* 801. DOI: 10.1088/0004-637X/801/2/79.

Robertson, P., Stefansson, G., Mahadevan, S., Endl, M., Cochran, W. D., Beard, C., Bender, C. F., Diddams, S. A., Duong, N., Ford, E. B., et al. (2020). "Persistent Starspot Signals on M Dwarfs: Multiwavelength Doppler Observations with the Habitable-Zone Planet Finder and Keck/HIRES". *The Astrophysical Journal* 897. DOI: 10.3847/1538-4357/ab989f.

Rodríguez-López, C., MacDonald, J., Amado, P. J., Moya, A., and Mullan, D. (2014). "The Theoretical Instability Strip of M Dwarf Stars". *Monthly Notices of the Royal Astronomical Society* 438. DOI: 10.1093/mnras/stt2352.

Rodríguez-López, C. (2019). "The Quest for Pulsating M Dwarf Stars". *Frontiers in Astronomy and Space Sciences* 6. DOI: 10.3389/fspas.2019.00076.

Rodríguez, E., Rodríguez-López, C., López-González, M. J., Amado, P. J., Ocando, S., and Berdiñas, Z. M. (2016). "Search for Pulsations in M Dwarfs in the Kepler Short-Cadence Data Base". *Monthly Notices of the Royal Astronomical Society* 457. DOI: 10.1093/mnras/stw033.

Rosich, A., Herrero, E., Mallonn, M., Ribas, I., Morales, J. C., Perger, M., Anglada-Escudé, G., and Granzer, T. (2020). "Correcting for Chromatic Stellar Activity Effects in Transits with Multiband Photometric Monitoring: Application to WASP-52". *Astronomy and Astrophysics* 641. DOI: 10.1051/0004-6361/202037586.

Saar, S. H. (2003). "The Effects of Plage on Precision Radial Velocities". 294.

Saar, S. H. and Donahue, R. A. (1997). "Activity-Related Radial Velocity Variation in Cool Stars". *The Astrophysical Journal* 485.1. DOI: 10.1086/304392.

Saar, S. H. and Fischer, D. (2000). "Correcting Radial Velocities for Long-Term Magnetic Activity Variations". *The Astrophysical Journal Letters* 534. DOI: 10.1086/312648.

Salz, M., Czesla, S., Schneider, P. C., Nagel, E., Schmitt, J. H. M. M., Nortmann, L., Alonso-Floriano, F. J., López-Puertas, M., Lampón, M., Bauer, F. F., et al. (2018). "Detection of He I Λ10830 Å Absorption on HD 189733 b with CARMENES High-Resolution Transmission Spectroscopy". *Astronomy & Astrophysics* 620. DOI: 10.1051/0004-6361/201833694.

Sánchez-López, A., Alonso-Floriano, F. J., López-Puertas, M., Snellen, I. A. G., Funke, B., Nagel, E., Bauer, F. F., Amado, P. J., Caballero, J. A., Czesla, S., et al. (2019). "Water Vapor Detection in the Transmission Spectra of HD 209458 b with the CARMENES NIR Channel". *Astronomy & Astrophysics* 630. DOI: 10.1051/0004-6361/201936084.

Santos, N. C., Gomes da Silva, J., Lovis, C., and Melo, C. (2010). "Do Stellar Magnetic Cycles Influence the Measurement of Precise Radial Velocities?" *Astronomy & Astrophysics* 511. DOI: 10.1051/0004-6361/200913433.

Santos, N. C., Mortier, A., Faria, J. P., Dumusque, X., Adibekyan, V. Z., Delgado-Mena, E., Figueira, P., Benamati, L., Boisse, I., Cunha, D., et al. (2014). "The HARPS Search for Southern Extra-Solar Planets. XXXV. The Interesting Case of HD 41248: Stellar Activity, No Planets?" *Astronomy & Astrophysics* 566. DOI: 10.1051/0004-6361/201423808.

Scargle, J. D. (1982). "Studies in Astronomical Time Series Analysis. II - Statistical Aspects of Spectral Analysis of Unevenly Spaced Data". *The Astrophysical Journal* 263. DOI: 10.1086/160554.

Schatzman, E. (1962). "A Theory of the Role of Magnetic Activity during Star Formation". *Annales d'Astrophysique* 25.

Schlieder, J. E., Lépine, S., Rice, E., Simon, M., Fielding, D., and Tomasino, R. (2012). "The Na 8200 Å Doublet as an Age Indicator in Low-Mass Stars". *The Astronomical Journal* 143. DOI: 10.1088/0004-6256/143/5/114.

Schmidt, S. J., Kowalski, A. F., Hawley, S. L., Hilton, E. J., Wisniewski, J. P., and Tofflemire, B. M. (2012). "Probing the Flare Atmospheres of M Dwarfs Using Infrared Emission Lines". *The Astrophysical Journal* 745. DOI: 10.1088/0004-637X/745/1/14.

Schöfer, P., Jeffers, S. V., Reiners, A., Shulyak, D., Fuhrmeister, B., Johnson, E. N., Zechmeister, M., Ribas, I., Quirrenbach, A., Amado, P. J., et al. (2019). "The CARMENES Search for Exoplanets around M Dwarfs. Activity Indicators at Visible and near-Infrared Wavelengths". *Astronomy & Astrophysics* 623. DOI: 10.1051/0004-6361/201834114.

Schöfer, P., Jeffers, S. V., Reiners, A., Zechmeister, M., Fuhrmeister, B., Lafarga, M., Ribas, I., Quirrenbach, A., Amado, P. J., Caballero, J. A., et al. (submitted). "The CARMENES Search for Exoplanets around M Dwarfs. Rotational Variation in Activity Indicators of EV Lac, YZ CMi, and Two Northern Slow Rotators".

Schrijver, C. J. and Zwaan, C. (2000). *Solar and Stellar Magnetic Activity*.

Schuster, A. (1898). "On the Investigation of Hidden Periodicities with Application to a Supposed 26 Day Period of Meteorological Phenomena". *Terrestrial Magnetism (Journal of Geophysical Research)* 3. DOI: 10.1029/TM003i001p00013.

Schweitzer, A., Passegger, V. M., Cifuentes, C., Béjar, V. J. S., Cortés-Contreras, M., Caballero, J. A., Burgo, C. del, Czesla, S., Kürster, M., Montes, D., et al. (2019). "The CARMENES Search for Exoplanets around M Dwarfs. Different Roads to Radii and Masses of the Target Stars". *Astronomy & Astrophysics* 625. DOI: 10.1051/0004-6361/201834965.

Seifahrt, A., Stürmer, J., Bean, J. L., and Schwab, C. (2018). "MAROON-X: A Radial Velocity Spectrograph for the Gemini Observatory". 0702. DOI: 10.1117/12.2312936.

Shulyak, D., Reiners, A., Nagel, E., Tal-Or, L., Caballero, J. A., Zechmeister, M., Béjar, V. J. S., Cortés-Contreras, M., Martin, E. L., Kaminski, A., et al. (2019). "Magnetic Fields in M Dwarfs from the CARMENES Survey". *Astronomy & Astrophysics* 626. DOI: 10.1051/0004-6361/201935315.

Simola, U., Dumusque, X., and Cisewski-Kehe, J. (2019). "Measuring Precise Radial Velocities and Cross-Correlation Function Line-Profile Variations Using a Skew Normal Density". *Astronomy & Astrophysics* 622. DOI: 10.1051/0004-6361/201833895.

Skrutskie, M. F., Cutri, R. M., Stiening, R., Weinberg, M. D., Schneider, S., Carpenter, J. M., Beichman, C., Capps, R., Chester, T., Elias, J., et al. (2006). "The Two Micron All Sky Survey (2MASS)". *The Astronomical Journal* 131.2. DOI: 10.1086/498708.

Skumanich, A. (1972). "Time Scales for Ca II Emission Decay, Rotational Braking, and Lithium Depletion". *The Astrophysical Journal* 171. DOI: 10.1086/151310.

Spiegel, E. A. and Zahn, J.-P. (1992). "The Solar Tachocline". *Astronomy & Astrophysics* 265.

Spina, L., Nordlander, T., Casey, A. R., Bedell, M., D'Orazi, V., Meléndez, J., Karakas, A. I., Desidera, S., Baratella, M., Yana Galarza, J. J., et al. (2020). "How Magnetic Activity Alters What We Learn from Stellar Spectra". *The Astrophysical Journal* 895. DOI: 10.3847/1538-4357/ab8bd7.

Stauffer, J. R. and Hartmann, L. W. (1986). "Chromospheric Activity, Kinematics, and Metallicities of Nearby M Dwarfs". *The Astrophysical Journal Supplement Series* 61. DOI: 10.1086/191123.

Strassmeier, K. G. (2009). "Starspots". *Astronomy and Astrophysics Review* 17. DOI: 10.1007/s00159-009-0020-6.

Suárez Mascareño, A., Rebolo, R., and González Hernández, J. I. (2016). "Magnetic Cycles and Rotation Periods of Late-Type Stars from Photometric Time Series". *Astronomy & Astrophysics* 595. DOI: 10.1051/0004-6361/201628586.

Suárez Mascareño, A., Rebolo, R., González Hernández, J. I., and Esposito, M. (2015). "Rotation Periods of Late-Type Dwarf Stars from Time Series High-Resolution Spectroscopy of Chromospheric Indicators". *Monthly Notices of the Royal Astronomical Society* 452. DOI: 10.1093/mnras/stv1441.

Suárez Mascareño, A., Rebolo, R., González Hernández, J. I., and Esposito, M. (2017). "Characterization of the Radial Velocity Signal Induced by Rotation in Late-Type Dwarfs". *Monthly Notices of the Royal Astronomical Society* 468. DOI: 10.1093/mnras/stx771.

Suárez Mascareño, A., Rebolo, R., González Hernández, J. I., Toledo-Padrón, B., Perger, M., Ribas, I., Affer, L., Micela, G., Damasso, M., Maldonado, J., et al. (2018). "HADES RV Programme with HARPS-N at TNG. VII. Rotation and Activity of M-Dwarfs from Time-Series High-Resolution Spectroscopy of Chromospheric Indicators". *Astronomy & Astrophysics* 612. DOI: 10.1051/0004-6361/201732143.

Tal-Or, L., Zechmeister, M., Reiners, A., Jeffers, S. V., Schöfer, P., Quirrenbach, A., Amado, P. J., Ribas, I., Caballero, J. A., Aceituno, J., et al. (2018). "The CARMENES Search for Exoplanets around M Dwarfs: Radial-Velocity Variations of Active Stars in Visual-Channel Spectra". *Astronomy & Astrophysics* 614. DOI: 10.1051/0004-6361/201732362.

Tal-Or, L., Trifonov, T., Zucker, S., Mazeh, T., and Zechmeister, M. (2019). "Correcting HIRES/Keck Radial Velocities for Small Systematic Errors". *Monthly Notices of the Royal Astronomical Society* 484.1. DOI: 10.1093/mnrasl/sly227.

Thompson, A. P. G., Watson, C. A., de Mooij, E. J. W., and Jess, D. B. (2017). "The Changing Face of α Centauri B: Probing Plage and Stellar Activity in K Dwarfs". *Monthly Notices of the Royal Astronomical Society: Letters* 468.1. DOI: 10.1093/mnrasl/slx018.

Thompson, A. P. G., Watson, C. A., Haywood, R. D., Costes, J. C., de Mooij, E., Collier Cameron, A., Dumusque, X., Phillips, D. F., Saar, S. H., Mortier, A., et al. (2020). "The Spectral Impact of Magnetic Activity on Disc-Integrated HARPS-N Solar Observations: Exploring New Activity Indicators". *Monthly Notices of the Royal Astronomical Society* 494. DOI: 10.1093/mnras/staa1010.

Torres, C. A. O., Quast, G. R., da Silva, L., de La Reza, R., Melo, C. H. F., and Sterzik, M. (2006). "Search for Associations Containing Young Stars (SACY). I. Sample and Searching Method". *Astronomy & Astrophysics* 460. DOI: 10.1051/0004-6361:20065602.

Trifonov, T., Kürster, M., Zechmeister, M., Tal-Or, L., Caballero, J. A., Quirrenbach, A., Amado, P. J., Ribas, I., Reiners, A., Reffert, S., et al. (2018). "The CARMENES Search for Exoplanets around M Dwarfs . First Visual-Channel Radial-Velocity Measurements and Orbital Parameter Updates of Seven M-Dwarf Planetary Systems". *Astronomy & Astrophysics* 609. DOI: 10.1051/0004-6361/201731442.

Tuomi, M., Jones, H. R. A., Butler, R. P., Arriagada, P., Vogt, S. S., Burt, J., Laughlin, G., Holden, B., Shectman, S. A., Crane, J. D., et al. (2019). "Frequency of Planets Orbiting M Dwarfs in the Solar Neighbourhood". *arXiv:1906.04644* [*astro-ph*]. arXiv: 1906.04644 [astro-ph].

Tuomi, M., Jones, H. R. A., Barnes, J. R., Anglada-Escudé, G., Butler, R. P., Kiraga, M., and Vogt, S. S. (2018). "AD Leonis: Radial Velocity Signal of Stellar Rotation or Spin-Orbit Resonance?" *The Astronomical Journal* 155. DOI: 10.3847/1538-3881/aab09c.

van Kerkwijk, M. H., van Paradijs, J., Zuiderwijk, E. J., Hammerschlag-Hensberge, G., Kaper, L., and Sterken, C. (1995). "Spectroscopy of HD77581 and the Mass of VELA X-1." *Astronomy & Astrophysics* 303.

VanderPlas, J. T. (2018). "Understanding the Lomb-Scargle Periodogram". *The Astrophysical Journal Supplement Series* 236.1. DOI: 10.3847/1538-4365/aab766.

Vaughan, A. H., Preston, G. W., and Wilson, O. C. (1978). "Flux Measurements of CA II H and K Emission". *Publications of the Astronomical Society of the Pacific* 90. DOI: 10.1086/130324.

Vogt, S. S., Allen, S. L., Bigelow, B. C., Bresee, L., Brown, B., Cantrall, T., Conrad, A., Couture, M., Delaney, C., Epps, H. W., et al. (1994). "HIRES: The High-Resolution Echelle Spectrometer on the Keck 10-m Telescope". 2198. DOI: 10.1117/12.176725.

Watson, C. L., Henden, A. A., and Price, A. (2006). "The International Variable Star Index (VSX)". *Society for Astronomical Sciences Annual Symposium* 25.

West, A. A., Hawley, S. L., Walkowicz, L. M., Covey, K. R., Silvestri, N. M., Raymond, S. N., Harris, H. C., Munn, J. A., McGehee, P. M., Ivezić, Ž., et al. (2004). "Spectroscopic Properties of Cool Stars in the Sloan Digital Sky Survey: An Analysis of Magnetic Activity and a Search for Subdwarfs". *The Astronomical Journal* 128. DOI: 10.1086/421364.

Wilson, O. C. (1963). "A Probable Correlation Between Chromospheric Activity and Age in Main-Sequence Stars." *The Astrophysical Journal* 138. DOI: 10.1086/147689.

— (1968). "Flux Measurements at the Centers of Stellar H- and K-Lines". *The Astrophysical Journal* 153. DOI: 10.1086/149652.

— (1978). "Chromospheric Variations in Main-Sequence Stars". *The Astrophysical Journal* 226. DOI: 10.1086/156618.

Wise, A. W., Dodson-Robinson, S. E., Bevenour, K., and Provini, A. (2018). "New Methods for Finding Activity-Sensitive Spectral Lines: Combined Visual Identification and an Automated Pipeline Find a Set of 40 Activity Indicators". *The Astronomical Journal* 156.4. DOI: 10.3847/1538-3881/aadd94.

Wright, N. J. and Drake, J. J. (2016). "Solar-Type Dynamo Behaviour in Fully Convective Stars without a Tachocline". *Nature* 535.7613. DOI: 10.1038/nature18638.

Wright, N. J., Newton, E. R., Williams, P. K. G., Drake, J. J., and Yadav, R. K. (2018). "The Stellar Rotation–Activity Relationship in Fully Convective M Dwarfs". *Monthly Notices of the Royal Astronomical Society* 479.2. DOI: 10.1093/mnras/sty1670.

Young, A., Skumanich, A., Stauffer, J. R., Bopp, B. W., and Harlan, E. (1989). "A Study of Excess H-Alpha Emission in Chromospherically Active M Dwarf". *The Astrophysical Journal* 344. DOI: 10.1086/167810.

Zechmeister, M., Anglada-Escudé, G., and Reiners, A. (2014). "Flat-Relative Optimal Extraction. A Quick and Efficient Algorithm for Stabilised Spectrographs". *Astronomy & Astrophysics* 561. DOI: 10.1051/0004-6361/201322746.

Zechmeister, M., Dreizler, S., Ribas, I., Reiners, A., Caballero, J. A., Bauer, F. F., Béjar, V. J. S., González-Cuesta, L., Herrero, E., Lalitha, S., et al. (2019). "The CARMENES Search for Exoplanets around M Dwarfs. Two Temperate Earth-Mass Planet Candidates around Teegarden's Star". *Astronomy & Astrophysics* 627. DOI: 10.1051/0004-6361/201935460.

Zechmeister, M. and Kürster, M. (2009). "The Generalised Lomb-Scargle Periodogram. A New Formalism for the Floating-Mean and Keplerian Periodograms". *Astronomy & Astrophysics* 496.2. DOI: 10.1051/0004-6361:200811296.

Zechmeister, M., Kürster, M., and Endl, M. (2009). "The M Dwarf Planet Search Programme at the ESO VLT + UVES. A Search for Terrestrial Planets in the Habitable Zone of M Dwarfs". *Astronomy & Astrophysics* 505.2. DOI: 10.1051/0004-6361/200912479.

Zechmeister, M., Reiners, A., Amado, P. J., Azzaro, M., Bauer, F. F., Béjar, V. J. S., Caballero, J. A., Guenther, E. W., Hagen, H.-J., Jeffers, S. V., et al. (2018). "Spectrum Radial Velocity Analyser (SERVAL). High-Precision Radial Velocities and Two Alternative Spectral Indicators". *Astronomy & Astrophysics* 609. DOI: 10.1051/0004-6361/201731483.

Zhao, J. and Tinney, C. G. (2020). "FIESTA - Disentangling Stellar Variability from Exoplanets in the Fourier Domain". *Monthly Notices of the Royal Astronomical Society* 491. DOI: 10.1093/mnras/stz3254.